FRACTURE TOUGHNESS AND ACOUSTIC EMISSION OF ALUMINA

A thesis
presented for the degree of
Doctor of Philosophy of the University of London

by
ABBAS FAKHR, B.Sc., M.Tech.

Metallurgy and Materials Science Department,
Royal School of Mines,
Imperial College of Science and Technology,
London S.W.7

January 1979

ABSTRACT

Samples of commercial polycrystalline alumina have been characterised in terms of their porosity, pore distribution, mean grain size, grain size distribution, density and the minor phases present. The acoustic emissions from these samples were monitored during modulus of rupture and fracture toughness testing.

At room temperature, emissions attributed to subcritical crack growth were observed prior to catastrophic failure in the three different test piece geometries commonly used for fracture toughness determination. The reliability of the test geometries and test procedures were evaluated from the fracture toughness and acoustic emission data, and the need to correct the initial stress intensity factor values for subcritical crack growth has been established.

The acoustic emission correction procedures were successfully applied to the experimental data for aluminas and porcelain, giving consistent results for the fracture toughness values. A theoretical expression has been derived on the basis of experimental results which relates the generated stress wave emission and the stress intensity factor of the material.

The influence of microstructural variables, such as grain size, porosity and second phase particles, on the acoustic emission and fracture toughness of alumina at room temperature, has been studied. For all microstructures the fracture was mainly intercrystalline, but some transcrystalline failure was also observed, usually confined to isolated large grains. However, the acoustic response and fracture toughness varied considerably with microstructure.

It was found that in aluminas of similar porosity, the stress wave emissions increased with increasing grain size, and the critical stress intensity values decreased with increasing grain size. If the porosity varied significantly, it was predominant in determining both the acoustic emission and fracture toughness values. Incorporation of second phase ZrO_2 particles in the

alumina matrix was found to increase the fracture toughness and acoustic response of the material, reaching a maximum at a certain volume fraction of ZrO_2.

Acoustic emission monitoring has also proved suitable for fracture toughness measurements at elevated temperatures. Deformation attributed to the flow of a grain boundary glassy phase was observed in alumina at high temperatures. Fracture surfaces of specimens tested above 650°C exhibited indications of the glassy phase flow at the grain boundaries. The temperature dependence of the fracture toughness, and the acoustic emission of different aluminas has been measured and the results interpreted in terms of the microstructure.

ACKNOWLEDGEMENTS

I would like to thank Dr. R.D. Rawlings who provided much encouragement and advice in supervising this work. I also wish to thank Professor J.G. Ball for the provision of research facilities and the Atomic Energy Organization of Iran for the financial support.

I am indebted to my research colleague, Dr. B.J. Dalgleish, for the valuable discussions and his collaboration in producing the micrographs. Thanks are also due to the members of the College technical staff for their help.

Finally I wish to thank my wife, for her continued patience, encouragement and assistance throughout my study.

CONTENTS

			Page
Abstract			
Acknowledgements			
Chapter 1:	Introduction		1
Chapter 2:	Basic Principles and Literature Review		5
2.1	Alumina		5
	2.1.1	General Considerations	5
	2.1.2	Structure of Alumina	5
	2.1.3	Fabrication Techniques	7
	2.1.4	Microstructure of Alumina	8
2.2	Fracture		9
	2.2.1	General Considerations	9
	2.2.2	Fracture Strength	11
	2.2.3	Fracture Toughness & K-V Diagram	11
	2.2.4	Fracture Strength and Toughness of Alumina at Room Temperature	14
	2.2.5	High Temperature Fracture Strength and Toughness of Alumina	21
	2.2.6	Second Phase Dispersion of ZrO_2 in an Alumina Matrix	23
2.3	Acoustic Emission		23
	2.3.1	General Considerations	23
	2.3.2	Generation of Acoustic Emission	26
	2.3.3	Propagation of Stress Waves	27
	2.3.4	The Detection of Stress Waves	28
	2.3.5	Signal Processing	30
	2.3.6	Factors influencing the AE Results	36
	2.3.7	Acoustic Response of Alumina	38
Chapter 3:	Apparatus and Experimental Procedure		41
3.1	Materials		41
3.2	Chemical and Minor Phase Analysis		42
3.3	Microstructural Analysis		42
	3.3.1	Grain Size and Pore Size Measurements	43
	3.3.2	Density Measurements	43
	3.3.3	Porosity Measurements	43

			Page
3.4	Mechanical Testing		44
	3.4.1	Specimen Preparation	44
	3.4.2	Loading Techniques	44
	3.4.3	Fracture Strength Determination at Room Temperature	45
	3.4.4	Fracture Toughness Determination at Room Temperature	46
3.5	Mechanical Testing at Elevated Temperatures		55
3.6	Acoustic Emission Measurements		57
	3.6.1	Data Acquisition Techniques	57
	3.6.2	The Transducer and its Coupling	60
	3.6.3	Pre-amplifier	60
	3.6.4	The Ring-down Counting Technique	61
	3.6.5	Amplitude and Pulse Width Distribution	61
3.7	Detection of AE at Elevated Temperatures		64
3.8	The Use of AE for Sub-critical Crack Measurements		65
Chapter 4:	Results and Discussion		68
4.1	Chemical Analysis		68
4.2	Microstructural Analysis		69
	4.2.1	Grain Size and Pore Size	69
	4.2.2	Density and Porosity	79
	4.2.3	Young's Modulus	80
4.3	Evaluation of Fracture Toughness Tests by AE		80
	4.3.1	Sub-critical Crack Growth during Fracture Toughness Tests	80
	4.3.2	The Influence of the Test Geometry on Fracture Toughness and AE	89
	4.3.3	The Influence of Notching Technique	101
	4.3.4	Mechanical Testing and AE at Various Strain Rates	108
	4.3.5	The Influence of the Initial Notch Length on Fracture Toughness and AE	119
4.4	The Microstructural Dependence of Mechanical Properties and Acoustic Response of Alumina		122
	4.4.1	The Microstructural Dependence of Fracture Strength and AE	122
	4.4.2	The Microstructural Dependence of Fracture Toughness and AE	126
	4.4.3	The Influence of Second Phase Dispersions in Alumina	141

Page

4.5 The Correlation of Fracture Toughness and the AE 147

4.6 Fracture Toughness and Acoustic Emission at Elevated Temperatures 149

Chapter 5: Conclusions and Suggestions for Further Work 164

5.1 Conclusions 164

5.1.1 Effect of Test Geometry, Notching Technique and the Notch Length 164

5.1.2 Effect of Strain Rate 165

5.1.3 The Influence of Microstructure 166

5.1.4 High Temperature Toughness and AE 167

5.2 Suggestions for Further Work 168

Appendix: The Fracture Toughness and AE of Porcelain 170

References: 178

CHAPTER 1

INTRODUCTION

The mechanical failure of ceramic materials is almost completely controlled by brittle fracture. The brittle behaviour, combined with the presence of inherent, and sometimes machining, flaws leads to poor mechanical properties compared with ductile metals, and puts a severe limitation on the use of ceramics as structural materials.

Brittleness is an inherent characteristic of ceramics and they often exhibit low and unpredictable tensile and bending strength. Any improvement in the mechanical properties of ceramics would be aided by a better understanding of: (i) the current testing procedure for fracture toughness determination, and (ii) the effect of microstructure on the mechanical properties. Both these aspects are covered in the present work.

The mechanical properties of ceramics are discussed in terms of their fracture strength and toughness, and these parameters are defined on the basis of the "flaw" concept introduced by A.A. Griffith in 1920[18]. Analytical solutions for the fracture strength and toughness are available for a variety of test-piece geometries. Specimens used for fracture toughness determination generally contain an initial crack, and it is assumed that no crack growth occurs prior to catastrophic failure. The standard procedure for brittle ceramics is to accept a fracture toughness test if there is a linear relationship between the load and displacement up to the point of failure, i.e. assume there is no subcritical crack growth. Fracture toughness is a material constant, thus if the standard procedure is met, the values obtained for a given material should be independent of the test geometry.

Alumina is a high quality ceramic having a fairly good strength and toughness, compared with the majority of ceramics. The strength and toughness of alumina have been the subject of

much investigation, but discrepancies still exist, and the precise role of microstructure in determining these parameters requires further study.

A comparison of the values reported for the room temperature fracture toughness of alumina does not always reveal clear trends. Some variation will undoubtedly be due to differences in the microstructural characteristics that influence toughness, and the difficulty of studying them independently. Nevertheless, toughness values have been reported, which, for example, either decrease[1-3], or increase[4] with increasing grain size. Furthermore, the values reported for the fracture toughness of a given material vary with test-piece geometry[5,6,3] especially as grain size increases. Simpson[6] concluded that the discrepancy was due to the use of different test geometries, and Pratt[7] subsequently suggested that the disagreement in the dependence of toughness on grain size could also stem partly from the fact that different test procedures were used. Thus it is essential to establish the reliability of the various test procedures if the influence of microstructure on fracture toughness is to be understood.

The single edge-notched beam (SENB), double torsion (DT) and double cantilever beam (DCB) specimen geometries are the most widely used for determining the fracture toughness of ceramics. These geometries contain a flaw, either in the form of a sharp pre-crack or a blunt machined notch. This difference in the flaw type has been an additional complication in comparing published data. Some reports indicate an increase of toughness in blunt-notched specimens[8,9] compared with sharp-cracked, whereas others show a decrease[3,10].

Thus there are conflicting views as to which test procedure should be employed for the purpose of comparing the effect of microstructural variables, on mechanical properties. The objective of the present work was:

(i) An assessment of the reliability of selected fracture toughness test-piece geometries by means of acoustic emission monitoring.

(ii) An evaluation of how reliability is influenced by specimen preparation and test procedure, and therefore to establish optimum test conditions.

(iii) To apply the findings of (i) and (ii) in a study of the influence of microstructure on the mechanical properties of polycrystalline alumina.

A pure mechanical approach to the testing of ceramics does not reveal much information regarding the behaviour of the material during crack propagation, deformation and fracture. Thus a new technique capable of continuously monitoring these processes is required. The acoustic emission technique can provide such information.

Acoustic emission (AE) is the term applied to the stress waves released as a result of dynamic processes, such as crack growth and plastic deformation, occurring within a material. With modern equipment the stress waves associated with these processes can be monitored. Consequently the acoustic emission has great potential as an in-service surveillance technique. At present the use of acoustic emission as a surveillance technique is limited by the lack of knowledge of the acoustic response of materials and the difficulties of detecting emissions from deformation processes and growing flaws against the high background noise usually present. Nevertheless, acoustic emission is a suitable technique for the continuous monitoring of fracture toughness tests under controlled laboratory conditions. The technique has been widely used in deformation studies on metals, but as yet limited information is available on the acoustic response of ceramics. With current interest in using ceramics as structural elements, the desirability of extending acoustic emission technology to the study of such brittle materials is obvious.

The continued application of acoustic emission as a technique for monitoring the deformation and fracture processes in materials, may lead to increased understanding of fracture in structural components. The technique is established as the only

method of non-destructive inspection which can be correlated with the crack tip stress intensity factor[11]. This correlation creates the demand for the development of acoustic emission test facilities, and the application of the technique to failure prediction in large structural systems.

CHAPTER 2

BASIC PRINCIPLES AND LITERATURE REVIEW

2.1 ALUMINA (Al_2O_3)

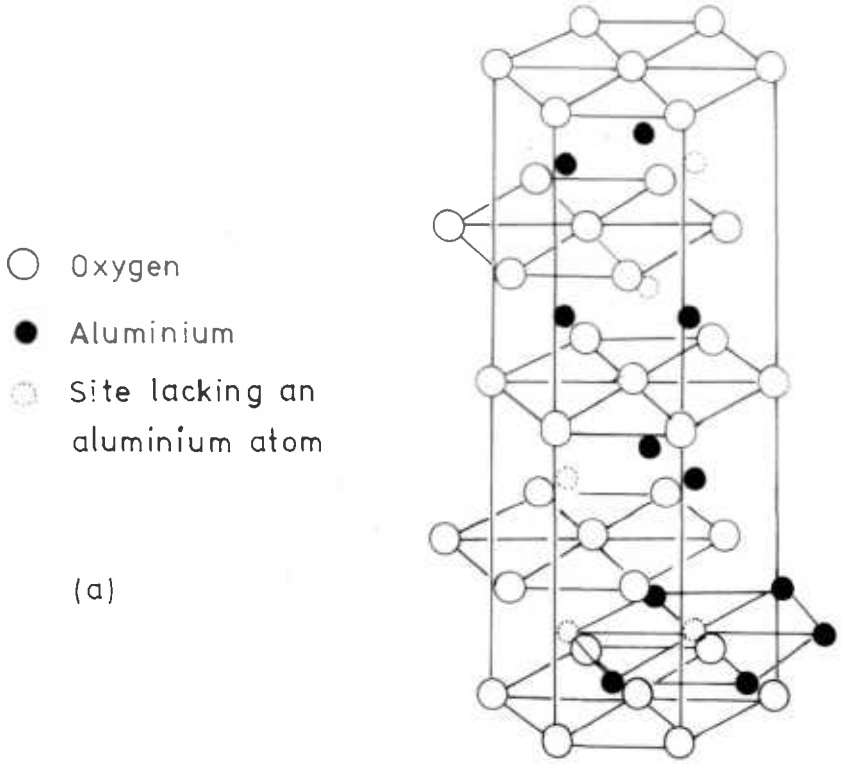
2.1.1 General Considerations

Alumina is among the most abundant constituents of the earth's crust and represents approximately 25% of the weight of solid rocks on the earth's surface[12]. Pure free alumina, corundum, is, however, a comparatively rare mineral. Essentially composed of alumina hydrates such as $Al(OH)_3$ [or $Al_2O_3.3H_2O$] known as gibbsite or hydrogillite, $Al_2(O)(OH)_4$ [or $Al_2O_3.2H_2O$] known as bauxite, and AlOOH [or $Al_2O_3.H_2O$] known as boehmite and diaspore. In most cases these minerals are mixed together and, in addition, exist with other oxide hydrates such as Fe_2O_3, TiO_2, SiO_2 and Cr_2O_3.

Technologically the most important aluminium mineral is bauxite, which is used for the production of alumina. Several techniques have been used to produce alumina on a commercial scale from its minerals. These techniques are based on decomposition of ores at high temperatures using chemicals, such as Na_2CO_3 and Na_2SO_4. High grade commercial alumina contains impurities of about 0.1-5 %, usually of the above-mentioned oxides. High purity alumina (99.99% pure) produced by more expensive processes is called Lucalox.

2.1.2 Strucure of Alumina

The most well-defined crystalline modification of aluminium oxide is alpha-alumina, which occurs naturally as corundum and is the terminal product of calcination of any other form of alumina above 1200°C[13]. The crystallographic structure of α-alumina has been determined by W.H. Zacharian (Fig. 2.1) in which hexagonally close-packed oxygen atoms enclose aluminium atoms. The density of zero



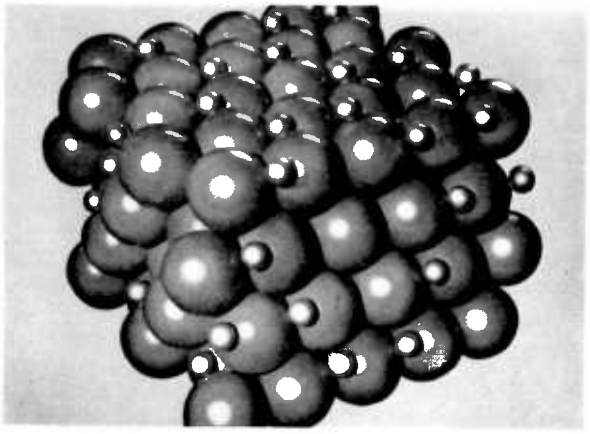


Fig.2.1. The structure of α-alumina.
a-Ref. (98)
b-Ref. (13)

porosity α-alumina is calculated[13] to be 3.89 g/cm^3. However, values obtained from direct measurements of pure corundum range from[14,15] 3.9 to 4.0 g/cm^3, and as a result of accurate determinations from X-ray data it is generally accepted that defect-free alumina would have a theoretical density of 3.986 g/cm^3 [14].

2.1.3 Fabrication Techniques

Alumina is available in dry powder form, having been prepared by chemical processing of less pure materials. The raw alumina has a fine particle size, but further grinding and milling may be necessary according to the fabrication process employed. There are several fabrication methods available which are characterized by their ability to form alumina components of different shapes and sizes, and to produce aluminas with a range of physical properties. These processes are:

(i) Powder Pressing. This process is used for forming the majority of ceramics and is accomplished by compacting a dry or damp powder in a metallic die under pressure.

(ii) Isostatic Powder Pressing. The powder is compacted under uniform pressure. This is carried out by charging a rubber mould with the powder and immersing the mould in a suitable fluid through which the pressure is applied.

(iii) Sintering. The "green" pressing from (i) and (ii) is dried and heated to elevated temperature so that sintering can take place. Sintering is the consolidation of an aggregate of fine particles into a dense product.

(iv) Uniaxial Hot Pressing. Ceramics made by cold pressing followed by sintering are generally porous owing to the difficulty of achieving complete densification. Also grain growth occurs when high sintering temperatures and long sintering times are employed. Hot pressing is a technique whereby densification of a compact occurs under the dual influence of high temperature and

pressure. A correct combination of temperature, pressure and time results in high ceramic density without extensive grain growth.

(v) Hot Isostatic Pressing. The process consists of placing the component to be hot isostatically pressed into a pressure vessel and applying high temperature and pressure. An inert gas is used to transfer the pressure[16]. Alumina specimens with densities up to 3.98 g/cm^3 (virtually theoretical density) can be produced using the HIP technique.

2.1.4 Microstructure of Alumina

The term microstructure is used to describe the internal structure of the material which can be seen using a light or electron microscope. The microstructure of alumina consists of α-alumina grains, pores, cracks and second phase distributions. The mechanical properties of alumina are strongly dependent on its microstructure and the microstructure is controlled by the choice of raw material and fabrication technique.

The body of pure alumina is very strong and consists of a network of fine-grained microscopically small crystallites, bonded together without any foreign binder. Examination of a polished surface of alumina in an optical microscope reveals irregular grains of varied size, ranging from a few microns in diameter up to sometimes 100μm. The irregularity of grain size is a result of fabrication. Hot pressing techniques provide aluminas of fairly uniform grain size, whilst the distribution of grain size in aluminas produced by cold pressing and air-sintering is quite extensive. The mean grain size and grain size distribution will normally influence the mechanical properties of the material and this influence will be discussed in more detail in Section 2.2.4.

Pure corundum contains no porosity and its theoretical density is 3.986 g/cm^3. Commercially produced aluminas contain porosity to a varied extent, which again is dependent on fabrication.

Materials produced by hot pressing techniques normally contain less porosity than those produced using cold pressing followed by sintering. Two types of pore occur in alumina; those situated intergranularly, being irregular and sometimes quite large, and those situated intragranularly being spherical and generally small. Some porosity observed in microscopical examination may be due to grain pull-out during polishing; this normally appears as irregular sharp-edged shapes.

The presence of other phases in alumina could produce inherent microcracks during fabrication, if the thermal expansion coefficient of the second phase is considerably different from that of the matrix. The existence of microcracks in some dispersed aluminas has been shown[17] using transmission electron microscopy. In less pure aluminas, impurities form a glassy phase which is situated predominantly at grain boundaries. The glassy phase cannot be easily observed, but its presence is particularly important in determining the high temperature mechanical properties.

The intracrystalline forces, holding the crystal lattice elements together, and the intercrystalline forces, acting between the individual crystallites, can sometines be equivalent in magnitude[18] especially in regions of large grain size. However, scanning electron micrographs of alumina fracture surfaces reveal that fracture is generally predominantly intercrystalline, but there is also evidence of intracrystalline failure.

2.2 FRACTURE

2.2.1 General Considerations

Most structural materials contain flaws or cracks that are introduced during fabrication or service. Under various combinations of static and alternating loads, and reactive environments, these flaws may grow slowly and stably. Unstable fracture occurs in a structure when a flaw has reached a critical size.

One of the earliest models for a crack system was that due to Griffith[18] who considered the crack system in terms of a reversible thermodynamical process. He discussed the total energy, U, of an elastic body subjected to external loading and containing an internal crack, in terms of three individual energies. These were: the work of the applied load causing some displacement on the outer boundary, W_L, the strain potential energy stored in the body due to the presence of the crack, U_E, and the energy required to create new crack surfaces, U_S:

$$U = (-W_L + U_E) + U_S \tag{2.1}$$

Thermodynamic equilibrium is then attained by balancing the mechanical and surface energy terms over a virtual crack extension, da, i.e.:

$$\frac{dU}{da} = 0 \tag{2.2}$$

For plane stress conditions, the Griffith equilibrium equation leads to a critical stress for fracture given by:

$$\sigma = \left(\frac{2E\gamma}{\pi a}\right)^{\frac{1}{2}} \tag{2.3}$$

where: σ is the applied tensile stress, γ is the surface energy per unit area, a is the crack length, and E is the Young's modulus. This equation was later modified by Irwin[19] and Orowan[20] to the form of:

$$\sigma = \frac{1}{Y}\left(\frac{2E\gamma_i}{C}\right)^{\frac{1}{2}} \tag{2.4}$$

for plane stress conditions, and:

$$\sigma = \frac{1}{Y}\left(\frac{2E\gamma_i}{C(1-\nu^2)}\right)^{\frac{1}{2}} \tag{2.5}$$

for plain strain conditions, where γ_i is the effective surface energy for fracture initiation, C is the flaw size, ν is the Poisson's ratio, and Y is a geometrical constant.

2.2.2 Fracture Strength

The strength (σ_f) of ceramics is discussed generally in terms of the modified Griffith equations, (2.4) or (2.5). The relevant textural parameters are those that affect γ_i and C. The microstructural dependence of γ_i varies from one material to another and will be discussed for alumina in Section 2.2.4(II). The flaw size, C, has a direct influence on the strength as illustrated in the equations, i.e. the decrease in strength with increasing flaw size. For most materials, the flaw size can be related to the pore size or the grain size. It is the largest flaw that affects strength and the relative size of the pores and grains dictates which of these is important.

The strength of a ceramic can be measured in a modulus of rupture test[21], in which the specimen is broken in bending in a 3- or 4-point loading system. Since the compressive strength of ceramic materials is much greater than the tensile strength, the tensile stresses are responsible for failure in bending.

2.2.3 Fracture Toughness

The presence of cracks in materials under stress causes stress concentrations at crack tips. Fracture occurs when the stress at the tip of a stable crack has reached a critical value, or when a moving crack has developed to a critical size. The fracture toughness of a material is a measure of its resistance to failure in the presence of a crack. It is sometimes given the term "notch brittleness"[22]. Low values of fracture toughness indicate brittle materials. There are two main approaches for measuring the fracture toughness of a material:

(i) The Stress Intensity Factor:

From the Griffith equation (2.3), a simple criterion for fracture is that $\sigma^2 a$ exceeds a particular value for a given material. The square root of the parameter $\pi\sigma^2 a$ is defined as the stress intensity factor and denoted by K:

$$K = \sigma\sqrt{\pi a} \qquad (2.6)$$

Thus, K is a direct function of the applied stress and the crack length. Introducing the geometrical parameter, Y, and the mode of fracture being the opening mode (mode I) for most fracture tests in ceramics,[23] then the stress intensity factor is given by:

$$K_I = Y \sigma a^{\frac{1}{2}} \qquad (2.7)$$

It is reasonable to consider that in ceramics fracture occurs when the stress intensity factor in the vicinity of the crack tip reaches a critical value:

$$K_{IC} = Y \sigma_F a^{\frac{1}{2}} \qquad (2.8)$$

where σ_F is the fracture stress. The geometric factor of Y can be calculated from the appropriate elasticity equations given by Paris and Sih[24].

(ii) Surface Energy and Strain Energy Release Rate:

Fracture problems can also be investigated using the surface energy method, which is based on the calculation of the energy required to create new surfaces. A general relationship between the fracture load, P, surface energy, γ_i, and experimental parameters can be derived[18] using the mechanical energy balanced with surface energy. The relationship is:

$$\gamma_i = \frac{P^2}{4b}\left(\frac{\delta\lambda}{\delta a}\right) \qquad (2.9)$$

where b is the specimen thickness, and λ is the elastic compliance. The strain energy release rate, G, may be defined as the crack extension force per unit area of crack and is equal to twice the fracture surface energy[23]:

$$G = 2\gamma_i \qquad (2.10)$$

Thus to obtain values for γ_i or G, a suitable load monitor and compliance calibration is required.

In parallel to the critical stress intensity factor definitions, there is also a critical strain energy release rate for catastrophic failure, G_{IC}, which is related to K_{IC} by the following equations[19]:

$$G_{IC} = \frac{K_{IC}^2}{E} \qquad (2.11)$$

for plane stress conditions, and:

$$G_{IC} = \frac{K_{IC}^2(1-\nu^2)}{E} \qquad (2.12)$$

for plane strain conditions. E and ν are the Young's modulus and Poisson's ratio, respectively. K and G are the fracture toughness parameters of a material and depend on the physical processes occurring at the crack tip during fracture.

The correct use of equations (2.11) and (2.12) requires a knowledge of Young's modulus which varies with porosity[1] and temperature[26]. Young's modulus of alumina can be measured by a resonant bar technique[27]. Knowing the Young's modulus of fully dense material, E_o, Kingery[28] showed that the modulus values for the same material of other densities could be calculated using the expression :

$$E = E_o(1 - 1.9\text{Þ} + 0.9\,\text{Þ}^2) \qquad (2.13)$$

where E is the Young's modulus for a material of fractional porosity, Þ. Spriggs[29] obtained another expression for cold-pressed and sintered materials, i.e.:

$$E = E_o\, e^{-3.5\text{Þ}} \qquad (2.14)$$

where E, E_o and Þ are the same as those defined for Kingery's equation. The Young's modulus of monocrystalline corundum at room temperature is reported to be[94] $\simeq 4\times10^{11}\,Nm^{-2}$.

(iii) Stress Intensity Factor-Crack Velocity Diagram

The dynamic of crack propagation can be described uniquely by the stress intensity factor (K_I) and the crack velocity (V) for many ceramics[63]. An idealized K-V diagram is shown in Fig. 2.2.a. There are up to three regimes of crack growth as K_I varies from K_{IO} to K_{IC}. K_{IO} is considered to be a threshold value of K_I below which no crack growth occurs in the particular test environment. There is still considerable debate on whether a true threshold value of K_I exists or K_{IO} reflects the lower limit of the sensitivity of the current techniques for crack monitoring. However, particularly in glasses there is some evidence for the occurrence of unique K_{IO} values. The concept of the existence of K_{IO} in a ceramic enables safe region of operation to be defined.

At low K_I, the rate of the chemical reaction (adsorption, diffusion, etc.) near the crack tip controls growth. This sub-critical crack growth which is attributable to the chemical reaction is of course a form of corrosion. In this region:

$$V = \alpha_1 K_I^n$$

where α_1 and n are constants. At intermediate K_I, region II, the sub-cratical growth is controlled by the supply, probably by diffusion, of the corrosive species to the crack tip. In region II, V is constant, i.e.:

$$V = \alpha_2$$

Region III occurs when K_I is close to K_{IC}. In this region there is a mixture of corrosive and mechanical failure, with the mechanical aspects generally predominant. In most cases the time spent by cracks in regime III is small. The K - V diagrams are particularly useful in determining the time dependence of strength.

A number of test techniques may be used to obtain K -V curves. The DCB and the DT tests are the most widely used (see section 3.4.4.). For transparent materials it is possible to follow the crack optically to obtain values for both V and K_I at constant load. Alternatively, for both transparent and opaque materials, the crack velocity can be obtained using DT geometry as described by Evans[63]. The crack velocity is measured from expression :

$$V = - \frac{a_i \, P_i}{P^2} \left(\frac{dP}{dt} \right)$$

in which V is obtained directly from the rate of load relaxation at constant displacement. A specimen of initial crack length, a_i, is loaded up to a load P_i at high crosshead speeds so that no significant crack extension occurs prior to relaxation. When P_i is reached the test machine is held at constant deflection (load relaxation) and the decay of load with time $\frac{dP}{dt}$ is analysed. The corresponding values of K_I are found directly from the load P (for each $\frac{dP}{dt}$) via equation :

$$K_I = AP$$

where A is a geometry factor (see Section 3.4.4.ii).

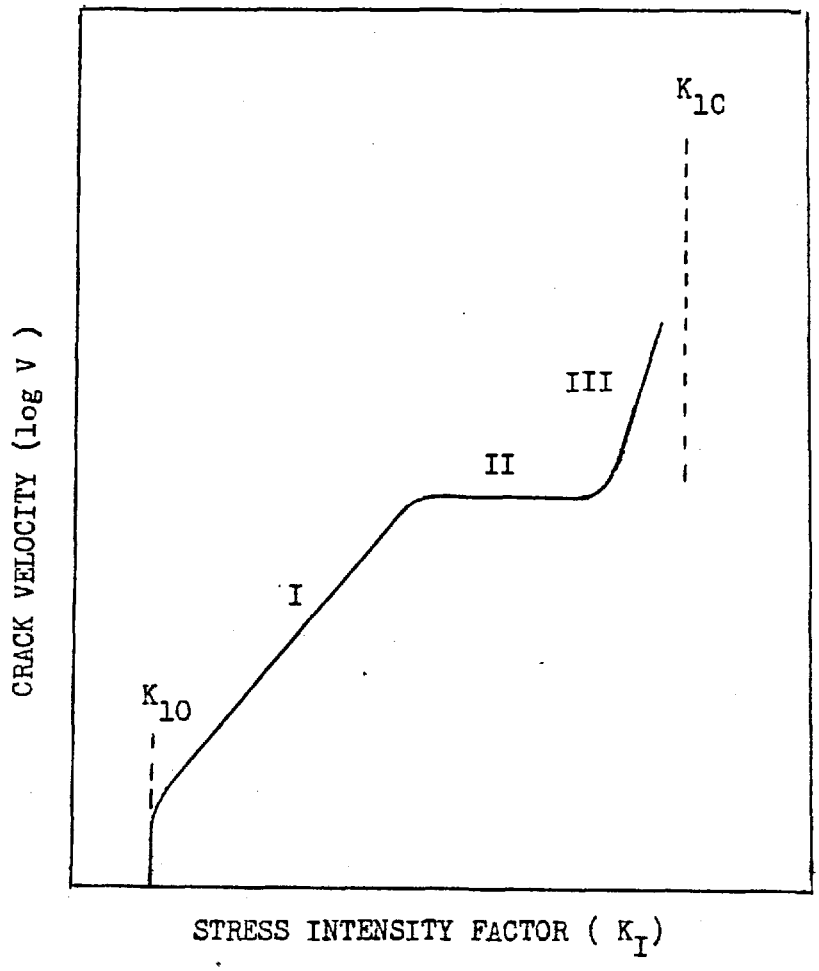


Fig.2.2.a. The variation of stress intensity factor with crack velocity for a ceramic subjected to a stress corrosive environment.

2.2.4 Fracture Strength and Toughness of Alumina at Room Temperature

In assessing the potential of alumina as an engineering ceramic, the important mechanical properties include fracture strength and fracture toughness.

(i) Fracture Strength:

The fracture strength of alumina is influenced by its microstructure. Data showing the effect of porosity on the strength of alumina are presented by Coble and Kingery[30] who showed a decrease in the strength with increase in porosity. The relationship was of the form of:

$$\sigma_f = \sigma_o e^{-BP} \qquad (2.15)$$

where σ_o is the strength of a zero-porosity body, P is the fractional porosity, and B is a constant. A value of $B \approx 4$ was obtained for a series of alumina specimens containing 5-10% porosity.

The percentage porosity, P, may not be the only important porosity parameter. The shape of the pores and their size distribution are probably important but have not yet received much investigation. However, there are some results concerning the effect of surface flaw size on the strength of alumina. A study by Bradt and Tressler[31] on surface finish strength-grain size relationship of dense aluminas showed that, in large grain size materials, surface finish did not affect the strength as long as the sample preparation flaws were smaller than the intrinsic microstructural flaws, which in that case were the grains. The effects of extrinsic surface machining flaws were more serious in the fine-grained dense aluminas, where they were predominantly strength controlling. In studies on porous aluminas, Meredith et al[2] reported that specimens of 10-20% volume porosity with surfaces polished to 1 μm, gave a $\simeq$ 5% increase in strength compared with specimens prepared by normal sawing and grinding with 40 μm silicon carbide abrasive.

The inherent flaw size, i.e. pore size or grain size, has always been considered an important factor determining the strength of alumina. The basic idea is the Griffith equation:

$$\sigma_f = \frac{1}{Y}\left(\frac{2E\gamma_i}{C}\right)^{\frac{1}{2}} \qquad (2.16)$$

where the flaw size C, could be pore size or grain size depending on which is larger. Knudsen[32] was one of the first to show the dependence of the strength of polycrystalline brittle materials on the grain size in the expression:

$$\sigma_f = A\, g^{-\frac{1}{2}} \qquad (2.17)$$

where g is the grain size and A is a constant. Here the flaw size in the Griffith equation is substituted by the grain size. Another form of strength-grain size relationship is attributed to Petch[33], who showed:

$$\sigma_f = \sigma_o + A\, g^{-\frac{1}{2}} \qquad (2.18)$$

where σ_o is an empirical constant. The data obtained by Carniglia[34] for dense aluminas of large grain size fitted the Knudsen equation and those of fine grain size, the Petch plot. The combined effect of porosity and grain size on the strength of brittle polycrystalline materials was considered by Knudsen, who proposed a general equation:

$$\sigma_f = (\sigma_o + A\, g^{-c})e^{-BP} \qquad (2.19)$$

which is effectively a combination of equations (2.15) and (2.18).

Rice[35] measured the strength of a wide variety of dense hot-pressed and sintered aluminas and obtained a decrease of strength with the increase of grain size. For sintered aluminas, he found that strengths agreed quite well with those of denser materials, when corrections were made for porosity by means of equation (2.19), with $B \sim 7$ compared with a value of 4 originally reported by Coble and Kingery. Rice[36] then later suggested that

in aluminas of $g > C$, grain size directly influenced strength by limiting crack growth, leading to the Knudsen equation. In aluminas of $g < C$, the strength was indirectly influenced by g, through the g-dependence of γ_i and possibly of flaw shape. Thus a non-zero intercept on a Petch equation was obtained. The two plots met each other at the point of $C \approx g$, as shown in Fig. 2.2. The strength-grain size relationships obtained by different authors for porous and dense aluminas are shown in Figs. 2.3 and 2.4, respectively. For porous aluminas, in general, the Knudsen equation is applicable whilst for the dense materials a combination of Knudsen and Petch plots can be fitted with the experimental data.

(ii) The Fracture Toughness of Alumina:

The fracture toughness of a material should be independent of the test method, but the values reported for the room temperature fracture toughness of alumina vary with test-piece geometry. A number of factors contribute to this conflict of findings, such as the material microstructure and the specimen preparation method. It was the work of Simpson[6] which first suggested that the test-piece geometry used could also be an important factor. For 3 μm grain size alumina he reported comparable results from SENB and DCB test-pieces, whereas for a material of 20 μm grain size, the DCB values were almost twice those from SENB tests. The DCB specimens were pre-cracked, whilst the SENB specimens contained blunt notches. Further work by Simpson, Ritchie and Lloyd[37] suggested that the DCB test was the more reliable since the effect of machining a blunt notch in the SENB geometry may be to form isolated microcracks at the notch root which link during loading to give a discontinuous form of subcritical crack growth. Thus the crack length at the point of fracture would be longer than the pre-loading value and correcting for this behaviour would increase the fracture energy towards agreement with DCB results. In addition, their DT specimens yielded fracture energies which were in agreement with DCB data.

The toughness values obtained by Meredith and Pratt[2] with DCB tests on alumina of mean grain size 3.5 μm were only

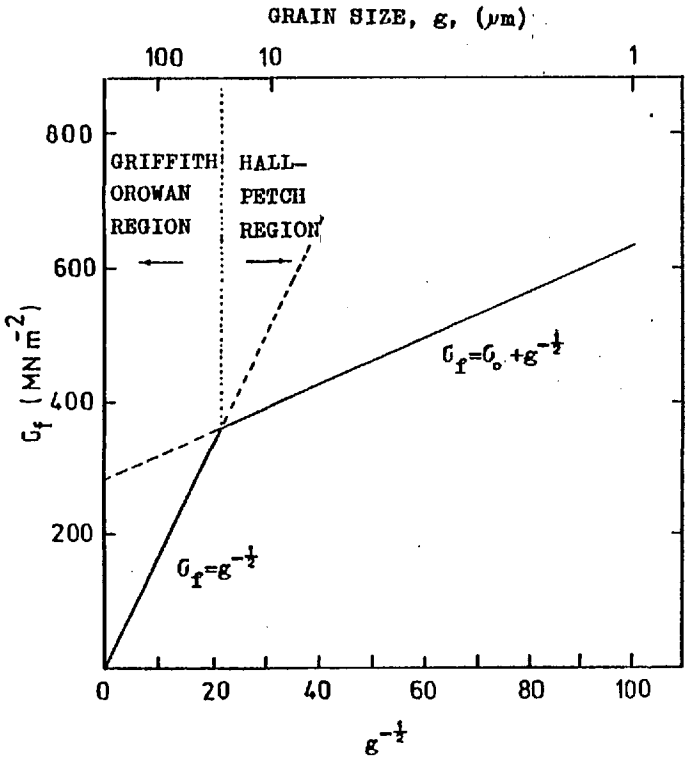


Fig.2.2. The classic strength-grain size dependence, (Ref.36).

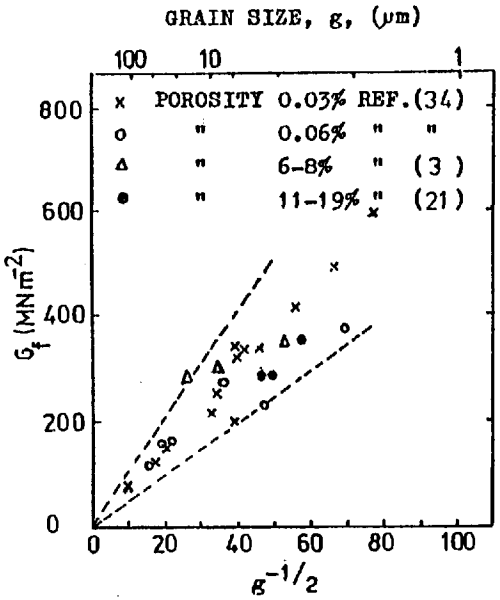


Fig.2.3. Strength-grain size dependence of porous aluminas.

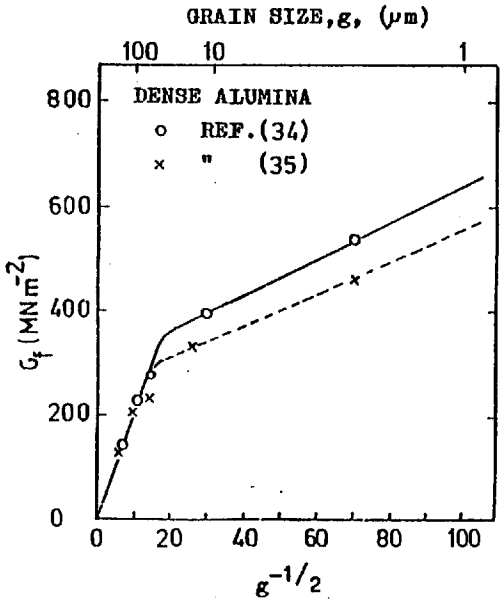


Fig.2.4. Strength-grain size dependence of dense aluminas.

slightly higher than those obtained from SENB tests. Dalgleish, Pratt and Sandford[3] reported that the fracture toughness of a given alumina varied with test geometry in the order DCB $\geq$ DT $>$ SENB. Their SENB and DCB data showed a decrease in fracture toughness with increasing grain size, although the DCB results were consistently the higher especially when coarse-grained alumina was subjected to repeated crack propagation. Double torsion values showed little variation with grain size. The discrepancy between SENB and DCB data was less pronounced when the SENB specimens contained sharp pre-cracks. However, they suggested that in DCB specimens some of the energy supplied by the loading system was absorbed in opening a network of cracks inclined to the main crack.

Thus there are conflicting views as to which test geometry should be employed for the purpose of comparing the effect of several microstructures on mechanical properties. Although there is some discrepancy in the literature, it would appear that, in general, the fracture toughness values obtained using the DCB test geometry are often over-estimated, whilst the SENB values are slightly under-estimated. The more accurate results are perhaps those obtained using DT specimens which yield values falling between those obtained using DCB and SENB specimens.

Additional complicating results concerning the type of initial crack have been reported for fracture toughness of a given alumina. Simpson's[9] results from a study of fine-grained alumina showed that the fracture energies determined from SENB specimens with as-cut notches of 0.75 mm and 0.20 mm widths and pre-cracked DCB specimens were different. The wider notch yielded considerably larger fracture energies and the results for the narrow notched SENB specimens were about 15% higher than those of DCB. In contradiction to these results, Dalgleish, Pratt and Sandford[3] and Evans, Linzer and Russell[10] found that notched beams gave K_{IC} values up to 10% lower than pre-cracked specimens. Dalgleish et al found that the 10% increase achieved by pre-cracking was insufficient for agreement with DCB data. On the other hand, Davidge and Tappin[38] reported that for coarse-grained alumina, machining damage during the

sawing of the notch was sufficient to yield results in agreement with those for specimens containing sharp cracks. Claussen, Pabst and Lahmann[8] also concluded that no sharp crack is needed in SENB specimens, as long as the notch width, R, is small enough, i.e. $R \leqslant 50$ μm will yield suitable K_{IC} values.

It appears that the state of the notch root is important in determination of fracture toughness. The reported values show an increase in K_{IC} for blunt notched specimens compared with sharp-cracked values, but in these cases the specimens may have been notched very carefully. Other less consistent values may well have been obtained using poorly machined specimens. However, although the mathematical solutions for the fracture toughness test geometries describe zero volume cracks, introducing sharp cracks is difficult especially in the SENB case. The use of sawn notches also gives realistic results, if notches are introduced with sufficient care.

The microstructure of alumina also plays an important role in determining fracture toughness values, some examples have been already mentioned. In the effect of density on fracture toughness, it is to be expected that increasing the density or reducing the porosity, will improve the mechanical properties of a material. This is found to be so for alumina[1,8,39], as shown in Fig. 2.5.

But a review of the literature on the grain size dependence of the fracture energy reveals a conflict of results. Many workers agree with the simple prediction that the strength, σ_f, and thus fracture toughness should decrease with increase of grain size. Some others report either no effect or an increase. Gutshall and Gross[4] reported an increase in the fracture energy of Lucalux with increasing grain size which was related to an increase in the extent of transgranular fracture, whilst in aluminas examined by Dalgleish et al[3] the fracture toughness values measured using DT tests showed little variation with grain size, and those obtained by SENB and DCB showed a decrease in K_{IC} with increase in grain size (Fig. 2.6). Simpson[1] measured the fracture surface energy of alumina with a range of density and grain size using both the Tattersall-Tappin[66] technique and analytical methods. In most

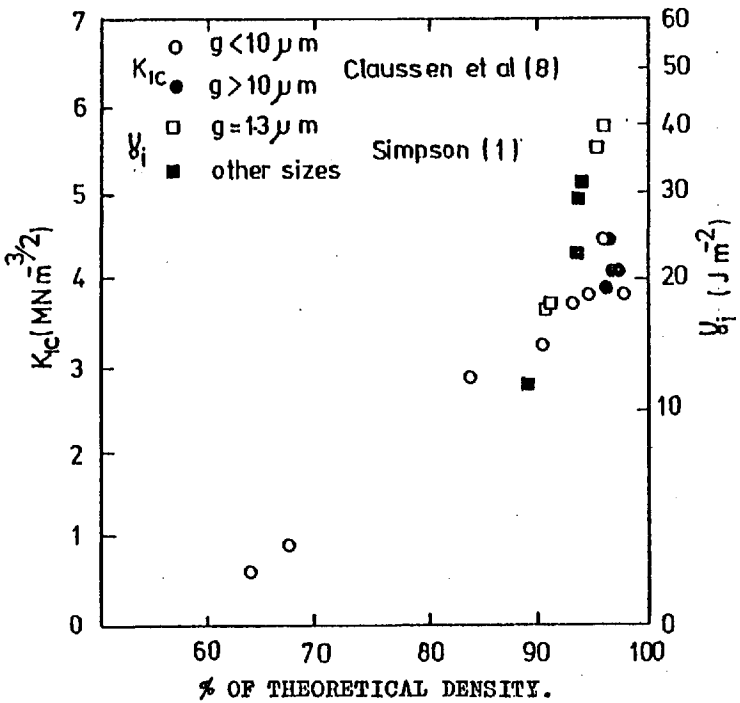


Fig.2.5. Dependence of fracture toughness of alumina on density.

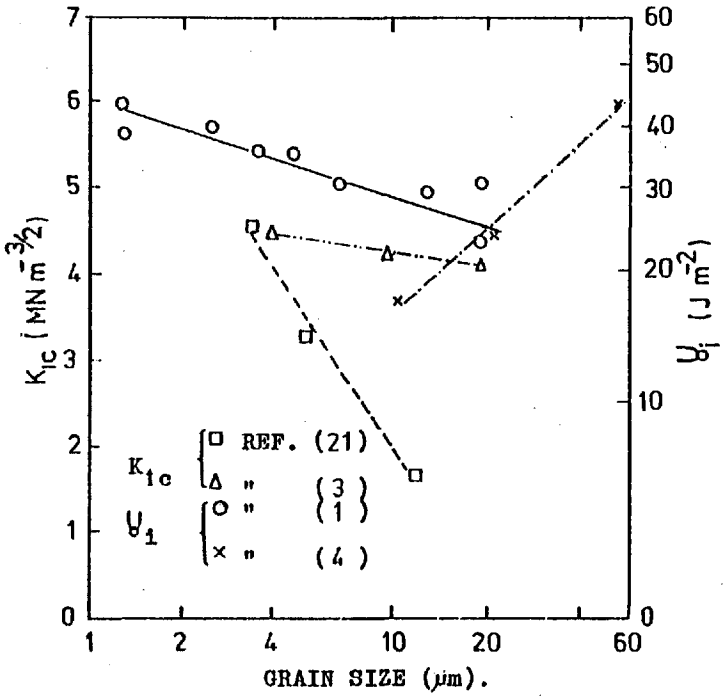


Fig.2.6. Dependence of fracture toughness of alumina on grain size.

cases both techniques followed the same trend, although the values were not necessarily equivalent. Simpson's results showed a considerable fall of fracture energy with increase in porosity in the low density ($< 97\%$ of theoretical density) materials, in contrast to the behaviour of dense ($> 97\%$) materials where the grain size effect appeared to predominate and the inverse fracture energy-grain size dependence existed. He concluded that the inverse dependence of fracture toughness on grain size might result from the increase in residual strain energy with increasing grain size due to anisotropic thermal contractions during cooling after sintering.

Claussen et al[8] presented fracture toughness data for commercial sintered alumina and concluded that "a straight line dependency between K_{IC} and density or grain size is not readily apparent". However, they believed that as long as the fracture is mainly intercrystalline, K_{IC} is higher for small grain size materials than those with large grains. In a review of the influence of microstructural factors controlling the fracture energy, Davidge[40] concluded that because of the numerous factors affecting the grain size dependence of the fracture energy, no general conclusion can be drawn. However, in materials where there is a transition from intercrystalline to transcrystalline fracture with increase in grain size, the fracture energy should increase, and in materials without a transition the fracture energy should decrease.

2.2.5 High Temperature Fracture Strength and Toughness of Alumina

Davidge and Tappin[38] examined the temperature-dependence of the strength of a pure (99.5%) and a debased (95%) alumina (Fig. 2.7). They observed a decrease in the strength of pure alumina with temperature, due to the temperature dependence of Young's modulus. In contrast, the debased material showed a peak at 850°C, and their conclusion was that plastic flow of the glassy phase was responsible for this phenomenon. Later, Meredith, Newey

and Pratt[21] investigated the strength of three debased aluminas with purities of A = 95.5%, B = 89.5% and C = 94.4%, Fig. 2.7. In RT-700°C range, the strength rose to a maximum at ≈150°C in alumina A and C, then fell slowly to ≈700°C, while the strength of alumina B rose to a broad maximum at ≈300°C before falling to 700°C. In the temperature range of 700°C to 1000°C the strength of alumina C decreased slowly, but A and B showed a pronounced strength peak at ≈850°C. They concluded that the higher peak in material B resulted from the greater volume fraction of glass in this material compared with A, but A and B glasses had a similar temperature-dependence of viscosity.

The temperature dependence of the fracture toughness of Lucalox was studied by Evans, Linzer and Russell[10]. The K_{IC} values obtained using DT specimens were constant up to about 600°C and decreased at temperatures above 600°C (Fig. 2.8). The lack of impurities in the Lucalox showed no evidence of a peak in the K_{IC}-temperature curve and the decrease of K_{IC} above 600°C was perhaps due to grain boundary softening.

Claussen, Pabst and Lahmann[8] investigated the fracture toughness of a range of aluminas with densities of 3.82, 3.65 and 2.58 g/cm^3. There was no difference in composition except in the case of alumina of density 3.65 g/cm^3, which contained a greater volume of the glassy phase (Fig. 2.8). The K_{IC} values of all the materials was constant up to ≈600°C. Above 600°C the low density aluminas showed a small increase in K_{IC} before the typical drop at higher temperatures. The high density material exhibited a decrease of K_{IC} at temperatures above 750°C. Alumina containing the glassy phase showed a sharp increase in fracture toughness above 700°C with a maximum at 960°C followed by a decrease beyond this temperature. Claussen et al supported the conclusion of Davidge et al that at temperatures above 700°C, energy was dissipated by deformation of the softening glassy phase, whilst at still higher temperatures the viscosity became so low that the resistance to fracture was considerably reduced.

2.2.6 Second Phase Dispersion of ZrO_2 in an Alumina Matrix

The fracture energy of alumina can be increased by a dispersion of second phase particles such as MgO and ZrO_2[17]. The increase in fracture energy is attributed to interaction of the crack front with the second phase, the possible energy absorbing mechanisms being crack blunting, crack deviations and crack front elongation. Another mechanism which can also improve fracture toughness under certain conditions is the interaction of the crack front with pre-existing microcracks. The safest method of creating controlled microcracks in a ceramic matrix is the incorporation of second phase particles with a considerably lower coefficient of expansion than that of the matrix. When such a composite is cooled from its fabrication temperature, highly localized stresses arise which can cause cracking of the matrix.

Claussen[17] used two-phase composites of alumina containing different percentages of ZrO_2. The fracture toughness values vs. the volume fraction of ZrO_2 are shown in Fig. 2.9. The increased K_{IC} of the composite, compared to that of the single-phase Al_2O_3 was explained in terms of energy absorption in an extended microcrack zone in front of the crack tip. The absorption processes were assumed to be microcrack opening and subcritical crack propagation. The density of microcracks increased with increasing number of ZrO_2 particles, which in turn increased the toughness of the material. At volume fractions beyond the optimum, the microcracks joined up between the particles, thus decreasing K_{IC}.

2.3 ACOUSTIC EMISSION

2.3.1 General Considerations

Acoustic emission (AE) or stress wave emission is the noise emitted by materials undergoing deformation, fracture or phase transformations. In materials under stress, the source of emission

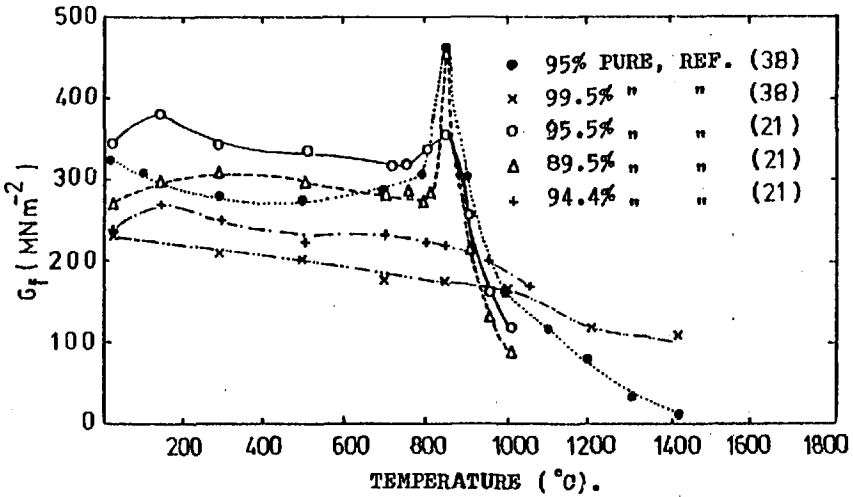


Fig.2.7. The temperature dependence of strength of alumina.

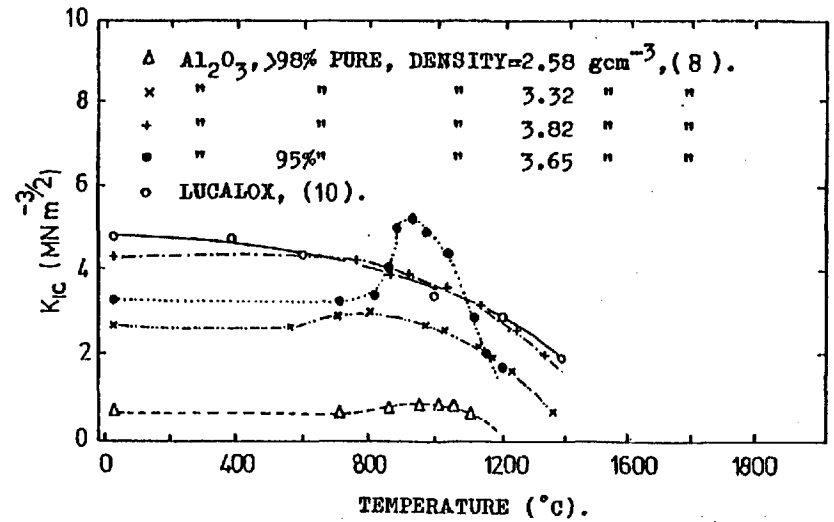


Fig.2.8. The temperature dependence of fracture toughness of alumina.

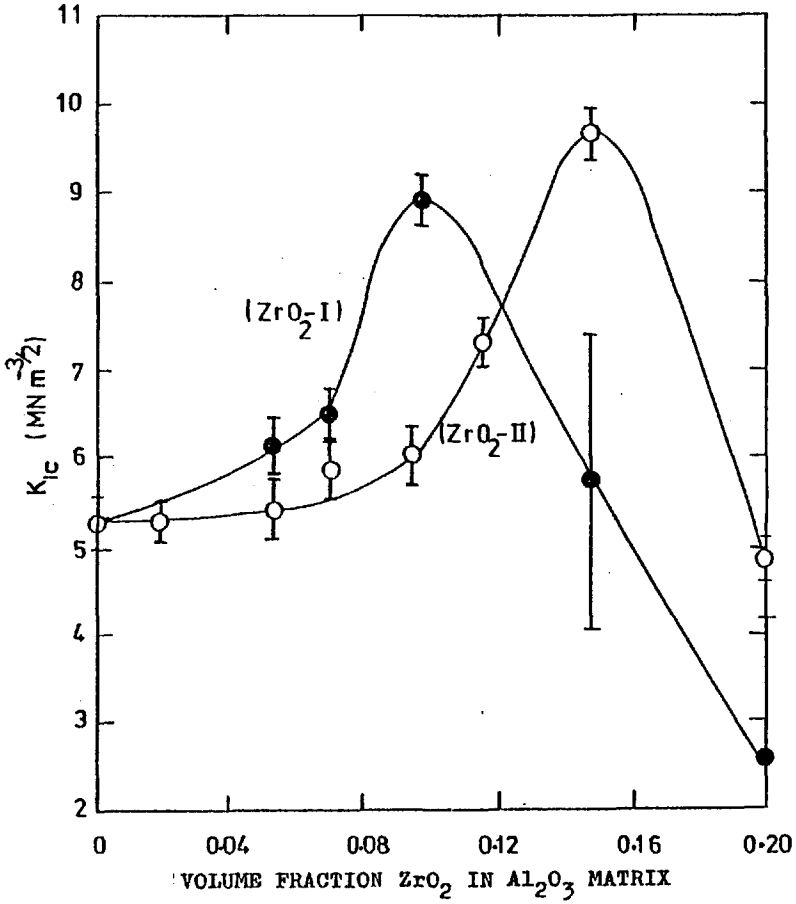


Fig.2.9. Effect of the second phase dispersion of ZrO_2 in alumina matrix on the toughness of the composite(Ref.17).

might be dislocation motion in ductile materials, interparticle motion or microcracking and fracture in brittle materials.

Historically, the earliest use of acoustic emission analysis occurred in seismology. Analysis of the elastic waves produced by an earthquake was used to characterize fault movement in terms of energy released, location and depth. In 1923, Hodgson[41] proposed the use of subaudible noises to predict rock bursts and earthquakes. Early indications of acoustic emissions in metals were made by "tin cry" which is produced when the metal twins, and steelworks have long noted audible clicks caused by martensitic transformations.

Josef Kaiser's research[42] published in 1950, is generally considered to be the beginning of the present era of acoustic emission study. Although his conclusion that the noises were produced primarily by grain boundary sliding has since been disproven, his observation that the noises were of two types, a low amplitude continuous sound with high amplitude bursts superimposed, has been confirmed many times. Probably his greatest contribution was the observation of the irreversibility of acoustic emission, i.e. no emissions were generated in a previously loaded sample during reloading until the stress level exceeded its previous value. The behaviour has been named the "Kaiser effect" and it has been utilized in determining the stresses which structures have undergone in service.

Kaiser's work was furthered in 1958 when Lean, Plateau, Backet and Crussand[43] investigated the deformation processes in materials, using electronic instrumentation to record the acoustic emission. Somewhat later, Schofield[44] and Tatro[45] initiated research in an attempt to identify the sources of acoustic emission. Schofield discovered that the grain boundaries were not the sole sources of emissions, since single crystals also emitted noise under stress. Further investigations led him to tentatively conclude that dislocation motion was responsible for acoustic emission. Tatro supported this, suggesting that barriers to dislocation movement, such as surface oxide layers, changed in emission spectra.

In 1964 a mechanical engineer suggested that the "new" technique of acoustic emission would be suitable to test the integrity of an engineering structure. Since then, acoustic emission has been applied to industrial problems. The technique has developed rapidly, mainly because the inherent sensitivity of the technique enabled microscopic processes occurring in materials to be studied. Consequently extensive research has started in many different fields. Metallurgists have used the technique to study the effect of structural and microstructural variables on the acoustic response of metals[67-69]. Materials scientists have applied the phenomenon to study dislocation and fracture mechanisms[69,70]. The detection of growing flaws and cracks has been found to be an important application for acoustic emission, and the feasibility of using this technique has been studied[70-73].

More recently, the possibility of using the acoustic emission technique for in-service surveillance of structures, especially those operating in a hostile environment, has received increasing attention [73-76]. Much of the work in the field of acoustic emission has been carried out on ductile materials, whereas ceramics have received very little attention. Nevertheless, some excellent papers[46-50] have been published describing the use of the AE technique to investigate various ceramic and glassy systems. The technique has proved useful for both the technological application and fundamental scientific study[77] of this type of brittle material.

2.3.2 Generation of Acoustic Emission

The generation of emissions is best explained by using an analogy[43]. Consider a mass suspended between two stretched springs and held in position by a string, as shown in Fig. 2.10. If the tension on the string is released suddenly, i.e. in a time which is short compared to the resonant frequency of the system, then the mass will oscillate about the equilibrium position. If, on the other hand, the tension is released slowly, i.e. in a time which is long compared to the resonant frequency, then the mass

will proceed smoothly to the equilibrium position and fewer oscillations will be observed. Putting this analogy into perspective, if the mass represents an atom and the springs the binding forces between other atoms in a crystal, then the slow release of tension in the spring is a crude description of a ductile deformation, while the sudden release of tension is a description of a brittle fracture. The oscillation of the mass after the release of tension models the source of a stress wave emission.

An estimate of the amount of energy released during a deformation or fracture process in a material can be made (Section 2.2.3). Some of the energy released is transferred to the stress waves. The amount of energy carried by a stress wave depends upon the time during which the deformation process takes place, the extent of deformation giving rise to it, and the magnitude of deformation, as was shown in the spring-mass analogy.

From the theoretical point of view, Stephens and Pollock[52] believed that the source stress waveform has an essentially broad-band spectrum. They proved that only a pulse-like function of stress for the emission source wave could satisfy the physical constraints.

2.3.3 Propagation of Stress Waves

The generated stress waves are radiated in all directions and travel both through the bulk and along the surface of the material, where they are attenuated or reflected. Only a fraction of the generated waves reach the detection system. Attenuation of acoustic waves is caused by the physical structure of the material and can be explained in terms of scattering and absorption. The former is due to the partial reflection of the propagating waves by the distributed discontinuities and the latter refers to loss of energy due to transformation into other forms of energy.

Acoustic waves undergo reflection at the specimen surfaces, and attenuation on reflection occurs when some of the wave energy is

transferred into the neighbouring medium. The multiple reflected waves provide a large contribution to the final signal reaching the detector. Acoustic waves travel through the bulk of material in two different modes, longitudinal waves and transverse or shear waves. Surface or Rayleigh waves propagate in a combined mode. The velocities of propagation and the rate of attenuation vary for each mode and conversion from one mode to another occurs on surface reflections. Thus the stress waves arriving at the detection system have different characteristics to those of the source emission.

2.3.4 The Detection of Stress Waves

The key to effective utilization of stress waves to provide information about material failure, is a transducer capable of efficiently and faithfully converting the mechanical waves into electrical signals. The low energy content and high bandwidth of acoustic emission waves restricts the choice of transducer types to two broad categories: piezoelectric and capacitive transducers.

Piezoelectric transducers are made from materials which generate a surface charge density under an applied stress. The appearance of the piezoelectric effect arises from the lack of symmetry in the structure of the crystal (see Fig. 2.11[53]). Several naturally occurring substances, notably quartz, produce the effect, but the most popular piezoelectric material for acoustic emission work is polarized lead-zirconate-titanate, because of its low electrical impedance and high electromechanical coupling coefficient. The problem associated with the use of a piezoelectric transducer is a restricted bandwidth, due to the fact that it is inherently a resonant device.

Capacitive transducers, as their name implies, depend upon changes in capacitance for their operation. Capacitive transducers are inherently broadband, but they suffer from lack of sensitivity. The choice of transducer for the detection of stress

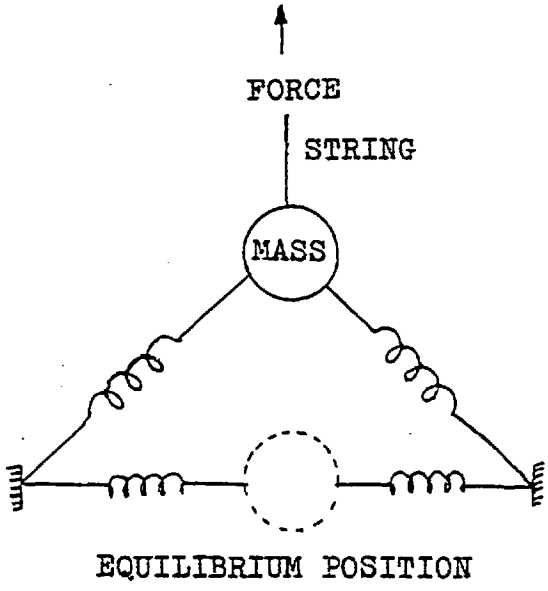


Fig.2.10. An analogy for the generation of acoustic emission.

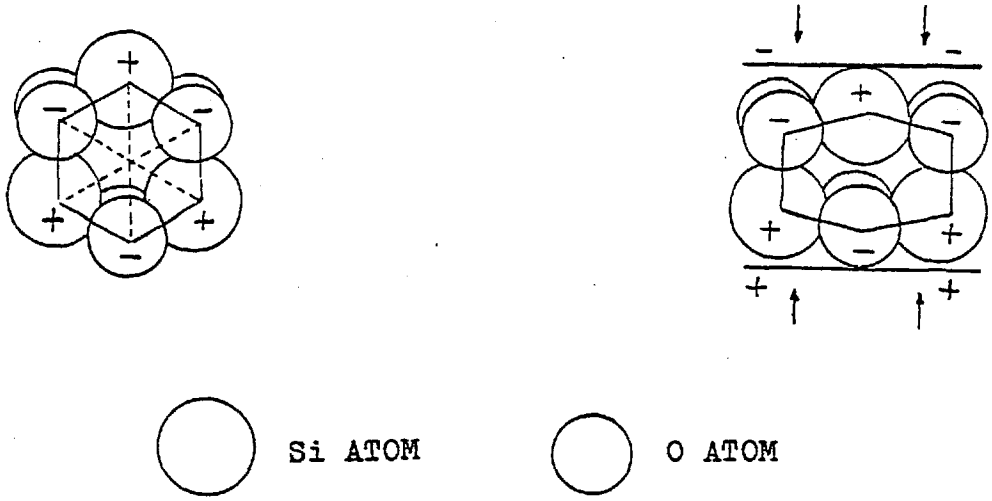


Fig.2.11. Mechanism of piezoelectric effect in quartz,(Ref.53).

waves depends on the test conditions, environment and material under test. Compromise may be achieved between the response of the transducer and the frequency band width. A transducer provides a good sensitivity to a given input when it responds fairly linearly over a relatively wide frequency range.

The acoustic emission signals which are picked up by a transducer are converted into a varying electrical voltage which can be further processed. Fig. 2.12 shows a typical transducer output signal which represents one of the hundreds of similar acoustic emission bursts produced from an experiment.

2.3.5 Signal Processing

Signal processing for acoustic emission is defined as the analysis of collected data in order to obtain meaningful information about the process under observation. Part of that is dedicated to collecting only the data which is relevant to the experiment, and the other part to analysing that data with the use of some known experimental conditions.

Good experimental design is the first step to eliminating extraneous signals from a stress wave emission. Particular attention must be paid to the loading mechanism because it is the primary cause of external noise, both mechanical and electrical. Satisfactory results can be obtained using commercial universal testing machines, provided that the specimen-loading jigs and gripping systems have been designed with care (see Section 3.4.2). Noise transmitted through the air, i.e. air-borne electrical interference, can also be removed by surrounding the sample with a mesh box (see Section 3.6.2). Thus careful attention to details during experimentation will ensure that only specimen-created signals will be present in the output signal.

The wave-form of an output signal from the transducer which is shown in Fig. 2.12 may be conveniently represented as a decaying sinusoid oscillation, Fig. 2.13, by the equation[54]:

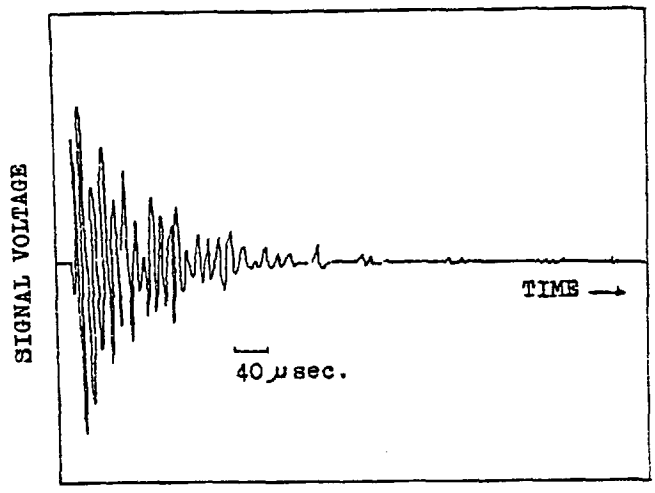


Fig.2.12. A typical acoustic emission signal output of the transducer, (Ref.55).

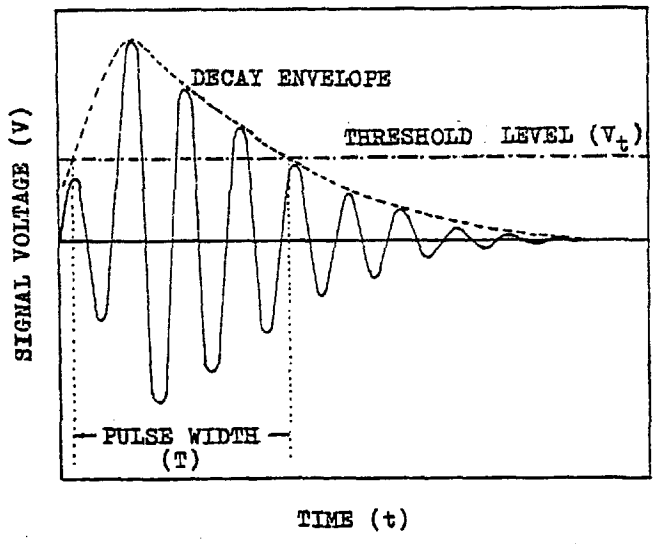


Fig.2.13. An acoustic emission may be considered as a decaying sine wave, (Ref.55).

$$V = V_o e^{-\beta t} \sin 2\pi ft \qquad (2.20)$$

where V_o is the peak amplitude of a signal, f is the frequency, t is the time and β is the decrement factor.

Once an electrical analog of the desired acoustic emission event has been obtained, the next step is to amplify the low level signal to a value which can be conveniently handled and then filtered to remove unwanted frequencies, such as low frequency vibrations from mechanical equipment, which are filtered out below about 100 kHz[55].

Having attained a useful signal level, several different signal processing techniques can be used. Fig. 2.14 shows, in schematic form, an acoustic emission measuring system.

a. Ring-down and event counting:

The principle of ring-down counting is to count the number of times a threshold voltage is exceeded by the oscillating transducer output caused by acoustic emission. For the idealized signal in Fig. 2.13 the detector will only recognize three waves in the pulse. If the signal is then fed into a counter, a count of three will be recorded. Thus larger bursts will record larger counts. The alternative is to count a whole burst of oscillations as one event[56]. Ring-down counting has an advantage over event counting in that the count obtained from a given event increases with signal amplitude and there are consequently more ring-down counts for events of larger energy. The number of ring-down counts which results from an input signal will be given by[46]:

$$N_{RT} = \frac{f}{\beta} \ln \frac{V}{V_t} \qquad (2.21)$$

where f is the frequency of the signal, β is the logarithmic decrement factor, V is the initial output voltage of the transducer, and V_t is the thresbold voltage. The signal produced by the transducer will be proportional to the energy released in the acoustic emission source event. Therefore the number of counts

recorded will also be proportional to the energy released, and will indicate the amount of damage occurring per second, thus obtaining the rate at which damage is occurring in the sample. This type of analysis is both useful and easy to perform, but it is, however, subject to the criticism that it is a function of frequency. It also considers the signal amplitude only indirectly and no direct relationship between the count and a physically meaningful parameter can be obtained.

b. Amplitude Analysis:

In any test, the peak amplitudes of the individual emissions vary over several orders of magnitude. It is commonly found that larger numbers of emissions are present at lower amplitudes[54]. A distribution of peak amplitudes can be obtained by using a convenient threshold level. Pollock[56] showed that the fraction of the emission population whose peak amplitude exceeds a certain level is given by:

$$n(V) = \left(\frac{V}{V_t}\right)^{-b} \qquad (2.22)$$

where V is the amplitude of the level in question, V_t is the lowest detectable amplitude, and b is termed the amplitude distribution characteristic. The parameter b has a physical meaning. When a deformation or fracture process proceeds by a large number of small steps, i.e. in an almost continuous manner, there is a large proportion of low amplitude emissions and the value of b is large. But when the deformation or fracture proceeds in a small number of large steps, a larger proportion of high amplitude emission can be obtained, and b is small. Thus the type of failure process can be identified by measuring the value of b.

It is possible to relate the number of acoustic emission ring-down counts above the threshold level V_t, to the b value if it is assumed that: (i) equation (2.20) describes the emission waveform, (ii) the peak emission amplitudes are distributed according to equation (2.22), and (iii) the number of counts for

each event is given by equation (2.21). For a set of emissions of N_{ET} events with amplitude in excess of V, the total ring-down count, N_{RT}, above the threshold level is equal to[57]:

$$N_{RT} = N_{ET} \frac{f}{b\beta} \left(\frac{V}{V_t}\right)^b \qquad (2.23)$$

This equation gives an approximate theoretical relationship between ring-down counts and system gain (which affects V), the threshold level and the amplitude distribution parameter, b. It must be noted that the logarithmic form of the number of counts for a single event, equation (2.21), is replaced by a power-law relationship when we take into account that not all emissions have the same amplitude.

c. Spectral Analysis of Acoustic Emission:

Emission waveforms carry information about the structure of the source event[52]. They are often modified by reflection and the transducer response, but they can be obtained in a specially designed specimen, using an oscilloscope equipped with a camera. The main advantage of examining waveforms is that very small perturbations of shape can be easily recognized, allowing minute variations of the acoustic emission process to be detected.

Frequency spectra of emission are fairly difficult to obtain, but can be produced using a transient recorder to capture an individual emission, and then transferring the output of the recorder to an analog frequency spectrum analyzer where the frequency of emissions may be obtained against their amplitude. This method has the obvious limitation that only post-test analysis is possible, and it is also very difficult to ensure that emissions are processed one at a time. An alternative method uses a high speed analog to digital converter to enable a computer to perform a fast Fourier transform of the emission data in real time.

Some information regarding the source properties such as size, shape, proximity to neighbouring surface and interfaces, and

load stiffness in the region of deformation can be obtained by emission spectral analysis[58]. In practice some difficulties arise from frequency-dependent modification processes close to the emission source, to the position of the detector and to the whole specimen geometry. Also, there are limitations of bandwidth in the detector and associated electronics. Nevertheless, the acoustic emission spectral analysis can be used as a complementary technique to the other acoustic emission methods.

d. Energy and RMS Measurement:

Two physically meaningful parameters of the signal, i.e. the energy and the power, are measured by these techniques. The energy of a transient signal in the transducer can he defined as[59]:

$$\mathcal{E} = \frac{1}{R} \int_0^\infty V^2(t)dt \qquad (2.24)$$

where V(t) is the time dependent voltage, and R is the impedance of the circuit. Inserting equation (2.20) into equation (2.24) and integrating between 0 and T, where T is the time taken between the two crossings of the signal with the preset voltage of V_t, leads to:

$$\mathcal{E} = \frac{V_t^2 \, e^{2\beta T}}{4R\beta(1+\beta^2)} \qquad (2.25)$$

Thus the energy is proportional to the square of the preset voltage and is related to T through the term $e^{2\beta T}$. The result is based on the assumption that the decrement factor, β, does not change from one signal to another. The measurement of absolute $\mathcal{E}$ is very difficult due to the dependence of β on many variables and the difficulty of its analysis.

The RMS voltage measurement is perhaps the simplest technique which can be used for AE analysis due to the availability of the commercial RMS instruments. The technique consists of measuring the average voltage of input signals over a certain period of time, which is the response time of the meter and is in the order

of a second, instead of measuring an instantaneous voltage, and taking the root mean square (RMS) of the data. Thus the technique is only useful for continuous signals.

2.3.6 Factors Influencing the AE Results

In analysing the AE data, the factors governing the experimental results have to be considered. As mentioned by Pollock[60]:

(i) source and structural characteristics,
(ii) location and coupling of transducer,
(iii) frequency passband, and transducer sensitivity,
(iv) gain of amplifier and threshold,

are the important factors which operate successively in shaping the signals that are finally recorded as emission data.

The acoustic behaviour of a material depends on both its internal and external variables. The important external variables that influence the source and hence the emission data are: the specimen geometry, test environment and loading rate. The internal variables, i.e. the structural, microstructural, chemical, physical and mechanical characteristics of a material, all partially influence its acoustic response, providing considerable differences in the acoustic behaviour of different materials. The microstructure, for example, determines the deformation and fracture mechanisms and hence source characteristics. Microstructure can also affect the measured AE data through changes in attenuation by scattering at grain boundaries, second phase particles, etc., although only likely to be important in large specimens. The importance of understanding the material behaviour in relation to its acoustic emission is basic to the further development of this technology.

The stress waves undergo considerable changes between leaving the source and appearing at the transducer (see Section 2.3.3). Thus the location of the transducer on the specimen has to be considered. The further the transducer is from the source of emission, the more change in the wave characteristics may occur.

The coupling of the transducer to the specimen under study is of considerable importance, since a minor change in the thickness of the coupling media could affect the emission data, and very often calibration of the transducer coupling is needed. Several methods of calibration have been suggested[61,78,79] by various workers and these include:

(a) Dropping a small ball-bearing from a known height on the specimen to produce a constant amplitude pulse. The technique is simple and practical but produces unrealistically large pulses of around 10 ms impulse time.

(b) Generating a fast rise time ($\sim$1 μs) thermal stress pulse of known amplitude in the specimen by passing a current pulse, $\sim$ 320 nsec long and up to 100 ams amplitude, through a point contact formed by an electrode and the specimen surface[61]. This method can be applied only on conducting specimens.

(c) Producing a stress pulse of known characteristic by coupling a double action transducer to the specimen. The transmitter section is connected to a pulse generator, and the receiver part to the AE system.

The direct effect of frequency on the AE data is clear from equation (2.23). Furthermore, the attenuation of the signal in the transducer is proportional to frequency so that the value of fT is constant, T being the duration of the source event. The frequency bandpass of the transducer is limited, i.e. any transducer could operate to its highest sensitivity within a range of frequencies. The response spectrum of the structure and transducer is then integrated by the resonances which are excited by the source of emission, and the result appears in the output waveform.

Finally the gain and threshold level which are the variables of the electronic system, and can be changed according to the test environment, will normally affect the AE data. The gain dependence of the ring-down count rate was measured by Brindley et

al[56] for a period of constant emission activity during plastic zone growth; the results showed that the AE count rate increased with $(\text{gain})^{1.6}$. The effect of threshold level was mentioned by Pollock[54] who indicated that the lower the threshold level amplitude, the higher the number of emissions obtained.

2.3.7 Acoustic Response of Alumina

A variety of processes give rise to stress wave emission in different materials. Dislocation motion and twinning occur mostly in ductile materials, but microcracking, crack growth and interaction with secondary phases can occur in both ductile and brittle materials.

Attempts have been made to relate the AE characteristics of ductile materials, such as metals, with their fracture toughness. A theoretical model presented by Dunegan, Harris and Tatro[11] is based on the assumption that the AE count, N, is proportional to the size of the plastic zone in front of the crack tip. The plastic zone size in the vicinity of the crack tip is controlled by the stress intensity factor, K, of the material. Thus the AE can be related to K, the relationship taking the form:

$$N = A K^n \qquad (2.26)$$

where A and n are constants. The value of n = 4 was obtained theoretically for ductile materials, while the experimental results for aluminium and beryllium indicated n values of 6 to 8. A value of n = 5 has been reported[62] for stainless steel.

However, Brindley, Holt and Palmer[56] considered that equation (2.26) is inadequate for situations which involve appreciable yielding. They found that the emission behaviour of some ductile materials showed that the total count versus load fitted the relationship:

$$N = D a \left\{ \sec \left(\frac{\pi \sigma}{2\sigma_1} \right) - 1 \right\} \qquad (2.27)$$

where D is a constant of proportionality, depending on strain rate, temperature, geometry and microstructure, a is the crack length, σ the applied stress and σ_1 the yield stress.

The acoustic emission of brittle materials has not been the subject of extensive investigation[62-65]. Nevertheless, Evans et al have used the technique to study a few ceramics, and some conclusive results have been reported. In his work with Linzer and Russell[10], Evans used the model proposed by Dunegan et al[11] for brittle materials, substituting the crack increment of Δa as the cause of AE instead of the plastic zone. The DT results of the AE count rate versus the stress intensity factor for Lucalox, tested at low loading rates, are shown in Fig. 2.15. Later, Evans and Graham[51] developed a model for crack propagation in polycrystalline ceramics. Their model was based on experimental acoustic emission amplitude studies, and incorporated the analysis of the stress intensity factor variation along a contoured crack front, and the local variation in crack propagation resistance.

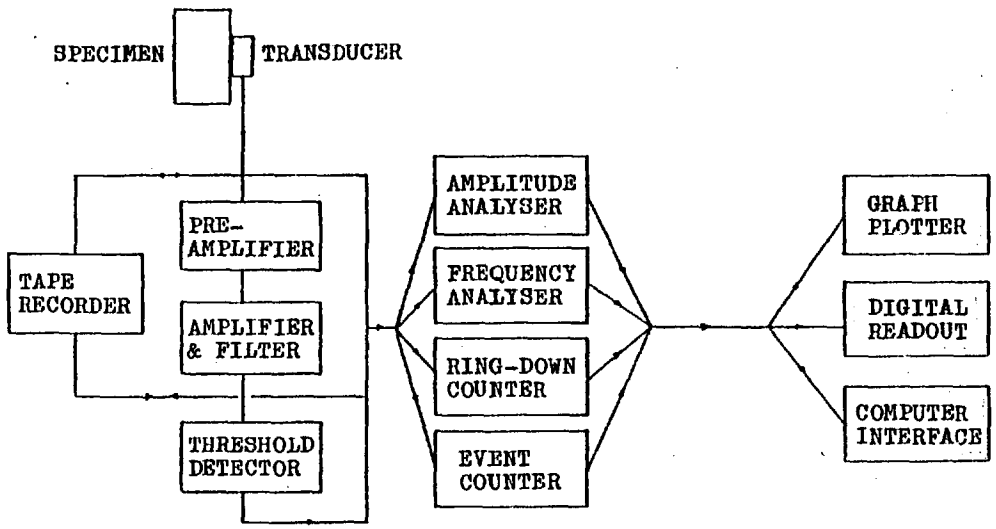


Fig.2.14. Several methods of processing emission are commonly used, the particular instrumentation and display are selected according to the kind of information required, (Ref.55) .

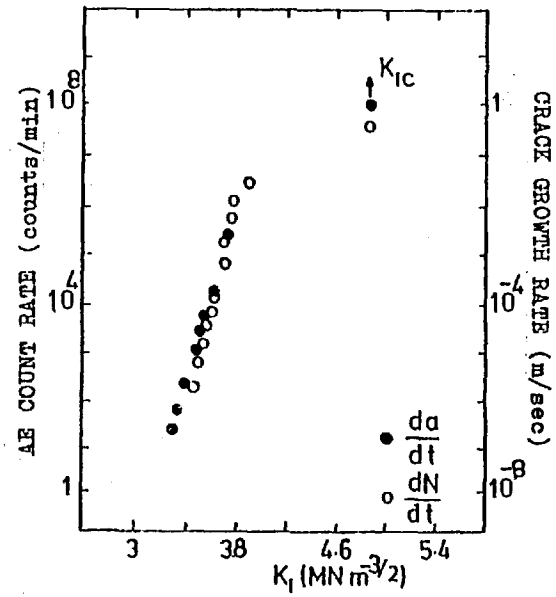


Fig.2.15. The crack growth rate and AE rate are plotted vs the stress intensity factor for Lucalox tested at RT in water using DT specimens (11).

CHAPTER 3

APPARATUS AND EXPERIMENTAL PROCEDURE

3.1 MATERIALS

The aluminas used during this investigation were supplied by commercial manufacturers, and were fabricated using different procedures and techniques. Therefore, materials of varied microstructure and properties were made available.

(i) Cold-Pressed and Sintered Aluminas:

The standard commercial alumina manufactured by Smiths Industries, FA0, was produced by isostatically cold-pressing and firing on commercial schedules. The FA0 alumina was then refired up to eight times on the commercial schedule to produce specimens designated FA1 to FA8.

The polycrystalline aluminas A and B supplied by Anderman and Ryder Ltd. were also produced by isostatically cold-pressing followed by firing on commercial schedules. The A and B aluminas are standard commercial materials, whereas alumina C was produced by refiring the alumina B on the commercial schedule. Aluminas A and D were also isostatically cold-pressed and fired materials produced by Anderman-Ryder Ltd.

(ii) Hot-Pressed Alumina:

A few bars of this material were supplied by Max-Planck Institut für Metallforschung, in West Germany. Alumina powder was hot-pressed in graphite dies under vacuum at a pressure of about 40 MN/m^2 for one hour at 1400°C. The resulting discs, 35 mm in diameter and 8 mm high, were cut into bars of 32 x 8 x 3 mm^3.

(iii) Alumina with ZrO_2 Dispersed Phase:

Composites were manufactured and supplied by the Max-Planck Institut. The compositions contained Al_2O_3 powder with 12, 15 and

18% by volume of unstabilized ZrO_2 powder. The powders were mixed in water in a planetary ball mill and hot-pressed using the same conditions as the above-mentioned hot-pressed pure alumina.

3.2 CHEMICAL AND MINOR PHASE ANALYSIS

A semi-quantitative analysis of the chemical composition of the aluminas A - E, and FA was performed by the Analytical Services Laboratory of Imperial College, using X-ray fluorescence. The aluminas were mechanically ground, sieved, and the -400 mesh fraction was compacted with cellulose to produce a specimen in the required pellet form.

X-ray analysis, using CuK_α, was obtained from a powder sample (-400 mesh) of each material. The measured interplanar spacings were compared with the ASTM powder index to identify the minor phases present.

3.3 MICROSTRUCTURAL ANALYSIS

Optical microscopy and scanning electron microscopy have been used to determine the microstructure of the aluminas.

Polished surfaces for optical microscopy were prepared by carefully grinding samples on 600 grade silicon carbide papers, and subsequent polishing on 6 μm, 3 μm and 1 μm diamond impregnated laps. Further polishing was carried out on nylon cloth loaded with α-alumina powder ($\frac{1}{4}$ μm) using water as lubricant. The polished samples were then etched either with 2% HF solution for 2 to 4 minutes, or by thermal treatment in air at 1600°C.

Scanning electron microscopy was used to examine fracture surfaces. The specimens were cleaned and mounted on standard aluminium stubs and their fracture surfaces were vacuum-coated with a 200°A layer of gold.

3.3.1 Grain Size and Pore Size Measurement

Optical micrographs taken from the polished surfaces of the specimens were used for pore size determinations and the grain size was measured from micrographs taken from the etched surfaces. All measurements were performed using the linear intercept method on several randomly selected areas. The mean grain size, the maximum grain size, the maximum pore size, and grain size and pore size distributions were obtained.

3.3.2 Density Measurements

Density measurements were made using a displacement technique in which each specimen was weighed in air and in distilled water at room temperature. Weighings were made on a balance reading to 1×10^{-5} g and for each specimen the mean value of ten weighings was used to calculate the density. The density of a specimen is given by:

$$\rho = \frac{W_A}{W_A - W_W}$$

where W_A and W_W are the weights of the specimen in air and in water respectively.

3.3.3 Porosity Measurements

The porosity of each material was calculated from its density data using the following relation:

$$\text{Porosity } \% = \frac{100(\rho_T - \rho_E)}{\rho_E} \qquad (3.1)$$

where ρ_T is the theoretical density of the material. A value of 3.986 g/cm^3 [14] was used for the theoretical density of pure alumina and values of 3.3[14], 3.57[14], 2.65[28], and 6.1[80] g/cm^3 were employed for the theoretical density, ρ_{Ti}, of the impurities, CaO, MgO,

SiO_2, and ZrO_2 respectively. The theoretical density of an alumina containing H_i percent impurities or second phase particles, was calculated using the following simple relation:

$$\rho_T = \frac{\sum \rho_{Ti} H_i + 3.986(100 - \Sigma H_i)}{100} \qquad (3.2)$$

Having measured the theoretical density and experimental density for each composite, the porosity was then determined from equation (3.1). The use of mercury porosimetry[81] was limited by the extent of closed porosity in the aluminas which prevented efficient access of mercury into the sample.

3.4 MECHANICAL TESTING

3.4.1 Specimen Preparation

Specimens were cut by diamond sawing from alumina plates in a Capco (Model Q-35) cutting machine using oil for lubrication, and a Maco slit-grinding machine using a water solution of ethyl alcohol (C_2H_5OH) as lubricant. The as cut surfaces of specimens were sufficiently smooth (average machined flaw size < 50 μm), thus no special treatment was carried out on specimens used for fracture toughness measurements. With the presence of machined cut notches and grooves on these specimens, further surface treatments, however, did not make much difference. Unnotched and ungrooved specimens used for strength measurements were, however, subjected to surface preparation prior to testing.

3.4.2 Loading Techniques

All tests were performed in air using a universal Instron machine for loading the specimens. A compression-tension load cell with a maximum loading capacity of 500 Kg was used. Simple jigs were designed for different test geometries enabling easy access to

the specimen for coupling to the AE transducer. The loading jigs consisted of an upper ram, which was attached to the load cell, and specimen mount which was fixed to the Instron cross-head. With the specimen in position, load was applied when the specimen mount was driven against the upper ram via the cross-head movement. Cross-head speeds in the range 0.001 to 0.1 cm/min were used.

To avoid monitoring extraneous noise due to the jig system, all loading points which were in direct contact with the specimen were acoustically insulated from the specimen by coating with PTFE tape. Furthermore, before testing commenced, a large or unnotched specimen was loaded to twice the estimated fracture load of test specimens to check the efficiency of acoustic insulation and to reduce noise in the loading system by the Kaiser effect.

3.4.3 Fracture Strength Determination at Room Temperature

The modulus of rupture tests were carried out using the 3-point bending jig shown in Fig. 3.1 for fracture strength measurement. The specimens, typically 4 x 3 x 2 5 mm^3 in size, were loaded between three parallel stainless steel rods so that the upper rod was situated exactly in the middle of the two lower supporting rods. The rods were 3 mm in diameter and were covered by PTFE tapes for acoustic insulation and fixed in grooves machined on the upper ram and the specimen mount. A number of grooves were machined in the specimen mount to allow for variation of the loading span. The specimens were broken using a 20 mm span. Since the use of a 1 μm specimen surface gave modulus of rupture values only $\approx 3\%$ higher than those obtained for specimens with as-ground surfaces (600 grade) [21], hence specimens were subsequently tested with the convenient as-ground surface. The AE sensor was attached to one side of the specimen approximately 10 mm from the centre using a high vacuum grease.

The modulus of rupture values were measured using the equation[21]:

$$\sigma_f = \frac{3Ps}{2b\ w^2}$$

where P is the fracture load, s is the distance between the outer knife edges (span), and b and w are the breadth and depth of the specimen respectively.

3.4.4 Fracture Toughness Determination at Room Temperature

The fracture toughness parameters may be measured either by the analytical methods in which the stress intensity factor is measured for a given geometry, or by determination of the surface energy and the strain energy release rate directly from the modified Griffith's equations. These are, however, related to each other by the equations (2.10), (2.11) and (2.12).

The fracture toughness parameters in this study were measured using analytical solutions for three different test geometries, i.e. single-edge notched bend specimens, double torsion specimens, and double cantilever beam specimens. The techniques were based on the assumption that crack motion occurred when the stress intensity in the vicinity of the crack tip reached a critical value. The analytical solutions of the modified Griffith equation for SENB, DT and DCB geometries[24,83] were used, in which K_I was expressed as a function of applied load, crack size and sample dimensions. (DT geometry was independent of crack length.) The critical stress intensity factor was then calculated from the critical load at failure.

(i) SENB Specimens in 3-Point Bending:

The specimen geometry and recommended proportional dimensions are shown in Fig. 3.2. The SENB specimens were compact and of simple geometry, so they were easily and cheaply prepared. They were typically 2 x 4 x 25 mm^3, but occasionally due to experimental limitation or material availability other sizes were also produced, taking care that dimensional proportionality was maintained. A blunt notch of length, a, approximately half the width of the specimen, was introduced midway along the specimen length in one of two ways:

(a) Sawn notches were made using a Capco diamond cutting machine, in which the specimen was moved forwards and against a high speed (4000 rpm) diamond blade of 0.25 mm cutting thickness. The specimen movement was stopped once the length of cut was achieved, and had to be reversed manually. Honilo 43-red oil flowed on the cutting point for lubrication and cooling the blade.

(b) Sawn notches were made using a Maco slit grinder in which the specimen moved under a diamond blade rotating at 2800 rpm. The blade height could be adjusted to give the required depth of cut. The cutting width of the blade was 0.3 mm and water solution of ethyl alcohol was used as the lubricant.

The SENB specimens were tested in a 3-point bending jig using a 20 mm loading span so that the upper rod was situated in the same plane as the notch and in the middle of the two lower supporting rods, as shown in Fig. 3.3. The AE sensor was coupled to one side of the specimen approximately 10 mm from the root of the notch.

The stress intensity factor was determined from the expression given by Paris and Sih[24]:

$$K_I = \frac{3}{2}\left[\frac{yPsa^{\frac{1}{2}}}{bw^2}\right]$$

where K_I is the stress intensity factor, P is the load, a is the crack length, b is specimen breadth, w is specimen width, s is loading span and y is a dimensional calibration factor to account for allowed variations in the ratio (a/w). The values of y calculated by Srawley and Brown[82] are shown in Fig. 3.4.

(ii) <u>DT Specimens in 4-Point Bending</u>:

The specimen geometry and loading configuration are shown in Fig. 3.5. DT specimens were plates typically 20 mm wide, 50 mm long and 2 mm thick, and grooved on one side to channel crack

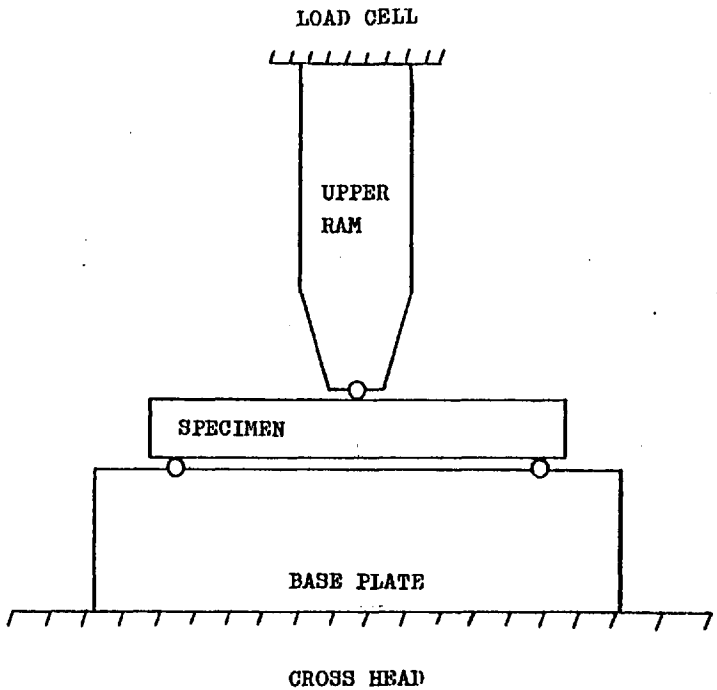


Fig.3.1. The 3-point bending jig.

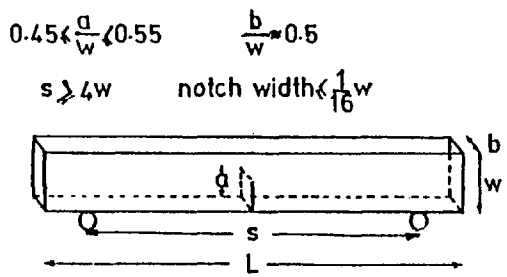


Fig.3.2. The SENB specimen and the recommended dimension proportional relations.

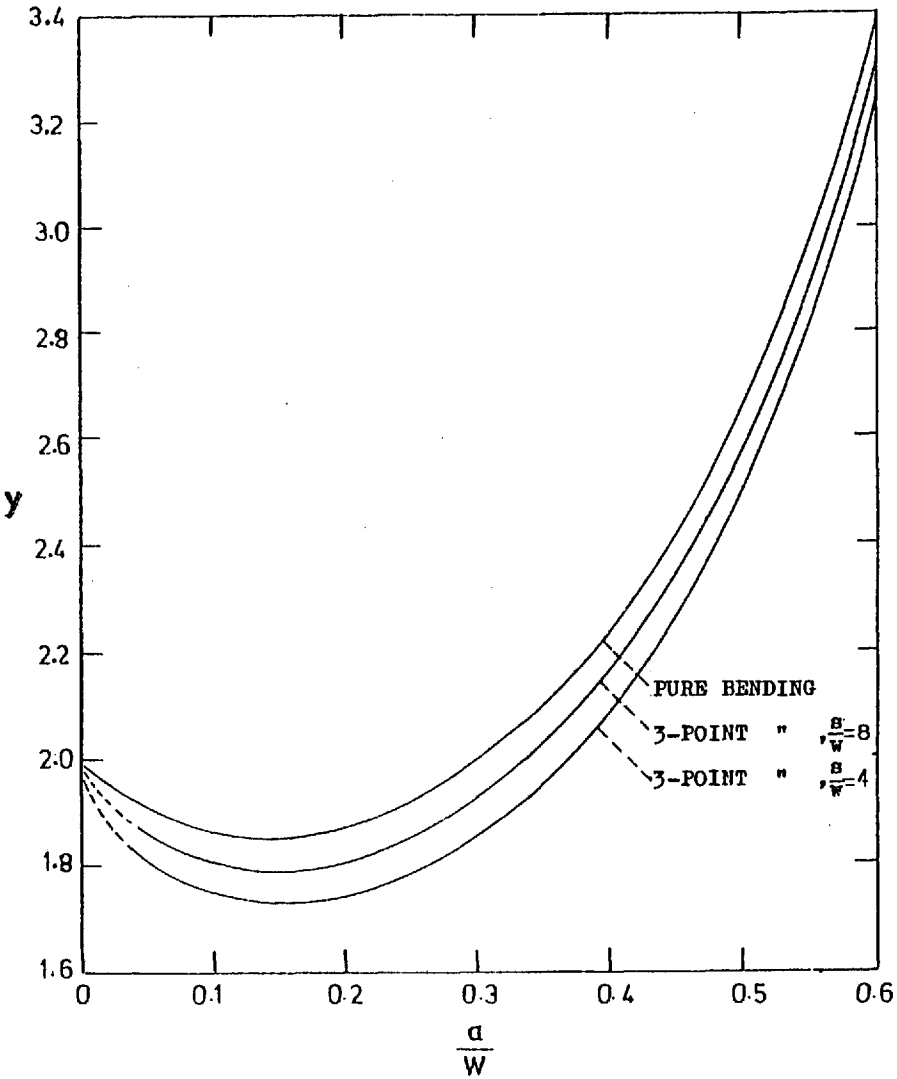


Fig.3.4. K calibration for bend specimen.

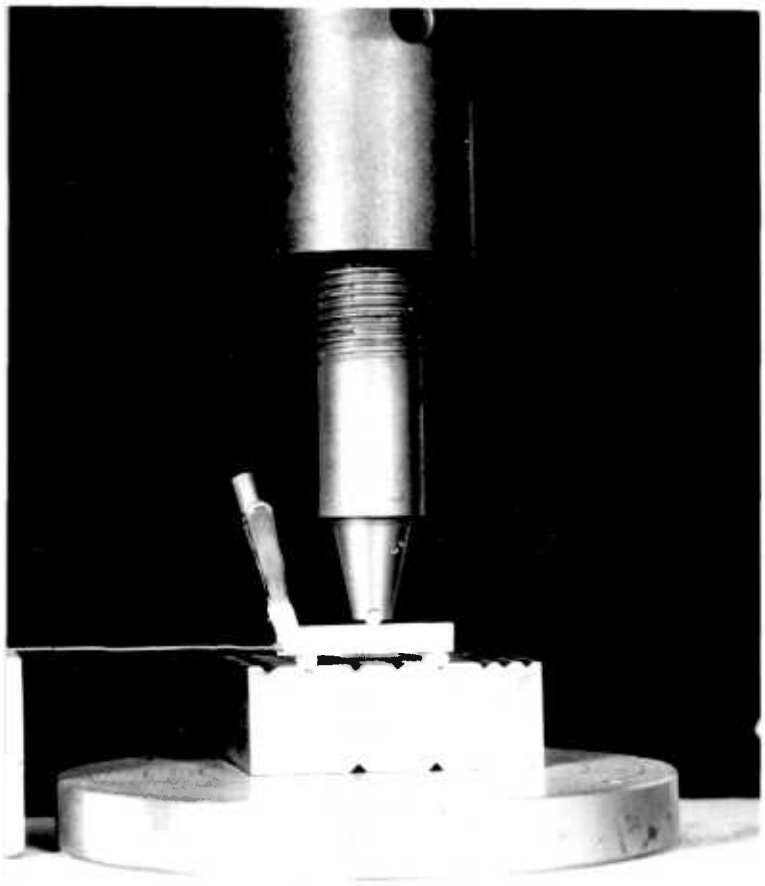
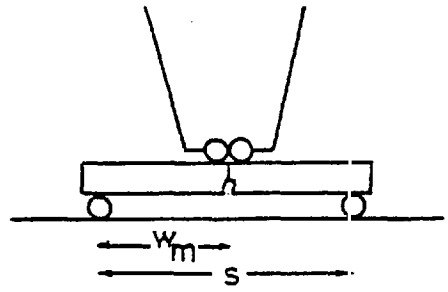
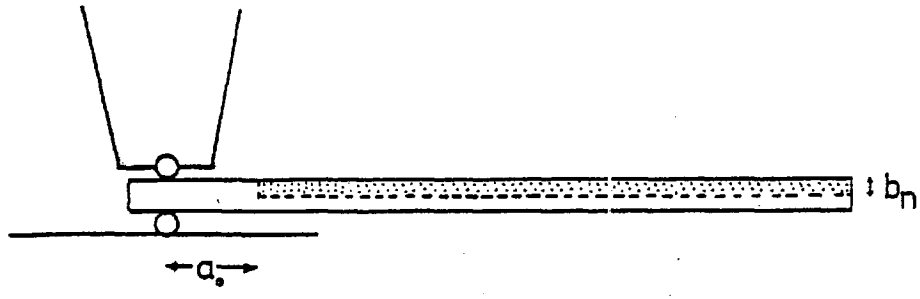


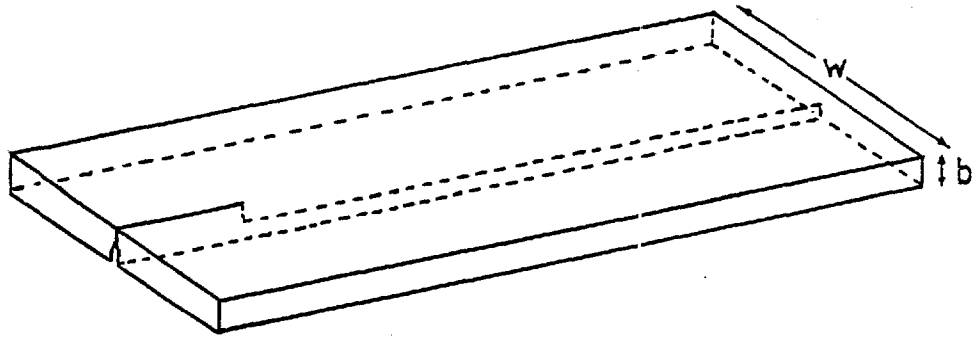
Fig.3.3. Three-point bend jig & the SENB specimen.



(a) END PROJECTION



(b) SIDE PROJECTION



(c) THE GENERAL VIEW

Fig.3.5. The double torsion specimen geometry and loading configuration.

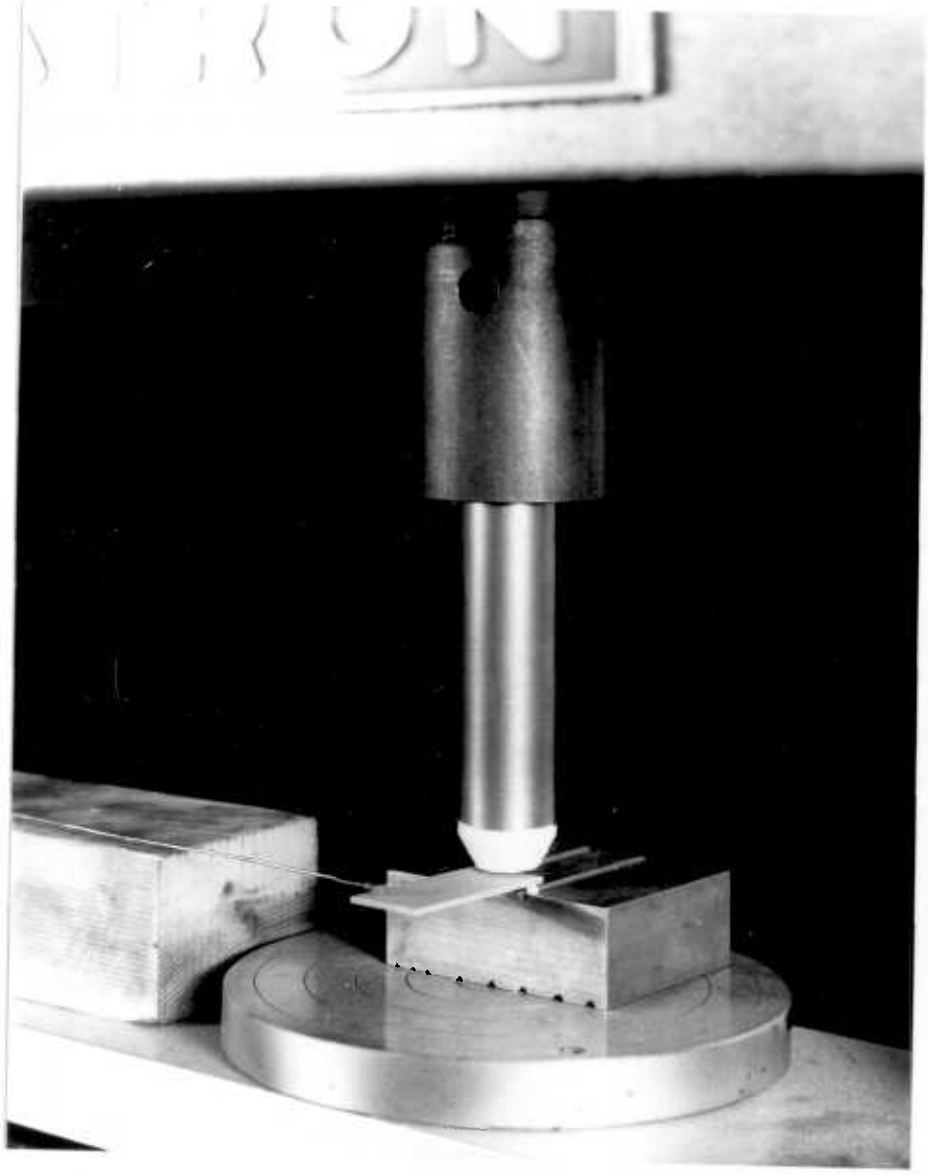


Fig.3.6. The DT specimen in 4-point bending.

propagation during testing. The depth of the groove was half the plate thickness. Blunt notches 8 mm long were introduced using a Capco diamond machine and sharp subcritical cracks were formed at the notch roots using the technique described in Section 3.8.

The DT specimens were tested in 4-point bending using the jig shown in Fig. 3.6 which is based on the technique developed by Kies and Clark[83]. The upper ram had two steel bearings set in its end surface so that the distance between the centres was 18 mm. Specimens were positioned in the system as shown in Fig. 3.5, the system being so aligned that the four bearings at the loading end were in the same plane perpendicular to the specimen notch with the specimen centrally placed between the bearings. The two halves of the specimen were, thus, subjected to equal torque by a four-point application of load. The AE transducer was situated on the specimen approximately 35 mm from the root of the blunt notch.

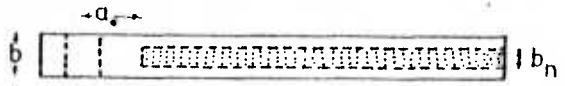
The values of stress intensity factor were calculated from the expression:

$$K_I = Pw_m \left[\frac{3(1+\nu)}{wb^3 b_n \zeta}\right]^{\frac{1}{2}}$$

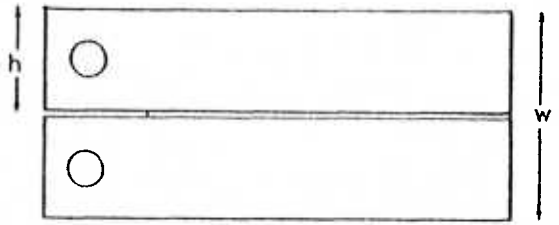
where P is the load, w_m is the distance between the inner and outer loading points on each beam, w is the specimen width, b is the specimen thickness, b_n is the crack plane width, $\zeta^{(3)}$ is a thickness factor = $1 - \frac{5}{4}(d/w)$, and ν is Poisson's ratio.

(iii) DCB Specimens in Tension:

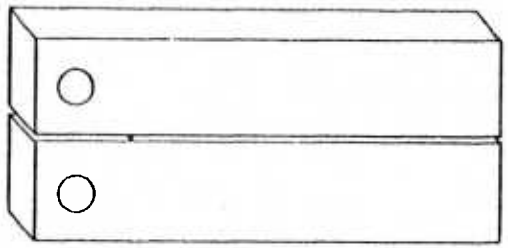
The DCB specimen geometry and loading system are shown in Figs. 3.7-3.9. The specimens were typically 20 mm high, 50 mm long and 5 mm thick, and contained a groove on each side to channel crack propagation. The depths of the grooves were such that the crack plane width was half the plate thickness. Two loading holes were drilled symmetrically about the crack line using a diamond core drill. A blunt notch was cut along the grooves using the Capco



(a) SIDE PROJECTION



(b) SURFACE PROJECTION



(c) GENERAL VIEW

Fig.3.7. The DCB specimen geometry.

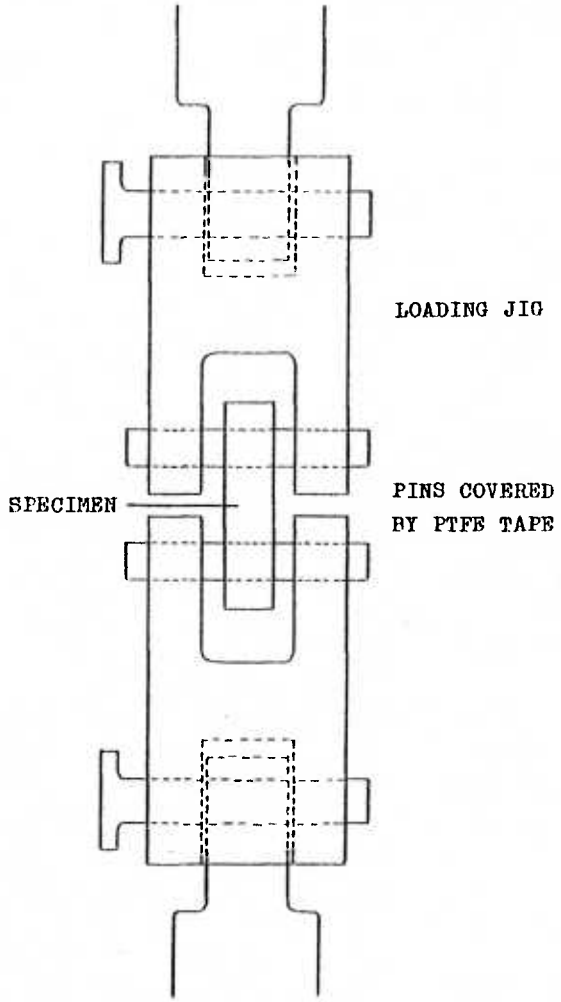


Fig.3.9. Side view of the DCB test jig.

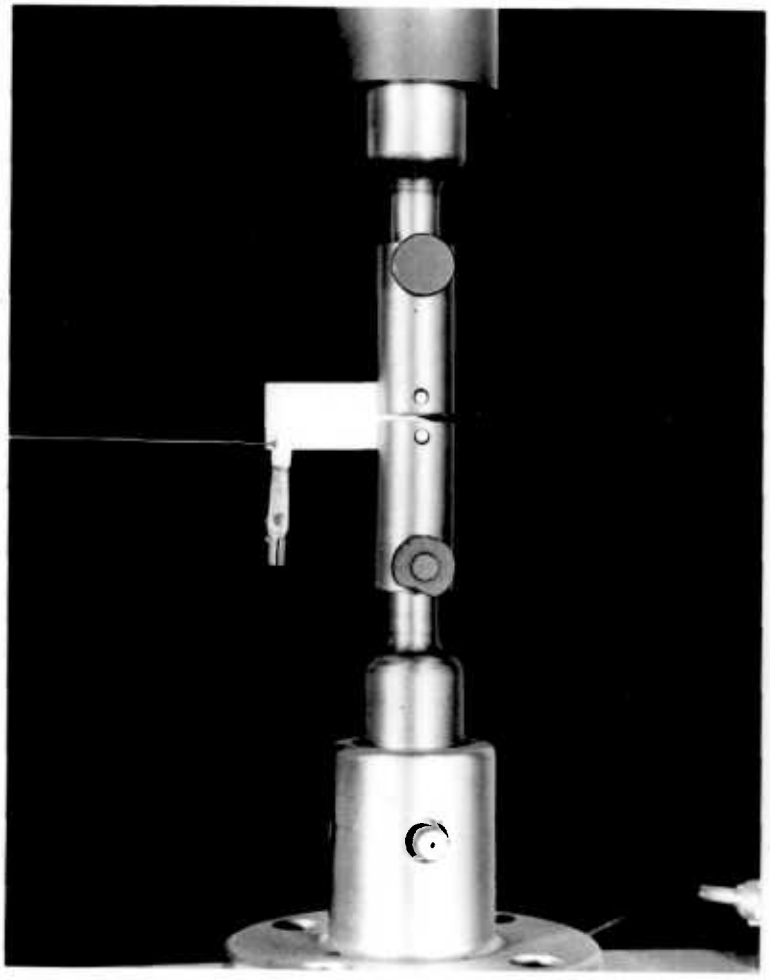


Fig.3.8. The DCB loading system.

machine so that it extended 5 mm past a line through the centres of the loading holes. Specimens were subjected to subcritical crack growth, as described in Section 3.8, to produce sharp pre-cracked specimens.

The DCB specimens were tested in tension, the load being applied via stainless steel rods which passed through the loading holes. The loading jig (Fig. 3.9) was designed so that there was no contact with the specimen except by the two loading rods which were covered with PTFE tape to ensure acoustic insulation. The AE transducer was situated on one side of the specimen, 35 mm from the blunt notch root.

The stress intensity factor was calculated from the expression[3]:

$$K_I = \frac{Pa}{b_n h^{3/2}} \left[3.467 + 2.315\left(\frac{h}{a}\right) \right] \left(\frac{b_n}{b}\right)^{\frac{1}{2}}$$

where P is the load, a is the crack length, b_n is the crack plane width, h is the beam half-height, b is the plate thickness and factor $\left(\frac{b_n}{b}\right)^{\frac{1}{2}}$ accounts for the effect of side grooving.

3.5 MECHANICAL TESTING AT ELEVATED TEMPERATURES

The furnace (Fig. 3.11) consisted of a silica tube, 8 cm in diameter and 18 cm high, housed in a 20 x 20 x 20 cm^3 asbestos box, which was mounted on a frame bolted to the Instron cross-head. The furnace was mounted on the frame in such a way that it could be moved up and down against two counterbalances. Provision was made for the thermocouple leads and the AE waveguide to pass through the top of the furnace to the specimen. The upper ram-load cell coupling was water-cooled to protect the load cell. Power was supplied to the furnace through a controller, and the position of the furnace over the specimen was determined after calibration to find the hot zone.

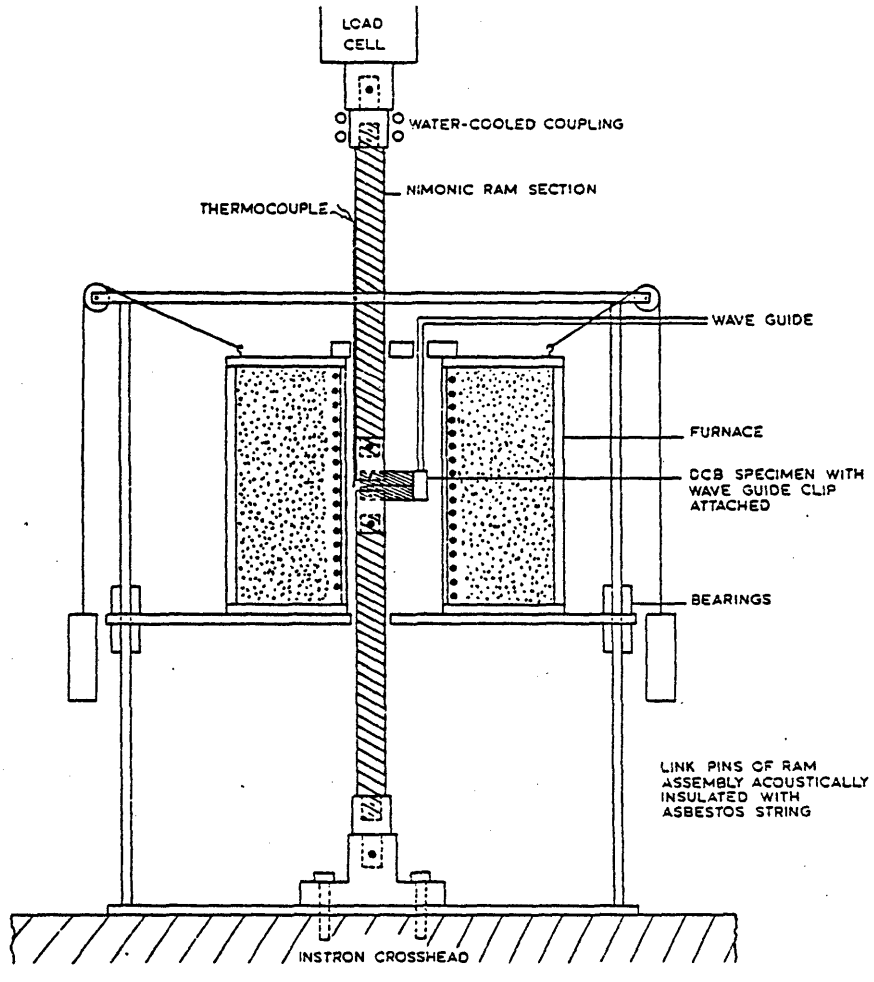


Fig.3.11. The high temperature furnace.

For high temperature tests, specimens were loaded and fractured in essentially the same way as for room temperature tests, except that asbestos string was used instead of PTFE as the acoustic insulator. The transducer was coupled to a stainless steel wave guide which was attached to the specimen using high temperature grease and asbestos string.

The fracture toughness parameters were determined using the DCB test piece since it proved to be fairly convenient geometry in terms of loading, and preliminary room temperature investigations had shown that it was acoustically more responsive than the SENB and DT geometries.

3.6 ACOUSTIC EMISSION MEASUREMENTS

3.6.1 Data Acquisition Techniques

The stress waves generated within the specimen during the fracture process were picked up by a transducer coupled to the specimen, and converted to very low energy electrical pulses. The output voltage of the transducer was then processed using the experimental set-up shown in Fig. 3.12. The AE equipment utilized was manufactured by Dunegan-Endevco (DE) and Acoustic Emission Consultants Limited (Tek).

The instrumentation consisted of a MC500 sensor (manufactured by Acoustic Emission Technology Corporation), a Tek pre-amplifier, a 105 Tek totaliser, a 921 DE amplitude detector, a DE 920 distribution analyser, and a DE 922 external memory. These items were connected together with two Omniscribe recorders, a 25000 A4 Bryans X-Y recorder and a Solatron oscilloscope, to form a system capable of providing a record of acoustic emission amplitude and pulse width distributions and the ring-down and event counts as a function of specimen load. Fig. 3.13 illustrates the AE equipment and the loading machine.

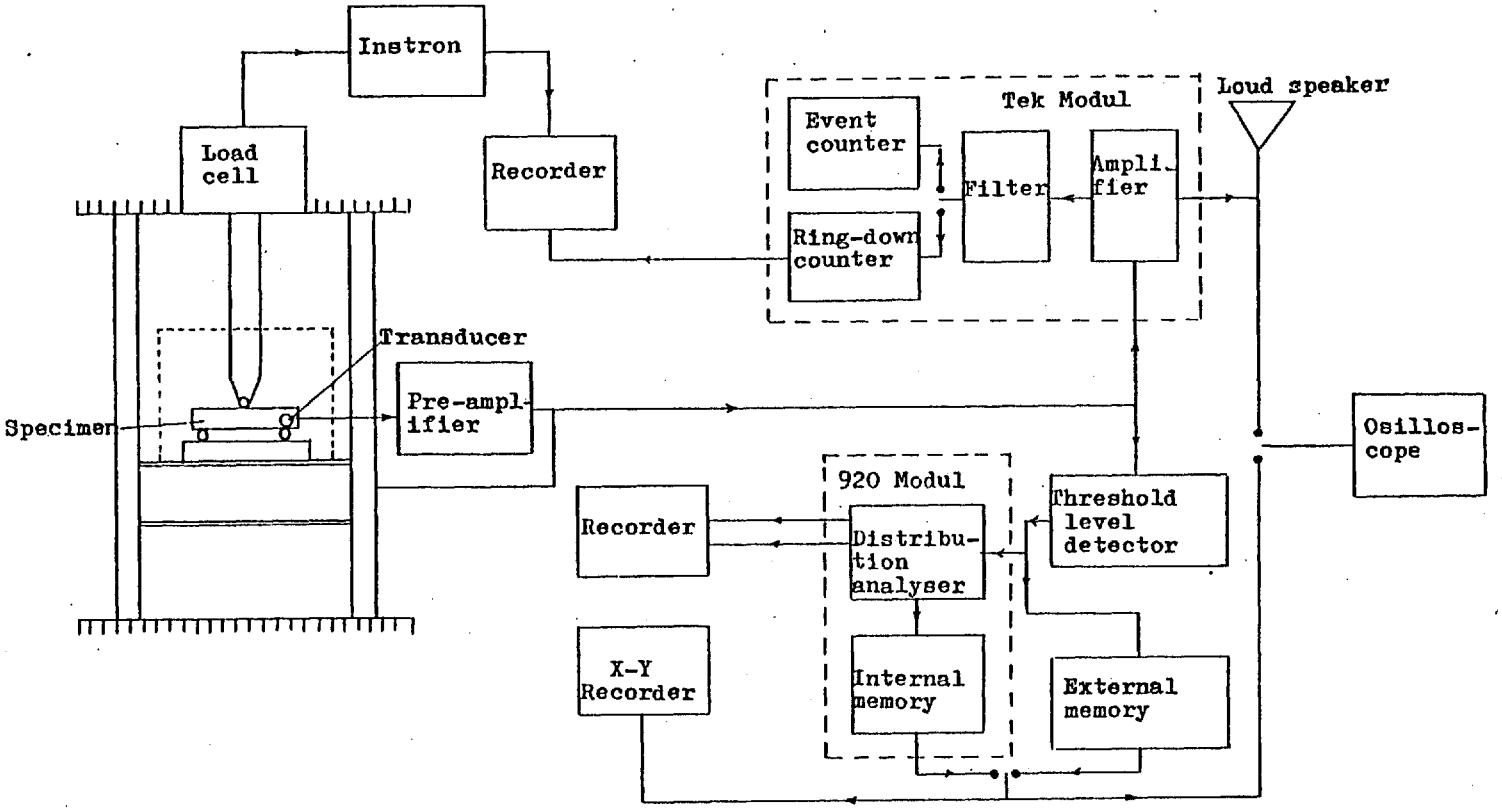


Fig.3.12. The experimental setup used for AE data acuisition.

Fig.3.13.

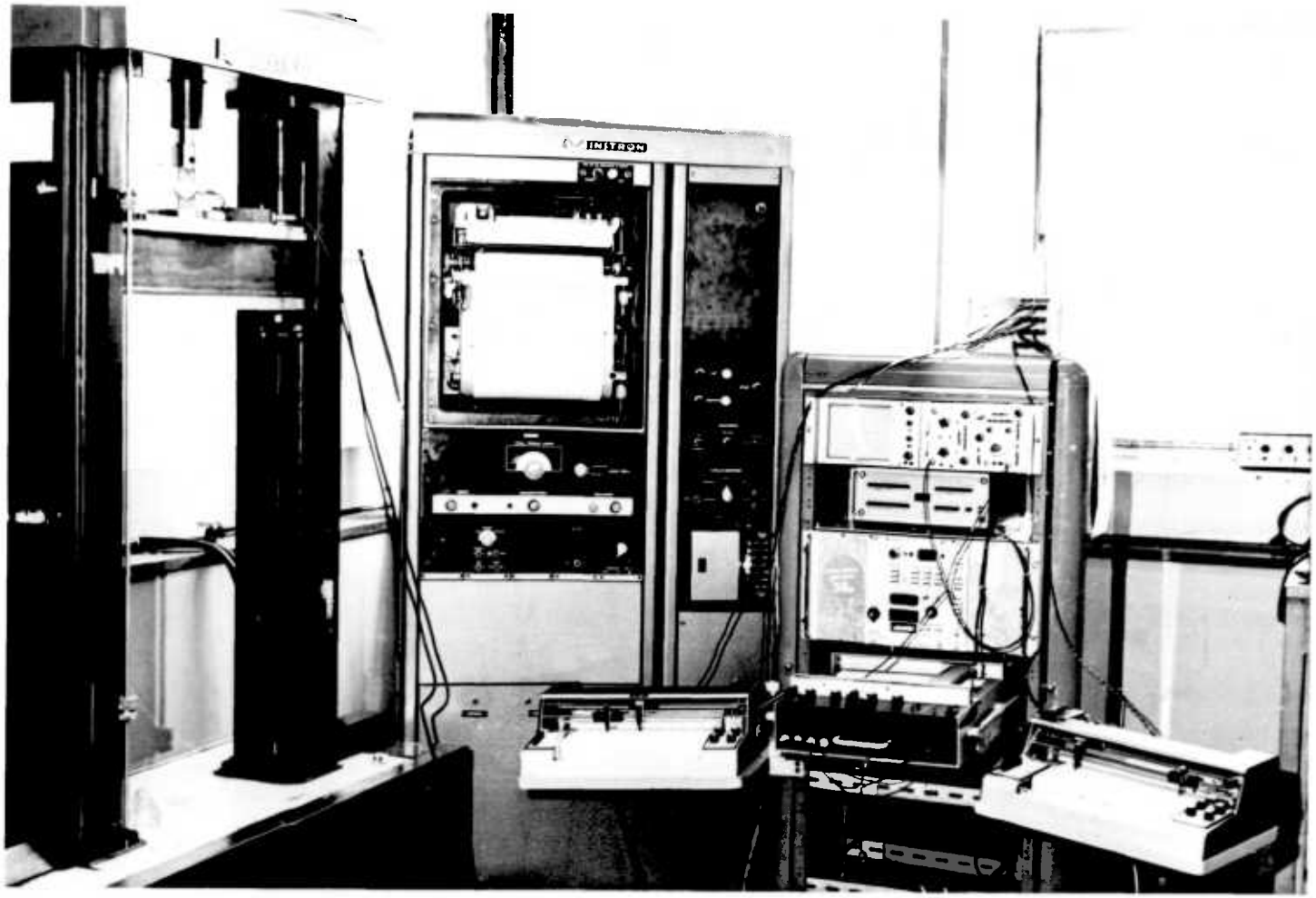


Fig.3.13. The acoustic emission and the mechanical testing equipment.

3.6.2 The Transducer and its Coupling

The transducer utilized was small and thus suitable for the small specimens employed in this investigation. It was 3.81 mm in diameter and 2.54 mm high and was easily coupled to the side of the specimen using vacuum grease and a small clip. The frequency response of the transducer is shown in Fig. 3.14[84] which shows an average response of about -85 dB over a range of frequencies from 150 KHz to 600 KHz. The calibration of the transducer-specimen coupling was carried out by dropping a small ball bearing from a known height at the beginning of experiments. A steel mesh box earthed together with the pre-amplifier to the loading system, was used around the specimen under test to prevent the outside electronic noises from reaching the transducer.

3.6.3 Pre-Amplifier

The pre-amplifier was a fixed gain amplifier which provided 40 dB of gain. The gain, i.e. the amplifying power, of the pre-amplifier is determined from the expression:

$$\text{Gain (dB)} = 20 \log \frac{V_{out}}{V_{in}}$$

where V_{out} is the output voltage of the pre-amplifier, and V_{in} is the input voltage which is equal to the output voltage of the transducer. The gain is measured as dB, therefore an amplifier with $V_{out}/V_{in} = 100$ has a gain of 40 dB. The amplified signals were then processed using two different techniques:

(i) At a constant threshold voltage, further amplification was provided for the ring-down counting technique, i.e. the gain of the system was increased to a value where the electronic noise level was below the pre-set threshold voltage.

(ii) At the constant gain provided by the pre-amplifier, the threshold voltage was changed to just above the background electronic noise level.

3.6.4 The Ring-down Counting Technique

The pre-amplified output was fed to the totaliser module for further amplification, filtration and ring-down counting. At a constant threshold voltage of 1 volt (selected by the manufacturer[85]) a further 55 dB gain was achieved from its maximum gain of 65 dB. The overall gain of 95 dB was constantly used in all experiments to eliminate the influence of the gain variation on AE results.

The totaliser also acted as a filter covering the frequency range of 20 KHz to 2 MHz, with the choice of operating within four frequency ranges, depending on the frequency response of the transducer in use. The frequency range 100 KHz to 300 KHz was that selected for the above-mentioned transducer. The signal output of the totaliser was displayed on an oscilloscope for the visual inspection of the background electronic noise level.

For AE ring-down counting, the totaliser measured the number of emission peaks exceeding the pre-set threshold voltage. Either the total number of AE ring-down counts was measured during a test, or a certain time interval, usually 1 sec., was selected and the counts were totalized over the chosen time interval to give the count rate. The output of the totaliser was recorded on the Omniscribe recorder against the output of the loading system, i.e. the Instron. The chart speed provided approximate data for the time lapse between crack initiation and final failure.

3.6.5 Amplitude and Pulse Width Distribution

The amplitude detector[86] provided the chance of selecting a suitable threshold level for the output signals of the pre-amplifier before they were fed to the distribution analyser for further processing. A threshold level of 24 dB was selected (this was often up to 3 dB above the electronic noise level) and kept the same for all tests. The use of a constant threshold level for all experiments eliminated this parameter as a variable to AE results.

The amplitude detector measured the peak amplitude of AE bursts exceeding the threshold level and converted them to logarithmic signals. Pulses proportional to the log of the peak amplitude (i.e. in dB) were sent to the distribution analyser for amplitude analysis. The distribution analyser[87] sorted the peak amplitudes of AE signals into 101 dB steps and then stored them in a memory containing 101 storage slots, each capable of storing a maximum 4095 events. An X-Y scope was driven by the distribution analyser for direct readout of the memory content. For permanent records the display was transferred to an X-Y recorder.

The amplitude distributions were output in two forms:

(i) In the normal-linear mode, the histogram of the number of events versus their amplitude was obtained.

(ii) In the sum-log mode, the events of each successive element were added to the higher elements for display on a log scale.

The slope of the distribution curve in the latter mode gave a measure of the b-value of the amplitude distribution (discussed in Section 2.3.5). The value of b and also the number of events were continuously recorded on a chart recorder.

The distribution analyser operating in conjunction with an external memory[88] was also used for the pulse width analysis. Operating in the pulse width mode, the distribution analyser contained a re-triggerable one-shot that was energized at the first pulse of the burst, remained energized during the burst and, after the last pulse of the burst, stayed energized for the period of time selected (dead time = 50 μsec in the present work). Fig. 3.15 is a schematic diagram of the pulse-width measuring technique. The end of the envelope time was defined as the end of an event and the duration of the envelope processor was the burst pulse width. The measured pulse widths were then fed to the external memory. The memory sorted the data, by appropriate selection, from 0 to 1000 μsec in tens of microsecond increments, or from 0 to 10^4 μsec in

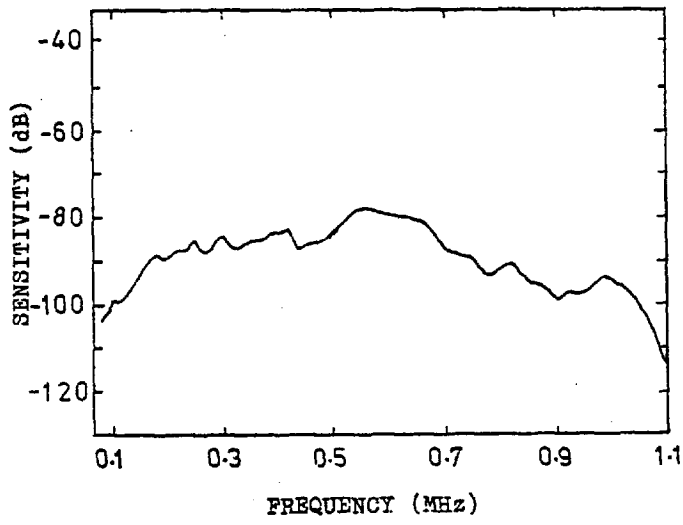


Fig.3.14. The frequency response of MC500 transducer.

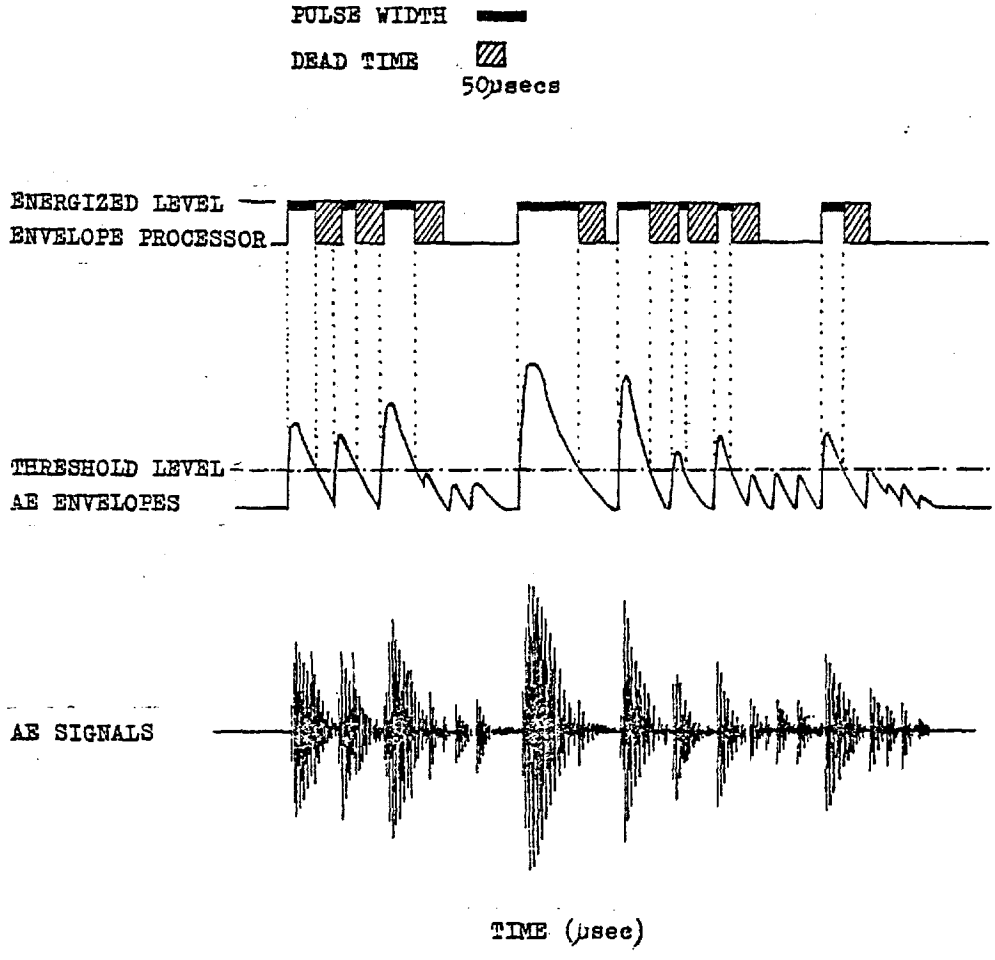


Fig.3.15. A schematic diagram showing the pulse width measuring method used.

hundreds of microsecond increments, and stored them in its 101 storage slots. The external memory content was displayed on the oscilloscope and recorded on an X-Y recorder in the same way as described for the amplitude distribution.

3.7 DETECTION OF AE AT ELEVATED TEMPERATURES

The use of a wave guide for transferring the AE signals from the specimen to a transducer situated outside the furnace was unavoidable, since presently available transducers cannot be used at temperatures higher than about 500^{0}C.

Rods of alumina, stainless steel and brass were compared for their suitability as high temperature wave guides and their AE behaviour at elevated temperatures was assessed.

The alumina wave guide had the advantage of having the same heat expansion coefficient as the specimens and therefore could be efficiently attached to the specimen. However, it was difficult to shape the alumina to serve in the specimen-furnace system employed, and the material was found to exhibit significant acoustic response during temperature changes.

The brass rods were more flexible and had reduced AE response during heating and cooling. However, they suffered from being easily deformed and oxidised at high temperatures, and had an increased expansion coefficient compared with alumina.

The stainless steel rods had the disadvantage of having a different expansion coefficient than the alumina specimens, and became oxidised at high temperature. However, the steel rods were ideal for shaping to the furnace and specimen system and their acoustic response was minimal as the temperature changed. Stainless steel was therefore the material chosen as the wave guide. The acoustic response due to oxidation during testing was minimised by heating for a short while at a temperature just above the test temperature and subsequently reducing the temperature to that required for testing.

The coupling of the wave guide to the specimen for high temperature use proved to be a problem, since none of the commonly used coupling greases and clips were stable at the temperature employed. Finally a high temperature grease was used as the intermediate coupling layer and asbestos string was used to bind the wave guide to the specimen. The grease contained graphite, so that at high temperature the oil evaporated leaving a thin layer of graphite between the specimen and the wave guide. Fig. 3.16 shows a wave guide attached to the specimen under test.

The use of the wave guide made it possible to employ a bigger and more sensitive transducer. Nevertheless, some loss in sensitivity was inevitable using the wave guide and remote transducer system. A Dunegan-Endevco D-140B transducer with an average response of -75 dB over the frequency range of 150 to 300 was used, which was 10 dB more sensitive than the small transducer employed for room temperature tests.

3.8 THE USE OF AE FOR SUB-CRITICAL CRACK MEASUREMENTS

The AE technique was used to monitor the slow crack growth in alumina specimens subjected to subcritical crack measurement. The blunt-notched SENB, DT and DCB specimens were loaded in the Instron at a low cross-bead speed (normally 0.01 cm/min) using all the loading and AE monitoring procedures required for a fracture toughness test. Soon after the first indications of acoustic emission and before specimen failure, the Instron cross-head direction was reversed (at faster rate of 0.05 cm/min) and the specimens were removed for sub-critical crack observation and measurement. A water-based dye penetrant was used to reveal the cracks and assist in the measurement of their length. The procedure was repeated, if necessary, until the required sharp crack length was obtained.

The crack growth was sufficiently controlled in DT and DCB specimens to allow each specimen to be used for several progressive crack extensions at relatively high cross-head speeds

for sub-critical crack and corresponding AE measurements. The control of crack growth in SENB specimens was poor and many specimens failed during the first loading.

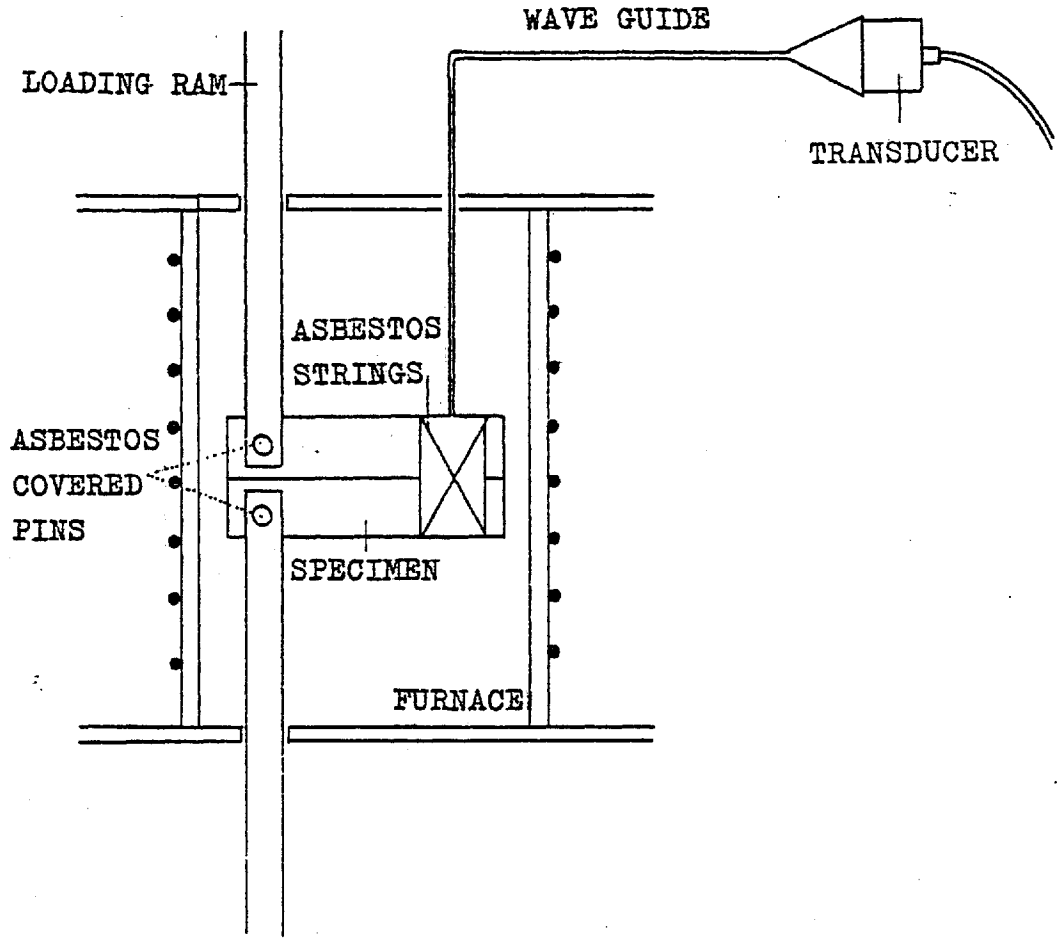


Fig.3.16. The wave guide coupling arrangement with the specimen for high temperature test.

CHAPTER 4

RESULTS AND DISCUSSION

4.1 CHEMICAL ANALYSIS

The trace impurity levels present in the aluminas are listed in Table 4.1, which indicates that aluminas produced by Smiths Industries (FA0-FA8) were 95% pure, whilst aluminas manufactured by Anderman Ltd. (A, B, C, D and E) were ≃ 97 % pure. These values are given by the manufacturers but these impurity levels were qualitatively confirmed by X-ray fluorescence measurements at the Imperial College.

X-ray analysis showed that the major phase in all materials was α-alumina, but also demonstrated the presence of minor phases. The principal minor phase in aluminas A to E was spinel ($MgO.Al_2O_3$); whilst there was some evidence for the presence of gehlenite ($2CaO.Al_2O_3.SiO_2$), and calcium hexaluminate ($CaO.6Al_2O_3$). In addition, the presence of anorthite ($CaO.Al_2O_3.2SiO_2$) in these aluminas was indicated. The level of impurity was much higher in FA0 to FA8 aluminas compared with A-E. The major minor phases in FA0-FA8 aluminas were calcium-based phases, mostly calcium hexaluminate and anorthite. There were also indications of the presence of sodium fluorouranate ($7NaF.6UF_4$), gehlenite and spinel in these aluminas. Finally, it was expected that all the aluminas contained a glassy phase.

TABLE 4.1 Chemical Analysis of Sintered Aluminas

Aluminas	% Elemental Impurity			
	SiO_2	MgO	CaO	ZrO_2
A,B,C,D,E	1.75	0.8	0.4	-
FA0-FA8	2.5	0.5	2	<0.3

4.2 MICROSTRUCTURAL ANALYSIS

4.2.1 Grain Size and Pore Size

The microstructure of alumina FA0 consisted of large grains of alumina up to 35 μm in diameter, within a matrix of finer-grained material and intergranular porosity, as shown in Fig. 4.1a. The mean grain size 4 μm and a maximum pore size of 30 μm were measured by the linear intercept method. The effect of refiring alumina FA0 on the standard production schedule was to coarsen the grain size, with a small increase in the total porosity, as illustrated in Figs. 4.1 and 4.2. The values of the mean grain size, the maximum grain size and the maximum pore size for all FA materials are presented in Table 4.2. The size of the intergranular pores increased correspondingly, as can be seen in Fig. 4.1, and the maximum grain size increased from 35 μm in FA0 to 50 μm in FA4 and 75 μm in FA8.

The distribution of the grain size vs. their relative frequency for aluminas FA0, FA4 and FA8 is shown in Fig. 4.3. Less than 5% of the FA0 grains were larger than 20 μm, while about 12% of FA4 and nearly 50% of FA8 grains were greater than 20 μm. The most frequent grain size corresponded to 2 to 4 μm in FA0, 10-12 μm in FA4 and 18-20 μm in FA8. Fig. 4.4 shows the pore size histograms for FA0, FA4 and FA8 aluminas. In FA0, 15% of the total pores were larger than 20 μm, while in FA4 about 21% and in FA8 about 19% of the pores were greater than 20 μm in diameter. Comparing the histograms for the grain size and the pore size, it can be seen that in all materials the maximum grain size is larger than the maximum pore size.

Alumina A consisted of grains up to 15 μm in diameter, within a matrix of fine-grained material with an average grain size of 2.8 μm as shown in Fig. 4.5a. Intergranular porosity was evident, some regions of which were interconnected, but generally it consisted of isolated voids, although these cannot be seen on the micrograph, Fig. 4.5a, due to etching.

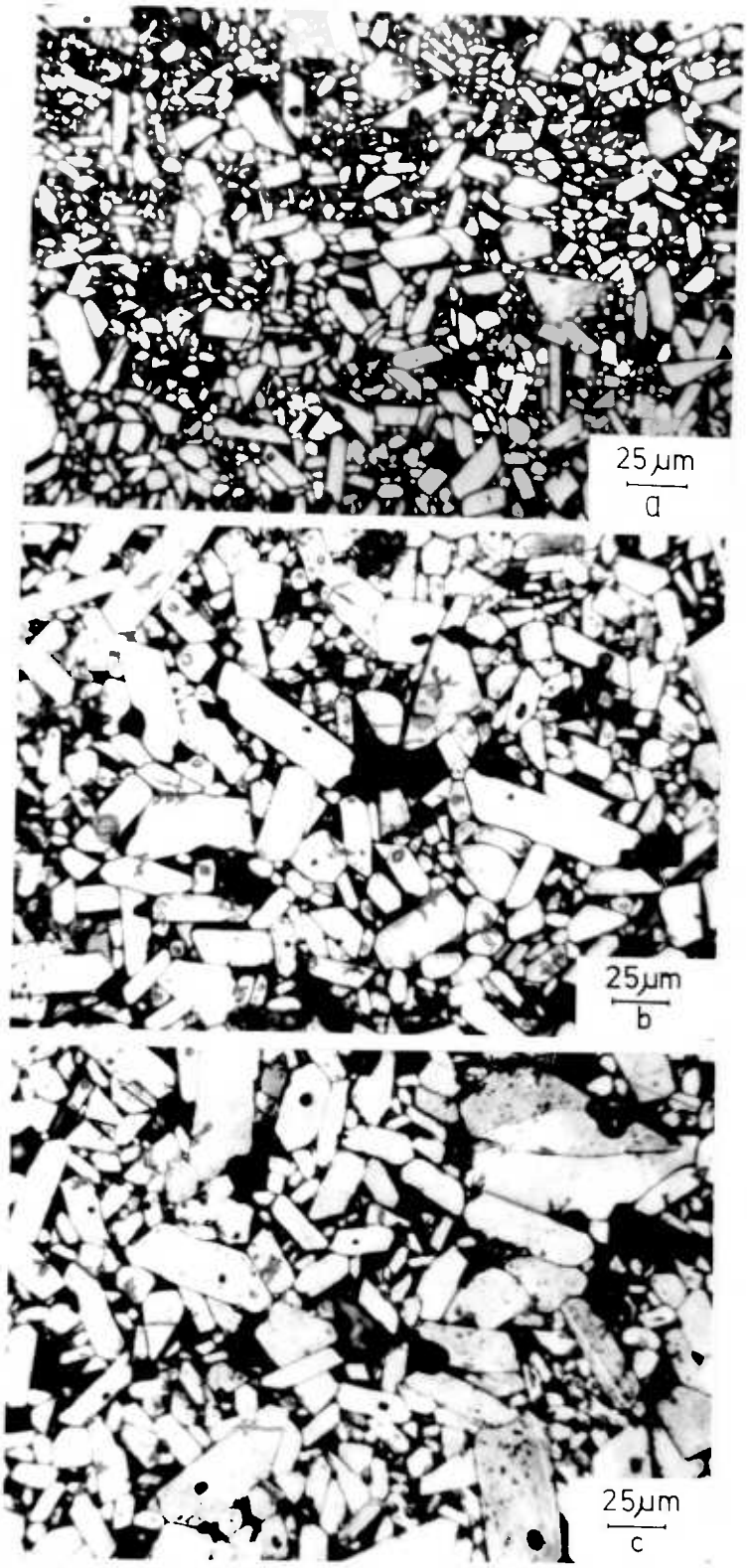


Fig.4.1. Optical micrographs from polished & thermally etched surfaces:
a - Alumina FA0.
b - " FA4.
c - " FA8.

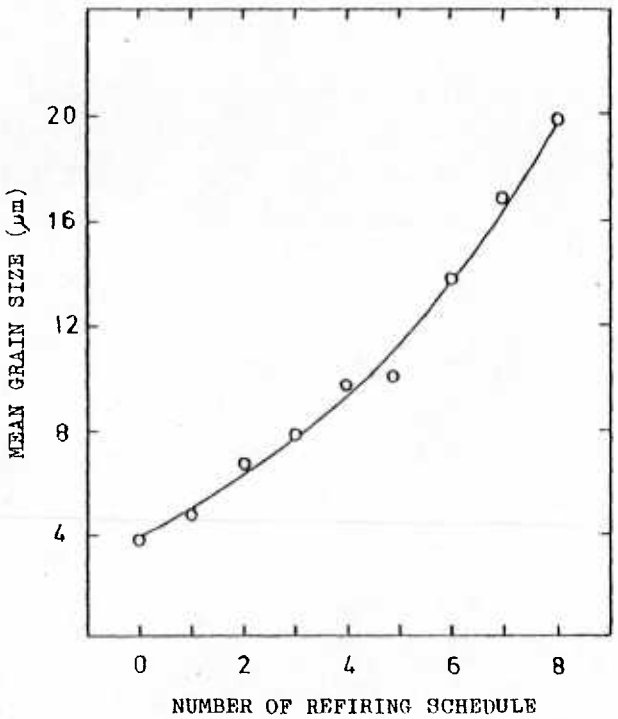


Fig.4.2. Effect of refiring on the grain size, (FA..aluminas).

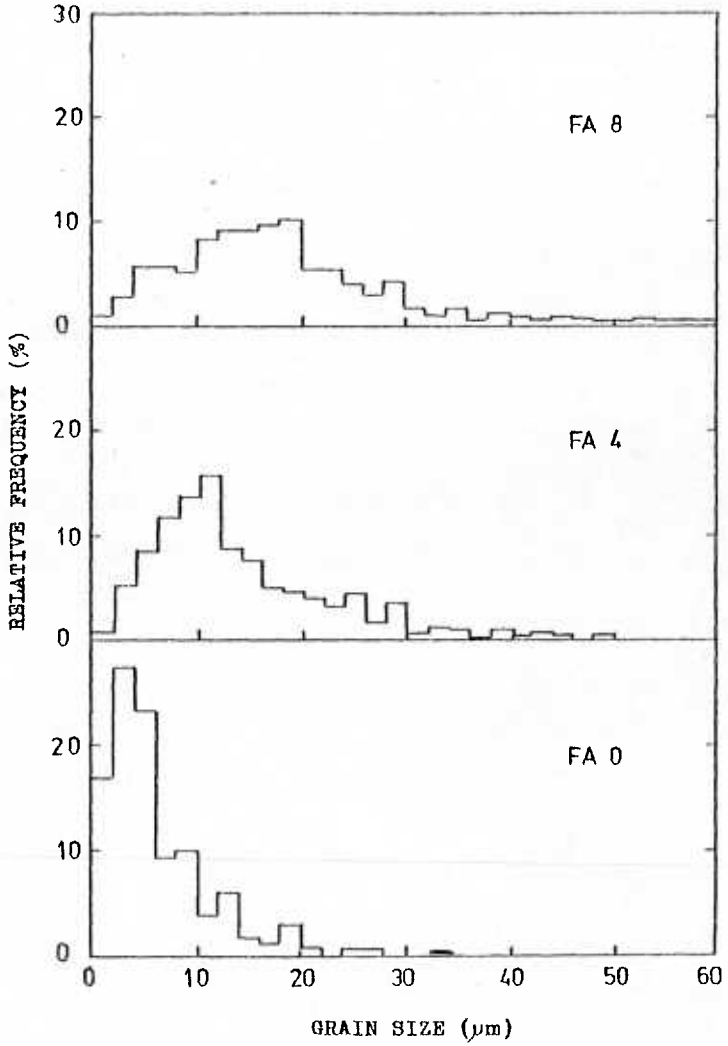


Fig.4.3. The grain size distribution of FA..aluminas.

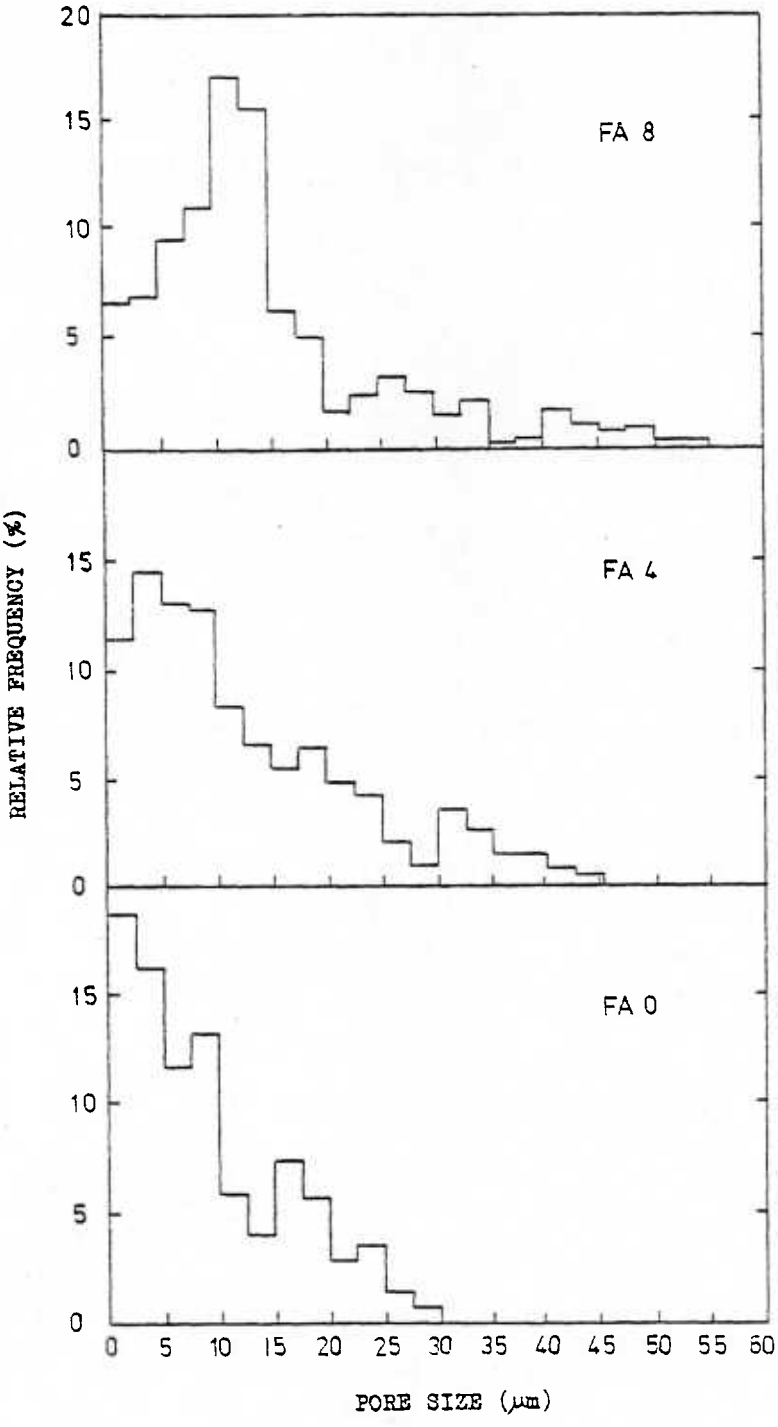


Fig.4.4. The pore size distribution of FA..aluminas.

Alumina B had a mean grain size of 3.8 μm and maximum grain size of 20 μm and was slightly less porous than alumina A. Isolated voids approaching 17 μm in size were present, and a general increase in the size of the intergranular pores was observed, as illustrated in Fig. 4.5b.

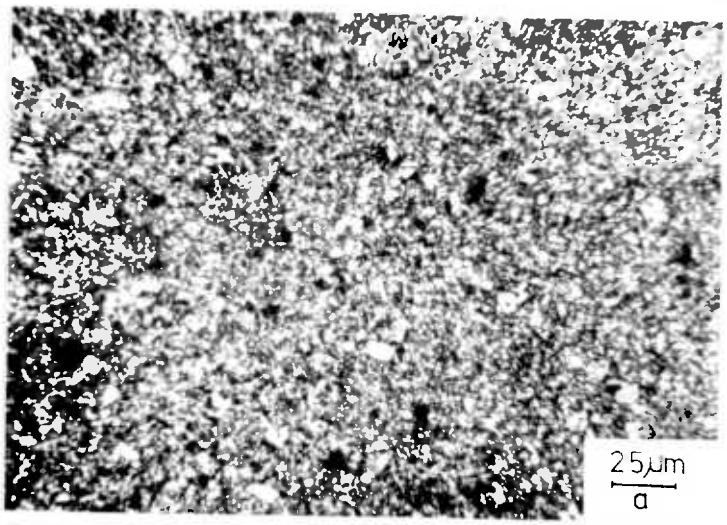
A mean grain size of 12 μm was found for amlnina C, while the maximum grain size was 60 μm and the total porosity increased by about 34% compared with alumina A and about 85% compared with alumina B to 7.12%. The size of the intergranular pores in the finer-grained matrix increased correspondingly with the increase of the grain size. Fig. 4.8a shows the microstructure of alumina C.

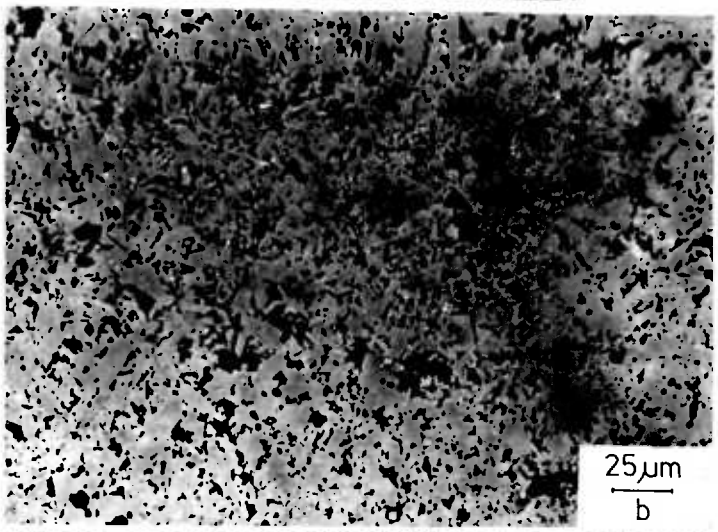
The histograms for the grain size and pore size of aluminas A, B and C are shown in Figs. 4.6 and 4.7, respectively, which illustrate that the microstructure of these aluminas is more even compared with FA aluminas.

Alumina D consisted of fine grains with the mean grain size of 2.3 μm and maximum grain size of 26 μm (Fig. 4.5c), whereas alumina E consisted of very large grains with the mean grain size of 23 μm, and maximum grain size of 98 μm. Fig. 4.8b shows the microstructure of alumina E.

The hot-pressed pure alumina had an average grain size of1.2 μm and was very much less porous than sintered aluminas, as shown in Fig. 4.9a. The grain sizes were fairly uniform, with the largest grain size of 5 μm. Pores were distributed intergranularly with some isolated pores approaching 3 μm in size.

The two-phase $Al_2O_3.ZrO_2$ composites showed a microstructure very similar to that of hot-pressed alumina except for the presence of small-grained ZrO_2 particles which had a mean grain size of 2 μm. The ZrO_2 grains could be easily identified on the optical micrographs by their white appearance, as can be seen in Fig. 4.9b. The microstructure of these composites is shown in more detail in scanning electron micrographs taken from the polished and thermally etched surfaces (see Fig. 4.10). X-ray maps can be





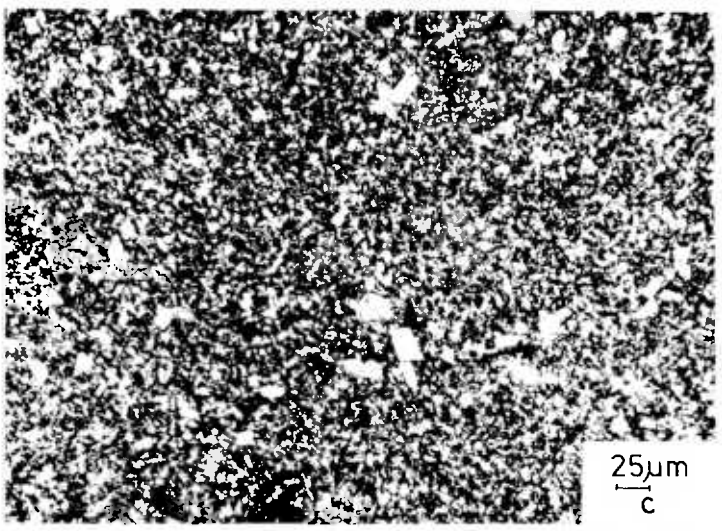


Fig. 4.5. Optical micrographs from polished & etched surfaces:
a - Alumina A (thermally etched),
b - " B (chemically "),
c - " D (thermally ").

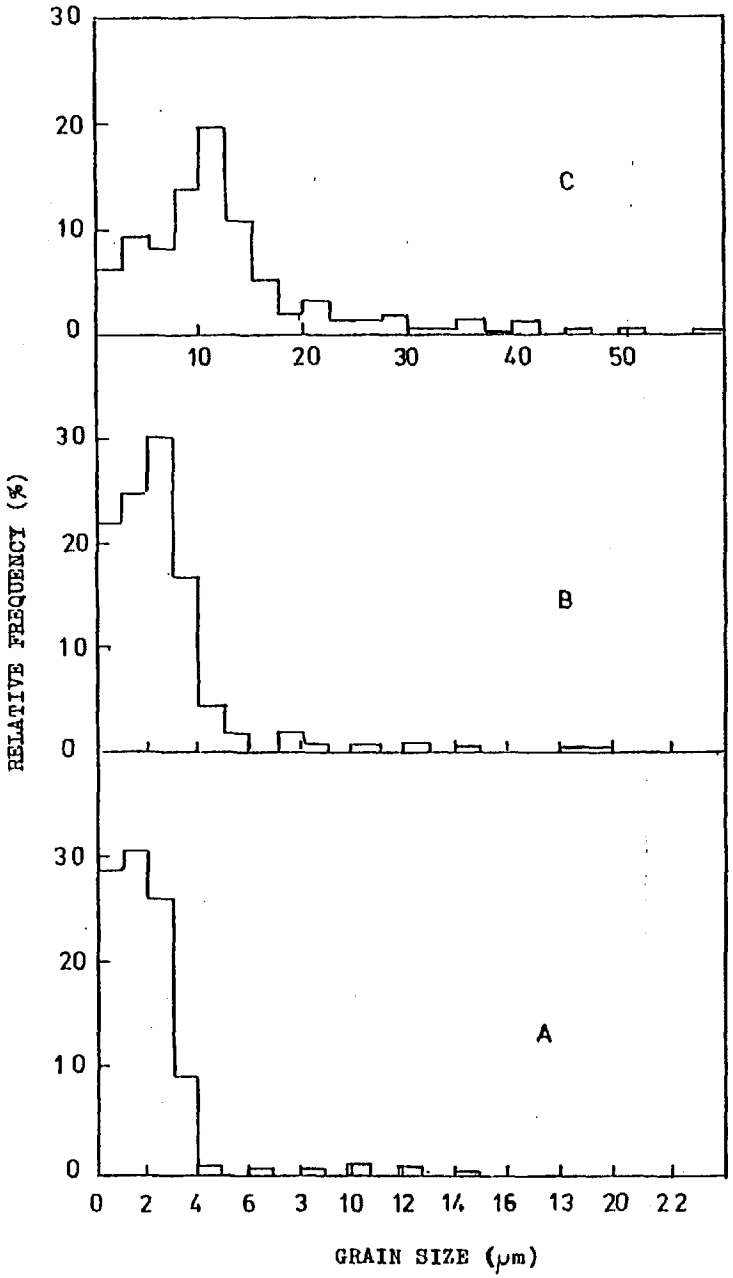


Fig.4.6. The grain size distribution of aluminas A, B, & C.

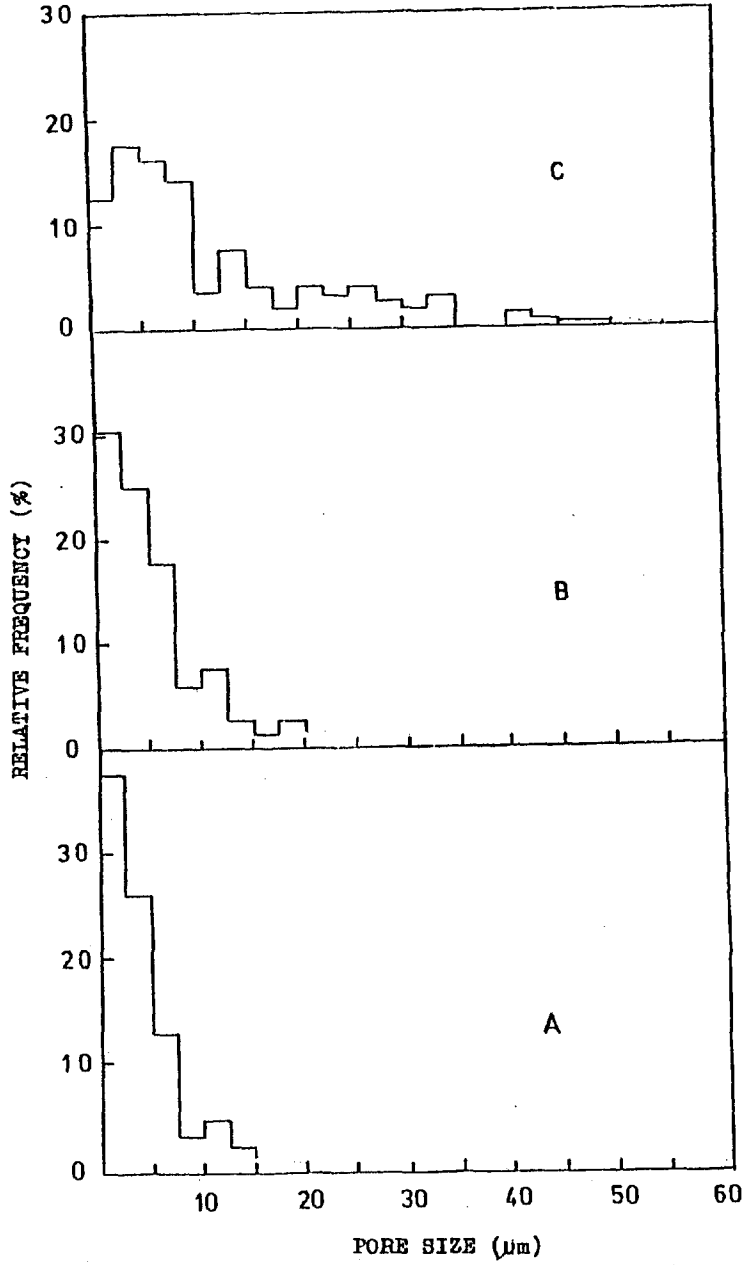


Fig.4.7. The pore size distribution of aluminas A,B& C.

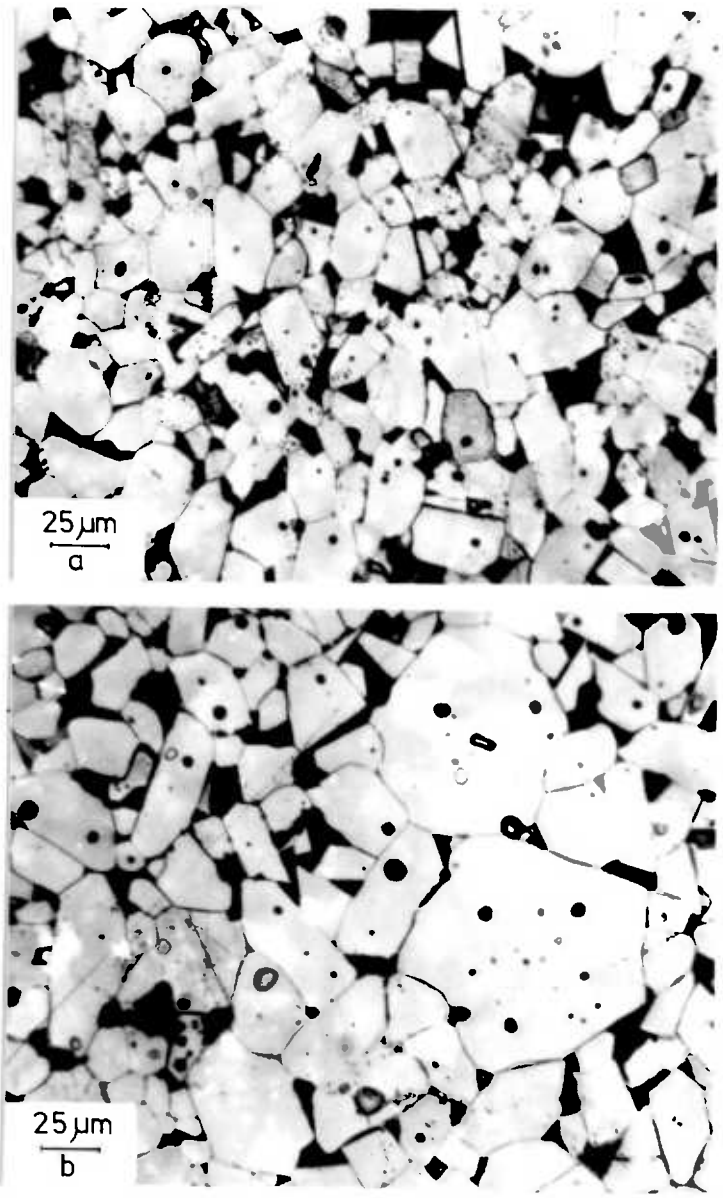


Fig. 4.8. Optical micrographs from polished & thermally etched surfaces:
a - Alumina C.
b - Alumina E.

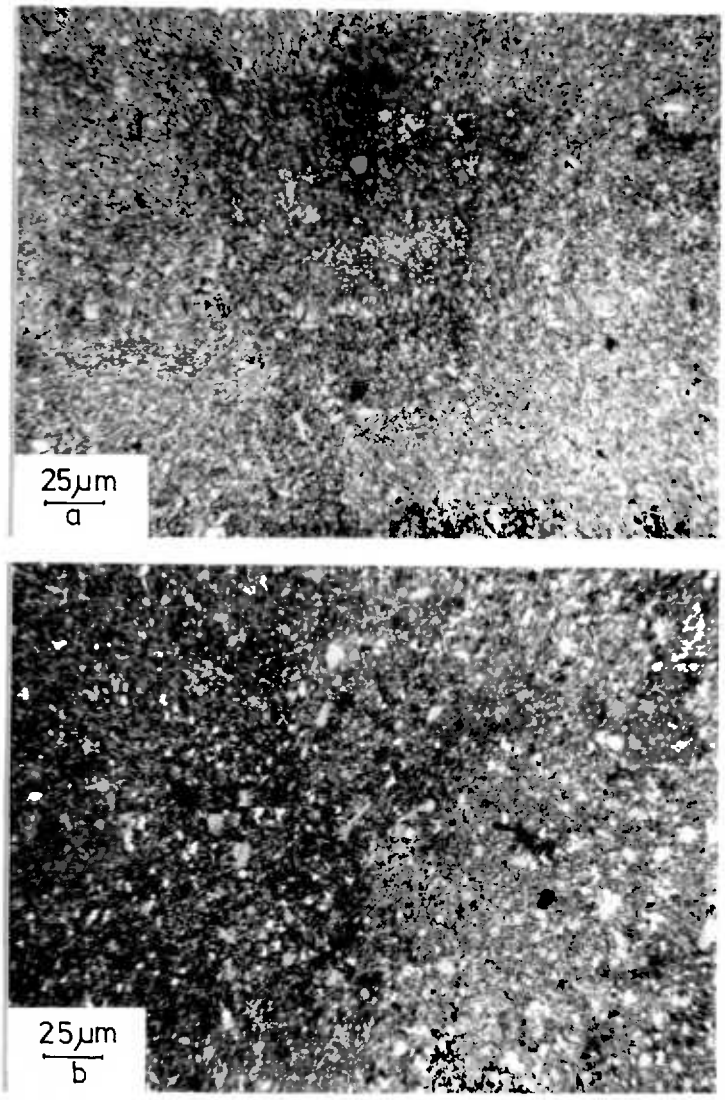


Fig. 4.9. Optical micrographs from polished & thermally etched surfaces
a - Hot pressed alumina H,
b - " " Al_2O_3:ZrO_2 HZ15

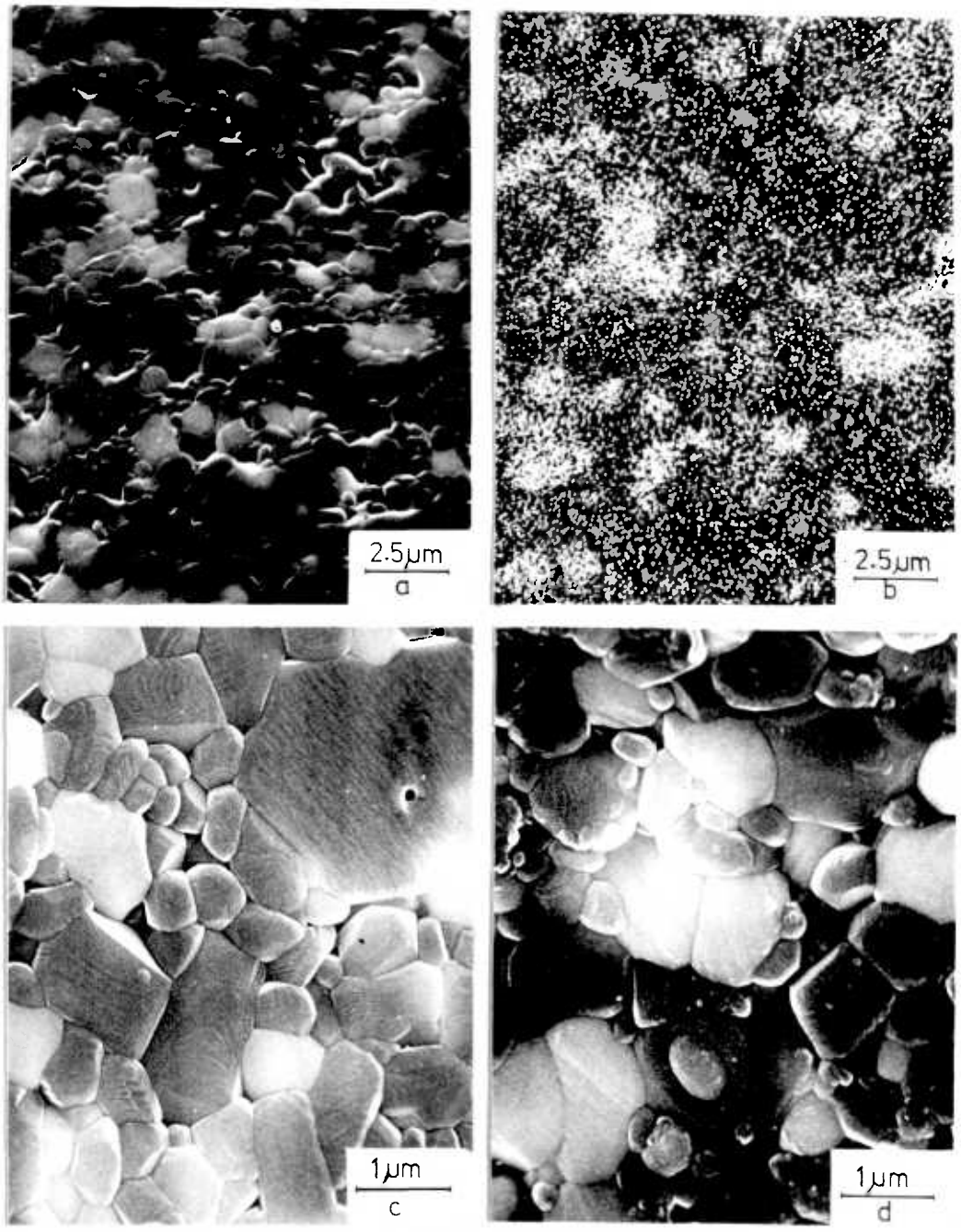


Fig. 4.10 . SEM, showing the polished & etched surfaces of $Al_2O_3ZrO_2$:
a- general view,
b- X ray map of (a), for Zr.
c-d- general microstructure.

produced from any field to identify the regions of ZrO_2, by locating the Temscan probe on a ZrO_2 grain and using the characteristic Zr wavelength for analysis. The regions of ZrO_2 appear in brighter areas, which also correspond to brighter grains on the SEM pictures. The mean grain size of the alumina matrix was 1.2 μm and the maximum grain size was about 8 μm. Intergranular porosity was also observed in the composites with a maximum pore size of 3 μm.

4.2.2 Density and Porosity

The alumina FA0 had a density of 3.75 $g.cm^{-3}$ and 4.99% porosity. The effect of subsequent refiring on the commercial schedule was to increase the total porosity and thus decrease the density as shown in Fig. 4.11. Aluminas A and B had a higher density than FA0, being 3.785 and 3.84 $g.cm^{-3}$, respectively, corresponding to porosities of 4.32% and 3.02%. The density of alumina D, 3.9 $g.cm^{-3}$, was among the highest that could be achieved for 97% pure alumina produced by conventional pressing and sintering techniques. The total porosity of alumina D was 2.00%. The aluminas C and E had an increased porosity of 6.31% and 8.98% and reduced density of 3.72 and 3.63 $g.cm^{-3}$, respectively.

These data show that, in general, aluminas produced by isostatic cold-pressing followed by sintering contained between 2 and 9% porosity by volume. Achieving complete densification is difficult. In sintering cold-pressed aluminas, grain growth occurs during the latter stages as a result many pores become isolated and consequently the rate of densification is sharply reduced. It follows that sintering for longer periods to obtain improved densities becomes impracticable. As is illustrated by the specimens which have been refired, subsequent refiring on the commercial schedule not only enlarged many of the isolated pores at the expense of small ones, but also slightly increased the total porosity.

The hot-pressed alumina contained 1.68% porosity and had a density of 3.92 $g.cm^{-3}$. The improved physical properties of the

hot-pressed alumina compared with the sintered aluminas indicate the greater technical potential of the hot-pressing technique.

The $Al_2O_3.ZrO_2$ composites had increased densities compared with the pure hot-pressed alumina, due to the higher (≈ 1.53 times) specific gravity of ZrO_2 compared with Al_2O_3 (see Table 4.2). However, the total porosity of the composite slightly increased with the increase of ZrO_2 content, as shown in Fig. 4.12. This is partly as a result of increased microcracks with increase in the amount of dispersed ZrO_2 particles. The microcracks were produced as a result of differences in the expansion coefficients of ZrO_2 and alumina.

4.2.3 Young's Modulus

The modulus of elasticity of the aluminiums at room temperature was calculated from the porosity data using the equations given by Kingery[28] (equation (2.13)) and Spriggs[29] (equation (2.14)) for porous materials. The Young's modulus of corundum ($4\times10^{11}Nm^{-2}$)[94] was used as the modulus of zero porosity alumina.

The modulus data determined using equation (2.13) were slightly greater than the experimental elastic moduli reported in the literature[8] for aluminas of similar porosity. In contrast the values obtained using Spriggs' equation were in good agreement with the reported experimental values. Thus the latter were employed in G_{IC} and γ_i determinations.

4.3 EVALUATION OF FRACTURE TOUGHNESS TESTS BY ACOUSTIC EMISSION

4.3.1 Subcritical Crack Growth during Fracture Toughness Tests

The standard procedure for brittle ceramics is to accept a fracture toughness test if there is a linear relationship between load and displacement up to the point of fracture. Even though

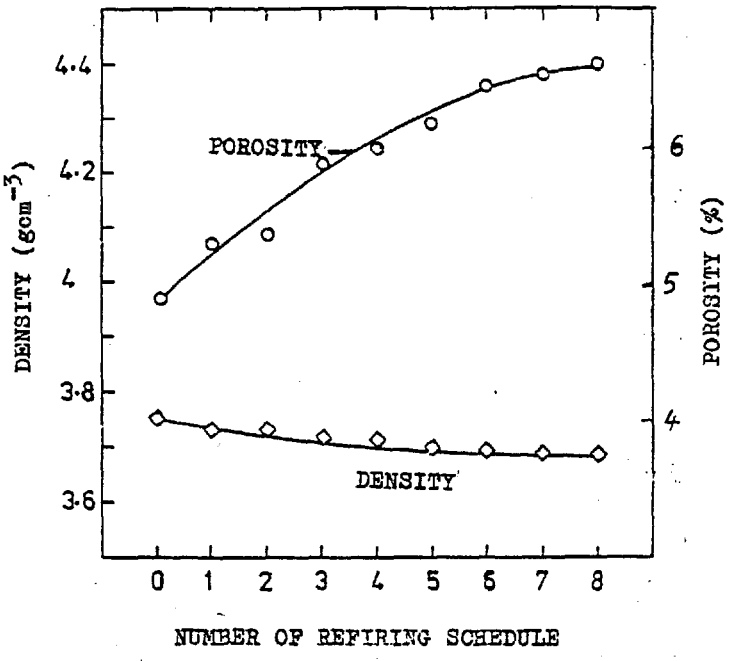


Fig.4.11. Variation of the density and total porosity of alumina FAO subjected to subsequent refiring.

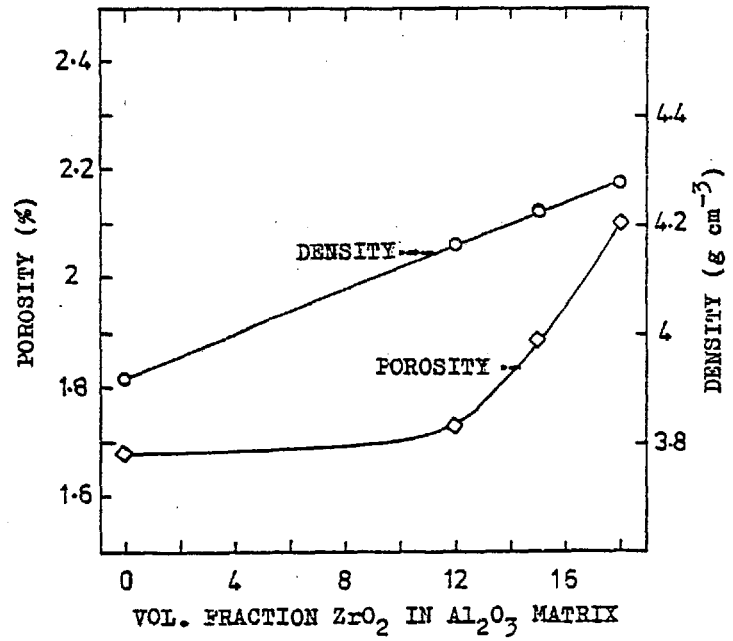


Fig.4.12. Variation of the density and porosity with the amount of ZrO^2 in alumina.

TABLE 4.2 Physical Properties of Aluminas.

Material		Grain Size (μm) Mean	Grain Size (μm) Maximum	Maximum Pore Size (μm)	Density g/cm^3	Porosity %	Young's Modulus x10^{11} Nm^{-2} Kingery Equation	Young's Modulus x10^{11} Nm^{-2} Spriggs Equation
Sintered Al_2O_3	FA0	4	35	30	3.750	4.99	3.63	3.36
Sintered Al_2O_3	FA1	5	38	32	3.736	5.38	3.60	3.31
Sintered Al_2O_3	FA2	7	44	39	3.734	5.45	3.59	3.30
Sintered Al_2O_3	FA3	8	49	44	3.716	5.95	3.56	3.25
Sintered Al_2O_3	FA4	10	50	45	3.712	6.06	3.55	3.23
Sintered Al_2O_3	FA5	10	54	38	3.705	6.26	3.54	3.21
Sintered Al_2O_3	FA6	14	60	52	3.696	6.52	3.52	3.18
Sintered Al_2O_3	FA7	17	72	50	3.693	6.60	3.51	3.17
Sintered Al_2O_3	FA8	20	75	58	3.690	6.69	3.50	3.16
Sintered Al_2O_3	A	2.8	15	14	3.785	4.32	3.68	3.43
Sintered Al_2O_3	B	3.8	20	17	3.840	3.02	3.88	3.59
Sintered Al_2O_3	C	12	60	50	3.721	6.31	3.53	3.20
Sintered Al_2O_3	D	2.3	15	12	3.900	2		
Sintered Al_2O_3	E	23	98	55	3.630	8.98		
Hot-pressed Al_2O_3	H	2	15	13	3.920	1.68	3.87	3.77
Hot-pressed $Al_2O_3.ZrO_2$	HZ_{12}	1.2 & 2	6	3	4.168	1.73		
Hot-pressed $Al_2O_3.ZrO_2$	HZ_{15}	1.2 & 2	5	3	4.224	1.89		
Hot-pressed $Al_2O_3.ZrO_2$	HZ_{18}	1.2 & 2	6	3	4.280	2.10		

there was a linear load-displacement up to P_F for the SENB, DT and DCB specimens tested at a cross-head speed of 0.01 cm/min., acoustic emission commenced at a load P_s, which was less than the fracture load P_F, as can be seen in Fig. 4.13.

The emissions started at particularly low loads in DCB and DT tests. Furthermore, the data for all geometries showed that emissions commenced earlier in the coarse-grained aluminas. Microscopical examination has clearly demonstrated that those emissions which occur prior to catastrophic failure are associated with subcritical crack growth, as illustrated in Fig. 4.15. Other mechanisms, such as twinning, have been reported[89,90] in room temperature compression and bending tests on alumina, but scanning electron microscopy of the subcritical cracks (Fig. 4.16) and catastrophic fracture surfaces (Fig. 4.28) revealed no evidence of this mode of deformation.

Both the ring-down and event counting rates increased with load up to fracture. At or within 0.5% of P_F, there was a rapid increase in count rate which was associated with the final fracture process. The number of ring-down and event counts during the final fracture stage were surprisingly low, being approximately 50% and 20% of the total ring-down counts and events, respectively.

It may be that the response time of the equipment was such that not all the counts associated with catastrophic failure were recorded especially in the event counting module (DE 920). Average values for the number of ring-down, N_{RT}, and event, N_{ET}, counts due to subcritical crack growth were obtained by measuring emission counts occurring up to 99% of the fracture load, P_F. These are given in Table 4.3. The DCB test-piece produced the largest values of N_{RT} and N_{ET}. This was consistent with the microscopical examination which revealed that subcritical crack growth was more extensive in DCB specimens than in the DT and SENB test-pieces.

The subcritical crack length was carefully measured in SENB, DT and DCB specimens subjected to progressive slow crack

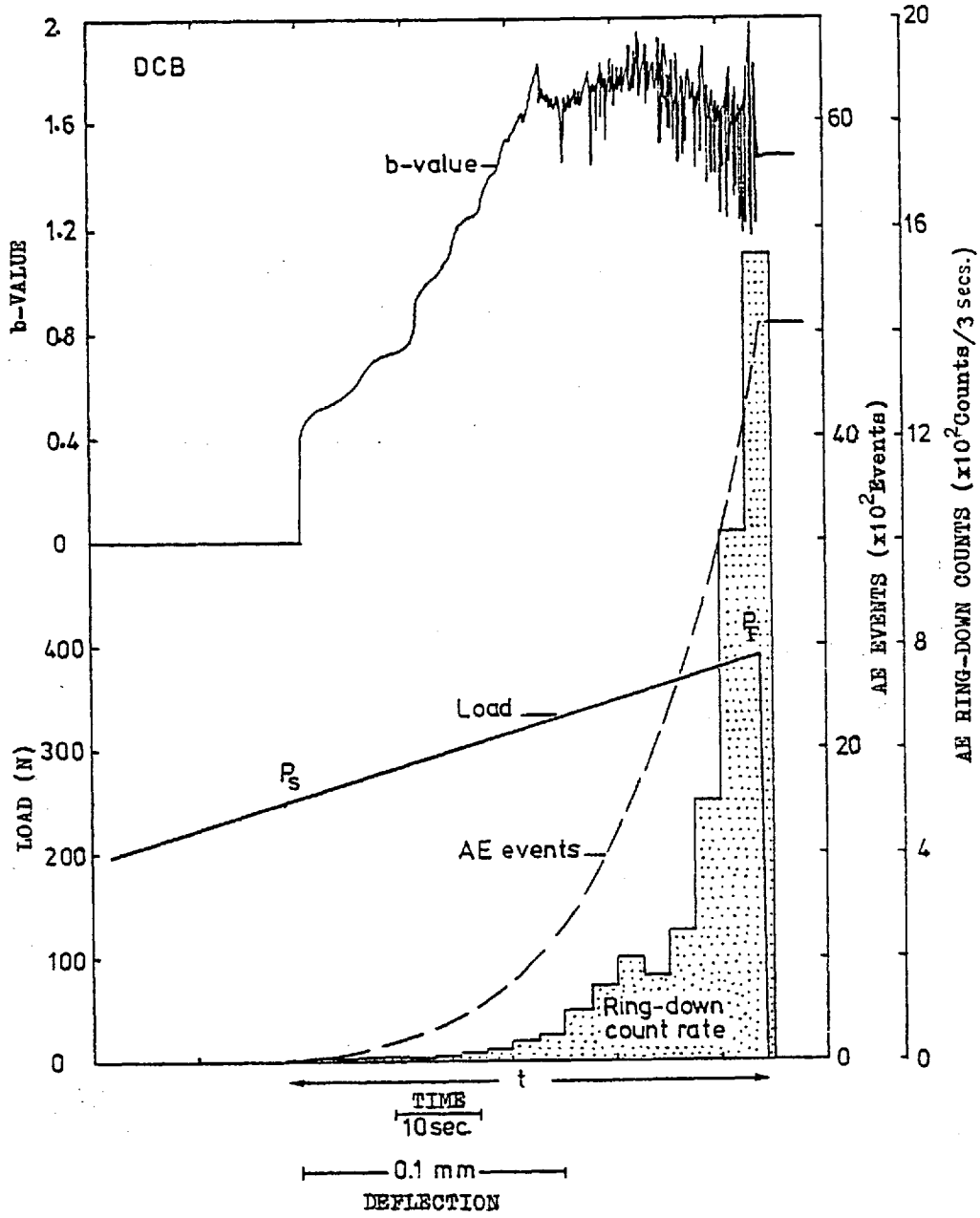


Fig.4.13. Load-deflection and AE-deflection curves showing the acoustic response of alumina during fracture toughness test.

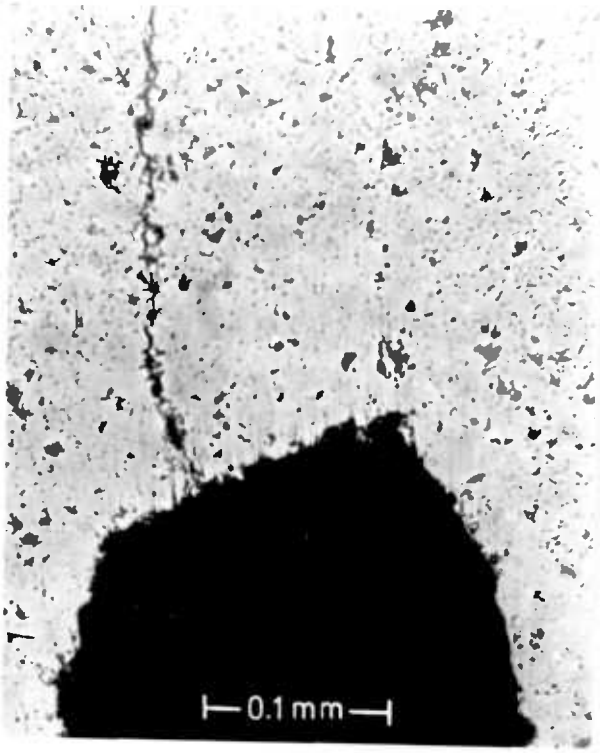


Fig. 4.15. Optical micrograph showing subcritical crack in a SENB specimen.

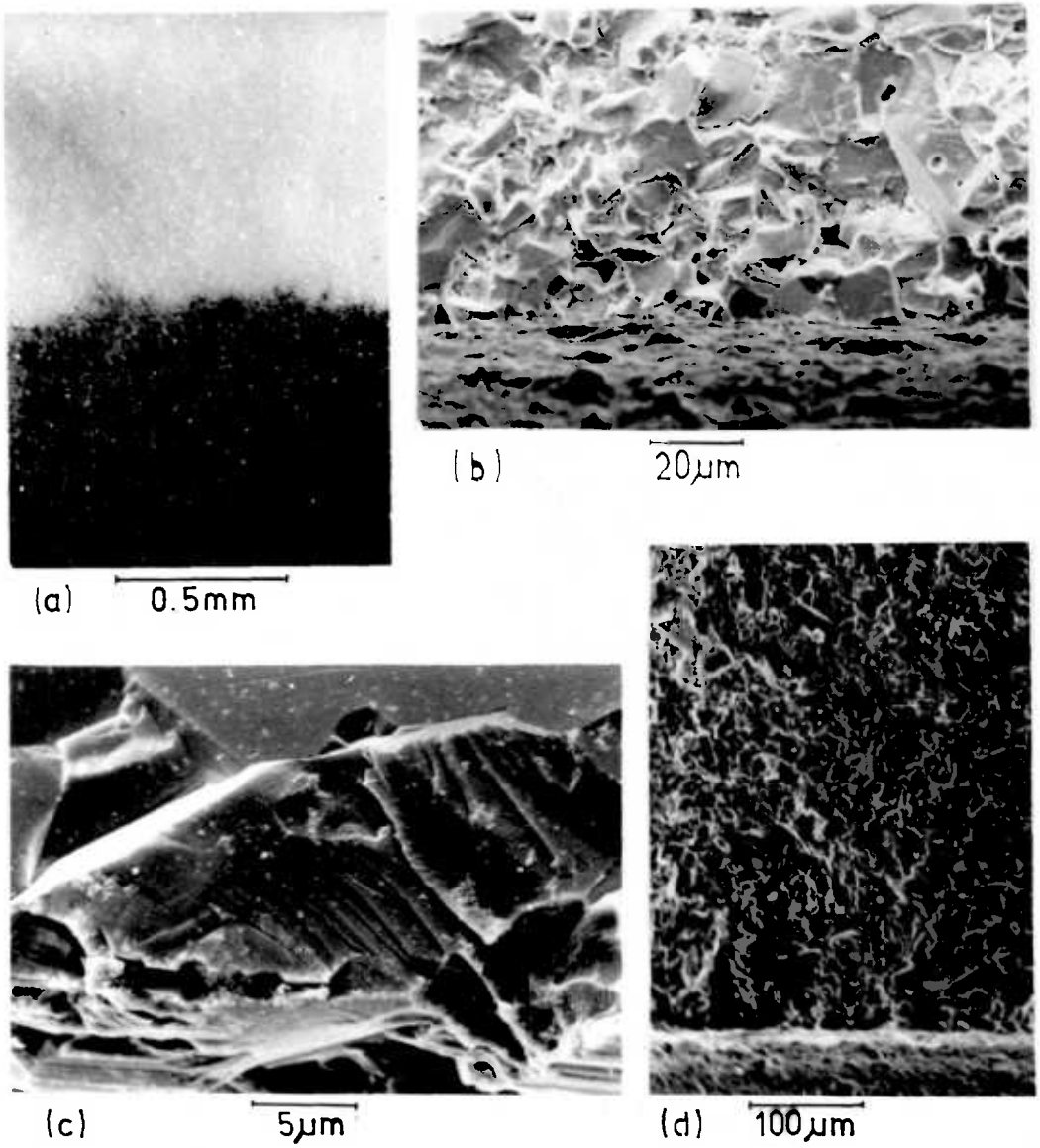


Fig. 4.16. Showing the tracture faces of subcritical crack.

a- Optical micrograph, crack face is indicated by dye penetrant.

b- SEM near notch root, microcracks.

c- " " " " cleavage.

d- " " " " general view.

growth, and the subcritical crack area (i.e. crack length x specimen thickness) was plotted versus the corresponding AE data. The results are illustrated in Figs. 4.17-4.22, which show that the number of ring-down and event counts are both a linear function of subcritical crack length or area.

These figures also demonstrate that the number of emissions from a given area of subcritical crack is different for FA aluminas compared with A, B, C. However, the emissions from 1 mm^2 of subcritical crack area are very similar for FA0, FA4 and FA8 aluminas, and for A, B and C aluminas. This indicates that for a group of aluminas of similar composition and manufacturing procedure, the acoustic emission generated is predominantly determined by the extent of subcritical crack area produced. The microstructural variables play their role in producing the extent of the subcritical crack.

Replotting Figs. 4.17-4.22 in Figs. 4.23 and 4.24 and comparing the slope of the curves, it can be seen that the N_{ET} and N_{RT} values per unit area of subcritical crack are in the order of DCB < DT < SENB. The attenuation of emission amplitudes during propagation from the emission source to the transducer is partly responsible for the reduced N_{RT}/mm^2 and N_{ET}/mm^2 values in DCB tests compared with DT and SENB tests. Fig. 4.25 compares attenuation of a known characteristic electronic signal produced by a pulse generator and passed into SENB, DT and DCB specimens by a transducer coupled to the specimen in front of the initial notch. The results clearly indicate that the shorter travelling distance for emissions in the SENB geometry compared with the DT and DCB geometries is a possible reason for the high N_{RT}/mm^2 and N_{ET}/mm^2 values in the former case. The reduced thickness of DT specimens compared with DCB specimens also contributes to increased N_{RT}/mm^2 and N_{ET}/mm^2 values in the former geometry.

Fig. 4.26 compares the amplitude distribution of the AE events obtained during subcritical crack growth and final fracture for the three geometries. The distributions generally indicate that the emissions due to subcritical crack growth are mostly of low

amplitude events and those produced at final fracture are the high amplitude emissions. The proportion of low amplitude events decreased in the order DCB > DT > SENB.

The overall results of amplitude distributions are reflected in the exponent b as shown in Table 4.3. The values of final b varied in the order DCB > DT > SENB.

The results of acoustic emission pulse width distributions (Fig. 4.27) indicated that the emissions produced during subcritical crack growth were those of narrow pulse width, compared with those obtained at final fracture. The proportion of narrow pulse width emissions obtained varied according to DCB > DT > SENB, i.e. in the same sequence as the proportion of low energy emissions.

Evans, Linzer and Russell[10] showed that acoustic emission in alumina at room temperature occurred from increments in the primary crack and from subsidiary microcracking in the process zone around the crack tip. The scanning electron microscopical examination of the notch root of specimens revealed microcracks originating from the root of the notch, as shown in Fig. 4.31. Further evidence (Fig. 4.15) suggested that microcracks extended in a stable manner to a relatively large subcritical crack before final failure, especially in the DCB and DT specimens. Subcritical crack growth was detected using the acoustic emission technique and was also identified at final failure by its comparatively low rate, low amplitude and narrow pulse width emissions. Although most emissions were of low amplitude and narrow pulse width, the wide range of values obtained for emission amplitude and pulse width during a test indicated that the subcritical crack moved intermittently, with the amplitude of each burst depending on the area swept out by the crack in each increment.

It follows from the preceding discussion that as a result of subcritical crack growth, the true crack length at failure, a_F, is greater than the initial crack length a_o. It is a_F that should be inserted into the equations to evaluate fracture toughness parameters. The extent of subcritical crack growth, and hence a_F, may be obtained by acoustic emission monitoring via curves such as

those given in Figs. 4.17-4.24. This approach also gives some indication as to which test geometry gives the most reliable and reproducible fracture toughness data in comparing the effect of several microstructures on mechanical properties.

4.3.2 The Influence of the Test Geometry

The values of critical stress intensity factor, K_{IC}, were determined for the SENB, DT and DCB specimens from the fracture load P_F and are presented in Table 4.3. The data for a given material varied with the test geometry in the order DCB > DT > SENB. Furthermore, the SENB and DCB data indicate that the fracture toughness of the fine-grained aluminas is greater than that of the coarse-grained material, while no significant variation of fracture toughness with grain size was observed in the DT geometry. The values for the FA aluminas were consistently higher than those obtained for materials A, B and C, although the latter were less porous and of higher purity.

The acoustic emission ring-down and event counts due to subcritical crack growth varied with the test geometry as well as with the material. For a given geometry increased emission was often obtained from the coarse-grained aluminas compared with the fine-grained materials. This was due to more extensive subcritical crack growth in coarse-grained aluminas, as revealed by microscopical examination.

Adding the subcritical crack length, a_s, to the initial crack length a_o (using the AE data given in column 5 of Table 4.3 and Figs. 4.17-4.24), the corrected K_{IC} values were determined (column 9, Table 4.3). It should be noted that the DT values remained unchanged as the fracture toughness in this test geometry is crack length independent, whereas the values for SENB and DCB have increased.

There is a good agreement between the corrected SENB values and the DT values. However, the DCB fracture toughness

values, even after correction for subcritical crack growth, are much larger than those obtained from the other test pieces. This would support the suggestion that, due to the geometry of the DCB test pieces, energy is absorbed in opening a network of cracks inclined to the main cracks[3].

Scanning electron micrographs taken from the fracture surfaces of SENB, DT and DCB alumina specimens (Fig. 4.28) showed very similar features in all geometries, i.e. fracture was predominantly intercrystalline. Evidence of crack branching was observed in all geometries, as shown in Fig. 4.28d-f, but this was more evident in the DCB specimens.

The SENB results show that there is negligible difference between the corrected K_{IC} for fine and coarse grained aluminas. The same conclusion may also be drawn from the DCB results, although for the reasons already mentioned, the values are greater in this case. With the limited amount of information available, it would appear that much of the grain size dependence of the fracture toughness reported in the literature may be due to differences in the extent of subcritical crack growth; acoustic emission and light microscopy have shown that the larger the grain size the more extensive is subcritical crack growth. The fact that no grain size dependence of the fracture toughness was observed for DT tests in the present work and in some other reports[3] supports this argument.

Acoustic emission monitoring, together with microscopy, can provide a calibration curve of the type shown in Figs. 4.17-4.24 to correct for subcritical crack growth. However, the determination of such curves is expensive in terms of specimens and time and a less tedious method would be desirable. A simple correction procedure which requires only the monitoring of the load P_s at which acoustic emissions start has been successfully used for alumina. Fig. 4.29 shows that to a good approximation for both fine and coarse grained material, tested using the DCB, DT and SENB geometries:

$$\frac{a_o}{a_F} = \tfrac{1}{2}\left(1 + \frac{P_s}{P_F}\right) \qquad (4.1)$$

This equation was obtained for the linear load-deflection conditions with a cross-head speed of 0.01 cm/min.

Thus, at least for this type of alumina and the above-mentioned conditions, a_F can be determined without interrupting the test or carrying out any microscopical examination.

From the above discussion it appears that due to sub-critical crack growth prior to catastrophic failure, certain geometries should be treated cautiously before they are accepted as reliable tests for fracture toughness determination. These results suggest that DCB geometry is the least reliable of the geometries, which is in contrast to the conclusions of Simpson et al[37].

The double torsion geometry is found to be the most reliable for both fracture toughness and AE measurements, since it is a crack length independent test with high acoustic response. However, due to the limited amount of material available, the SENB geometry was employed to investigate the effect of environment and microstructure on fracture toughness and acoustic response. Apart from the problem of reduced control over subcritical crack growth in SENB specimens and the slightly underestimated fracture toughness data that results, the geometry has the advantage of being simple and small so that it could be easily and economically prepared in large numbers and conveniently tested in a comparatively short time. Thus the rest of the experiments at room temperature were performed using SENB specimens.

In order to assess the general applicability of the acoustic emission technique described in Sections 4.3.1 and 4.3.2 for the investigation of the validity of fracture toughness tests the same procedures were employed during the fracture toughness testing of porcelain in two microstructural conditions. The details of the results are described in the Appendix. In both porcelains the critical stress intensity factor varied with geometry in the order DCB $>$ DT $>$ SENB, i.e. in the same sequence as for aluminas, and when correction for subcritical crack growth was applied the SENB results increased to nearly the same level as DT values, whilst the DCB discrepancy increased.

TABLE 4.3

Test geometry	Alumina	P_s/P_F	N_{IRT} due to subcritical crack x 10^2	N_{ET} due to subcritical crack x 10^2	Ave. final b value	As-measured K_{IC} $MNm^{-3/2}$	As-calculated $G_{IC} = 2\gamma_i$ $J\,m^{-2}$	Corrected K_{IC} $MNm^{-3/2}$	Corrected G_{IC} $J\,m^{-2}$
SENB	A	0.94	27 ± 8	33 ± 15	0.94	3.82 ± 0.31	40.4	4.00	44
	B	0.93	46 ± 9	110 ± 35	1.02	3.95 ± 0.29	41.2	4.20	46.7
	C	0.8	125 ± 30	215 ± 73	1.18	3.51 ± 0.18	36.6	4.03	48.2
	FA0	0.96	140 ± 84	100 ± 32	1.02	4.85 ± 0.20	66.5	5.05	72.1
	FA4	0.84	820 ± 250	790 ± 110	1.12	4.52 ± 0.15	60.0	5.12	77.1
	FA8	0.85	500 ± 150	490 ± 105	1.00	4.28 ± 0.12	55.1	5.03	76.0
DT	A	0.75	150 ± 40	260 ± 60	1.20	4.17 ± 0.3	48.2	4.17	48.2
	B								
	C								
	FA0	0.73	2400 ± 1300	1615 ± 540	1.50	4.69 ± 0.2	62.2	4.69	62.2
	FA4	0.71	3850 ± 1800	1835 ± 620	1.55	4.85 ± 0.18	69.2	4.85	69.2
	FA8	0.69	2700 ± 1050	1580 ± 490	1.45	4.68 ± 0.15	65.8	4.68	65.8
DCB	A	0.74	130 ± 30	240 ± 40	1.20	4.40 ± 0.8	53.6	4.51	56.3
	B	0.7	190 ± 30	340 ± 45	1.25	4.70 ± 0.26	58.5	4.90	63.5
	C	0.62	410 ± 98	750 ± 180	1.30	4.08 ± 0.51	49.4	4.41	57.7
	FA0	0.66	4700 ± 2800	2125 ± 840	1.60	5.50 ± 0.4	85.5	5.97	100.7
	FA4	0.64	10200 ± 3000	5050 ± 1080	1.70	5.08 ± 0.98	75.9	6.10	100.8
	FA8	0.59	6150 ± 2400	3840 ± 950	1.65	4.73 ± 0.22	67.3	5.71	98.0

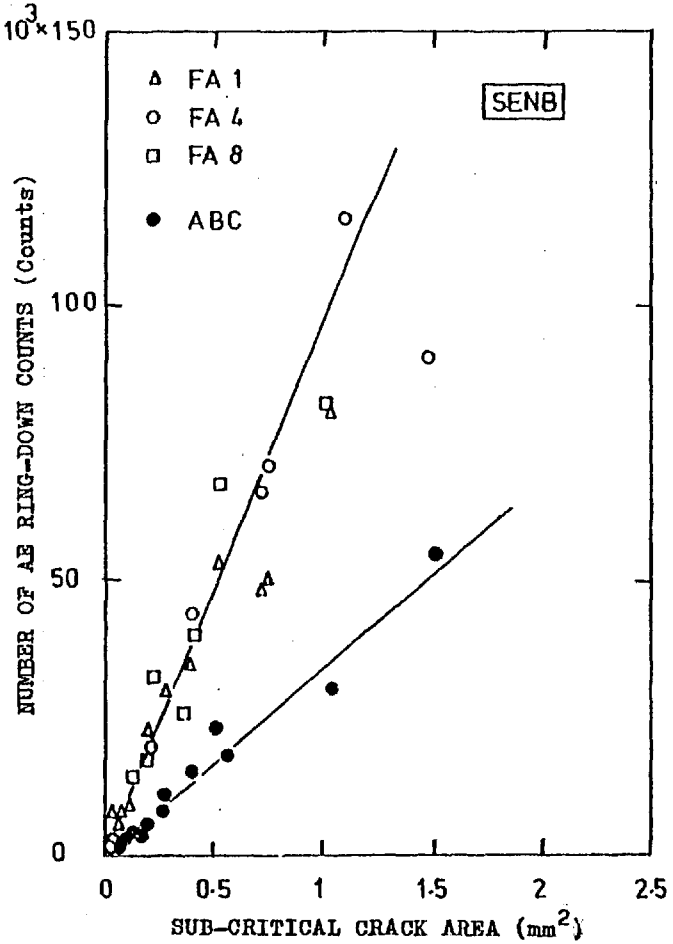
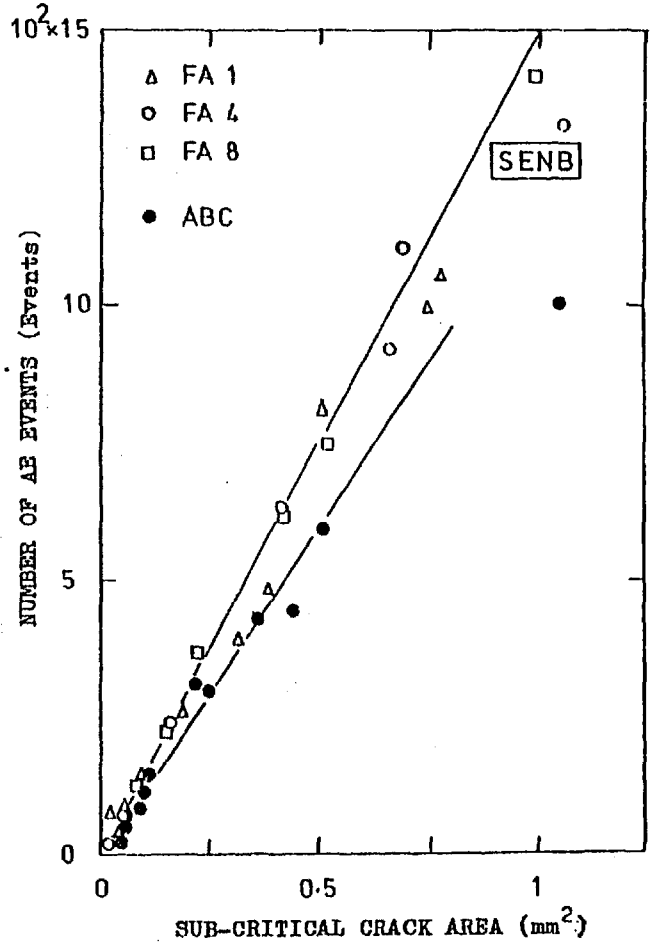


Fig.4.17. Subcritical crack area vs the AE ring-down counts for SENB specimens.



Fig,4.18. Subcritical crack area vs the AE events for SENB specimens of alumina.

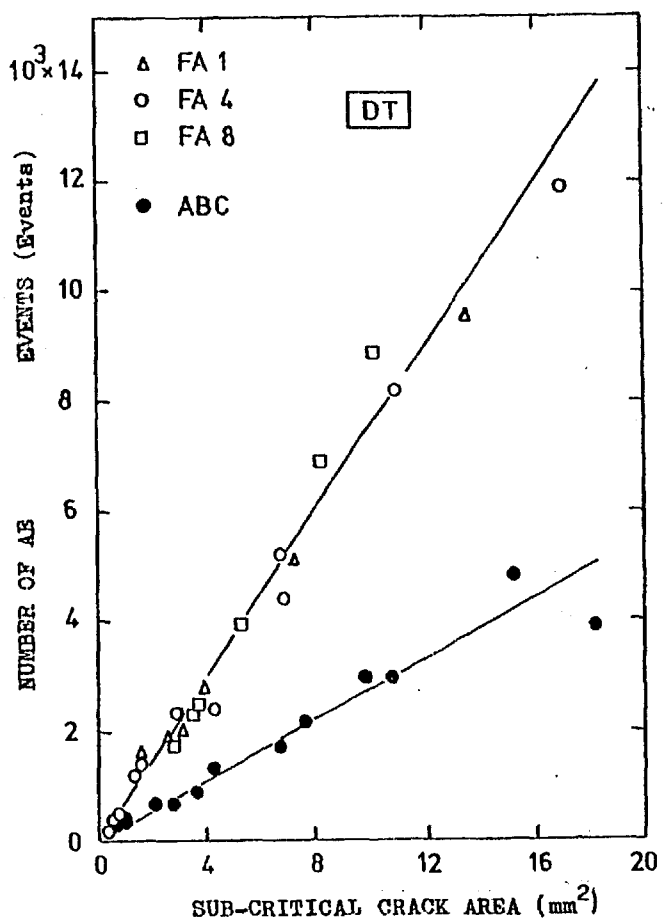


Fig.4.19. Subcritical crack area vs the AE events for DT specimens.

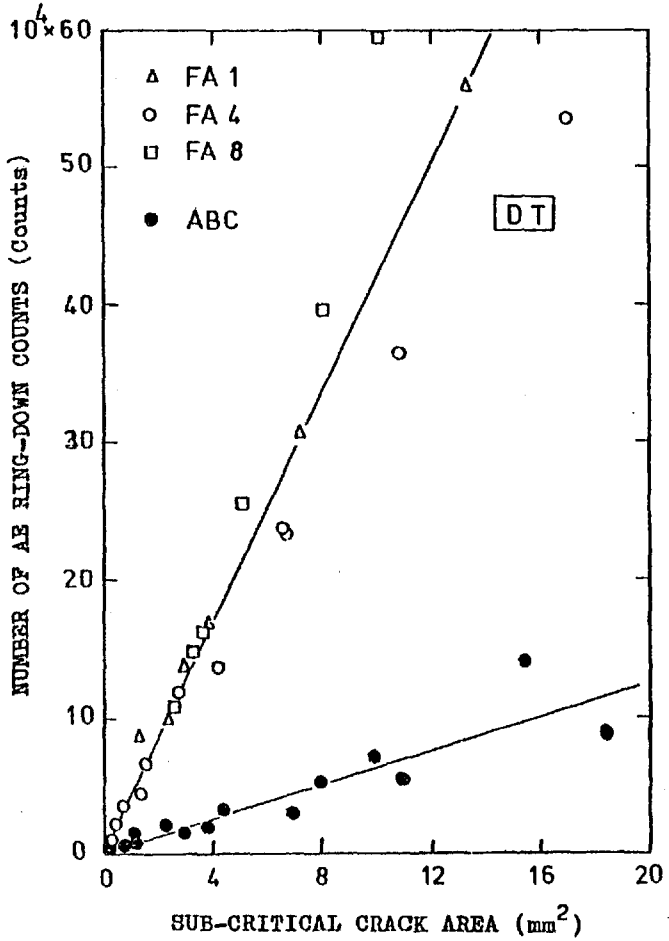


Fig.4.20. Subcritical crack area vs the AE counts for DT specimens.

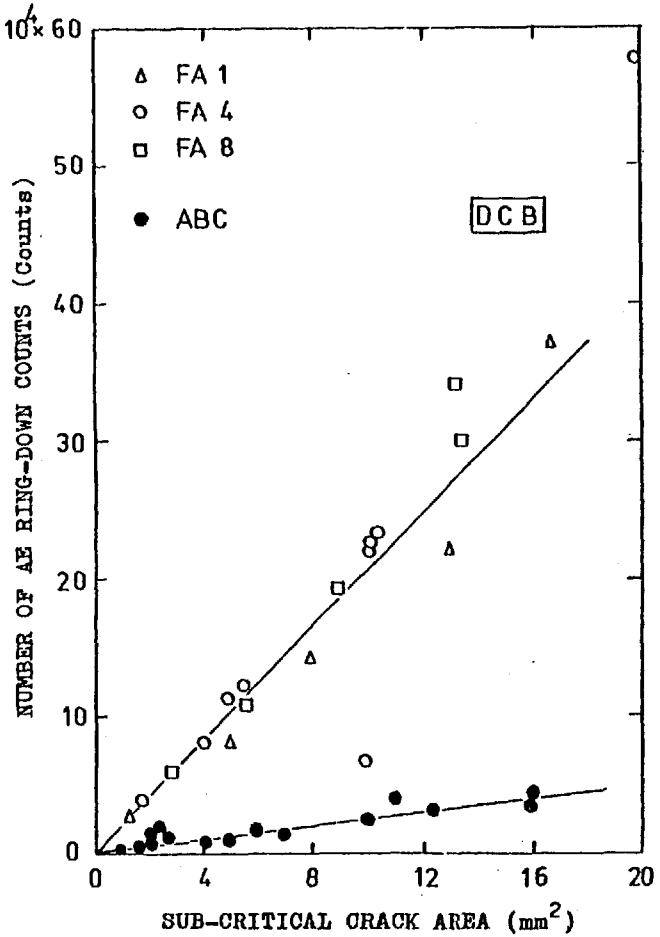


Fig.4.21. Subcritical crack area vs the AE ring-down counts for DCB specimens

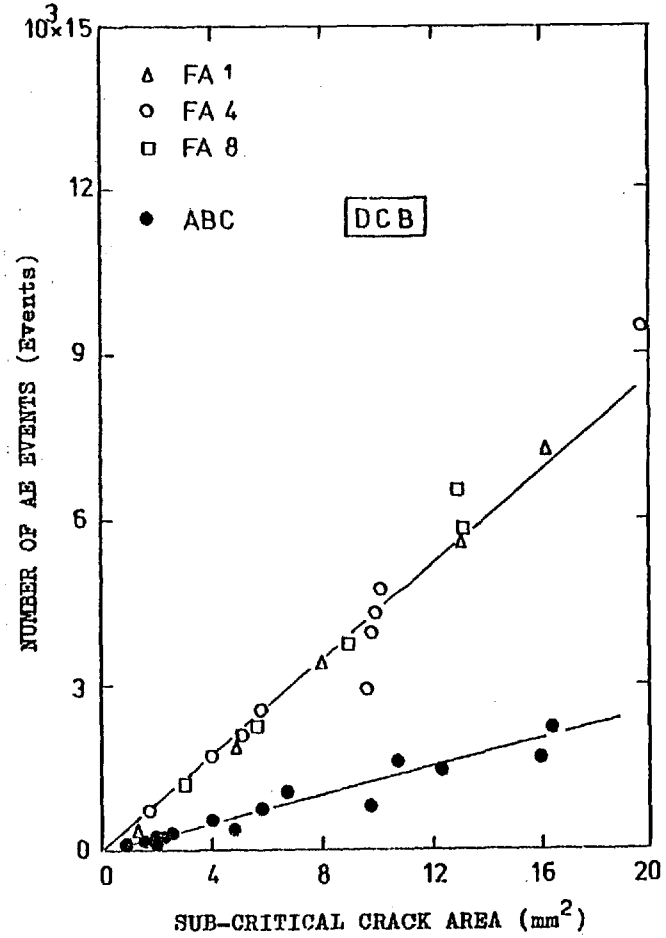


Fig.4.22. Subcritical crack area vs the AE events for DCB specimens.

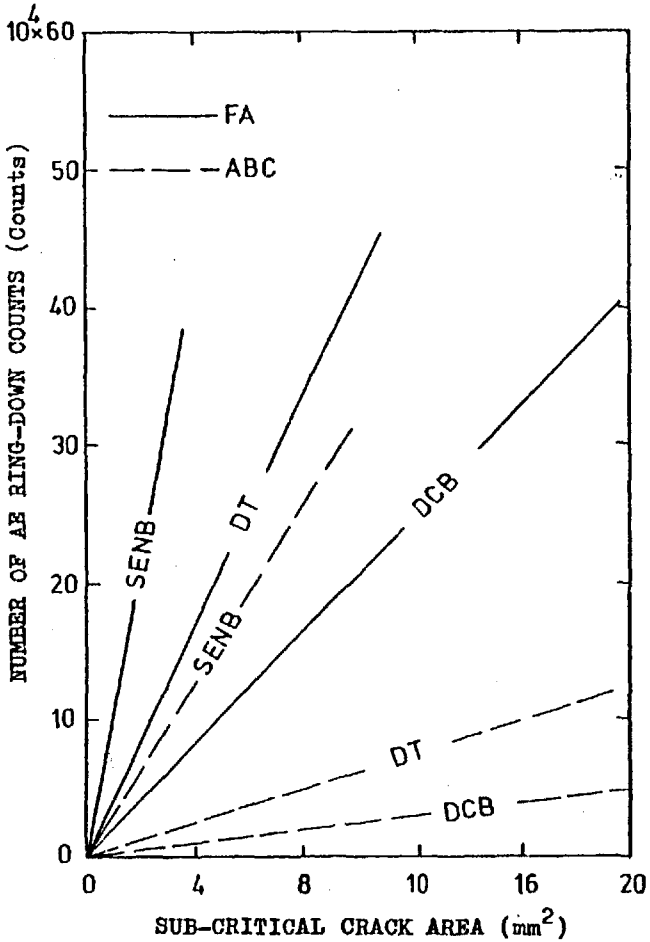


Fig.4.23. Subcritical crack area vs the AE ring-down counts for SENB,DT & DCB specimens.

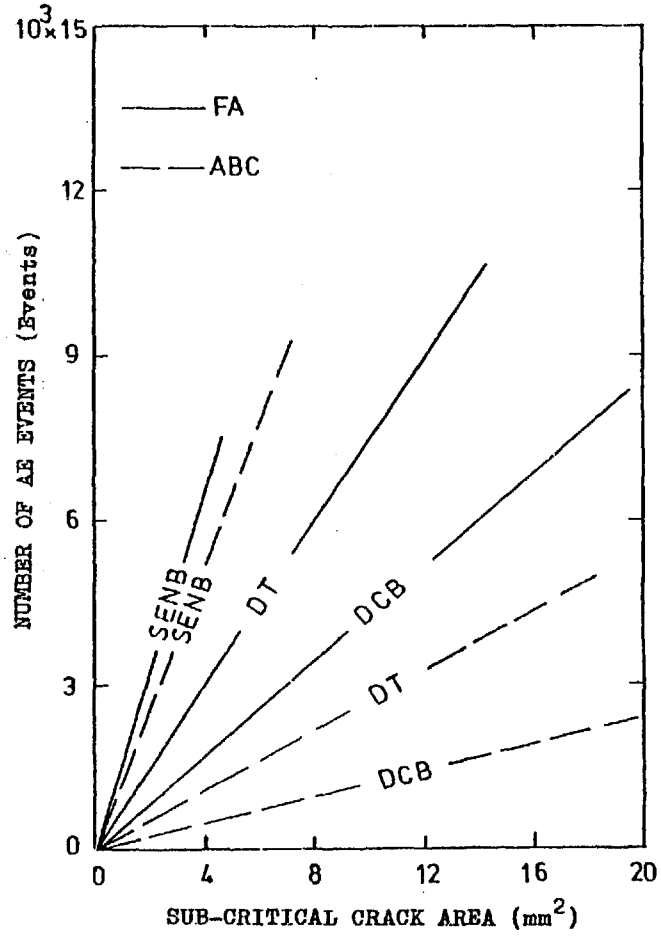


Fig.4.24. Subcritical crack area vs the AE events for SENB,DT,& DCB specimens.

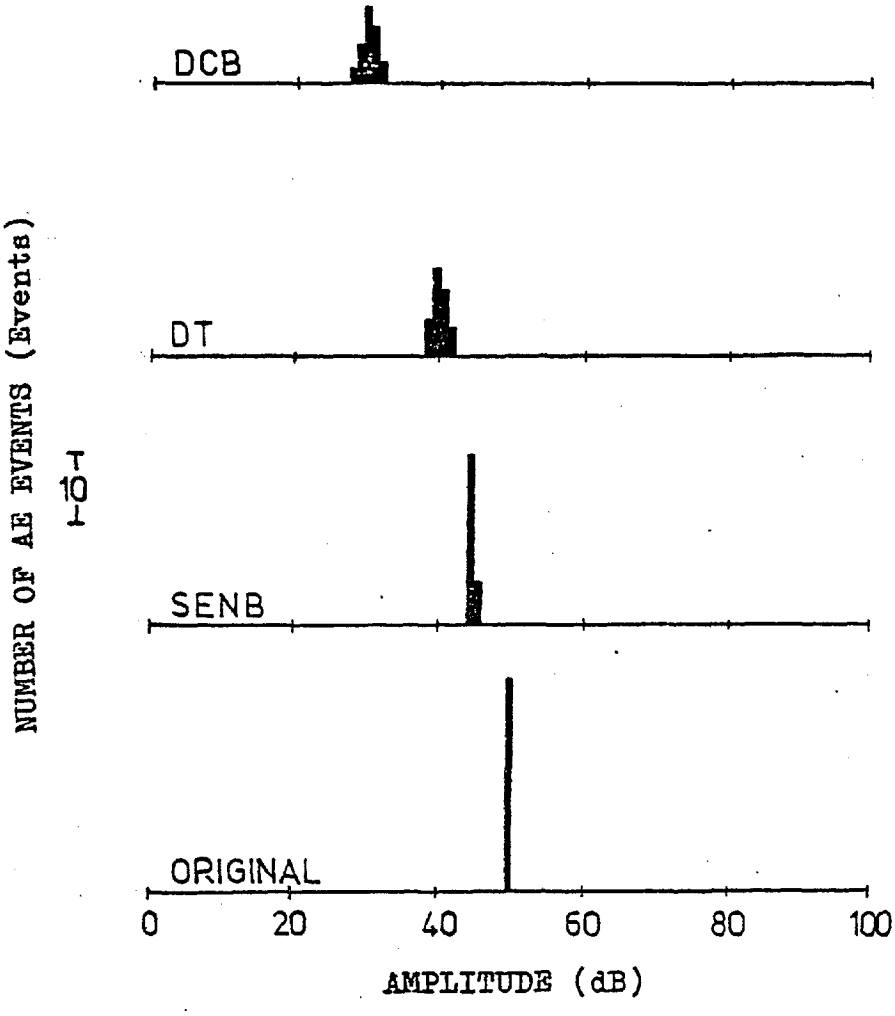


Fig.4.25. The change and attenuation of emission amplitude by specimen geometry.

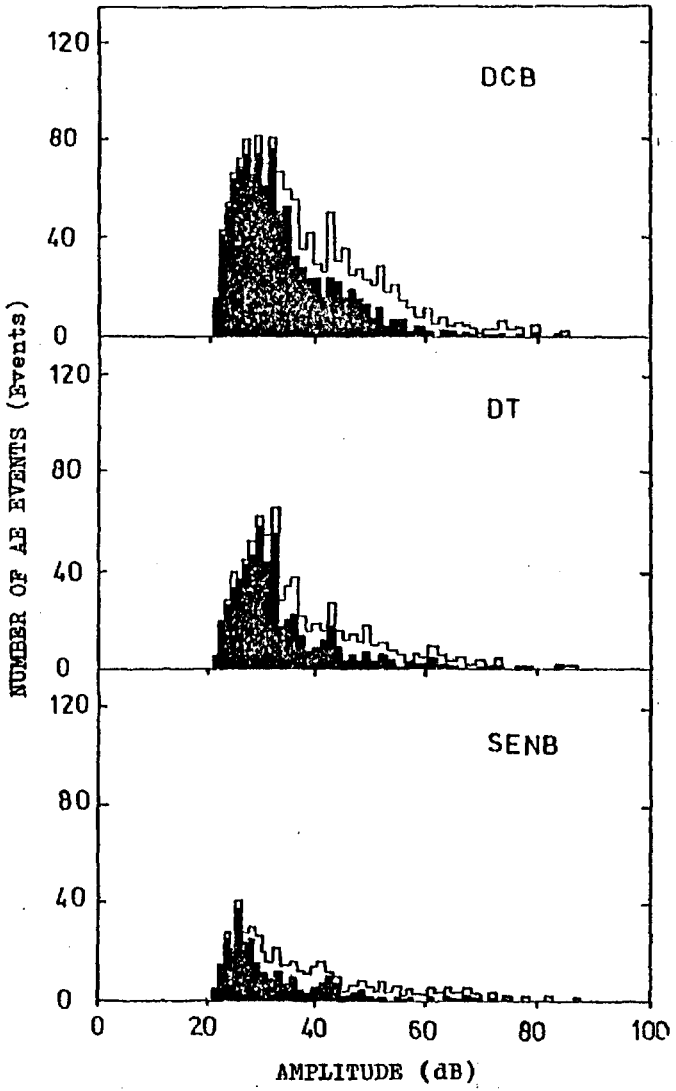


Fig.4.26. Typical amplitude distributions for SENB, DT and DCB test geometries obtained after subcritical crack growth and final failure.

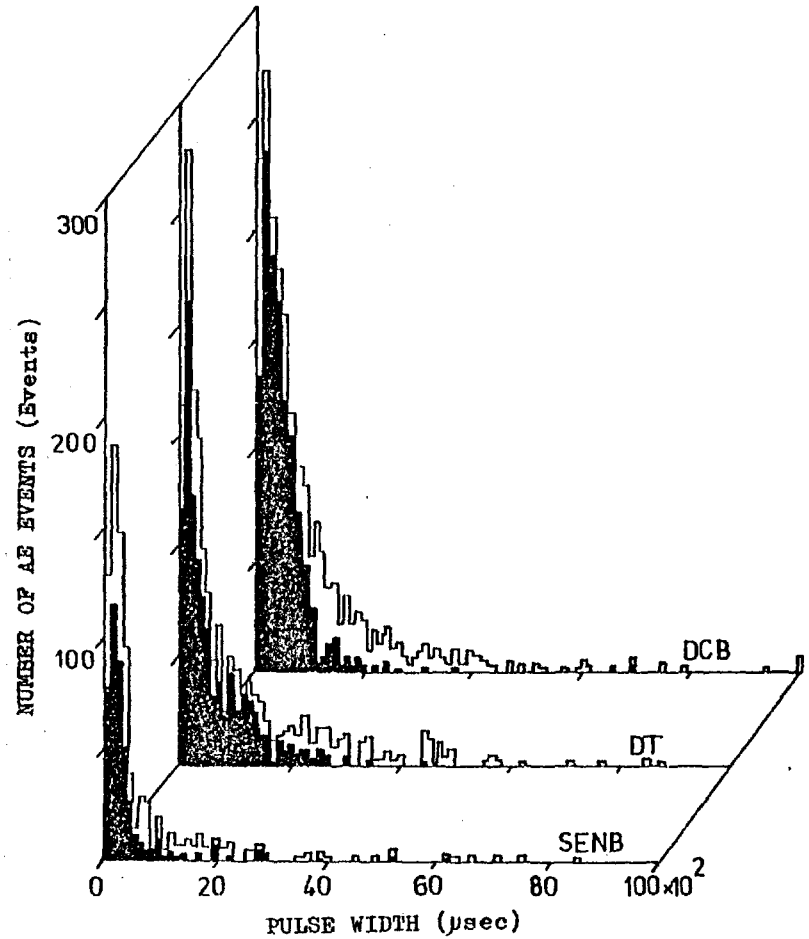


Fig.4.27. Typical pulse width distribution for SENB, DT and DCB test geometries obtained after subcritical crack growth and final failure.

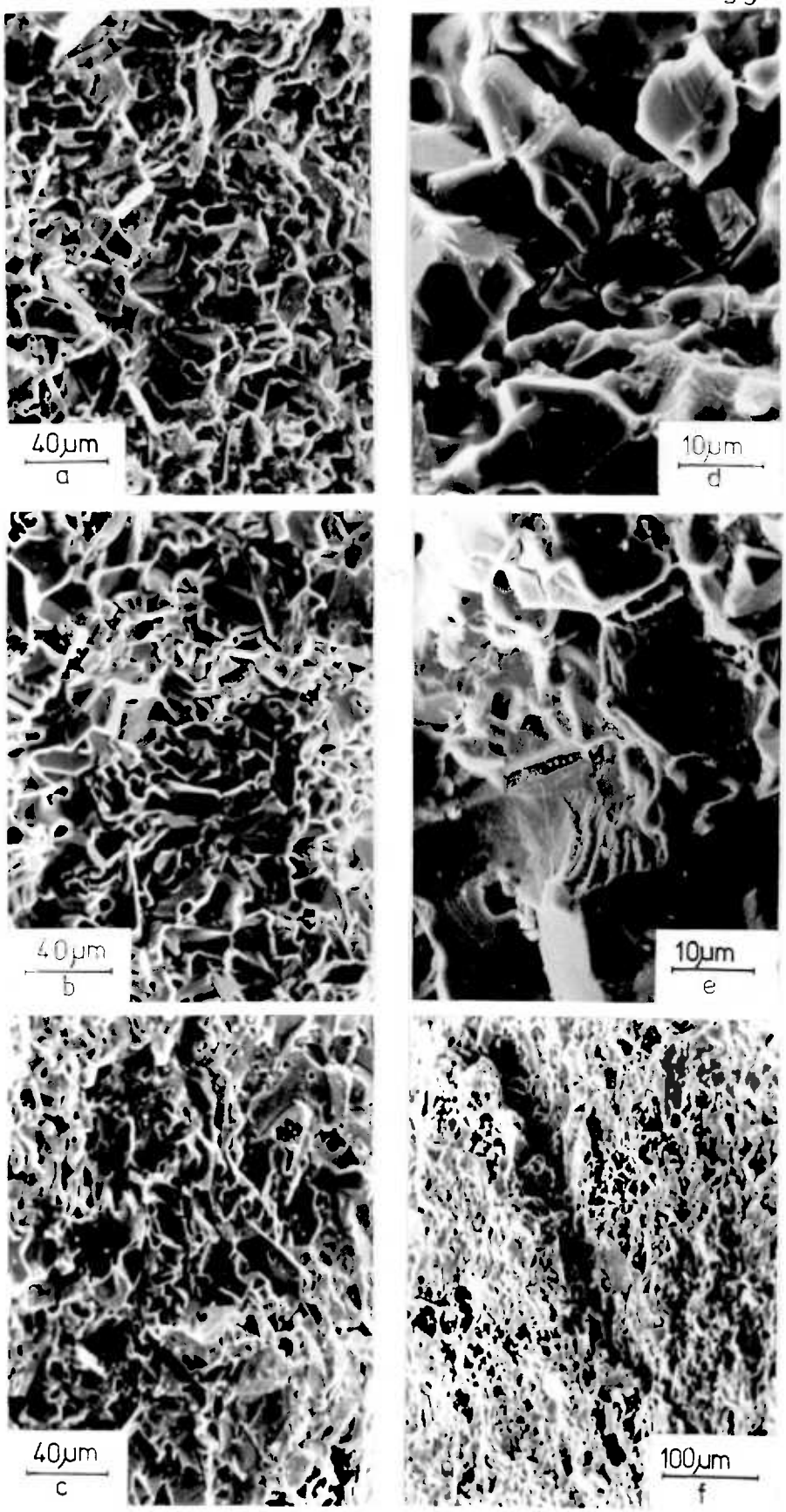


Fig.4.28. SEM, showing the fracture faces:
a - general view, SENB FA4,
b - " " DT " ,
c - " " DCB " ,
e - microcracks, cleavage fracture (SENB FA2),
d - crack branching (DT FA5),
f - secondary cracking (DCB FA0).

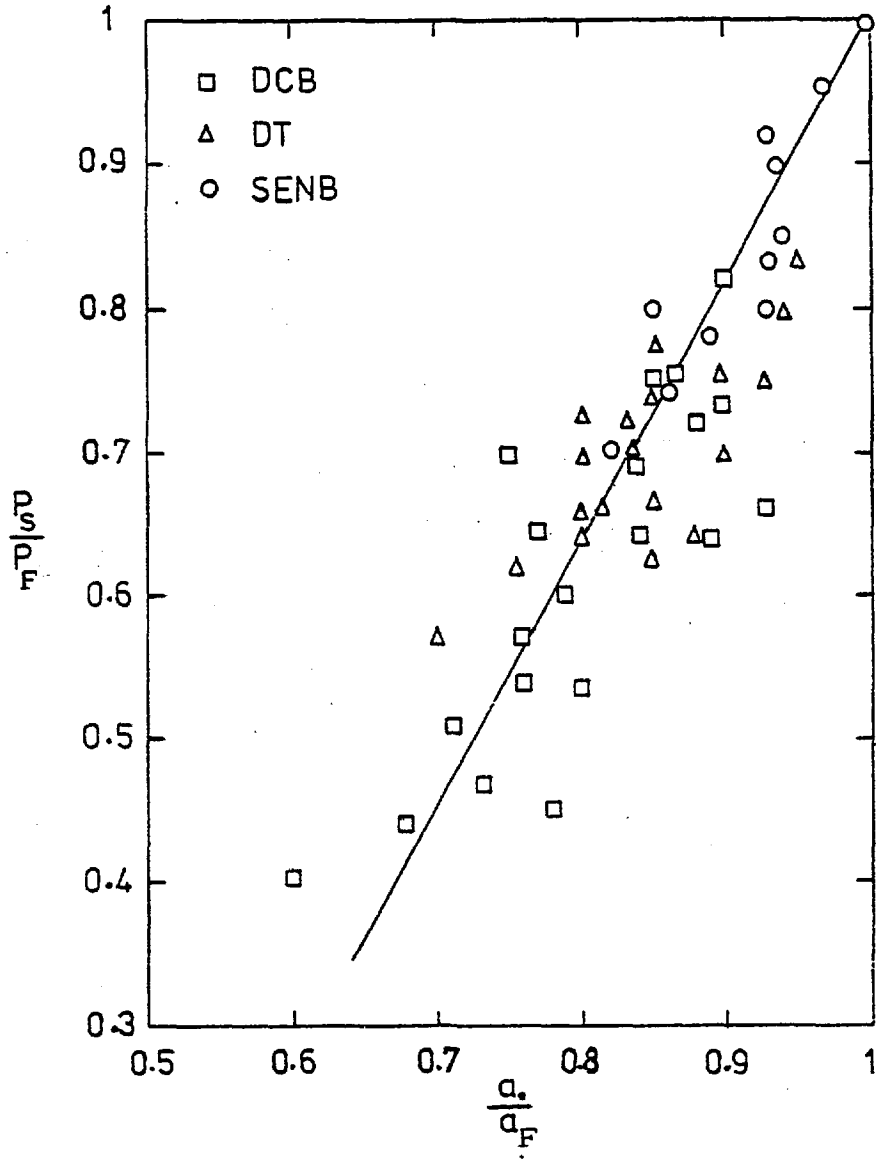


Fig.4.29. P_s/P_F vs $a_./a_F$ for alumina specimens tested at 0.01cm/Min strain rate where linear load-deflection curves existed.

The AE data also varied with geometry, as in the case of alumina. The total number of counts decreased in the order DCB > DT > SENB while the N_{RT}/mm^2 and N_{ET}/mm^2 for each geometry varied in the order SENB > DT > DCB. In fact the agreement of the results of alumina with those of porcelain in many aspects not only supported the validity of the technique but also indicated its possible application to other ceramics.

4.3.3 The Influence of Notching Technique

The mathematical solutions for the fracture toughness test geometries describe zero volume cracks. However, the introduction of sharp cracks in SENB specimens is difficult and time-consuming, and the use of machined-notched specimens is more convenient. In this section the K_{IC} values obtained for specimens of three aluminas of differing microstructures, and having different notches, are compared with the results of sharp-cracked specimens. The validity of the machined-notched data is assessed using microscopical examination of the notch roots and the obtained AE responses.

SENB specimens of aluminas A, B and C, containing sharp cracks and blunt notches were tested in 3-point bending under the same conditions. Blunt notches were produced on Capco and Maco-machines using 0.25 mm and 0.3 mm thick diamond blades, respectively. The details of sawing techniques are described in Sections 3.4.1 and 3.4.3. The sharp cracks were produced from notched specimens using the technique discussed in Section 3.8.

The K_{IC} values and AE data are summarised in Table 4.4. In general, the K_{IC} values obtained from blunt-notched specimens showed reduced values compared with data obtained for sharp-cracked specimens, as shown in Fig. 4.32a. However, Capco-notched K_{IC} values for the fine-grained aluminas A and B compared very favourably with sharp-crack values, indicating that damage introduced by diamond notching, in some cases, can effectively sharpen the notch. Light microscopy and dye penetration revealed no evidence of serious

machining damage drastically increasing crack length for fine-grained material (see Fig. 4.30a). On the other hand, in the coarse-grained aluminas more serious damage was observed in the Capco-notched specimens (see Fig. 4.30b) and K_{IC} values for coarse-grained material were lower than the sharp-crack values.

The fracture toughness values obtained for the above-mentioned alumina specimens notched in the Maco machine generally showed overall reduced values compared with sharp and Capco-notched specimens. The micrographs taken of the root of Maco-notched specimens indicated a damage zone for both fine- and coarse-grained materials.

The scanning electron micrographs taken of the fracture surface of the notch roots, indicated a series of microcracks originating from the notch tip, as shown in Fig. 4.31.

It has been shown that the apparent K_{IC} value increases with notch root width[8]. However, in the case of Maco-notched specimens this effect is masked by the extent of the damaged region (in coarse-grained alumina as large as 160 μm in length) which results in significantly reduced K_{IC} values. More accurate K_{IC} values could be obtained if the length of the damaged zone was added to the initial notch length.

The accurate measurement of this zone was only possible if specimen surfaces were carefully polished for optical examination under the microscope. When the notch root damage (see column 3 of Table 4.4) in the blunt-notched specimens was measured and added to the initial notch length, K_{IC} values increased (Fig. 4.3b).

Dalgleish et al[91] showed that subsequently annealing Capco-notched specimens of A, B and C aluminas had a significant effect on the measured K_{IC} values. The effect in materials A and B was to increase K_{IC} to values higher than sharp-cracked values, i.e. annealing appeared to have healed the notch-root damage to yield the more realistic blunt-notch toughness values. The effect of annealing blunt-notch specimens of material C was to increase K_{IC} to a value almost identical to the sharp-crack value.

On the basis of the results for aluminas A and B there appears to be no need for sharp-cracking fine-grained aluminas, if the blunt notches are carefully produced using a fine diamond wheel, as in the Capco machine. It is clear that for coarse-grained materials, K_{IC} values are best measured using pre-cracked specimens. If not, correction must be made for the increased notch length.

From the acoustic emission point of view, a similar response was obtained for all blunt-notched specimens, although alumina C was acoustically noisier than A and B (see Fig. 4.33). Sharp-cracked specimens produced slightly less emissions prior to failure than those of blunt-notched specimens, indicating that the generation of a series of microcracks in front of the notch tip and the subcritical crack growth before failure was more pronounced in blunt-notched specimens. In fact, the K_{IC} values should also be corrected for the subcritical crack length.

The values obtained for subcritical crack length were measured from Fig. 4.18 using the respective N_{ET} values from Table 4.4, and are summarised in column 8 of Table 4.4. Comparing the data obtained for subcritical crack length, a_s, with those measured for the damaged zone, a_d, two situations may exist, as shown in Fig. 4.34. For true K_{IC} measurements, the initial crack length, a_o, cannot be used, unless correction for damaged zone and subcritical crack length is made. When $a_s > a_d$, then (a_o+a_s) should be used, but when $a_d > a_s$, then (a_o+a_d) should be employed. However, the results of alumina A, B and C showed that in almost all cases a_s was greater than a_d. Thus if correction is made for subcritical crack growth, the damaged zone is also being considered.

The corrected K_{IC} values are shown in column 9 of Table 4.9. From these results it appears that the SENB specimens of fine-grained aluminas, blunt-notched in the Capco machine, could be used for fracture toughness measurements instead of the less convenient sharp-cracked specimens, since its K_{IC} data both before and after correction are consistent with those of sharp-crack specimens. For the coarse-grained aluminas, the as-measured K_{IC} data obtained from Capco-notched specimens should be treated with

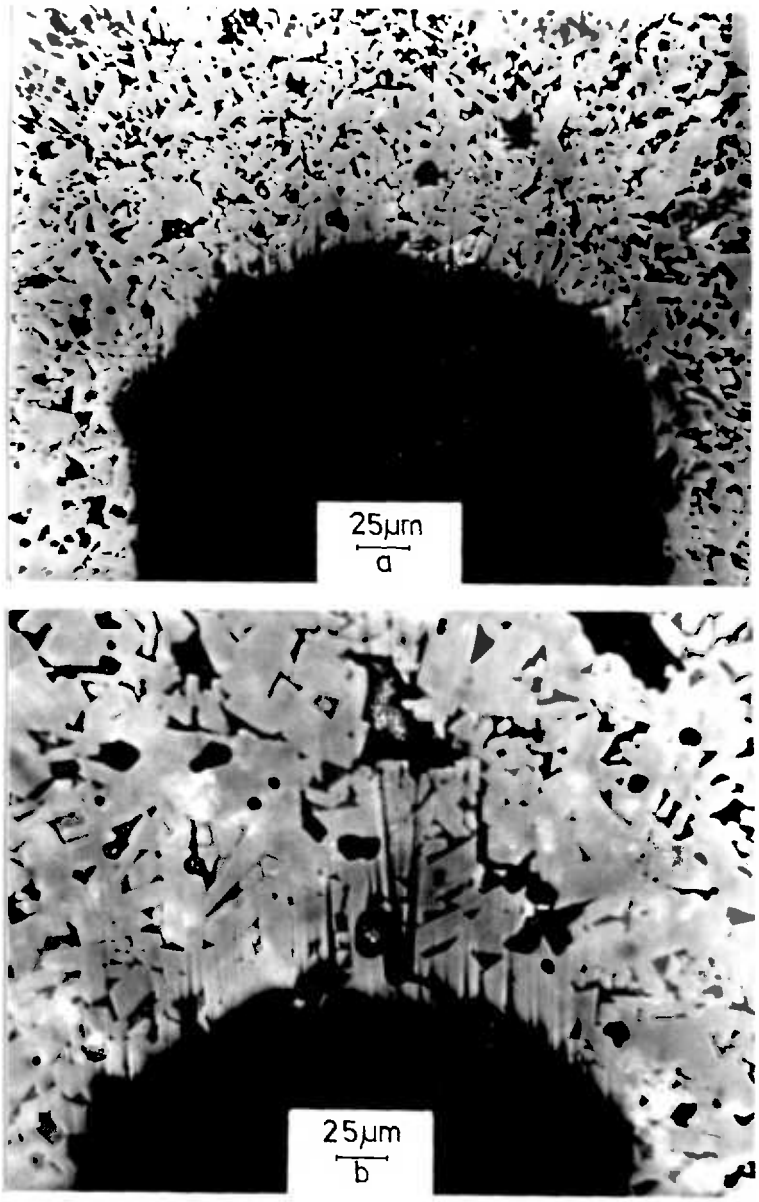


Fig. 4.30. Optical micrographs from polished faces of the notch root, showing the damaged zone.
a- Fine grained alumina.
b- Coarse " "

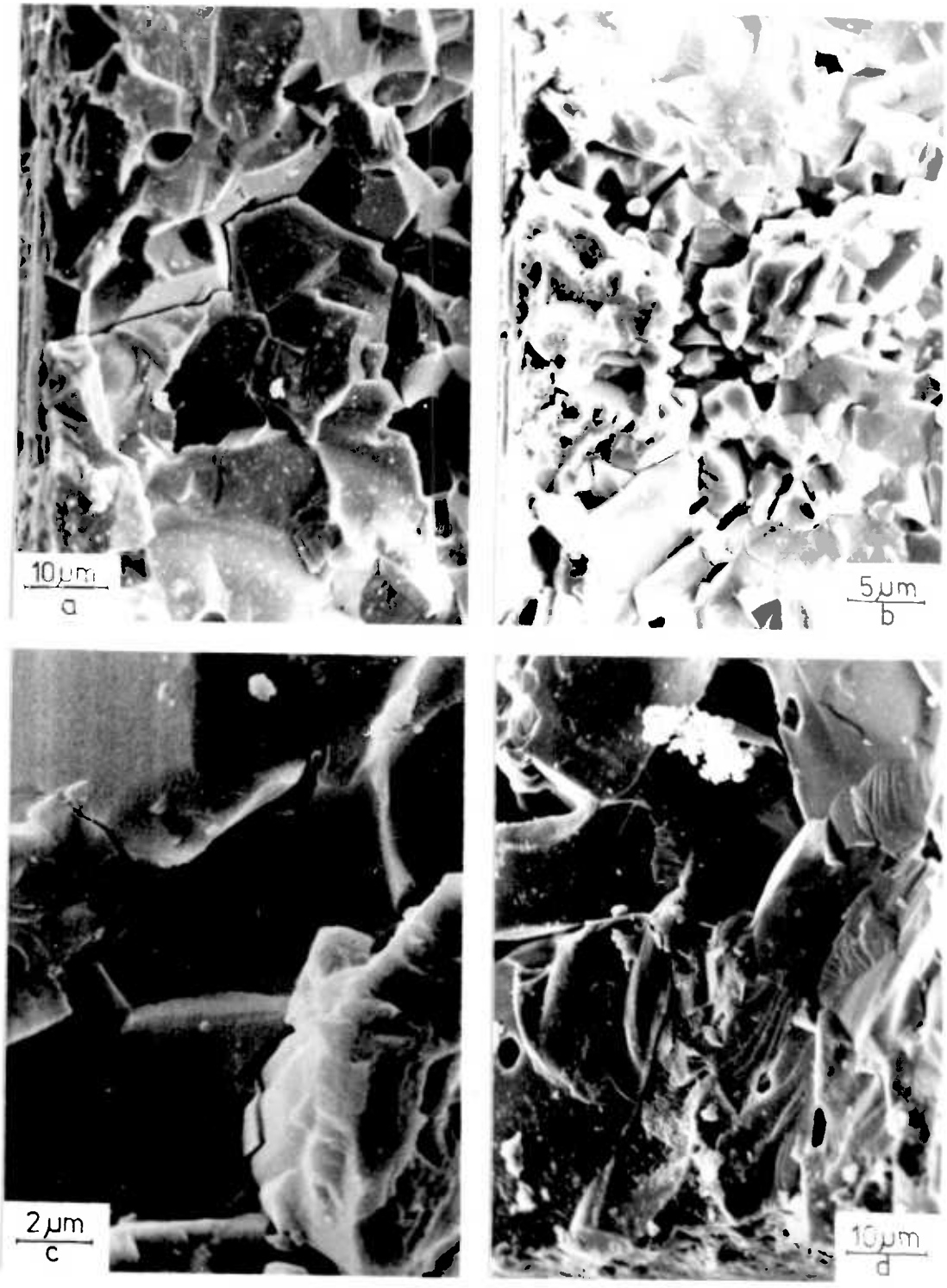


Fig. 4.31. SEM showing microcracks near the notch root

a - alumina C

b - " FA 6

c - " B

d - " FA 5

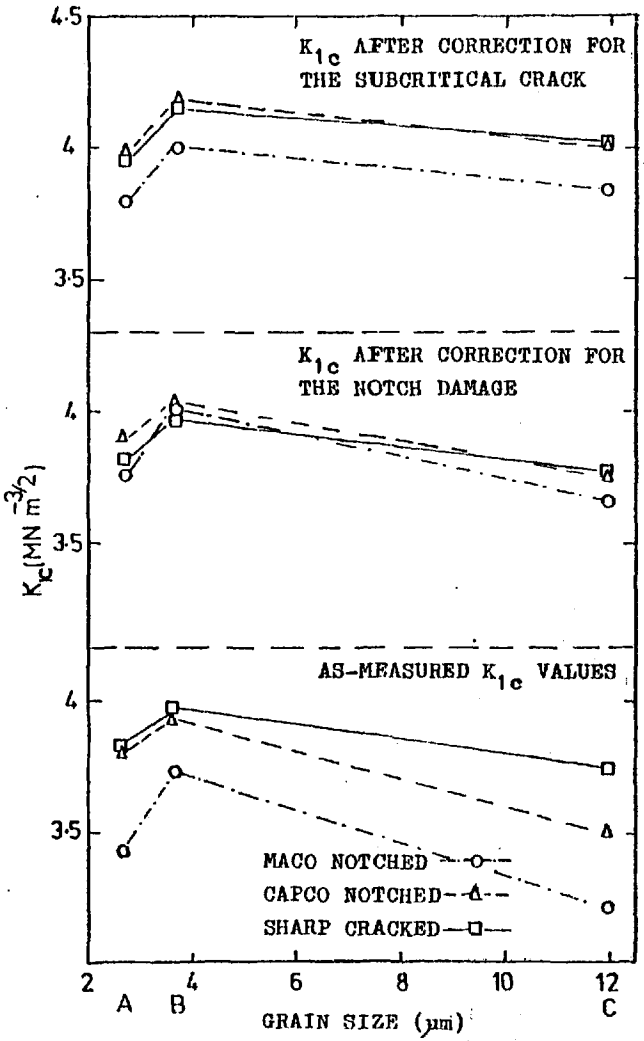


Fig.4.32. Comparison of the K_{1c} values obtained for aluminas A, B, and C by differently notched specimens before and after corrections.

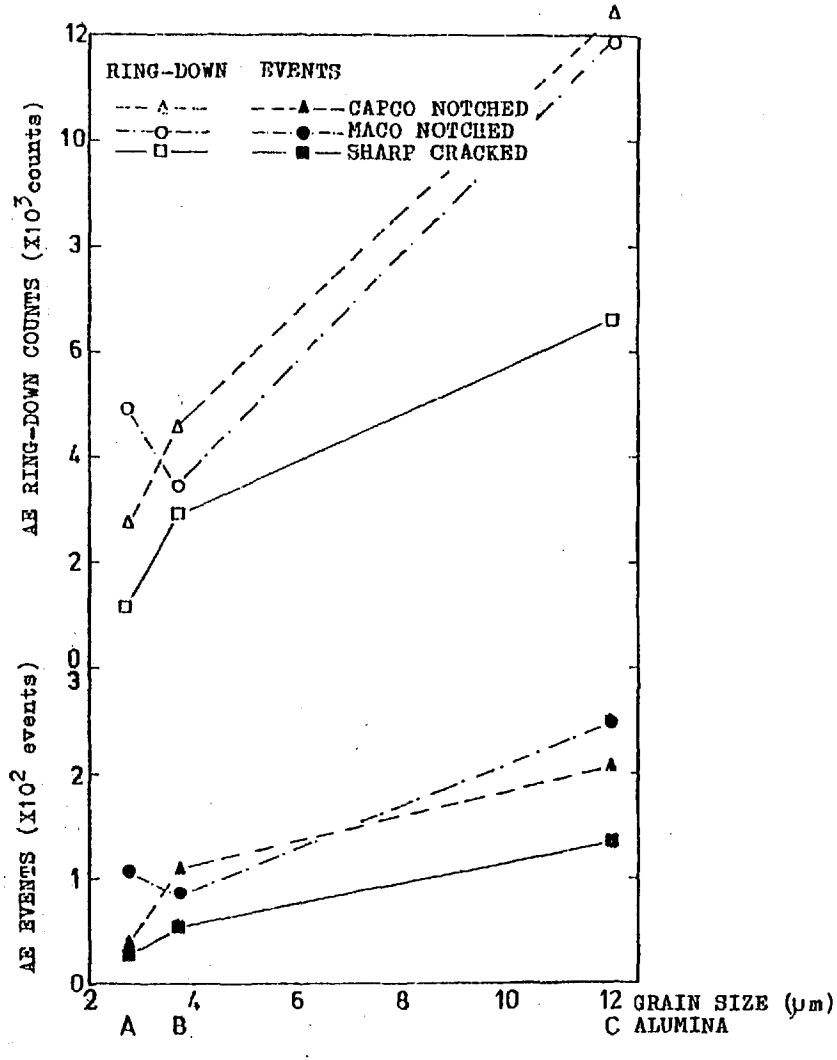


Fig.4.33. Acoustic response of SENB specimens with different initial notches.

TABLE 4.4 Effect of Notching Technique on K_{IC} and AE Response.

Aluminas	Notching technique	Ave. extent of damage (mm.)	N_{RT} due to subcritical crack	N_{ET} due to subcritical crack	K_{IC} $MNm^{-3/2}$	K_{IC} correction for the damage $MNm^{-3/2}$	Subcritical crack length (mm.)	K_{IC} after correction for subcritical crack $MNm^{-3/2}$
A	Maco-notched	$\approx$ 0.12	4800 $\pm$ 1200	105 $\pm$ 35	3.40$\pm$0.24	3.76	0.125	3.8
	Capco-notched	0.025	2700 $\pm$ 800	33 $\pm$ 15	3.82$\pm$0.31	3.90	0.06	4.0
	Sharp-cracked	-	1200 $\pm$ 400	25 $\pm$ 11	3.83$\pm$0.25	-	0.05	3.97
B	Maco-notched	0.10	3400 $\pm$ 1150	78 $\pm$ 23	3.72$\pm$0.22	4.02	0.08	4.0
	Capco-notched	0.02	4600 $\pm$ 1900	110 $\pm$ 35	3.95$\pm$0.29	4.03	0.12	4.2
	Sharp-cracked	-	2800 $\pm$ 800	54 $\pm$ 18	3.99$\pm$0.4	-	0.065	4.18
C	Maco-notched	0.16	11800 $\pm$ 1300	245 $\pm$ 85	3.20$\pm$0.13	3.66	0.175	3.84
	Capco-notched	0.09	12500 $\pm$ 3000	215 $\pm$ 53	3.51$\pm$0.18	3.77	0.22	4.03
	Sharp-cracked	-	6600 $\pm$1410	138 $\pm$ 56	3.75$\pm$0.15	-	0.1	4.04

some caution before accepting them as true values. For the aluminas used in the present investigation, an increase of ~7% should be applied to as-measured K_{IC} values of coarse-grained materials to increase the data to the same level as those obtained by the sharp-crack specimens. However, if the true values of K_{IC} are needed, all measured data should also be corrected for the subcritical crack growth according to their acoustic response prior to failure.

The true K_{IC} values determined for SENB specimens having various types of initial crack indicated that when the necessary corrections for the damaged zone and subcritical crack length are made, very consistent results are obtained.

4.3.4 Mechanical Testing and AE at Various Strain Rates

There is some evidence in the literature[38,92] suggesting a strain rate dependence of the strength and toughness of alumina, and of the slow crack growth prior to catastrophic failure. This section deals with the effect of strain rate on the strength, toughness and acoustic response of alumina. The influence of strain rate on the acoustic emission of alumina, indeed on ceramics in general, has only received limited attention to date.

The modulus of rupture beams and SENB specimens of Capco-notched alumina were tested in 3-point bending at various cross-head speeds ranging from 0.01 to 1 mm/min. using a 20 mm span between the two outer loading points. The strain rate is directly related to the cross-head speed, the relationship for rectangular beams being[92]:

$$\varepsilon' = \frac{6h}{s^2} y' \qquad (4.2)$$

where ε' is the strain rate, y' is the cross-head speed, and h and s are the specimen thickness and testing span, respectively. Thus for specimens of 2 mm thickness tested at a cross-head speed of 0.1 mm/min. a strain rate of 5×10^{-5} sec^{-1} is obtained.

The results of modulus of rupture tests at various strain rates showed that over the above-mentioned range of cross-head speeds, the load deflection curves were linear up to catastrophic failure. The fracture loads increased slightly with increasing strain rate, indicating a small positive strain rate dependence of the strength, as illustrated in Fig. 4.35. The acoustic response for all cases was similar, i.e. the emission occurred only at the point of failure, and no appreciable difference was observed in either the total number of ring-down counts (N_{RT}) or events (N_{ET}), as the strain rate was varied (Fig. 4.36).

The decrease in fracture strength of alumina with a decreasing strain rate followed the trend reported by Davidge et al[93], i.e.:

$$\left(\frac{\sigma_1}{\sigma_2}\right)^{m+1} = \frac{\dot{\varepsilon}_1}{\dot{\varepsilon}_2} \qquad (4.3)$$

where σ_1 and σ_2 are the mean strength at $\dot{\varepsilon}_1$ and $\dot{\varepsilon}_2$ strain rates, respectively, and m is a constant. Fig. 4.37 was obtained by substituting in equation (4.3) for σ_1 and σ_2 corresponding to appropriate values for $\dot{\varepsilon}_1$ and $\dot{\varepsilon}_2$ from Fig. 4.35. The average m-value of 45 was measured from Fig. 4.37, which is approximately twice the value of 21.5 reported by Davidge et al for a 95% pure alumina. A reason for disagreement in m values is probably due to using wider specimens (4 mm compared to 3 mm) in the present work, which results in a comparatively stiffer system. Both results suggest, however, that as the strain rate decreases the material exhibits the phenomenon of delayed fracture or static fatigue, in which failure occurs under the application of stress less than that required for short-term failure. The effect is believed[93] to be due to a stress-dependent chemical interaction (stress corrosion) between the material and the environment.

On the other hand, AE results indicate that there are no emissions prior to failure even when strain rate decreases. This suggests that the emissions occurring due to stress corrosion of the material are probably those of very low energy events, the peak amplitude of which remains below the threshold of the AE equipment.

Alternatively, it is possible that so few emissions occur that they are not distinguishable from the occasional background noise that exceeds the threshold voltage and are, therefore, insignificant compared with the emission associated with final catastrophic failure. The fact that the amount of sub-critical crack growth associated with stress corrosion at slow strain rates is insufficient to produce a reasonable number of detectable emissions can be demonstrated using information obtained from fracture toughness tests.

The flaws from which fracture originates in un-notched alumina specimens are usually of two types [2] as shown in Fig. 4.34.a.

(i) The semielliptical or semicircular flaw situated at the specimen surface which usually comprises several grains and pores. Flaw extension occurs when ligaments of material connecting pores and grains fracture.

(ii) A sub-surface flaw, which is extended by the fracture of a ligament connecting such a flaw to a surface flaw.

The Griffith equation (2.5) has to be modified to account for flaw shape by introducing a constant Z such that:

$$\sigma_f = \frac{Z}{Y}\left[\frac{2E\gamma_i}{C(1-\nu^2)}\right]^{\frac{1}{2}}$$

using equations 2.10 and 2.12 then:

$$\sigma_f = \frac{Z}{Y}\,\frac{K_{1C}}{C^{\frac{1}{2}}}$$

For the case of a semielliptical surface flaw, perhaps the more significant in alumina, it has been shown [99] that:

$$\sigma_f \sim \frac{1.68}{Y}\,\frac{K_{1C}}{A^{\frac{1}{4}}} \qquad (4.3b)$$

where A is the area of the flaw. If the fracture toughness is a material constant, the value of flaw size, A, at failure can be estimated using the above equation by measuring the strength.

For the alumina used in the experiments on the effect of strain rate, $K_{1C} = 4.6$ MN $m^{-\frac{3}{2}}$ was measured. The average geometry factor obtained for the beams was Y = 1.8 (obtained from Fig.3.4. for flaw depth a = 30-300μm). At fast strain rate ($\dot{\varepsilon}_1 = 50 \times 10^{-6}$ sec) the strength, σ_{f1}, found to be 375 MN m^{-2}. Putting these values in equation 4.3b, leads to the approximate flaw size of:

$$A_1 = 1.72 \times 10^{-2} \text{ mm}^2$$

From Fig.4.18 the number of AE signals expected for this fracture area is about 22 events. This is a small number of events but would have been detected if the amplitude of signals was above the threshold voltage of equipment. Emissions were not detected prior to failure; this suggests that pores link up together in a number of stages. In each stage only a fraction of the total flaw area is formed; this area is so small that the amplitude of emissions produced remains below the threshold level of acoustic emission equipment. This is consistant with the finding of Meredith and Pratt[2] who demonstrated, by microscopical examinations, that pores link together at different stress levels prior to the fracture stress.

At slow strain rate (0.5×10^{-6}-sec) where stress corrosion effect is more considerable and strength is reduced to $\sigma_{f2} = 345$ MN m^{-2}, the flaw size at failure was increased to:

$$A_2 = 2.40 \times 10^{-2} \text{ mm}^2$$

This shows that the maximum value for the flaw extension due to stress corrosion in the range of strain rates employed is :

$$A_2 - A_1 = 0.68 \times 10^{-2} \text{mm}^2$$

The additional number of emissions expected for this fracture area is about 8 events. In addition to the previous discussion, this value is insignificant compared with the number of emissions obtained at failure (60 ± 20). Thus the stress corrosion of alumina at room temperature in air does not produce an appreciable number of detectable acoustic emissions even at very slow strain rates.

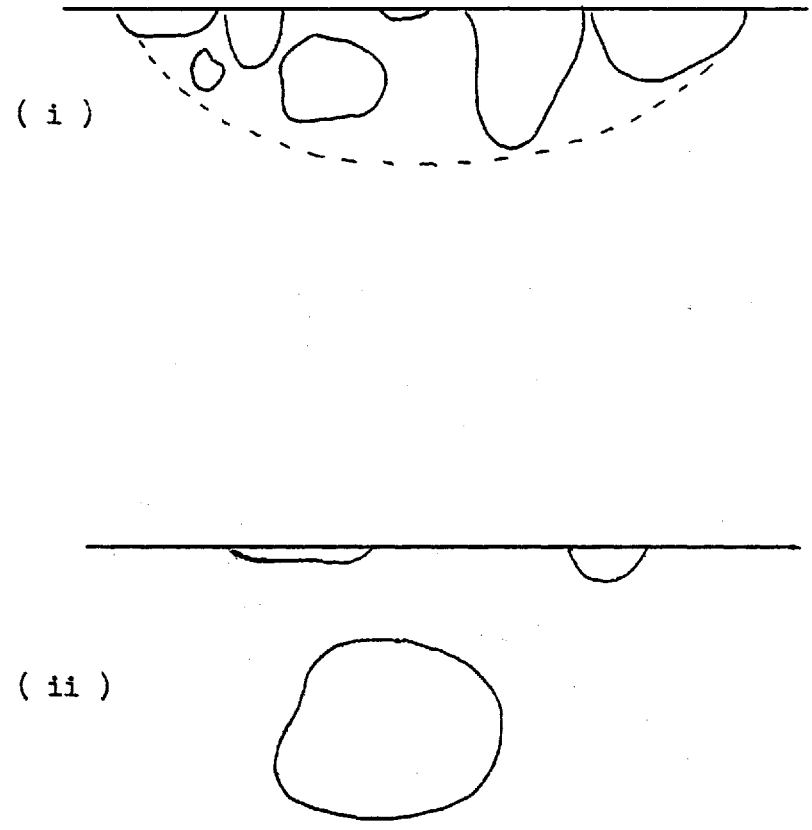


Fig.4.34.a. Schematic views of pores which link up together at sub-critical stresses to form a fracture initiating flaw.

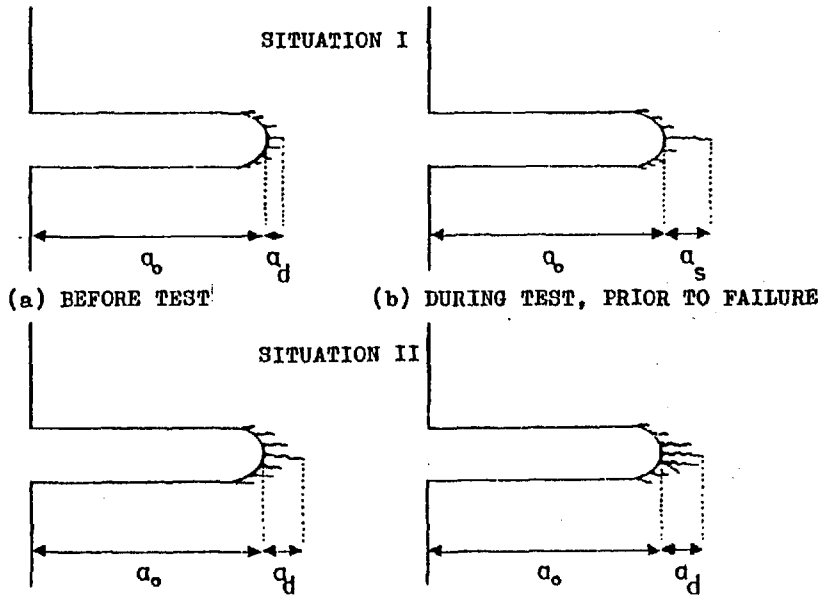


Fig.4.34. Two situations may exist in sawn-notched specimens just before fracture;
(i) the total crack length= $a_o + a_s$, or;
(ii) " " " " = $a_o + a_d$.

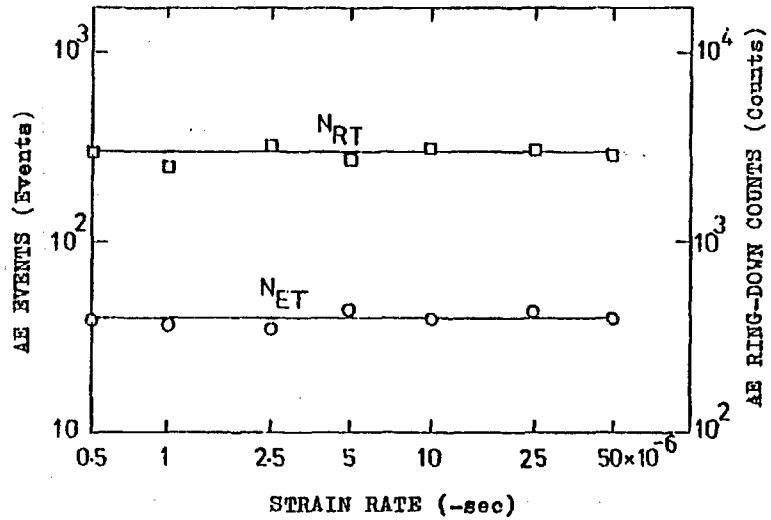


Fig.4.36. The AE obtained during strength tests vs the strain rate.

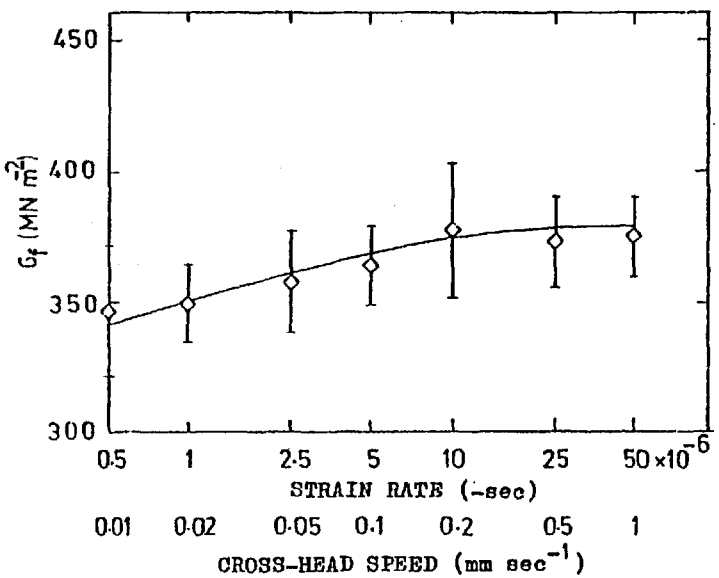


Fig.4.35. The strain rate dependence of strength.

The load-time and the AE events time curves for the SENB specimens tested at various strain rates are shown in Fig. 4.38. The load-time curves were linear for cross-head speeds $\geqslant 0.1$ mm/min, and failure occurred catastrophically at the maximum load, i.e. $P_F = P_{max}$. The critical stress intensity factor was measured from P_F and the results are presented in Fig. 4.39. The acoustic emission started at about 96% of the fracture load, and the emission rate increased with the load reaching a maximum at fracture.

Using a cross-head speed of less than 0.1 mm/min, the positive loading rate decreased at a point A before the maximum load, and a non-linear region appeared. As the cross-head speed was reduced, increased non-linearity was observed. AE commenced just before the beginning of non-linearity and increased with time until the load dropped to zero. The load P_s, at which AE commenced, remained unchanged with strain rate until a cross-head speed of 0.01 mm/min was used, at which P_s was slightly reduced.

The maximum load decreased with decreasing strain rate, as did the stress intensity factor corresponding to the maximum load, K_{IM} (Fig. 4.39).

Evans[63] described the strain rate-stress intensity factor relationship for alumina using double torsion specimens as follows:

$$\varepsilon' \approx K_I^{n+1} \qquad (4.4)$$

The present results agree with the above equation. The value of $n = 26$ was measured from Fig. 4.40, which was obtained by substituting for the ε_1' and ε_2' the corresponding values of K_{I1} and K_{I2} from Fig. 4.39 using the equation:

$$\frac{\varepsilon_1'}{\varepsilon_2'} = \left(\frac{K_{I1}}{K_{I2}}\right)^{n+1} \qquad (4.5)$$

K_{I1} and K_{I2} are the apparent fracture toughness values obtained from the loads P_{F1} and P_{F2}, respectively, for a constant initial notch length, a_o, thus:

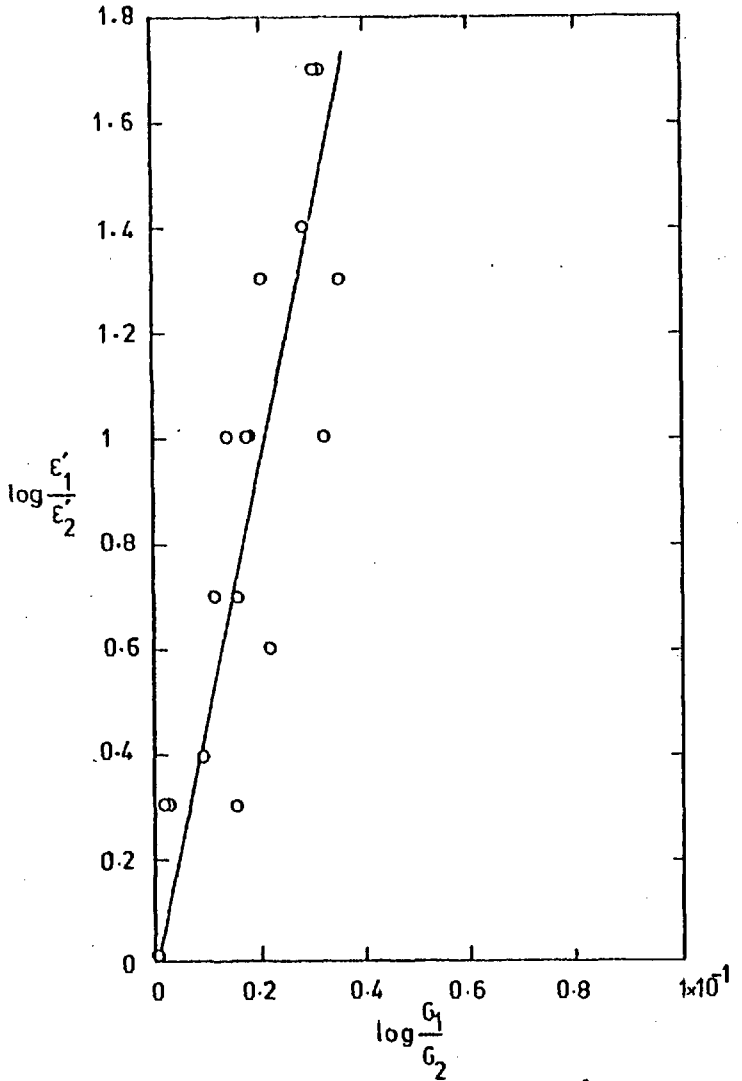


Fig.4.37. Log σ_1/σ_2 vs Log $\varepsilon'_1/\varepsilon'_2$.

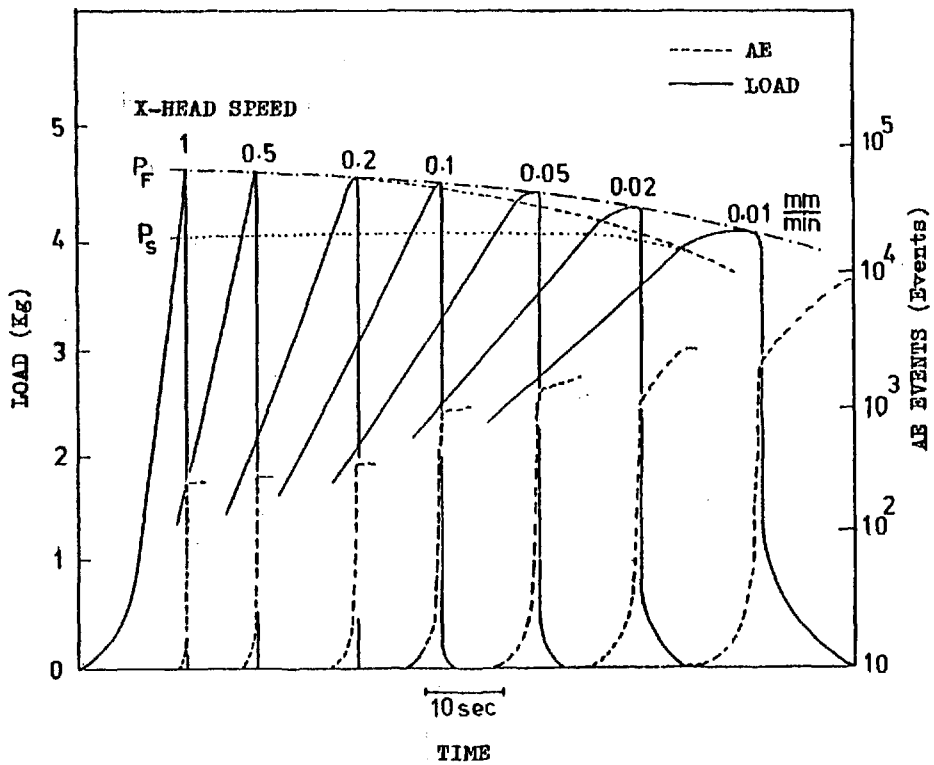


Fig.4.38. Load-time and AE ring-down counts-time curves at different strain rates.

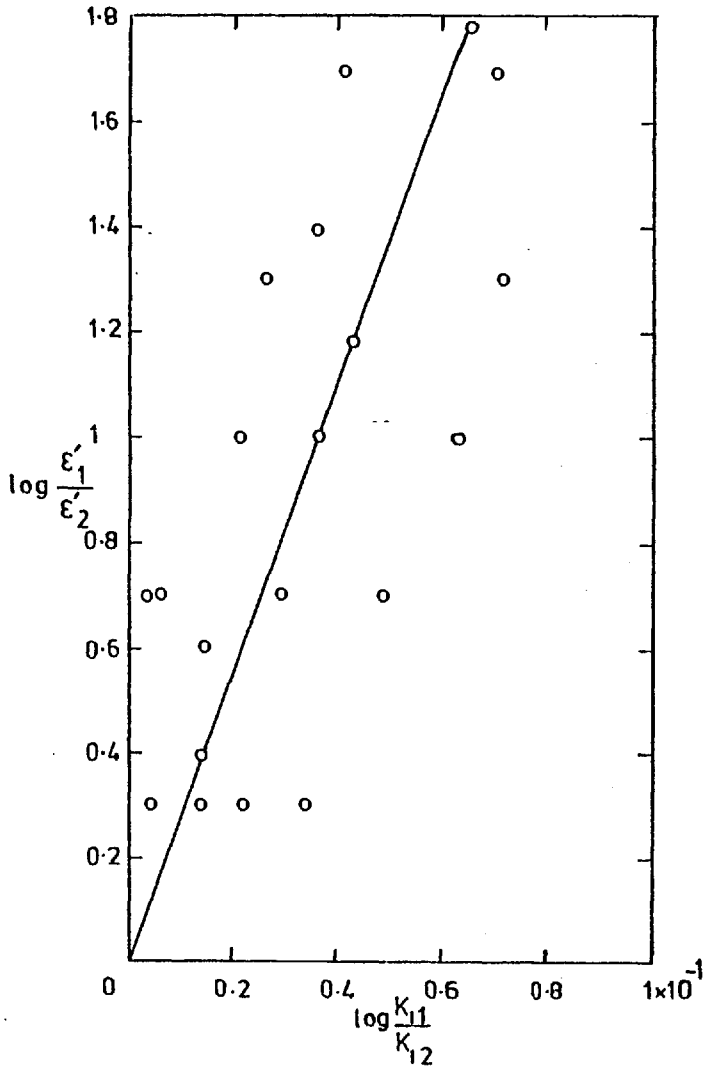


Fig.4.40. Log K_{11}/K_{12} vs Log $\varepsilon'_1/\varepsilon'_2$.

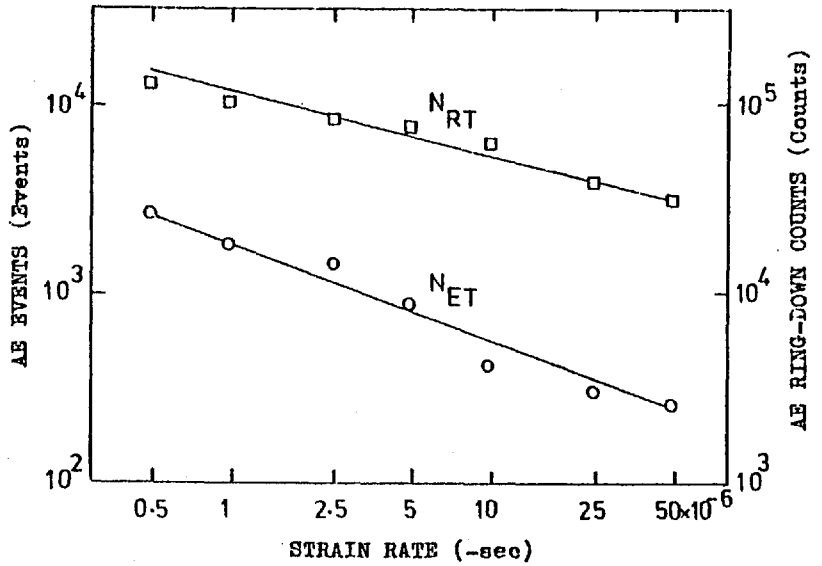


Fig.4.41. The AE obtained during fracture toughness tests,(SENB), vs the strain rate.

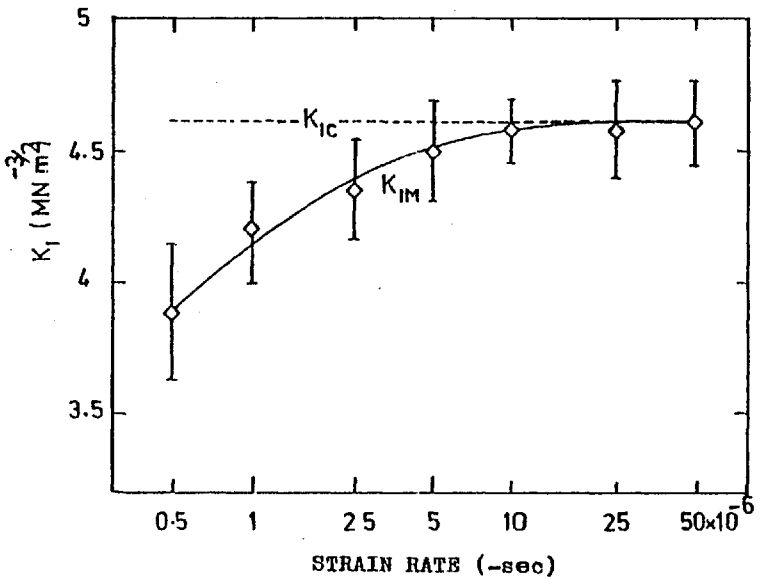


Fig.4.39. The strain rate dependence of stress intensity factor obtained from the maximum load.

$$\frac{K_{I1}}{K_{I2}} = \frac{P_{F1}}{P_{F2}} \qquad (4.6)$$

The AE behaviour of specimens also varied with strain rate. In general, the total ring-down and event counts increased with decreasing strain rate (see Fig. 4.41) but the rate of emission was increased with increasing strain rate.

At cross-head speeds of $\geqslant 0.1$ mm/min there was a high rate of emission at the point of failure, but very little response before and after failure. As the strain rate was decreased, increased low rate emissions before the maximum load were recorded and a high rate of emission occurred at the load drop. Low rate emissions also continued after the load drop, until finally the load became zero. In contrast to the low strain rate modulus of rupture tests the extent of the sub-critical crack growth was such that a low rate of acoustic emissions were detected before the maximum load.

The number of high amplitude emissions recorded during the test did not vary very much with strain rate. However, with decreasing strain rate, low amplitude emissions associated with subcritical crack growth were observed and consequently the b-value increased with decreasing strain rate, as shown in Fig. 4.42. The pulse width distribution histograms are presented in the same way as the amplitude distributions, and the results showed that the fraction of low pulse width events was increased as the cross-head speed decreased, as shown in Fig. 4.43. This is, again, consistent with subcritical crack growth being more extensive at low strain rates, as it has been shown previously in Figs. 4.26 and 4.27 that the emissions during subcritical crack growth are of low amplitude and low pulse width.

In fracture toughness determinations, critical values of the fracture toughness parameters, K_{IC} and G_{IC}, are defined for the condition that unstable fracture occurs, i.e. the load-deflection curve is absolutely elastic and no subcritical crack growth takes place. In practice, however, subcritical crack growth may occur even though a linear load-deflection curve exists (see Section 4.3.1).

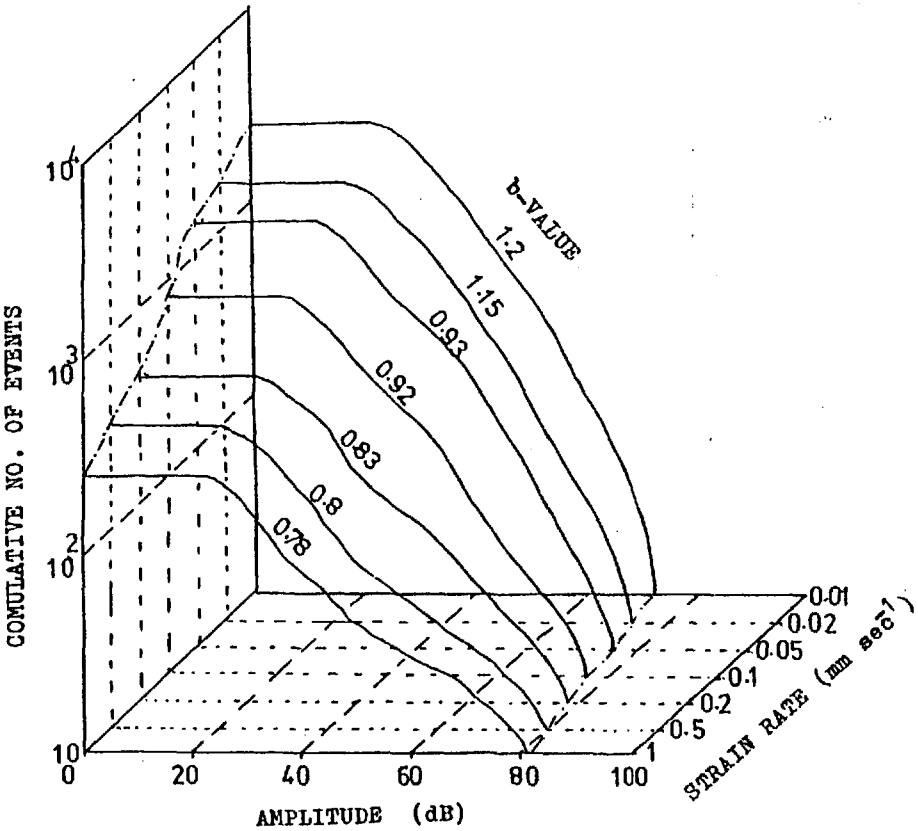


Fig.4.42. The AE amplitude distributions obtained using different strain rates, slope of the curves gives the corresponding b- value.

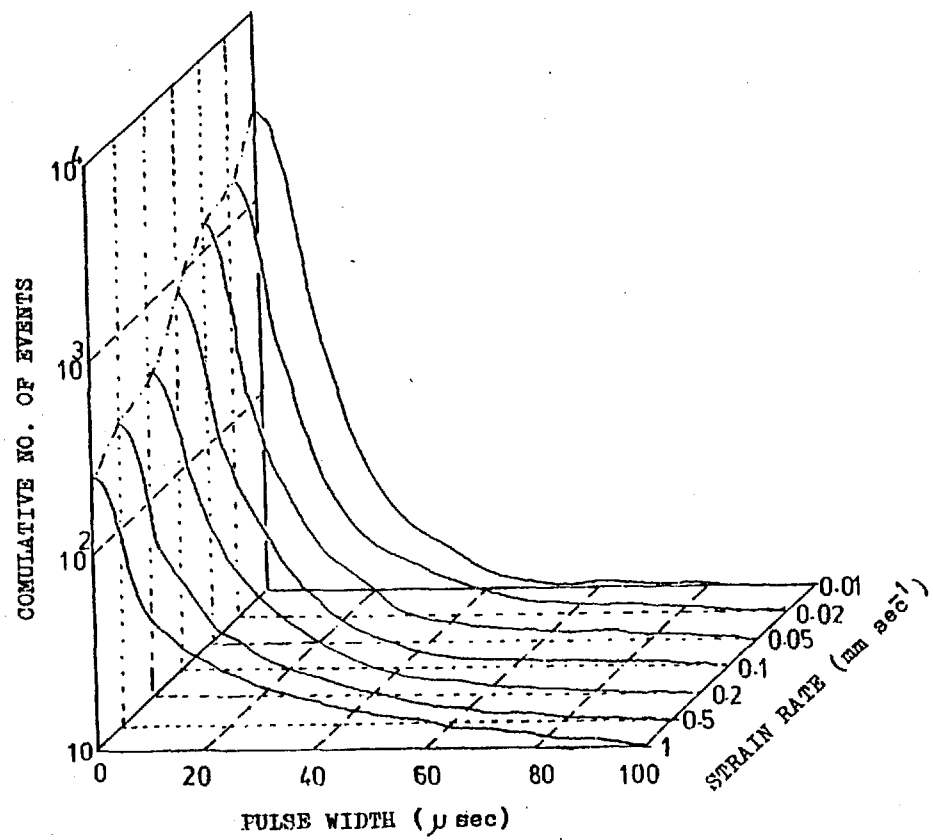


Fig.4.43. The AE pulse width distributions obtained using different strain rates,(SENB specimens).

As a result of increasing subcritical crack growth with decreasing strain rate, the fracture toughness values obtained from the maximum load are less than K_{IC}, as shown in Fig. 4.39. Thus for a true measurement of the K_{IC} value of a material with a given specimen geometry, the strain rate employed must be that which leads to unstable fracture. This condition can be established only by AE monitoring; that is, when no emission occurs prior to failure, a linear load-displacement curve is an inadequate criterion. The strain rate corresponding to such a condition is the optimum for K_{IC} measurement.

The extent of subcritical crack growth may be estimated by measuring the emission prior to failure, as shown in Section 4.3.1. These emissions are distinguished by their low rate and low energy characteristics. The increase in the number of ring-down and event counts prior to failure, and the increase in the b-value with decreasing strain rate indicate an increase in the extent of sub-critical crack growth as strain rate decreases, ie subcritical crack growth is mainly responsible for reduced K_{IC} values at low cross-head speeds. No indication of other fracture modes, such as plastic deformation or twinning, was observed on fracture surfaces of specimens tested at room temperature using different strain rates. The strain rate independence of P_s , i.e. the acoustic emission starting load, suggests that sub-critical crack growth occurs to an extent sufficient to produce detectable emissions, when this particular required load is reached regardless of the loading rate. Under defferent conditions, e.g. a more reactive environment, the load required for detectable emissions may be less than P_s observed for the present tests in air.

The extent of subcritical crack growth produced at strain rates less than the optimum can be estimated by considering the fact that the critical stress intensity factor of a material is independent of the test condition, but dependent on the fracture load, P_F, and the square root of the crack length at the point of failure, a_F, i.e.:

$$K_{IC} = A\, P_F (a_F)^{\frac{1}{2}} \qquad (4.7)$$

Therefore the specimen failing at a low strain rate, $\dot{\varepsilon}_i$, and having the failure load, P_{Fi}, must have an increased crack length of a_i, compared with the specimen failing in the absence of subcritical crack growth, and having a strain rate of $\dot{\varepsilon}_o$ and fracture load of P_{Fo}. From equation (4.7) K_{IC} is a material constant when:

$$P_{Fo}(a_o)^{\frac{1}{2}} = P_{Fi}(a_i)^{\frac{1}{2}} \tag{4.8}$$

where a_o is the initial crack length in the absence of subcritical crack growth.

From equations (4.5), (4.6) and (4.8) the following equation can be obtained:

$$\frac{\dot{\varepsilon}_o}{\dot{\varepsilon}_i} = \left(\frac{a_i}{a_o}\right)^{\frac{n+1}{2}} \tag{4.9}$$

which gives the extent of subcritical crack length, $a_s = a_i - a_o$, for a given material at a reduced strain rate.

The subcritical crack growth rate can be fitted to the following approximate relation[10]:

$$\frac{da_s}{dt} \propto K_I^n \tag{4.10}$$

For SENB specimens:

$$K_{Ii} = A\, P_i (a_i)^{\frac{1}{2}} \tag{4.11}$$

where A is a constant depending on the specimen geometry. Therefore:

$$\frac{da_s}{dt} \propto \left[P_i (a_i)^{\frac{1}{2}}\right]^n \tag{4.12}$$

The acoustic emission counts, N , increase linearly with increasing subcritical crack area (see Figs. 4.17-4.24) and for a constant thickness specimen with increasing subcritical length, i.e.:

$$N \propto a_s \tag{4.13}$$

If N_1 and N_2 are the AE total counts obtained at strain rates of $\dot{\varepsilon}_1'$ and $\dot{\varepsilon}_2'$, respectively, then from equation (4.13):

$$\frac{N_1}{N_2} = \frac{a_{s1}}{a_{s2}} \tag{4.14}$$

and from equation (4.12):

$$\frac{a_{s1}}{a_{s2}} = \left(\frac{P_1}{P_2}\right)^n \left(\frac{a_1}{a_2}\right)^{n/2} \frac{T_1}{T_2} \tag{4.15}$$

where T_1 and T_2 are the times taken for the crack to propagate to the lengths a_{s1} and a_{s2}, respectively. Since n in ceramics is much larger than 1, to a good approximation $n/2 \approx (n+1)/2$, and from equations (4.6), (4.9), (4.14) and (4.15):

$$\frac{N_1}{N_2} = \left(\frac{K_{I1}}{K_{I2}}\right)^n \left(\frac{\dot{\varepsilon}_2'}{\dot{\varepsilon}_1'}\right)\frac{T_1}{T_2} \tag{4.16}$$

Equation (4.16) gives the major factors influencing the acoustic response of a material with a given geometry. Thus in general the total acoustic emission counts can be shown as:

$$N = A(K_I)^n \left(\frac{T}{\dot{\varepsilon}'}\right) \tag{4.17}$$

where A is a constant depending on the specimen geometry, test environment (such as temperature), the physical and chemical characteristics of the material, and the acoustic emission measurement technique. For the count rate, equation (4.17) reduced to:

$$\frac{dN}{dt} = A(K_I)^n \frac{1}{\dot{\varepsilon}'} \tag{4.18}$$

and at constant strain rate equation (4.18) takes the form:

$$\frac{dN}{dt} = B\,K_I^{\,n} \tag{4.19}$$

Equation (4.19) provides a correlation between the acoustic emission data and the fracture toughness of the material. This equation is the same as that obtained by Dunegan et al[11] for ductile materials and used by Evans et al[10] for brittle materials.

4.3.5 The Influence of Initial Notch Length on Fracture Toughness and Acoustic Emission

The accurate measurement of K_{IC} is reported[82] to be limited to cases where the a/w ratio is within a certain limit for each test geometry. Using SENB specimens, a valid K_{IC} value can be obtained when $0.3 \leqslant a/w \leqslant 0.6$, but the recommended limit is $0.45 \leqslant a/w \leqslant 0.55$. The dependence of subcritical crack growth and acoustic response on notch length has not been previously investigated. This section deals with the study of the acoustic emission and the fracture toughness of SENB specimens having varied a/w ratios, all other factors such as strain rate, being kept constant.

Typical load-deflection and AE-deflection curves are shown in Fig. 4.44. They illustrate the effect of varying the notch length on the state of subcritical crack propagation and the generated acoustic emission. For specimens with a/w up to ≈ 0.5, a linear elastic condition existed and high rate emissions occurred at the point of failure. As deeper notches were used, the failure load decreased (Fig. 4.45), and stable crack propagation increased until for a notch ratio $a/w \approx 0.7$ it approached 100%. Although the instantaneous rate of emissions decreased, the total number of counts increased with increasing a/w, as shown in Fig. 4.46. The b-value in the amplitude distribution also increased with increasing values of a/w (see Fig. 4.47).

The load deflection curves and AE data indicate that as the a/w ratio increases the stiffness of the system is decreased and the extent of subcritical crack growth increases. However, the validity of AE data in the region of valid K_{IC} values (i.e. $0.3 \leqslant \frac{a}{w} \leqslant 0.6$) is important. The experimental data for the number of ring-down counts in this region had a mean value of 87×10^3 and a standard deviation of $\pm$ 58 x 10^3 where the value corresponding to a/w = 0.5 was $(83 \pm 20) \times 10^3$. The average of the experimental data for the number of events in the valid K_{IC} region was 726 ± 450 compared with the experimental value of 800 ± 220 obtained for a/w = 0.5. Such a comparison indicates that the variation of AE in the region of valid K_{IC} is further than the limit of experimental

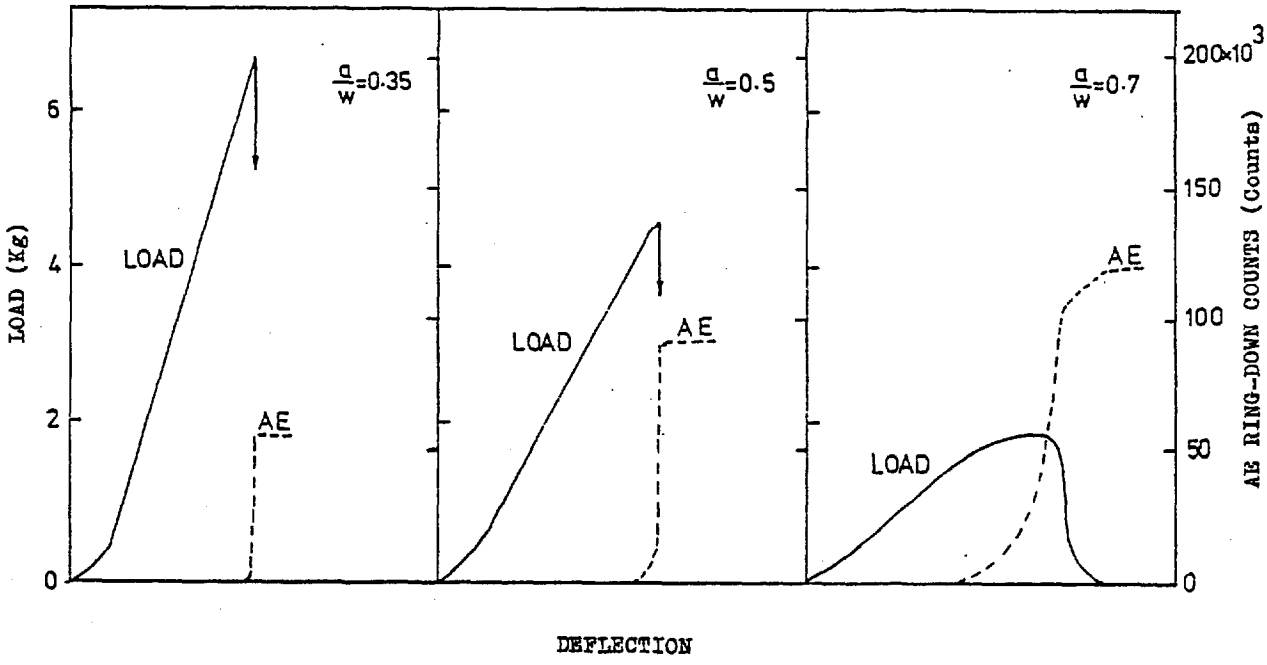


Fig.4.44. Load - deflection and AE ring-down counts-deflection curves obtained for SENB specimens of various initial notch length.

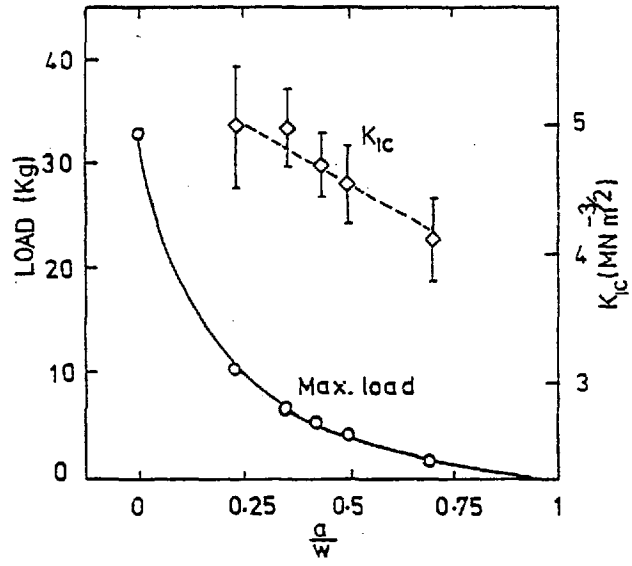


Fig.4.45. Fracture load and the apparent K_{1c} as a function of a/w, (SENB specimens).

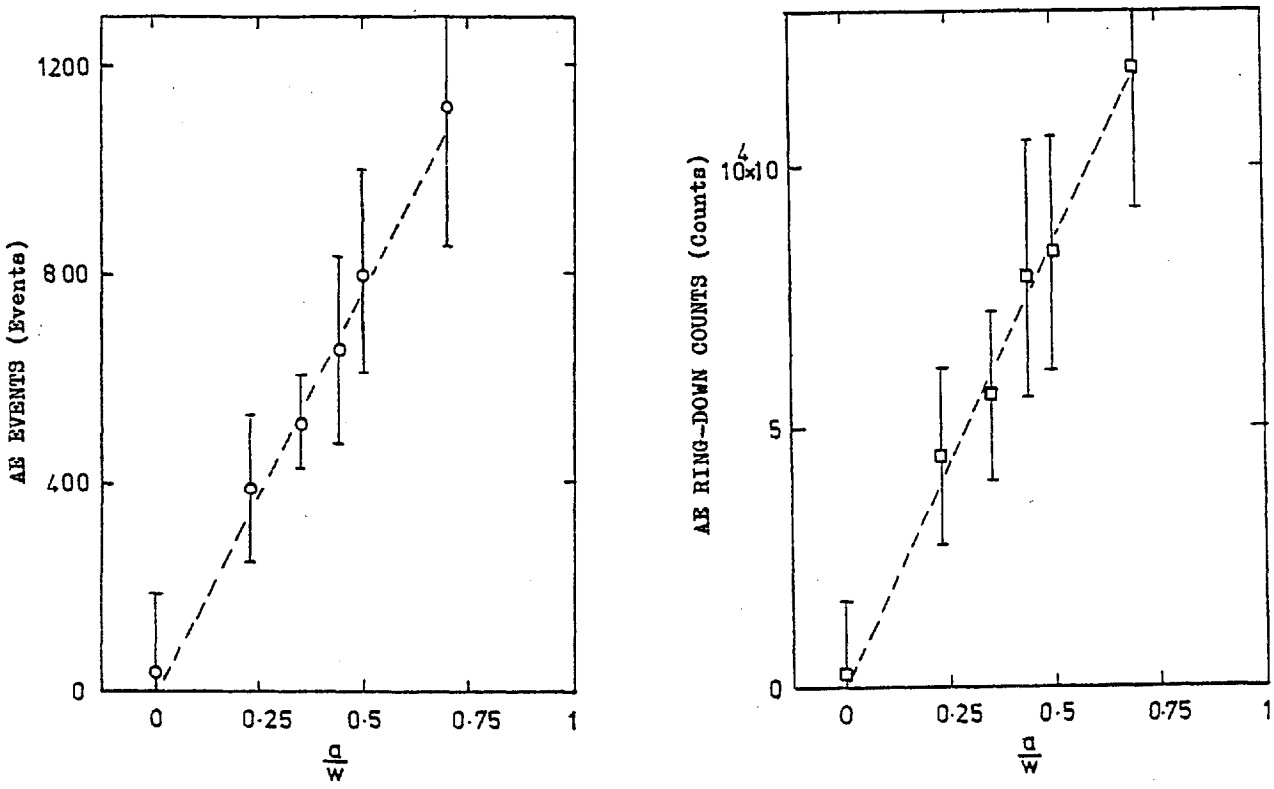


Fig.4.46. Acoustic response of SENB tests as a function of a/w.

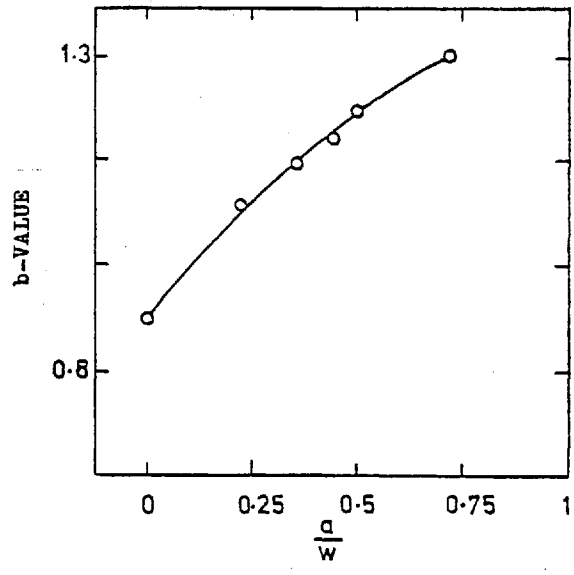


Fig.4.47. The b-value in the amplitude distribution as a function of a/w.

error. Thus the $0.3 \leqslant a/w \leqslant 0.6$ is not an accurate limit for valid AE determination. In contrast, the variation of AE data in the region $0.45 \leqslant a/w \leqslant 0.55$, which is recommended for accurate K_{IC} measurements, i.e. $N_{RT} = (85 \pm 18) \times 10^3$ and $N_{ET} = 780 \pm 170$, is not considerable and is within the standard deviation of experimental data for $a/w = 0.5$.

The apparent stress intensity factors calculated from the maximum loads, and illustrated in Fig. 4.45, indicate a decrease with increasing a/w. In the recommended region for a/w, the variation of K_{IC} is, however, less than the standard deviation of the results obtained for specimens of $a/w = 0.5$, the former value being 4.5 ± 0.11 $MNm^{-3/2}$ and the latter 4.5 ± 0.15 $MNm^{-3/2}$.

From the above results it would appear that the variation of initial notch length does not have a considerable effect on either AE response or the critical stress intensity factor as long as a/w is kept within the recommended limits. Therefore subsequent tests used SENB specimens having notch lengths within the range $0.45 \leqslant a/w \leqslant 0.55$.

4.4 THE MICROSTRUCTURAL DEPENDENCE OF MECHANICAL PROPERTIES AND ACOUSTIC RESPONSE OF ALUMINA

4.4.1 The Microstructural Dependence of Fracture Strength and AE

The modulus of rupture and AE data obtained for the varied alumina microstructures are summarised in Table 4.5. For all materials, the load-deflection curves were linear up to fracture, and failure occurred catastrophically at the maximum load. There was no emission prior to failure, but a high rate of emission was recorded at the fracture point.

Comparing the modulus of rupture values for FA0, FA4 and FA8, there is a general decrease in strength with increasing grain size and pore size. This is consistent with the modified Griffith

equation, in which the flaw size is the strength-determining factor. The acoustic emission counts for these aluminas increased as the materials became microstructurally coarser and more porous.

The improved strength of alumina B compared with FAO, both materials having a mean grain size of~4 μm, was mainly due to the reduced porosity of B. The total emissions were also greatly reduced in alumina B compared with FAO. Comparing alumina A with the coarser material B, the slight increase in strength observed for the latter was due to its increased density, although alumina A had a slightly finer microstructure. The acoustic response of the two materials was very similar since the coarser microstructure of B and the increased porosity in A were equally important in determining the acoustic response. Alumina C had reduced strength and increased emissions compared with A and B, due to the coarser grain structure and increased porosity.

A substantial increase in strength was observed when the hot-pressed alumina H was compared with the conventional air-sintered aluminas, because of the very fine microstructure and much reduced porosity of the hot-pressed material. As expected, the acoustic response of the hot-pressed alumina was significantly less than that of the air-sintered materials.

In the acoustic emission amplitude and pulse width distributions, for all aluminas, there were some events of high amplitude and large pulse width as well as the low amplitude and narrow pulse width events (Fig. 4.48). However, the number of events and ring-down counts decreased as the microstructure became finer and less porous. For coarse-grained, porous aluminas, the exponent b in the amplitude distribution power law, increased slightly, indicating that a larger proportion of low amplitude events was produced.

The low b-values for the modulus of rupture tests (0.55-0.70) compared with those from the SENB tests (0.94-1.18) at similar fast strain rates is consistent with the small amount of sub-critical crack growth that occurs in the rupture tests. The extensive sub-critical crack growth in the SENB tests results in many low energy emissions and hence high b-values.

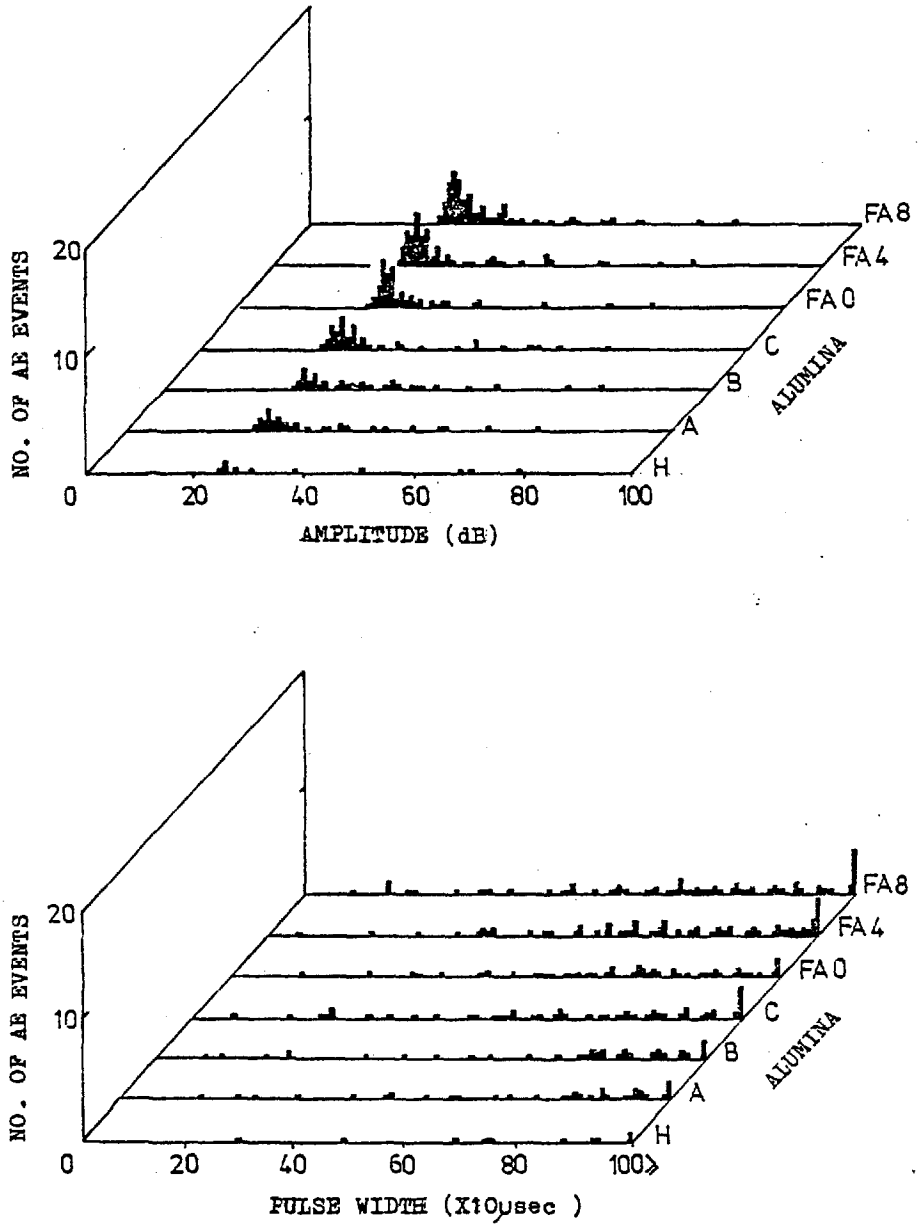


Fig.4.48. The amplitude and pulse width distributions obtained during strength measurements of different microstructural aluminas.

TABLE 4.5

Material	σ_f MNm^{-2}	Acoustic Emission			Porosity %	Max. pore size μm	Grain size		Max. pore area mm^2	Max. grain area mm^2	Flaw area mm^2
		Total counts N_{RT}	Total events N_{ET}	b exponent			max. μm	mean μm			
									$X10^{-3}$	$X10^{-3}$	$X10^{-3}$
FA0	340±20	2800 ± 400	45 ± 17	0.68	4.99	30	35	4	0.71	0.96	31.4
FA4	302±14	3950 ± 800	63 ± 15	0.72	6.06	45	50	10	1.59	1.96	38.0
FA8	295±18	3830 ± 510	67 ± 24	0.70	6.69	58	75	20	2.64	4.41	32.1
A	414±14	980 ± 185	25 ± 9	0.60	4.32	14	15	2.8	0.15	0.17	5.52
B	439±11	1010 ± 480	24 ± 12	0.65	3.02	17	20	3.8	0.22	0.31	4.97
C	270±17	1200 ± 510	47 ± 15	0.68	6.31	50	60	12	1.96	2.82	21.6
H	550±26	280 ± 94	11 ± 4	0.55	1.7	3	5	1.2	0.007	0.02	1.11

In assessing the dependence of fracture strength of a commercial alumina on microstructural features, such as the largest pore size, the maximum grain size, etc., an estimate of the failure initiating flaw size is important. As described in section 4.3.4, the area of the flaw at fracture can be caculated from the strength and toughness values using equation 4.3.b. The results are presented in table 4.5. A comparison of the fracture originating flaw area with the area of the largest pore or the largest grain (the latter are assumed to be areas of circles with diameters equal to the maximum pore size and the maximum grain size, respectively) indicates that the flaw size at fracture is considerably greater than the largest grain size and the largest pore size.

Assuming that no defects of the flaw size at failure existed in the material before testing, some subcritical crack growth must have occurred by fracture of ligaments connecting pores. Thus in commercial aluminas the failure originating site is a region of material comprising several pores and grains. These are situated in a such a way that they could link up, as discussed in section 4.3.4, at stresses less than that required to propagate a single flaw.

The fracture strength is not always a monotonic function of the fracture toughness, This was the case for the aluminas used in the present work, as shown in Fig.4.50. On the other hand there was a trend for the strength decreasing with the fracture initiating flaw size, as can be seen in Fig. 4.49. This indicates that the flaw size is a significant factor in determining the strength of alumina.

4.4.2 The Microstructural Dependence of Fracture Toughness and Acoustic Emission of Alumina

The fracture toughness and acoustic emission data obtained for SENB alumina specimens are presented in Table 4.6. The tests were performed on Capco-notched specimens in 3-point bending using a cross-head speed of 0.01 cm/min. The load-deflection curves were linear up to the point of failure and the critical stress intensity factor, K_{IC}, was measured from the fracture load, P_F. The strain

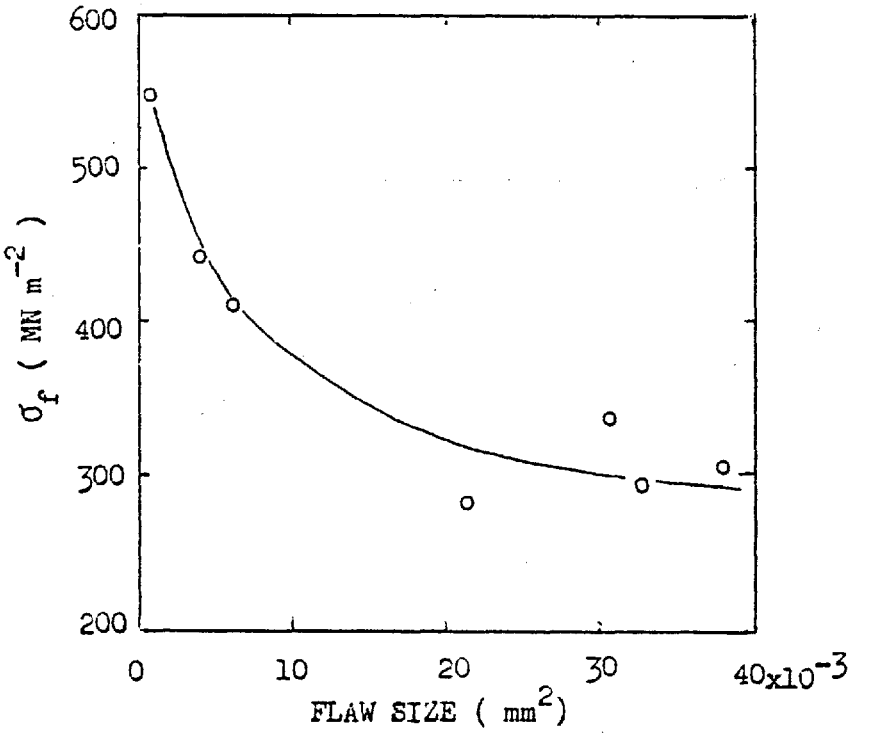


Fig.4.49. Fracture strength as a function of the fracture initiating flaw size.

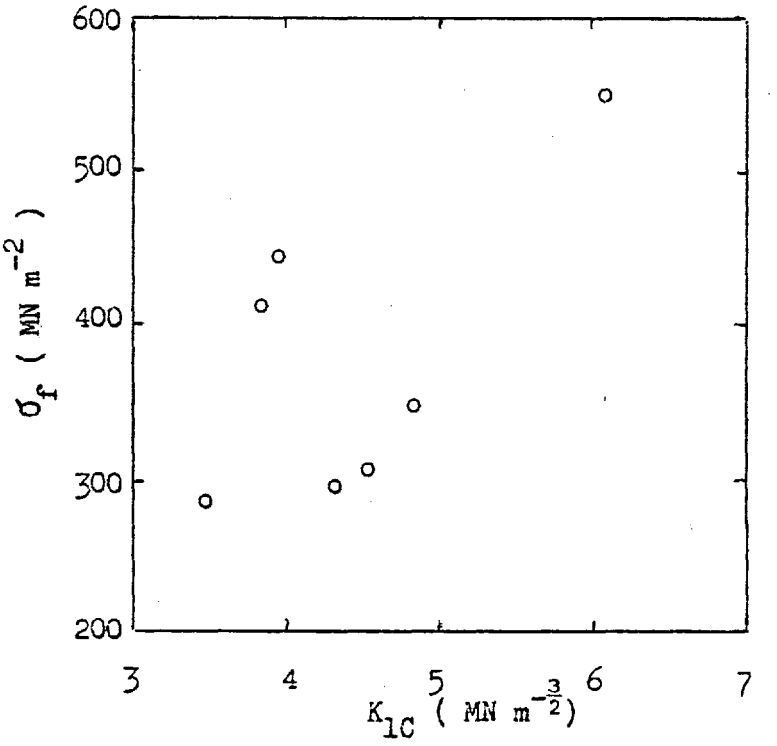


Fig.4.50. Fracture strength vs stress intensity factor for commercial aluminas.

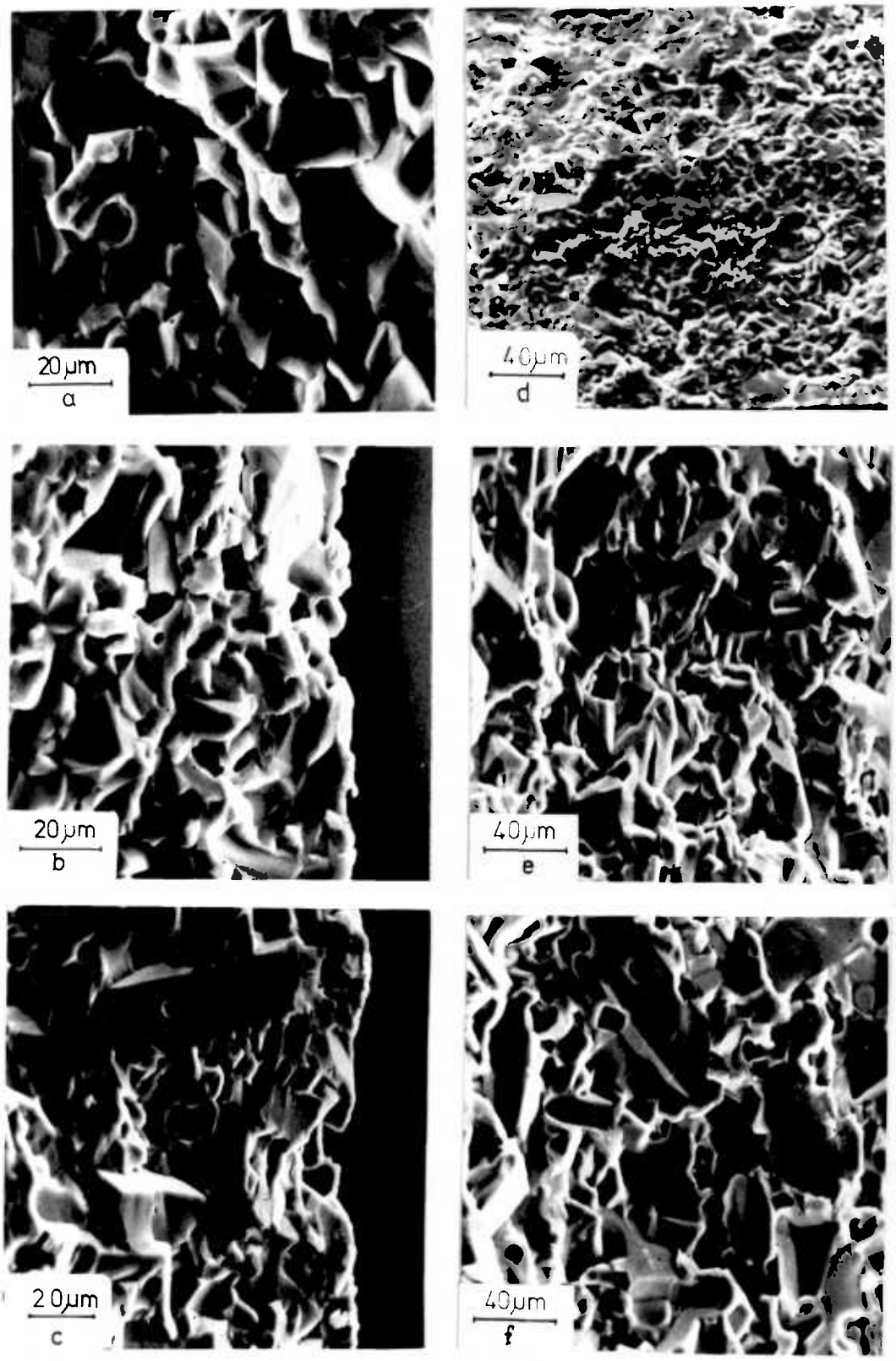


Fig. 4.52. Fracture faces of aluminas.
a - Modulus of rupture test, general view, FA 4.
b - " " " tension face, FA 0.
c - " " " " face, FA 8.
d - SENB test, general view, FA 0.
e - " " " " FA 4.
f - " " " " FA 8.

energy, G_{IC}, data was then calculated from the K_{IC} and Young's modulus for each material using the equation:

$$G_{IC} = 2\gamma_i = \frac{K_{IC}^2(1-\nu^2)}{E}$$

The value of Poisson's ratio used was $\nu = 0.22$[94].

The emissions started at loads P_s, less than the fracture load, the P_s/P_F ratio being dependent on the material. The K_{IC} and G_{IC} values were then corrected for subcritical crack growth. The subcritical crack length was determined from Fig. 4.29.

(i) Comparison of Aluminas FA1 to FA8 with standard FA0:

The standard FA0 alumina had a measured K_{IC} value of 4.85 ± 0.2 $MNm^{-3/2}$. As discussed in Section 4.2.1, the effect of refiring the FA0 material from one to eight times on the commercial schedule was to progressively coarsen the grain size (see Fig. 4.2) and to increase the maximum pore size and total porosity, as illustrated in Figs. 4.4 and 4.11. The as-measured fracture toughness results showed a decrease in K_{IC} as the grain size (number of refirings) increased. The K_{IC} values after correction for subcritical crack growth, showed consistent results with increasing grain size (porosity range 6.3 to 8%).

The decrease in the as-measured K_{IC} and G_{IC}, with increasing average grain size (Fig. 4.51), is in agreement with some previous work[1-3]. The inverse fracture toughness grain-size dependence is believed[2] to be partly due to the increase in the residual strain energy with grain size, caused by anisotropic thermal contractions during cooling from the firing temperature. In contrast, other work[4] indicates an increase in fracture toughness with increasing grain size, attributed to an increase in the extent of transgranular fracture. In the present work, scanning electron micrographs taken from fracture surfaces showed that fracture was predominantly intercrystalline with some transcrystalline failure occurring in isolated large grains of fine-grained aluminas, and increasing in extent in coarse-grained aluminas.

Fig. 4.52 shows a general view of the fracture surfaces of aluminas FA0, FA4 and FA8.

The AE results show a rapid increase in the number of counts due to subcritical crack growth up to a grain size of $\approx 7\,\mu m$, then decrease with the grain size (see Fig. 4.53). The b-exponent also shows a peak at grain size $\approx 7\,\mu m$ and then a fairly constant value of 1 for the remainder of the materials (Fig. 4.53). Thus it appears that there is not a unique correlation between the grain size and the number of emissions produced. When considering the total porosity versus the number of emissions (Fig. 4.54),a similar conclusion to that of grain size effect is obtained. The results, however, suggest that subcritical crack growth reaches a maximum in these aluminas at around $7\,\mu m$ grain size. Therefore probably other microstructural variables are involved in determining the extent of the subcritical crack, and thus AE.

The size of the pores, for example, is of considerable importance, as observed by Nadeau[95] for silicon carbide. Since the AE in alumina is produced during microcracking and subcritical crack growth, the interaction of the growing crack with flaws is one of the determining processes in AE. Flaws can be pores or large grains which pin the crack by blunting it and the local stresses increase before breakaway can occur. At breakaway the crack moves forward locally at various speeds, and sweeps surfaces of different areas. The speed of the crack determines the emission rate[95], and the area covered, the emission amplitude[95]. Thus a breakaway could result in a pulse of acoustic emission. The high number of emissions of various rates and amplitudes generated during the fracture of alumina, indicate that the fracture process in this material involves many small breakaways. The number of breakaways and thus the number of emissions is directly related to the number of flaws which could arrest the moving crack.

In the effect of pore size, Nadeau indicates that pores are strong pinning points but they produce acoustic emission only when they are big enough to pin a significant length of the moving crack. On the basis of this theory, and with reference to the

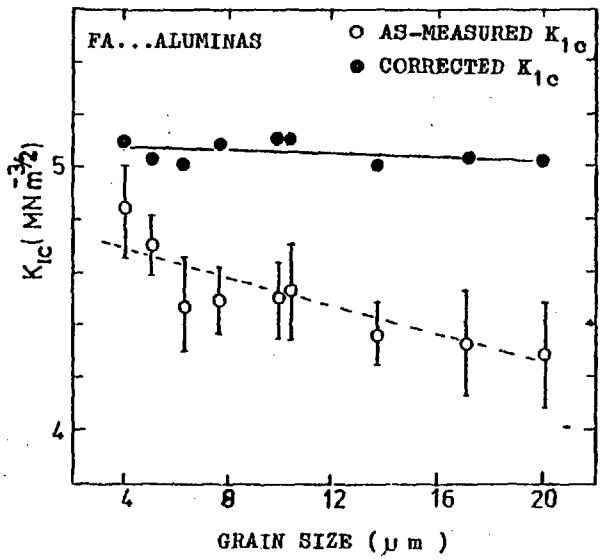


Fig.4.51. The grain size dependence of the as-measured and corrected K_{1c} ,(FA...).

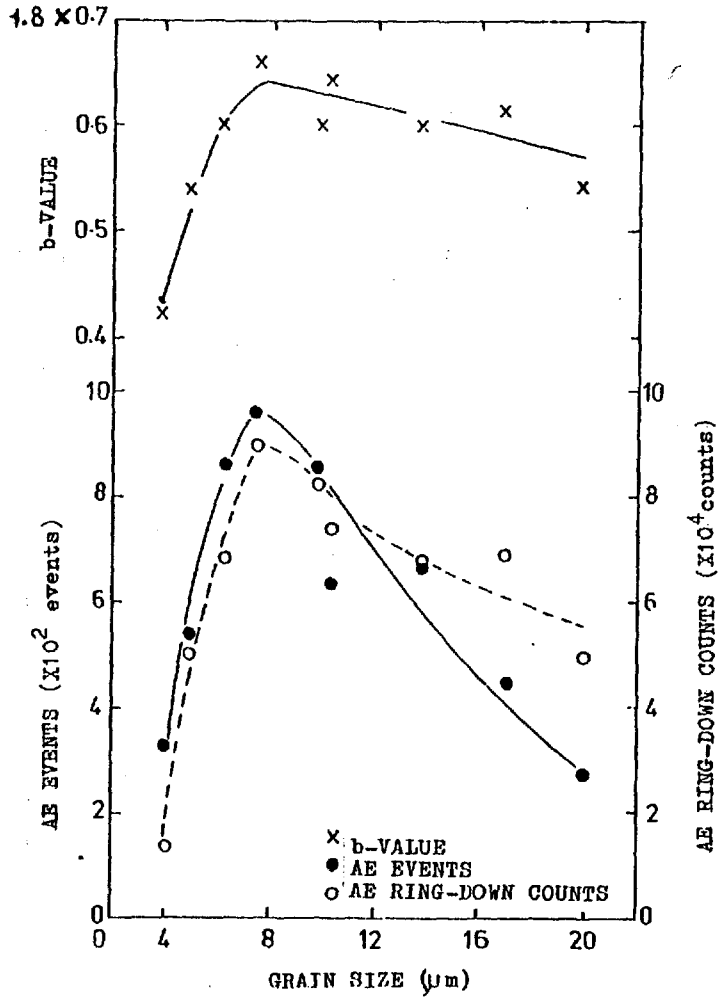


Fig.4.53. The grain size dependence of acoustic response of FA..aluminas.

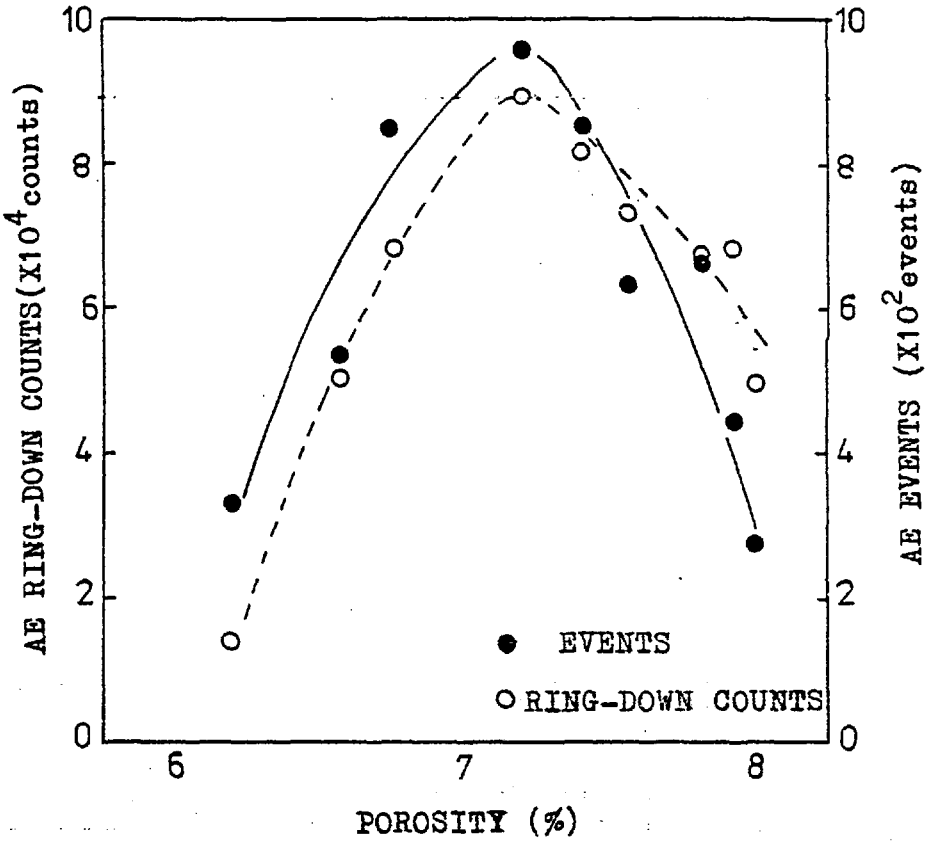


Fig.4.54. The acoustic response of FA..aluminas as a function of the total porosity.

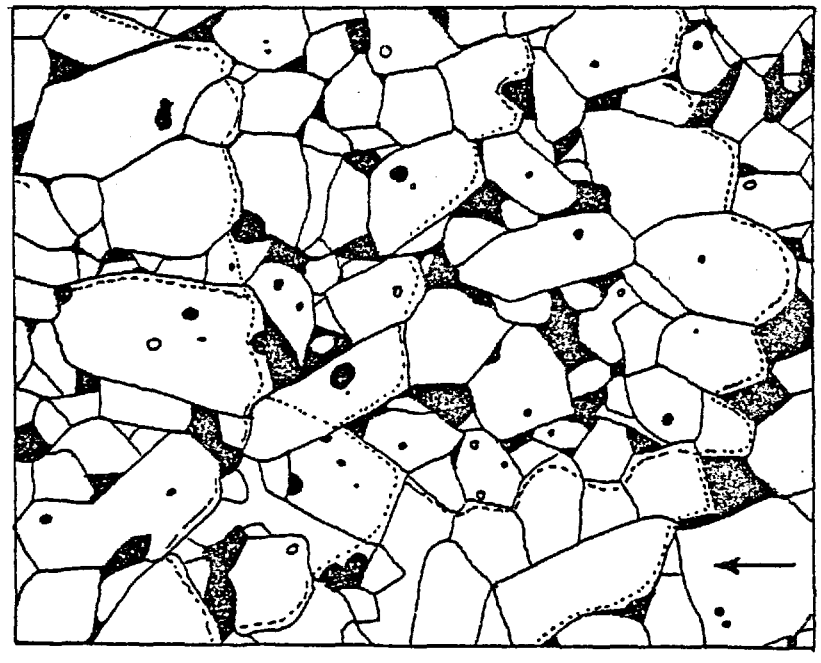


Fig.4.55. A schematic diagram showing the stages of crack movement.

micrographs and pore size histograms for FA0, FA4, and FA8 (Fig. 4.4) and the schematic Fig. 4.55, it can be said that in the fine-grained FA0 and FA1 aluminas, some large isolated pores and grains could arrest a short length of the crack and produce some events before the final breakaway took place. But there were also many small pores and grains that did not play a role in crack arrest. After two and three refirings, many more isolated large flaws were produced at the expense of small pores and grains. Thus the number of crack breakaways and arrests increased, and so also did the acoustic emissions. As the number of refiring schedules increased, large interconnected pores were produced, and thus the number of breakaways and the total emissions decreased.

From the above results and discussion it would appear that the microstructural variables influence the fracture toughness of alumina, and determine the extent to which subcritical crack growth occurs and thus the AE. The microstructure of aluminas FA0-FA8 influences the K_{IC} and AE as follows:

(a) The as-measured fracture toughness decreased with increasing porosity, whereas there was a tendency to a larger number of acoustic emissions, particularly as the number of large isolated flaws increased.

(b) An increase in grain size led to a decrease in the as-measured K_{IC} values; however, when the results were corrected for the subcritical crack length, more consistent K_{IC} values were obtained.

(ii) Comparison of A, B and C Aluminas:

The fracture toughness and acoustic emission data for aluminas A, B and C was discussed in Section 4.3.3, when the effect of notching technique was considered. In this section the results will be discussed in terms of the microstructural variables.

The as-measured fracture toughness of alumina A (K_{IC} = 3.82 ± 0.31) was slightly less than that of alumina B (K_{IC} =

3.95 ± 0.29) due to the slightly increased density of the latter. Alumina C had a reduced K_{IC} value compared with A and B, mainly because of its increased porosity and grain size. When the K_{IC} data was plotted versus porosity and grain size (see Figs. 4.56 and 4.57), the greater dependence appeared to be on porosity, the fracture toughness decreasing with increasing total porosity. In this respect these results are in agreement with those for the FA materials.

The acoustic response from aluminas A, B and C due to subcritical crack growth are shown in Table 4.6. Alumina B had higher counts compared with alumina A, mainly due to its increased number of large isolated flaws, arresting more of the crack. In comparison with both A and B, alumina C produced a higher number of emissions since the material contained significantly more large isolated pores and grains. Fig. 4.58 shows scanning electron micrographs taken from fracture surfaces of aluminas A, B and C. The fracture in these materials was also predominantly intercrystalline with some transcrystalline fracture, especially in large-grained alumina C.

(iii) Comparison of FA0, A and Hot-Pressed (H) Aluminas:

The fracture toughness for FA0 alumina was considerably higher than that for alumina A, although the latter had a finer microstructure and higher density. A possible reason for such behaviour may be due to the presence of the secondary phases in the less pure FA0 alumina. Due to the different thermal contraction coefficients of the phases[8,17], on cooling from the firing temperature, a micro-stress system is set up around the secondary phases, and microcracks may be produced. As a result, energy is absorbed in opening the microcracks and thus K_{IC} is increased.

Compared with the sintered aluminas, the hot-pressed alumina showed a considerable increase in fracture toughness. Such behaviour was to be expected from such a highly dense and fine-grained material. The K_{IC} value of 6.09 $MNm^{-3/2}$ was about 26% higher than that for FA0, and 60% higher than that for alumina A.

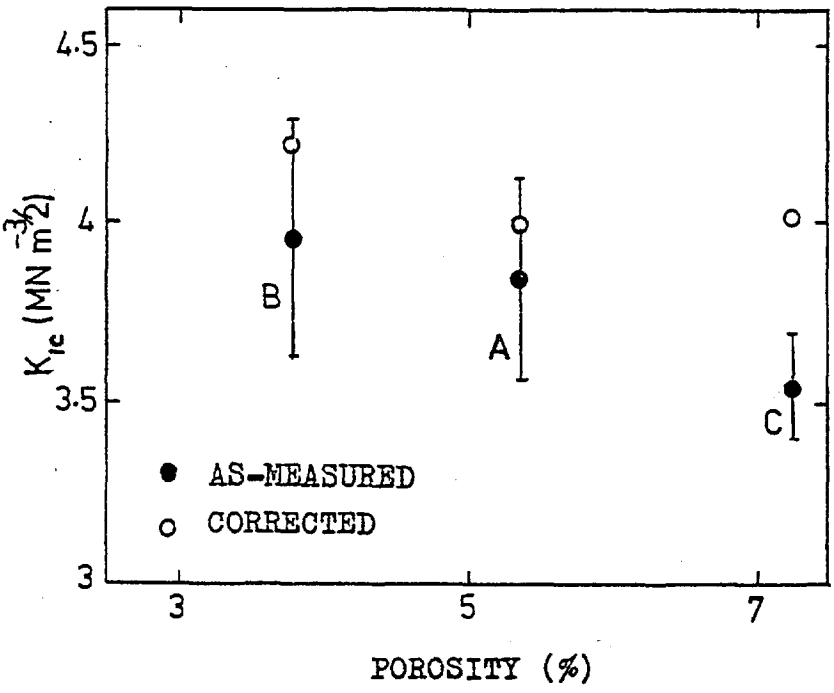


Fig.4.56. The as-measured and corrected K_{1c} values of aluminas A,B,and C as a function of the total porosity.

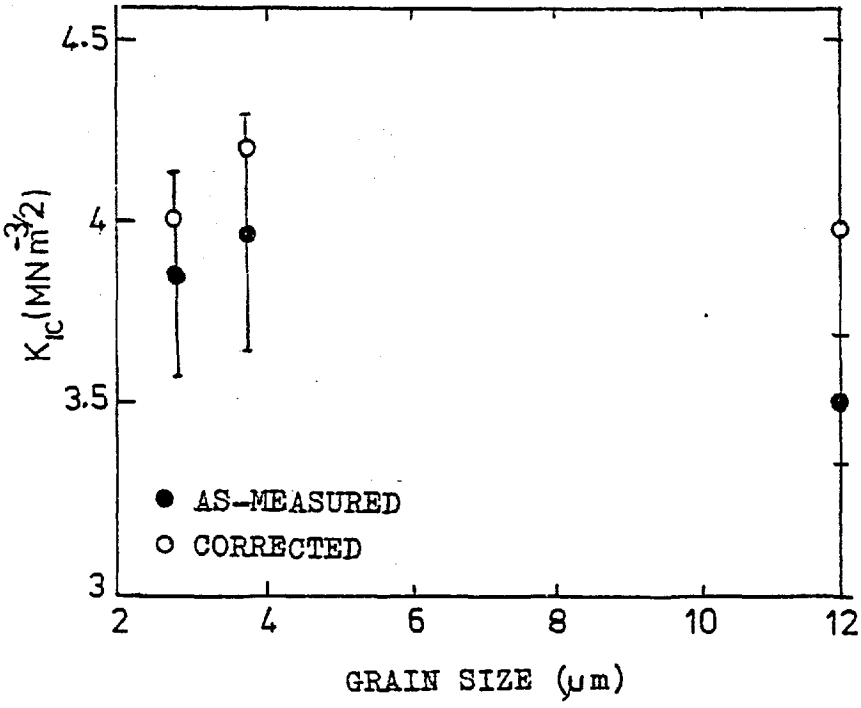


Fig.4.57. The as-measured and corrected K_{1c} values of aluminas A, B and C vs the mean grain size.

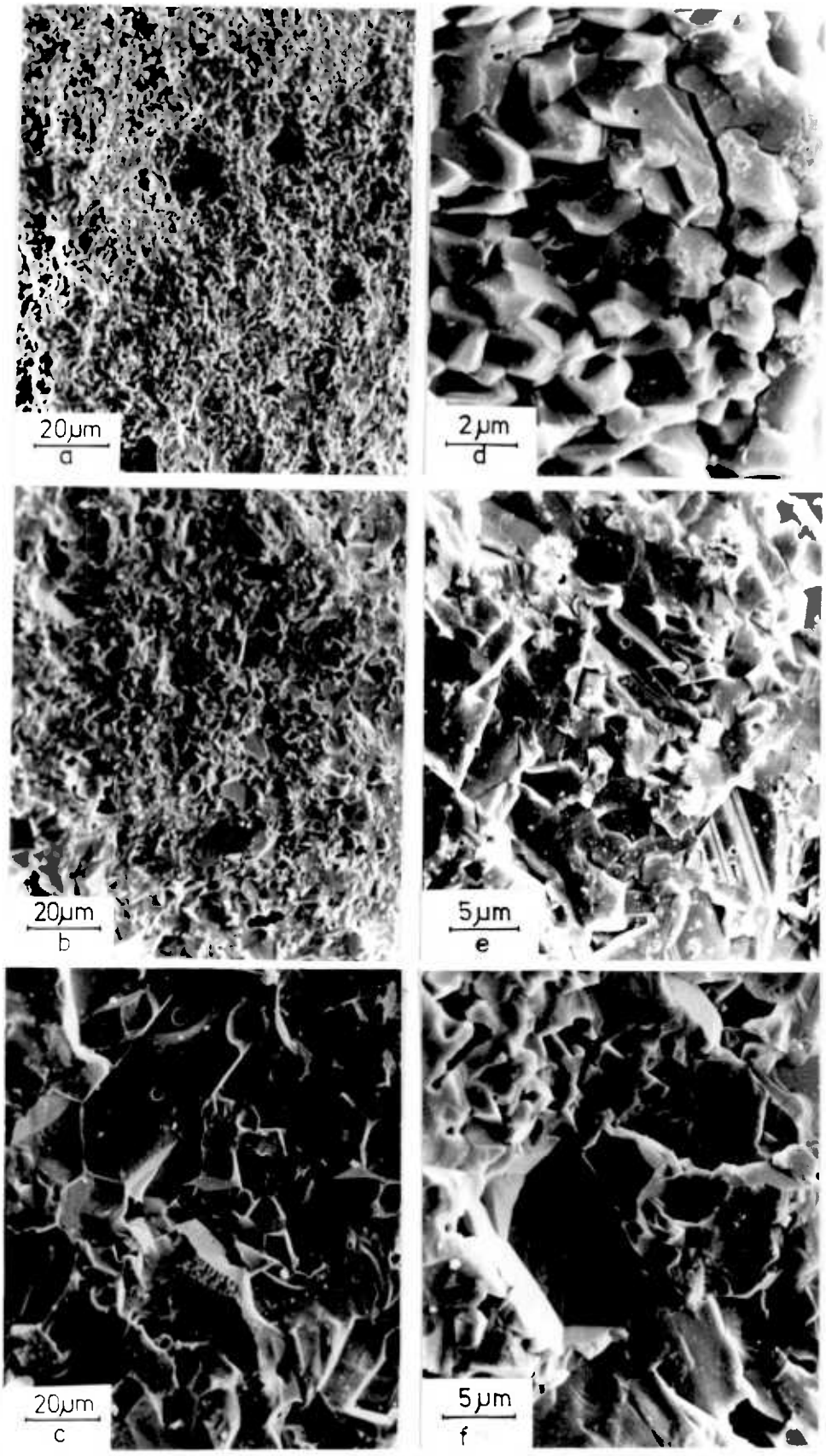


Fig. 4.58. Fracture faces of aluminas tested by SENB:
a - general view alumina (A),
b - " " " (B),
c - " " " (C),
d - crack near the surface (A),
e - intercrystalline & transcrystalline failure (B),
f - grain pulled out (C).

The acoustic response for these materials was consistent with their microstructure. The alumina FAO produced the largest values of N_{RT} and N_{ET}, since this material had the coarsest microstructure, the greatest amount of porosity, and a significant number of isolated large flaws. As the microstructure of the aluminas became finer and porosity decreased, along with the number of large isolated pores, the acoustic emission decreased in the order FAO $>$ A $>$ H. Fracture surfaces of alumina H (see Fig. 4.59) were smooth compared with aluminas FAO and A, and failure occurred in a predominantly intercrystalline manner.

From the above results and discussion, it would appear that there is no simple correlation between the values of critical stress intensity factor, K_{IC}, and the acoustic emission data (N_{RT}, N_{ET} and b). However, all the parameters showed a dependence on microstructural characteristics. In particular the acoustic emission was directly related to the amount of porosity and the number of isolated large pores and grains.

From the Griffith equilibrium criteria, brittle fracture occurs when the mechanical energy (stored energy + work of applied energy) of the system is balanced with the energy required to create new fracture surfaces. Thus the major part of the total energy released during brittle fracture is the surface energy, γ_i. Some energy is also converted into heat and acoustic emission.

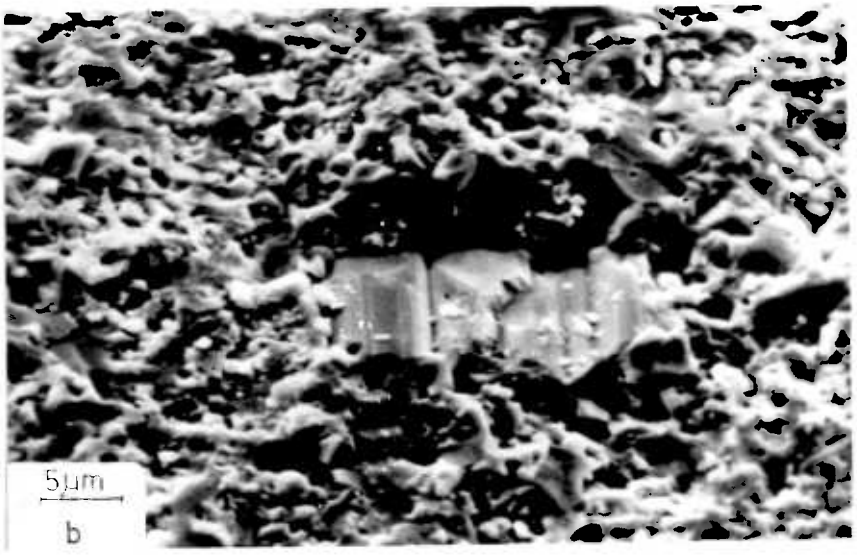
The energy of an AE signal can be obtained from:

$$\mathcal{E} = \frac{1}{R} \int_0^\infty V^2 \, dt \qquad (4.20)$$

where V is the time-dependent amplitude and R is the proportionality constant. In discrete form, the above equation becomes:

$$\mathcal{E} = \frac{1}{R} \sum_i^m V_i^2 \, \Delta t \qquad (4.21)$$

where V_i is the amplitude (voltage) of each signal and Δt is the time interval. Equation (4.21) was used for the measurement of the stress wave energy at the transducer, using the amplitude and pulse



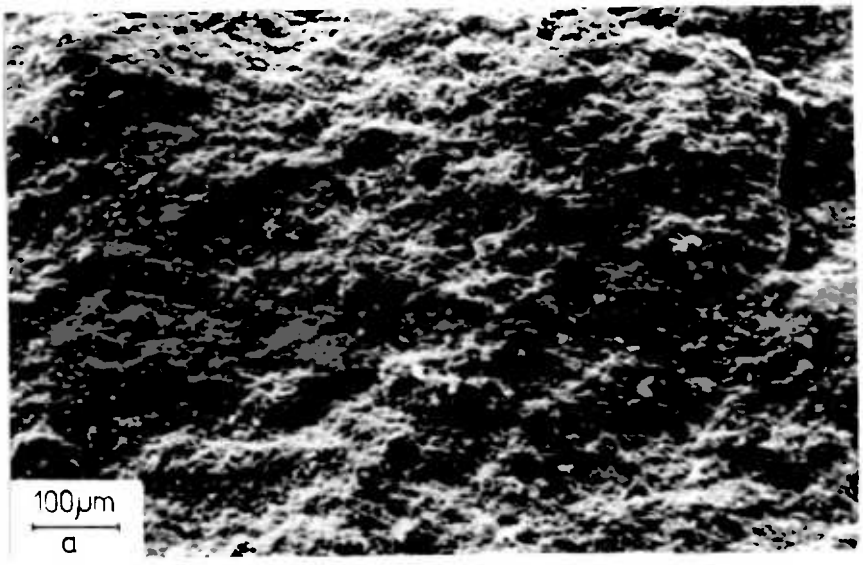


Fig. 4.59 SEM showing the fracture faces of:
a - hot-pressed alumina,
b - secondary cracking in $Al_2O_3ZrO_2$

width distribution histograms obtained for various aluminas. The total acoustic energy is equal to:

$$\mathcal{E}_T = A \sum_{i=24}^{100} n_i V_i^2 t$$

where V_i is the output voltage of the transducer, which can be calculated from the amplitude (in dB) of the i^{th} slot in the amplitude distribution histogram. n_i is the number of emissions counted by the slot i, t is the average pulse width, and A is the proportionality constant.

In amplitude distribution histograms, the peak amplitudes of AE bursts exceeding the threshold level (24 dB) are presented on a logarithmic scale (i.e. in dB), as slots of 1 dB steps, up to 100 dB. Thus, i varies from 24 to 100. The amplitude of slot i in dB was converted to the output voltage of the transducer using the specifications given for the 921 amplitude detector[86]. For a 40 dB pre-amplifier, 20 dB in amplitude distribution corresponds to 10 μvolts output voltage of the transducer, 40 dB to 100 μV, 60 dB to 1 mV, 80 dB to 10 mV and 100 dB to 100 mV. The value of t was obtained from the pulse width histograms in which the threshold crossing time of emissions (pulse width) is classified from 0 to 10^3 μsec in 10 μsec steps. The equation:

$$t = \frac{1}{N} \sum_{j=0}^{100} n_j t_j \qquad (4.21)$$

was used for the average pulse width measurements, where n_j is the number of emissions counted by the j^{th} slot corresponding to the pulse width of t_j in the pulse width distribution histogram, and N is the total number of emissions.

The link between the stress wave (mechanical) energy given to the transducer and the energy of the electronic pulse generated was established by dropping a small steel ball of mass m onto the transducer from height h, and recording the generated amplitude V, and duration t. Assuming that all mechanical energy is transferred to the transducer, the proportionality constant between the mechanical energy, E = mgh. and the converted electric

TABLE 4.6

Fabrication	Code Number	P_s/P_F	Fracture Toughness (measured)		Acoustic Emission			
			K_{IC} $MNm^{-3/2}$	$G_{IC}=2\gamma_i$ Jm^{-2}	N_{RT} $x10^2$	N_{ET}	b-value	E_{AE} Jm^{-2}
Sintered Al_2O_3 (Smiths Industries) production.	FA0	0.96	4.85 ± 0.2	66.5	140 ± 84	100 ± 32	1.02	0.45
	FA1	0.9	4.72 ± 0.11	63.9	502 ± 125	535 ± 115	1.05	2.3
	FA2	0.88	4.47 ± 0.18	57.5	680 ± 205	655 ± 110	1.11	2.7
	FA3	0.81	4.49 ± 0.12	58.9	880 ± 240	890 ± 250	1.24	3.16
	FA4	0.84	4.52 ± 0.15	60.0	820 ± 250	790 ± 110	1.12	3.02
	FA5	0.84	4.52 ± 0.08	60.4	740 ± 130	803 ± 120	1.20	3.11
	FA6	0.845	4.37 ± 0.10	57.7	675 ± 105	705 ± 95	1.13	2.63
	FA7	0.85	4.34 ± 0.06	57.2	690 ± 89	695 ± 91	1.14	2.5
	FA8	0.85	4.28 ± 0.12	55.1	500 ± 150	490 ± 105	1.00	1.83
Sintered Al_2O_3 (Anderman Ltd.) production	A	0.94	3.82 ± 0.31	40.4	27 ± 8	33 ± 15	0.94	0.16
	B	0.93	3.95 ± 0.29	41.3	46 ± 9	110 ± 35	1.02	0.51
	C	0.80	3.51 ± 0.18	36.6	125 ± 30	215 ± 53	1.18	0.06
Hot-pressed	H	0.98	6.09 ± 0.67	93.5	14.6 ± 6	30 ± 16	0.74	0.16

energy, $E = V^2t$, was established, which is:

$$1(\text{volts}^2\text{sec}) = 0.375 \times 10^3 \text{ Joules.}$$

The stress wave energy values at the transducer obtained by this method are shown in column 9 of Table 4.6. The released fracture energy is proportional to the surface energy, γ_i.

Comparing the γ_i data with the results obtained for the stress wave energy for each alumina, it can be seen that although the acoustic emission is part of the released fracture energy, it has no direct proportionality to the amount of released energy. In fact, the above approximate measurements showed that the detected acoustic energy is inversely proportional to the fracture surface energy.

4.4.3 The Influence of Second-Phase Dispersions in Alumina

The fracture toughness of alumina can be significantly increased by a dispersion of ZrO_2 particles in the alumina matrix[17]. The toughening mechanism is considered to be dependent on the interaction of the crack front with pre-existing microcracks. The microcracks occur in the alumina matrix due to the smaller coefficient of thermal expansion of ZrO_2 compared with alumina. This section discusses the fracture toughness and AE of $Al_2O_3.ZrO_2$ composites containing different volume fractions of ZrO_2. Both Capco- and Maco-notched specimens were used to investigate the interaction of microcracks produced during diamond sawing with those inherent in the material.

SENB specimens of the hot-pressed two-phase $Al_2O_3.ZrO_2$ composites with 12, 15 and 18 volume % of ZrO_2 were tested in 3-point bending using a cross-head speed of 0.01 cm/min and the results were compared with those of hot-pressed alumina H. The load curves were linear up to the point of catastrophic failure, P_F, and the K_{IC} values were measured from P_F. The emissions started at load P_s, prior to the fracture load, and the emission rate increased to a high rate at fracture.

The K_{IC} values for the composites are plotted versus volume fraction of ZrO_2 in Fig. 4.60. The K_{IC} curves exhibit a maximum before decreasing with increasing volume fraction of ZrO_2. The increased K_{IC} of the 12 volume % composite compared to the value for Al_2O_3 can be explained on the basis of energy absorption mechanisms. The absorption processes are assumed to be microcrack opening, subcritical crack propagation, and crack branching, as suggested by Claussen[17] in his studies of similar materials. The density of microcracks increases with increasing volume fraction of ZrO_2, and the toughness increases. At volume fractions beyond the maximum, the microcracks join up between the particles, thus decreasing K_{IC}.

Although a similar trend was observed for the K_{IC} data of Capco- and Maco-notched specimens, the results for the latter were slightly higher in the case of the pure hot-pressed alumina and very similar for the 12% vol ZrO_2 composite. However, this trend was reversed at high ZrO_2 contents and the rate of decrease in K_{IC} from the maximum was more rapid for the Maco-notched specimens compared with those notched with the Capco. Earlier it was shown (Section 4.3.3) that the diamond machining of a blunt notch produces a damaged zone in the notch root. In sintered aluminas of 3 to 12 μm grain size, the extent of damage was shown to be higher in Maco-notched specimens compared with Capco-notched, and the extent of damage increasing with grain size increase. Since the pure hot-pressed and $Al_2O_3.ZrO_2$ materials were of very small grain size ($\sim$ 2 μm) the machining damage caused by the two techniques was small and similar in extent. Thus the slightly increased K_{IC} values for the Maco-notched specimens of pure and 12% ZrO_2 aluminas resulted from their increased notch root radius. As the volume fraction of ZrO_2 increased, so did the amount of microcracks associated with the particles, and hence the effect of notching damage became more pronounced. This resulted in the previously observed trend with the Maco-notched specimens having higher K_{IC} values than the Capco-notched specimens. The high proportion of large microcracks also accounted for the fall in K_{IC} with increasing volume fraction of ZrO_2 (Fig. 4.60).

The acoustic emission results followed the same trend with volume fraction of ZrO_2 as the fracture toughness values (see Fig. 4.61). The pure alumina H was acoustically very quiet but the emission increased with increasing volume fraction of ZrO_2 to a maximum at 12 volume %. As the volume fraction of ZrO_2 was increased further, the AE response of the material decreased. The AE results of the Maco-notched specimens showed a reduced number of ring-down counts and events for materials with up to 12% ZrO_2 and higher values for the rest of the composites, compared with the results of Capco-notched specimens. The emissions were attributed to microcrack opening and subcritical crack growth, the extent of which varies not only with the volume fraction of ZrO_2, but also with the specimen notch. The acoustic emission results indicate that the increased N_{RT} and N_{ET} for the 12 volume % composite compared with pure alumina is also a result of extensive microcrack extension. At volume fractions beyond 12 vol. %, some microcracks are already connected, thus the AE is decreased.

In fact, the extent of subcritical crack growth must be added to the initial notch length for true K_{IC} measurements. The AE data could provide such a correction, as discussed in Section 4.3.1 if the subcritical crack length-AE curves such as those shown in Figs. 4.17-4.24 were available. Although such curves are not available for quantitative analysis of the fracture toughness results, nevertheless the emission data suggests that if such correction were to be made the maximum K_{IC} would increase to an even more distinct value, and the data from Capco- and Maco-notched specimens would be more similar.

Direct evidence for the existence of microcracks in the $Al_2O_3.ZrO_2$ composites is shown by the scanning electron micrographs taken from the carefully polished and etched surfaces of the composites. Fig. 4.62 illustrates microcracks in an unstressed region running from ZrO_2 particles into Al_2O_3 matrix. Some microcracks were also observed within the ZrO_2 grains. Scanning electron micrographs taken from the fracture surface of the composite revealed that fracture in $Al_2O_3.ZrO_2$ occurred mainly by separation at the grain boundaries, as illustrated in Fig. 4.63. However, trans-crystalline fracture was also evident in larger grains.

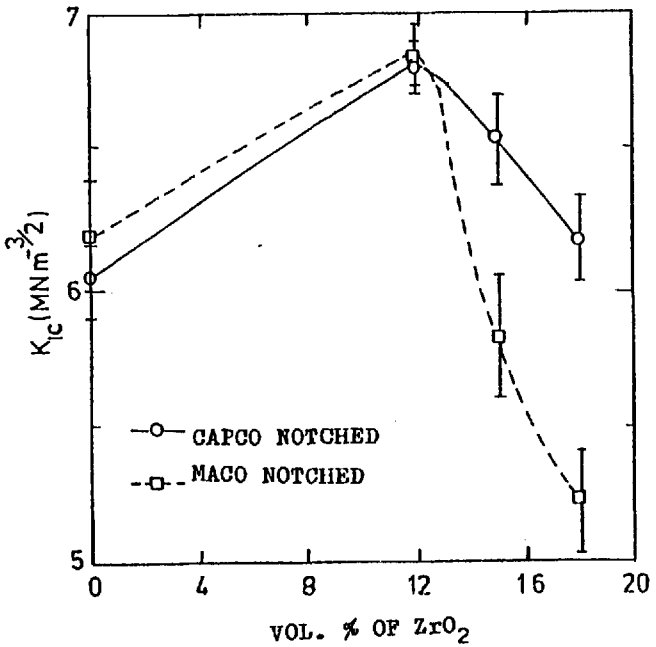


Fig.4.60. Fracture toughness as a function of volume fraction ZrO_2.

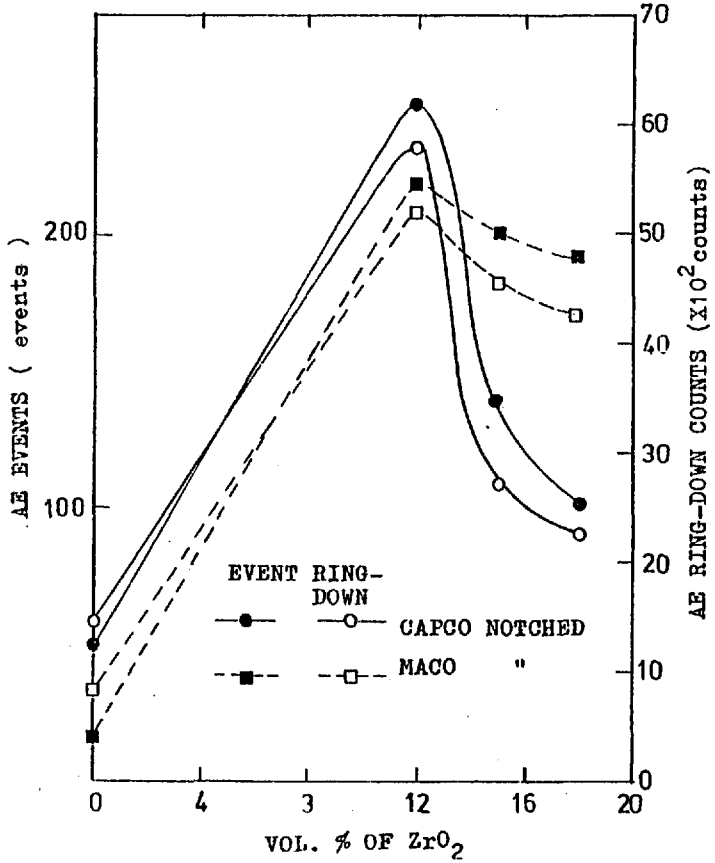


Fig.4.61. Acoustic emission as a function of volume fraction ZrO_2.

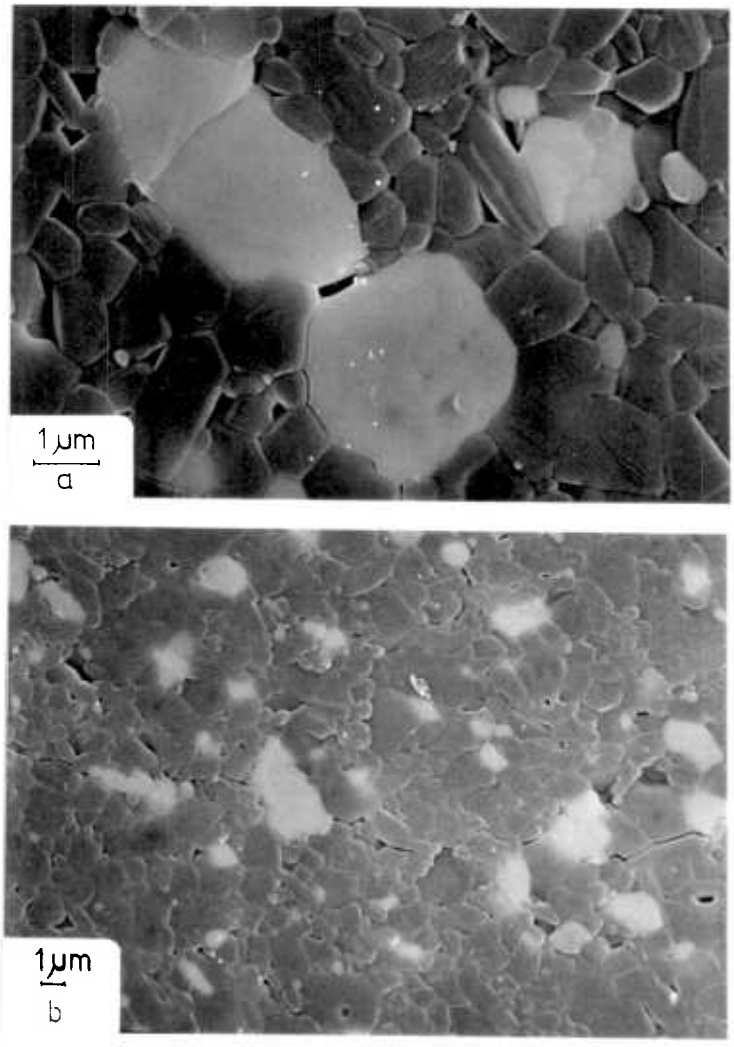


Fig. 4.62. SEM from polished & thermally etched faces of $Al_2O_3 Zr\,O_2$, showing pre-existing microcracks:
a - around ZrO_2 grains,
b - inter-connected microcracks.

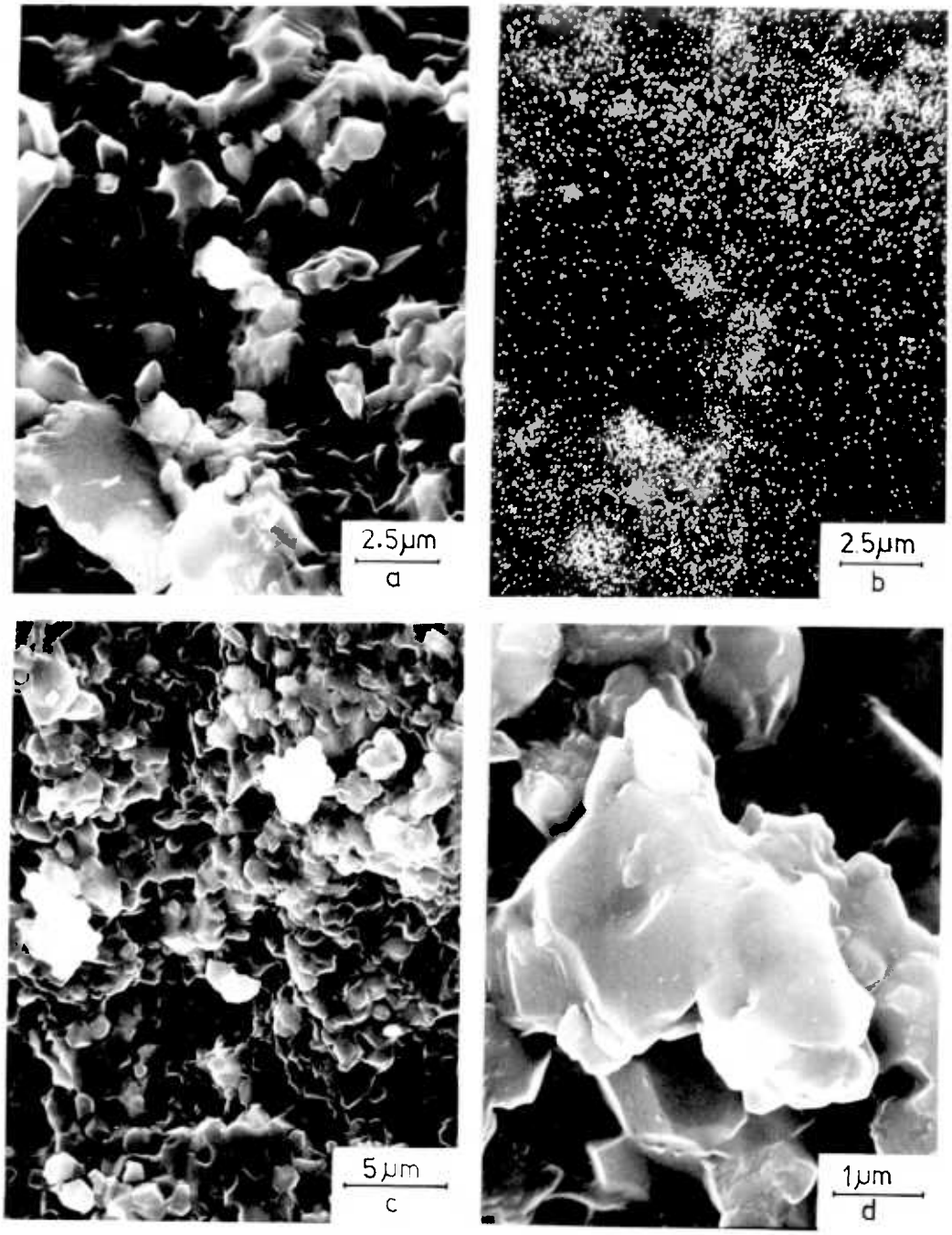


Fig. 4.63. SEM, showing the fracture facesof $Al_2O_3ZrO_2$:
a - general view,
b - x-ray map of (a), for Zr.
c - intergranular fracture,
d - fracture of ZrO_2 grains.

4.5 CORRELATION OF FRACTURE TOUGHNESS WITH AE

The correlation of fracture toughness and the acoustic emission data has always been considered as a major task in acoustic emission study of materials. The interesting area for application lies in failure prediction and the characterization of microscopic processes occurring in materials during deformation and fracture. Some progress has been made in this respect for ductile materials as discussed in Section 2.3.8, but very little work has been done in ceramics. In this section the correlation of AE with impending failure toughness values of alumina is discussed using SENB, DT and DCB specimens subjected to monotonically increasing loads.

The results are shown in Fig. 4.64, which demonstrate that the acoustic emission ring-down count rate, dN/dt, in alumina specimens containing a crack, is related to the applied stress intensity factor, K_I, in the following way:

$$\frac{dN}{dt} = B K_I^n \qquad (4.24)$$

where n and B are constants. This equation has already been obtained theoretically in Section 4.3.4, indicating the agreement of experimental results with basic theoretical solutions. These results illustrate that the exponent n and the B constant in the above relationship are dependent upon the material, its structural variables and the geometry of the cracked body. These constants also vary with the rate of load application and variables in detection equipment, as shown in Section 4.3.4.

In fracture toughness tests on steels[11,67], and in the first stage of stress corrosion cracking of porcelain in water[65], the exponent n was found to be ~5 and ~30 respectively. As shown by Fig. 4.64, the general equation (4.24) was obeyed for alumina which had the average exponent n = 18 in SENB, n = 17 in DT, and N = 14 in DCB specimens. Furthermore, the n values also varied slightly with the structural variables of alumina, such as grain size.

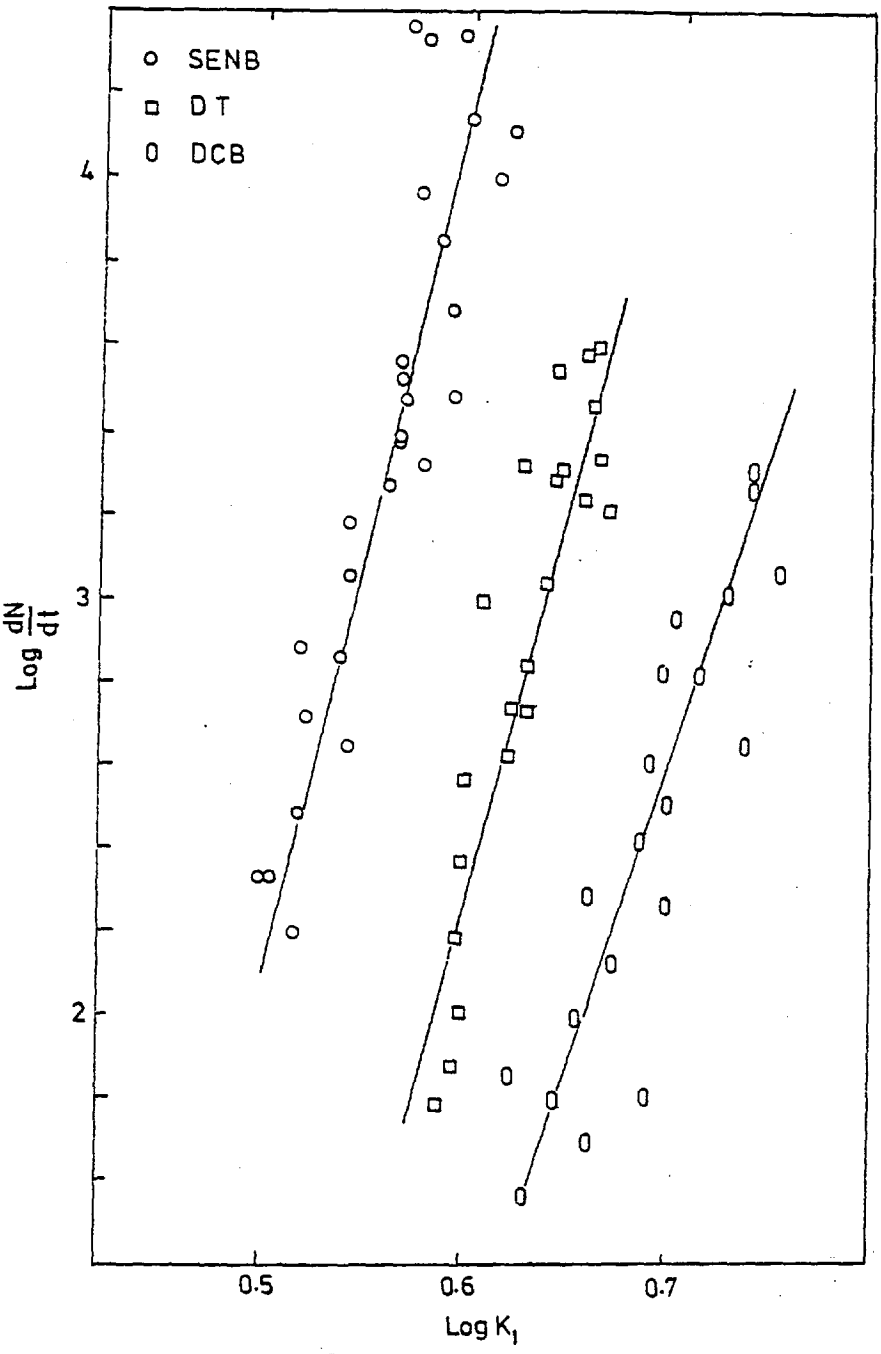


Fig.4.64. The correlation of AE with the fracture toughness of alumina for SENB, DT, AND DCB test geometries.

The consensus of opinion in the field[70-73] is that the sources of acoustic emissions in a cracked crystalline solid are the newly formed plastic zone (only in ductile materials), subcritical crack growth and the final catastrophic extension of the crack. Thus the acoustic emission is capable of detecting processes occurring prior to failure, and it has the potential of an in-service surveillance technique which may be used for failure prediction and prevention of catastrophic failure. In this respect the K_I dependence of dN/dt can often be used to identify the primary processes occurring prior to failure. A knowledge of the origin of the acoustic emission is not needed, of course, for the practical application to failure prediction. Once it has been established that dN/dt is uniquely related to K_I, then it is merely required to measure the acoustic emission rate associated with crack propagation to obtain an estimate of the stress intensity factor of the component compared with its critical value, and perhaps predict the remaining lifetime[49].

There are clearly many practical difficulties associated with isolating the acoustic emission due to crack growth from that of other sources, but the latter will not be discussed in this work. However, it must be pointed out that the suitability of the technique as an effective failure indicator must be established for each material. In the case of ductile materials, where n is relatively low, the first indications of the stress waves appear, normally, before the yield point where there is a distinct period before final failure and the structure can be unloaded. In the case of ceramics, where n is large, the effectiveness of acoustic emission for failure prediction is limited and depends largely on the rate of loading and the extent of subcritical crack growth that can be tolerated before final catastrophic failure.

4.6 FRACTURE TOUGHNESS AND AE AT ELEVATED TEMPERATURES

Some measure of the mechanical behaviour of alumina at elevated temperature has been obtained by means of three-point bending[21,89] and compression testing[21,90], but limited information[8,10] is available on the temperature dependence of

fracture toughness. Some AE data has been reported for temperatures up to $\simeq 400^{\circ}C$[96], but the acoustic response of alumina at higher temperatures has not been investigated. This section is concerned with the fracture toughness testing of alumina at temperatures up to $1000^{\circ}C$ with concomittant monitoring of the acoustic emission.

Although the room temperature tests suggested that the DCB geometry is the least reliable test-piece for fracture toughness determination, the specimens showed a high acoustic response for a longer period of time compared with DT and SENB specimens. Furthermore, the DCB specimens could be fairly easily and conveniently mounted in the Instron, and sufficient crack growth control could be achieved with this geometry. These factors contributed to the DCB geometry being the most convenient for elevated temperature tests.

Some loss in sensitivity was inevitable when employing a wave guide for transferring the AE signals from the specimen to a remote transducer. Most of the attenuation occurred at the specimen-wave guide coupling and very little change in amplitude was observed when the signal travelled along the wave guide. However, a comparison of room temperature DCB data with and without a wave guide (Figure 4.68 and Figure 4.69) showed that, although the wave guide reduced N_{ET} and N_{RT}, the stress P_s for the onset of emissions, and the distributions, were only marginally affected.

The oxidation of the wave guide and expansion of the whole system at elevated temperatures were the major sources of emissions. Fig. 4.65 shows the acoustic response of the wave guide during the first heating-cooling cycle. The rate of emissions was high only when the temperature was changed, whereas, at constant temperature, the emission rate was almost zero. The emission rate was observed to be much higher during cooling from elevated temperatures to room temperature, and was probably due to cracking of the oxidised layer during contraction of the wave guide. The rate of oxidation decreased as the number of heating-cooling cycles increased, and thus the emission rate decreased significantly after three heating cycles. Fig. 4.66 shows the acoustic response of the testing system over the range employed before any load was applied. There was a high rate of

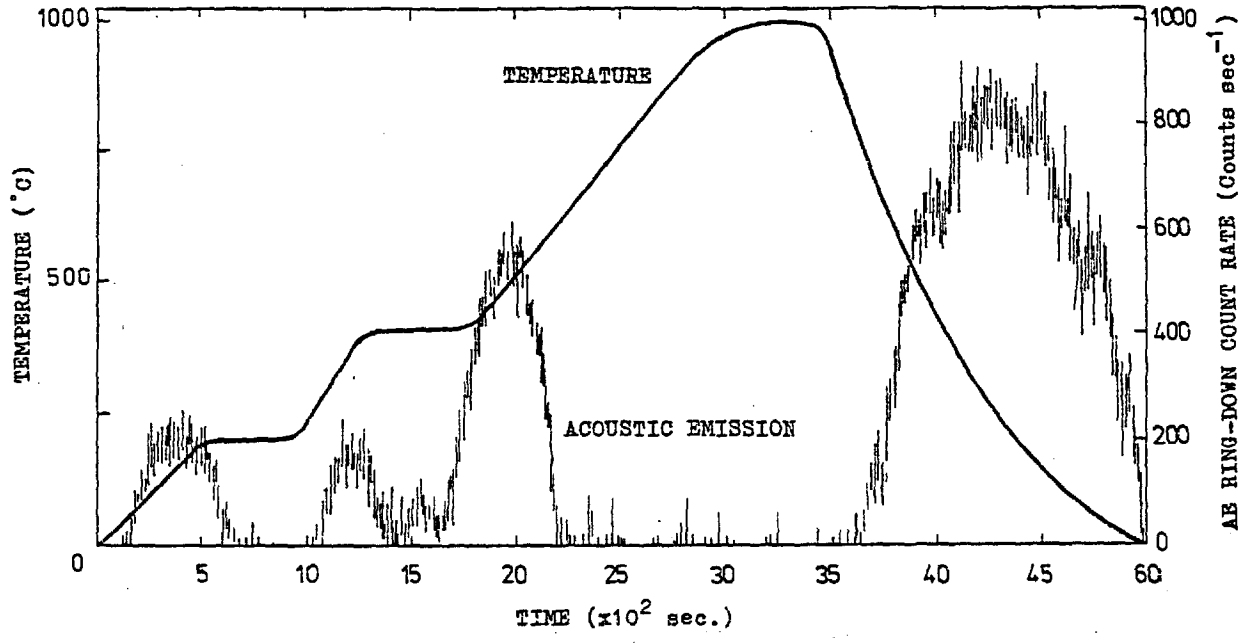


Fig.4.65. The acoustic response of the wave guide during the first heating cycle.

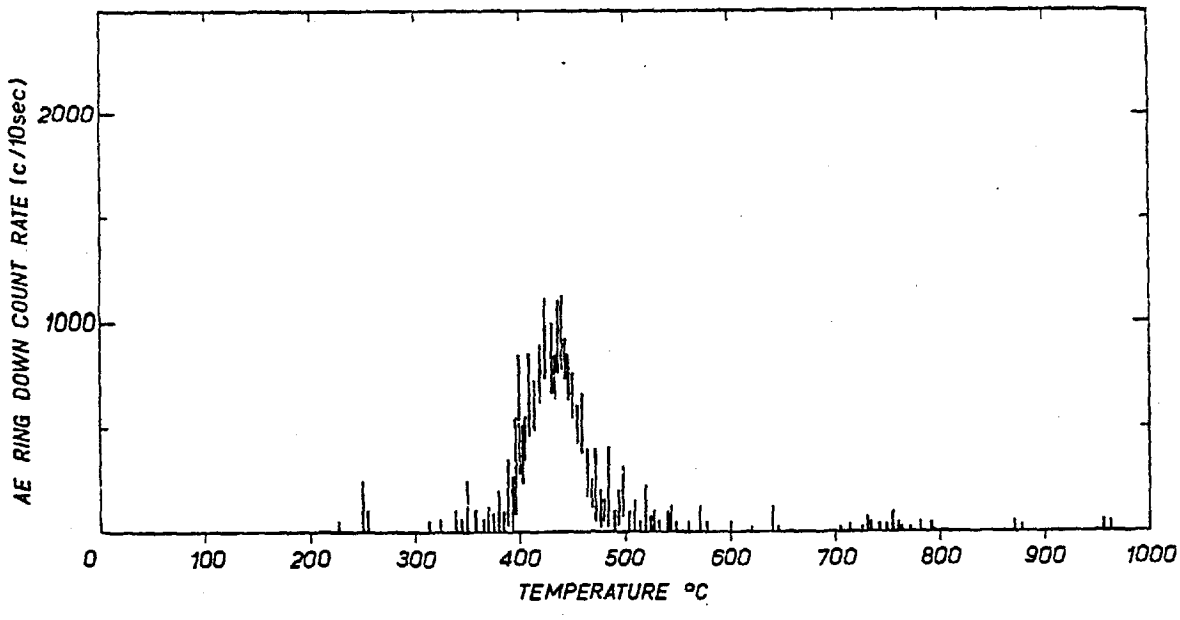


Fig.4.66. The acoustic response of testing system during heating at zero load.

emission around 450°C mainly due to the expansion of the system. A similar rate was obtained during each heating cycle, and thus the detection of emissions from the test specimens at around 450°C was difficult.

The load-deflection curves, together with the associated acoustic response, for a number of tests in the temperature range RT-1000°C are shown in Fig. 4.67. At temperatures below ≈600°C in all materials there was a linear relationship between load and displacement up to the fracture load, P_F, yet acoustic emission commenced at a load less than P_F. Non-linearity of the load-deflection curves was observed at temperatures in excess of ≈600°C, and increased with increasing temperature. Acoustic emission commenced prior to the load deflection curve becoming non-linear. The amplitude and pulse width distributions obtained at the end of a test are presented in Figs. 4.68 and 4.69, respectively, the former also including values of the b-exponent. It is clear that with increasing temperature there is a change in the mechanism(s) responsible for acoustic emission, since at the higher temperatures there is a greater proportion of low amplitude events and low pulse width events, and a much larger total number of events (see Fig. 4.70a). The mechanisms are believed to be softening of the glassy phase and the flow of the grain boundary glassy phase.

At a given temperature the acoustic response was influenced by the material grain size and porosity. For 97% pure alumina, increased emission was recorded in the range RT-600°C for the coarse-grained alumina E, compared with the fine-grained (2 μm) material D, but at temperatures above 600°C the reverse was the case. The 95% pure alumina (grain size = 4 μm) was generally noisier at elevated temperatures compared with the 97% pure materials.

Comparison of the amplitude distributions of the three materials obtained at room temperature, Fig. 4.71, and 900°C, (see Fig. 4.72) showed that the proportion of low amplitude events at room temperature was in the order FAO ≥ E > D, whilst at 900°C the order was FAO > D > E. Thus, at elevated temperatures the proportion of low amplitude events increased with increasing impurity content, but decreased with increasing grain size. Fig. 4.70b shows the temperature dependence of fracture toughness values for aluminas FAO, D and E.

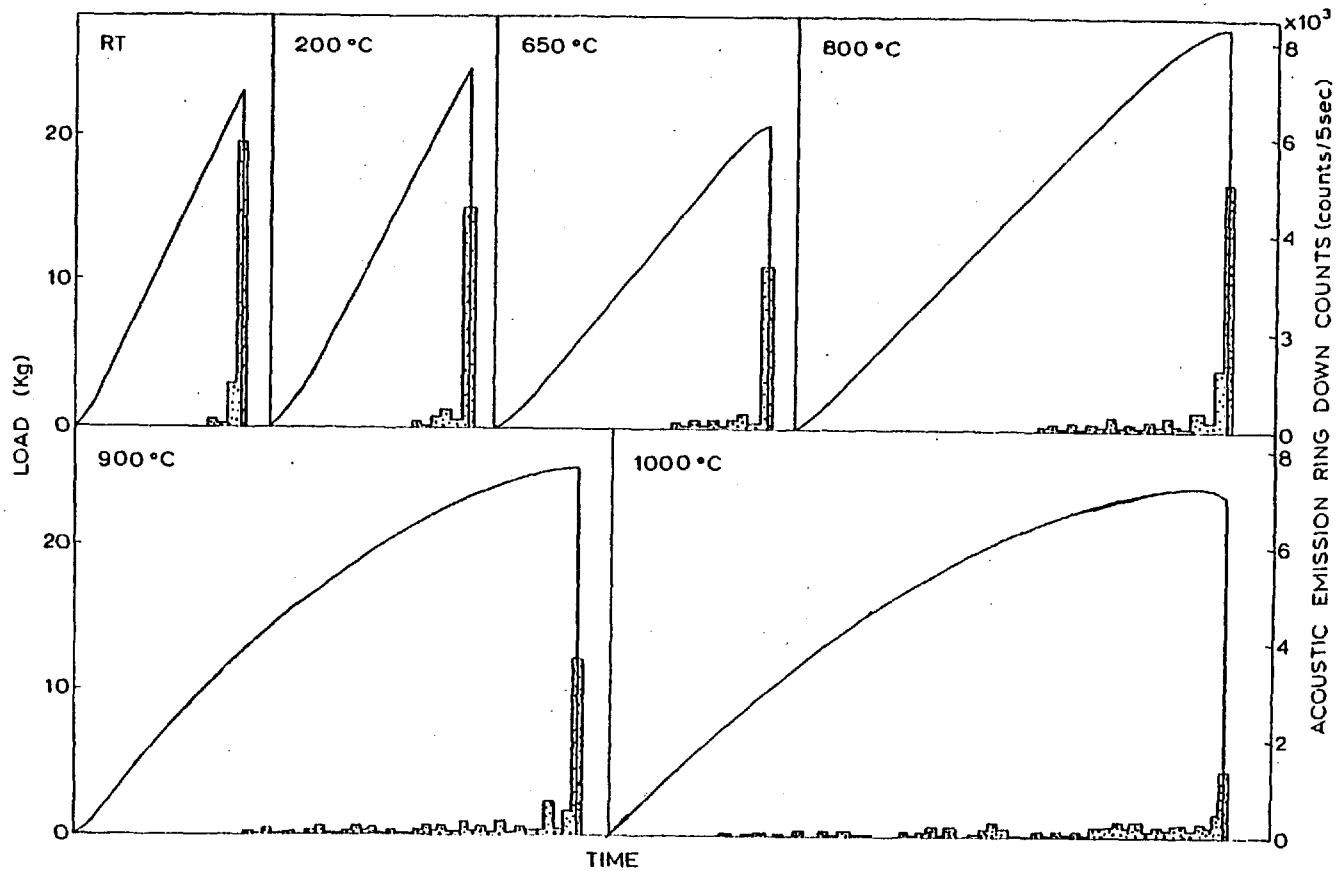


Fig.4.67. Load-deflection and AE-deflection curves at elevated temperatures,(alumina D).

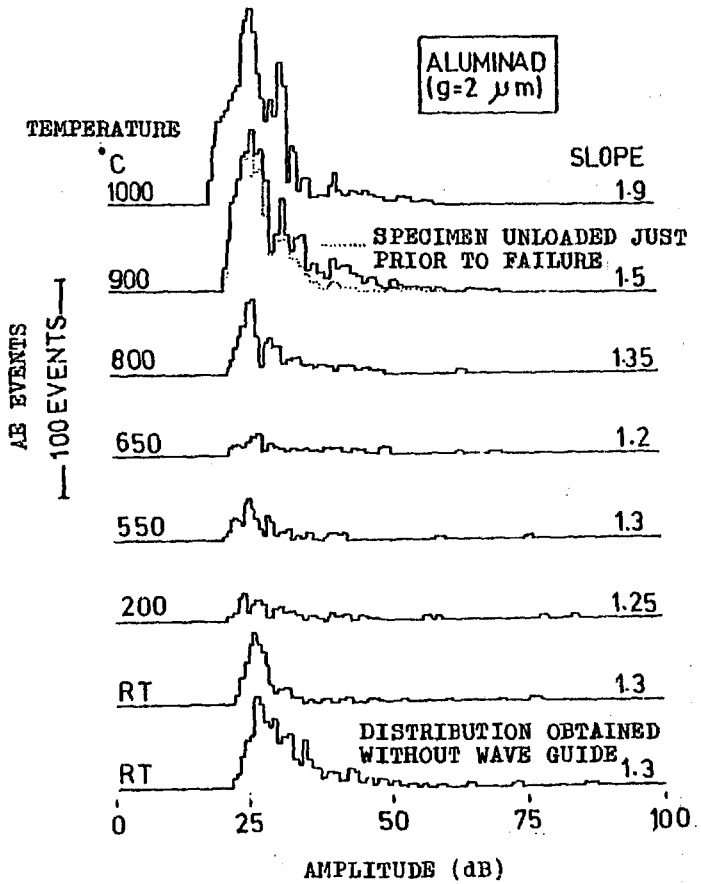


Fig.4.68. The AE amplitude distribution of alumina D at room and elevated temperatures.

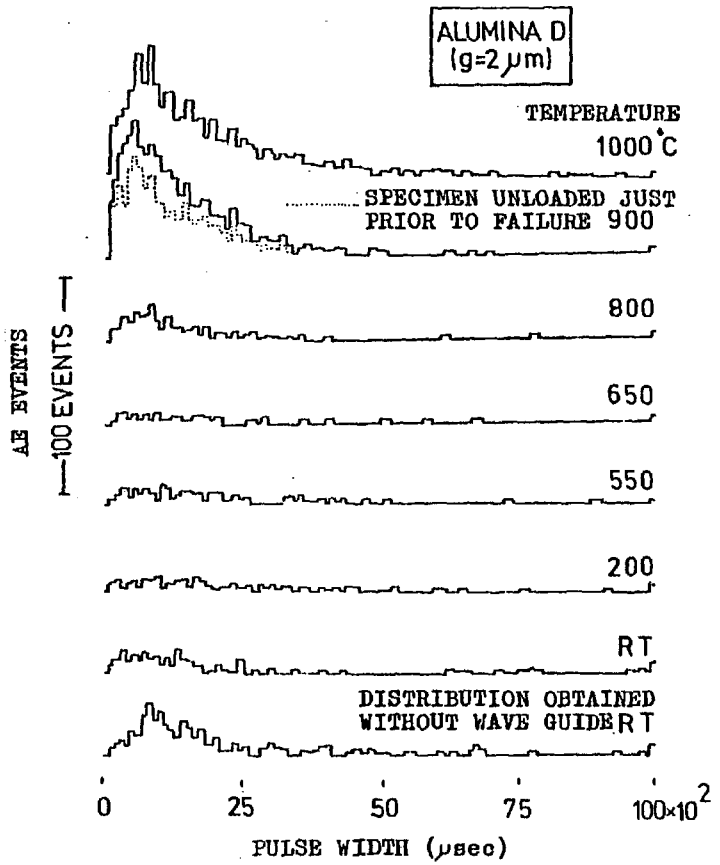


Fig.4.69. The AE pulse width distribution of alumina D at room and elevated temperatures.

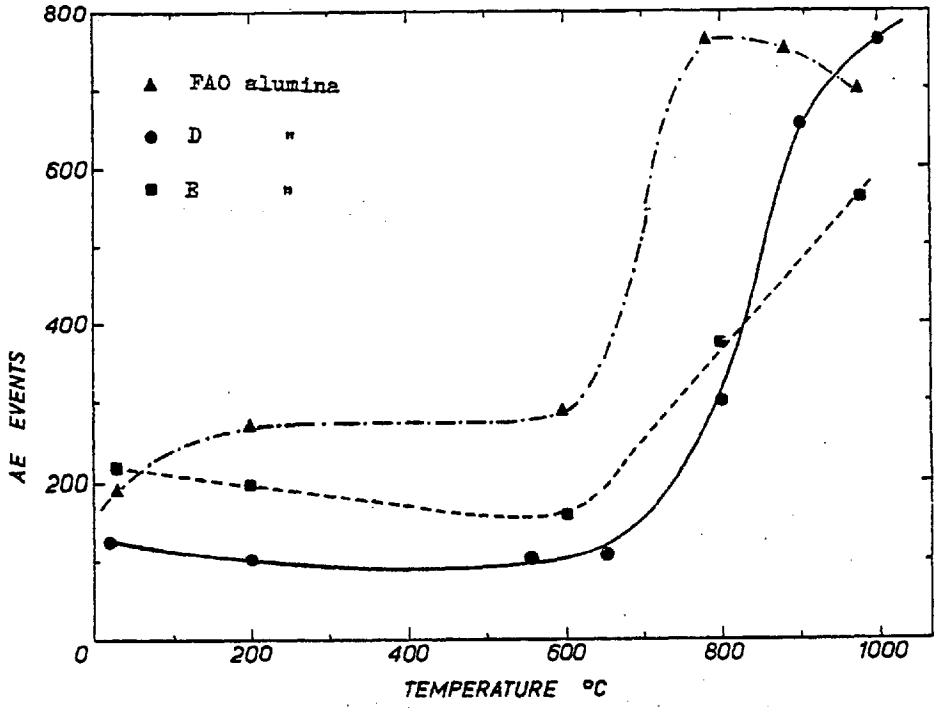


Fig.4.70.a. The temperature dependence of AE for FAO, D, and E aluminas.

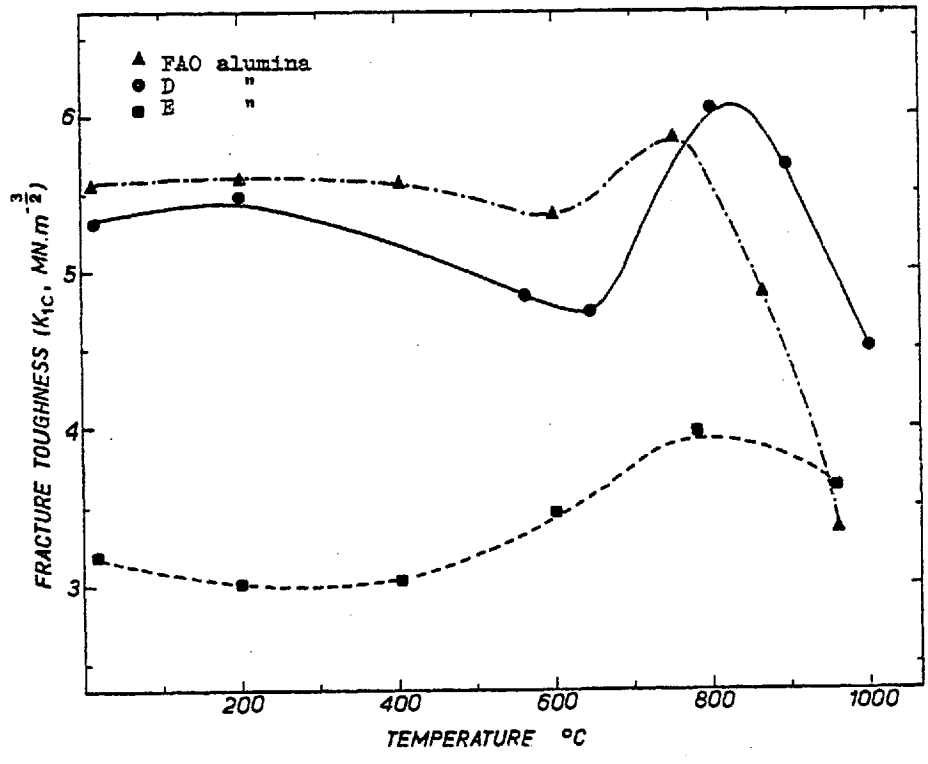


Fig.4.70.b. The temperature dependence of fracture toughness for FAO, D, and E aluminas.

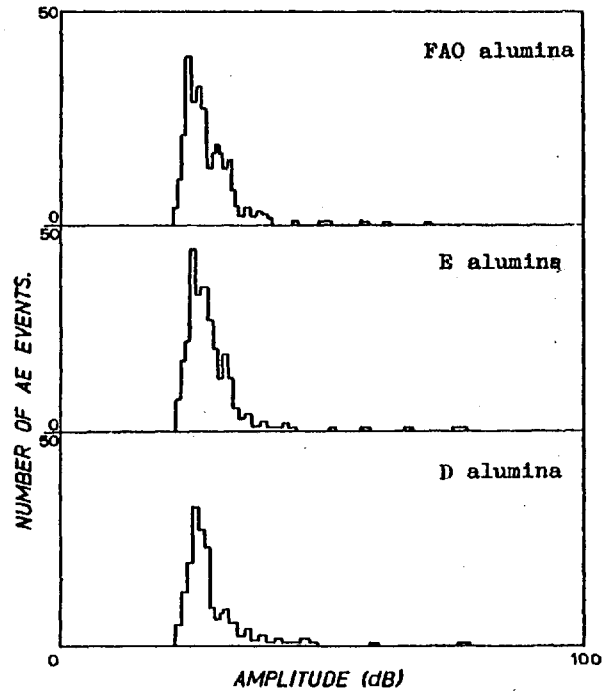
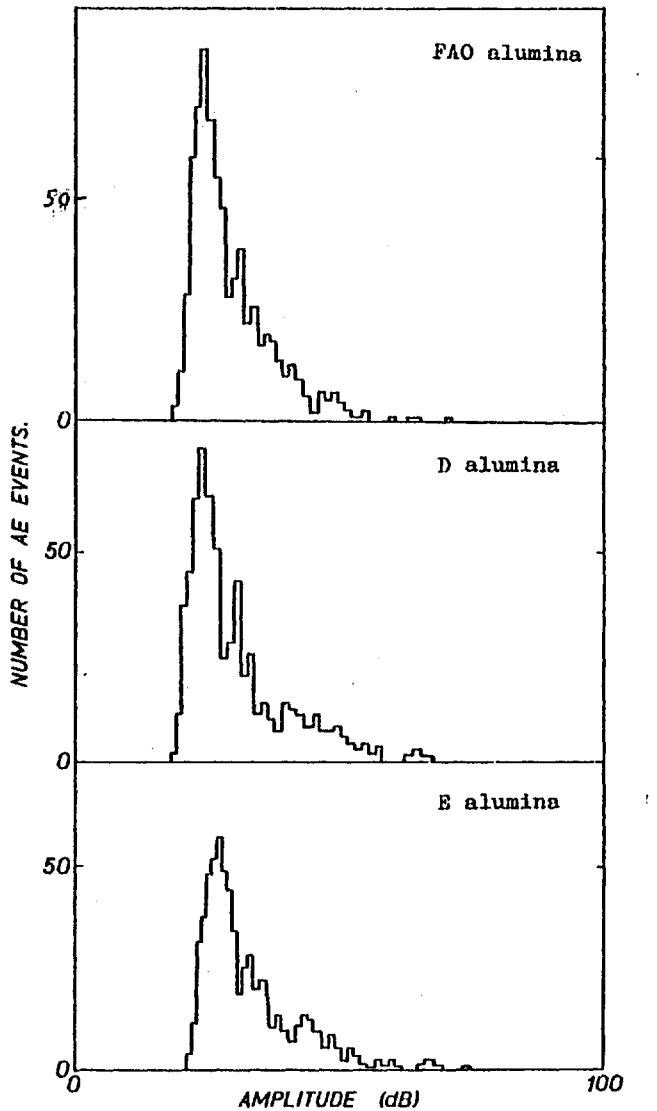


Fig.4.71. The amplitude distributions at room temperatures.



Fig,4.72. The amplitude distributions at 900°C.

The fracture toughness of all the aluminas between room temperature and 600°C remained fairly constant and the as-measured K_{IC} values varied in order FAO > D > E. The AE data indicated that subcritical crack growth occurred during tests at temperatures up to ≈600°C. Consequently the low temperature K_{IC} values were corrected for subcritical crack growth. The corrected K_{IC} values shown in Fig. 4.73 were calculated assuming the room temperature curve of Fig. 4.29 was applicable up to 600°C. After correction the K_{IC} values varied in the order FAO > D > E. The K_{IC} results, both before and after correction, showed that, of the two 97% pure aluminas, D was tougher than E probably because of its much reduced porosity and finer grain size. A possible reason for FAO being tougher than the denser material D, was the increased impurity content of the former. In the presence of second phases, microcracks may be produced in cooling from the sintering temperature and thus more energy was absorbed in opening the microcracks, as discussed in Section 4.4.2(iii).

At temperatures between 600°C and 1000°C, the fracture toughness of alumina C increased slightly before decreasing to roughly the same value as that obtained at room temperature. Aluminas D and FAO, on the other hand, showed a pronounced toughness peak at ~850°C and~750°C, respectively. This is due to the softening of the glassy phase so that energy is dissipated at the crack tip by deformation of this phase. The peak toughnesses were respectively 1.13 and 1.05 times those obtained at room temperatures. At still higher temperatures the viscosity becomes so low that the resistance to fracture is markedly reduced. Thus at temperratures above that for maximum fracture toughness, the K_{IC} value of both aluminas decreased sharply; so that at ~1000°C the K_{IC} values were 85% of the RT value in the case of alumina D, but 60% of the RT value in the case of alumina FAO. The higher grain boundary glassy phase content in the latter is probably a reason for its sharper K_{IC} decrease.

The scanning electron micrographs of Figs. 4.74-4.76 show, respectively, the fracture surfaces of alumina D specimens tested at RT, 550°C and 1000°C. For all samples, the micrographs

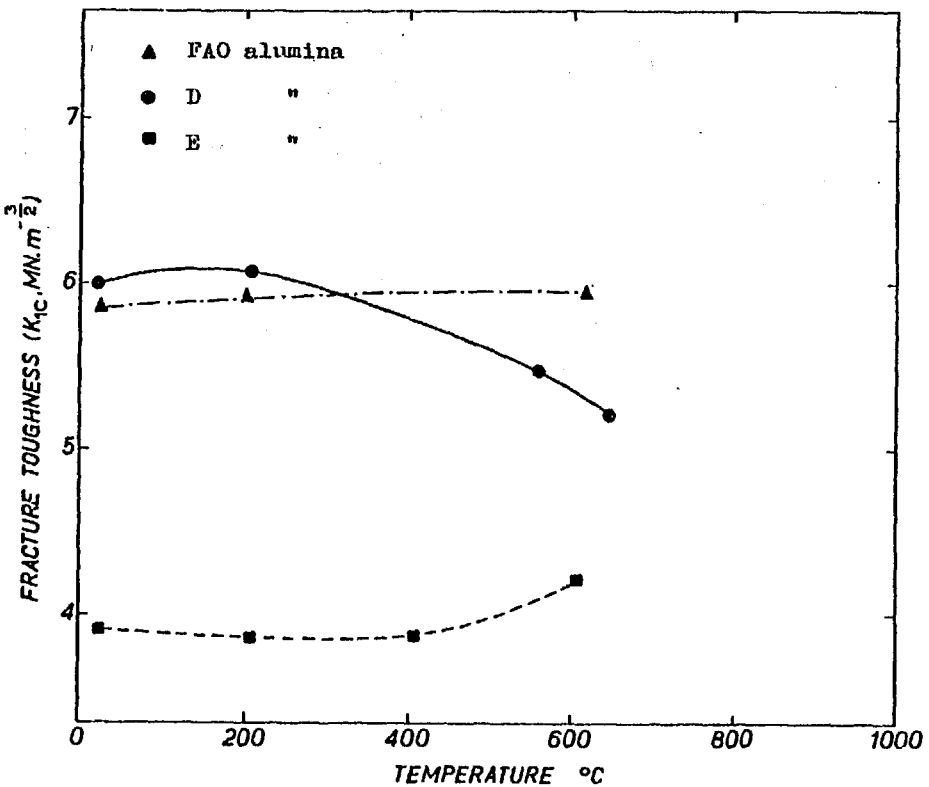


Fig.4.73. The corrected K_{1c} values at low temperatures.

show that fracture took place predominantly by separation at the grain boundaries. Some cleavage fracture was observed, but was less evident in specimens tested at temperatures above 650°C. Fracture surfaces of specimens tested above 800°C exhibited some voidage and cracking at the grain boundaries. Furthermore, the fracture faces of alumina FAO, containing Ca base impurities, tested above 600°C showed flow of glassy phase on the grain boundaries, as shown in Fig. 4.77. These observations are consistent with grain boundary deformation due to viscous glassy phase.

Comparing the fracture toughness and AE results obtained for the three aluminas above 600°C, two features can be discussed. Firstly, the large difference in the height of the peaks for aluminas D and E, both 97% pure, implies that the smaller grain size of D, and thus the larger grain boundary area for flow of glassy phase, is responsible for the increased peak height, and acoustic response of the material. Secondly, the K_{IC} maxima for FAO and D occurred at different temperatures. This implies that the FAO and D glasses have different temperature dependences of viscosity; FAO has the lower value since the Ca base glasses are more viscous compared with Mg base glasses. Furthermore, the decrease in K_{IC} after the maximum is more pronounced in FAO compared with D, mainly because of its increased impurity content.

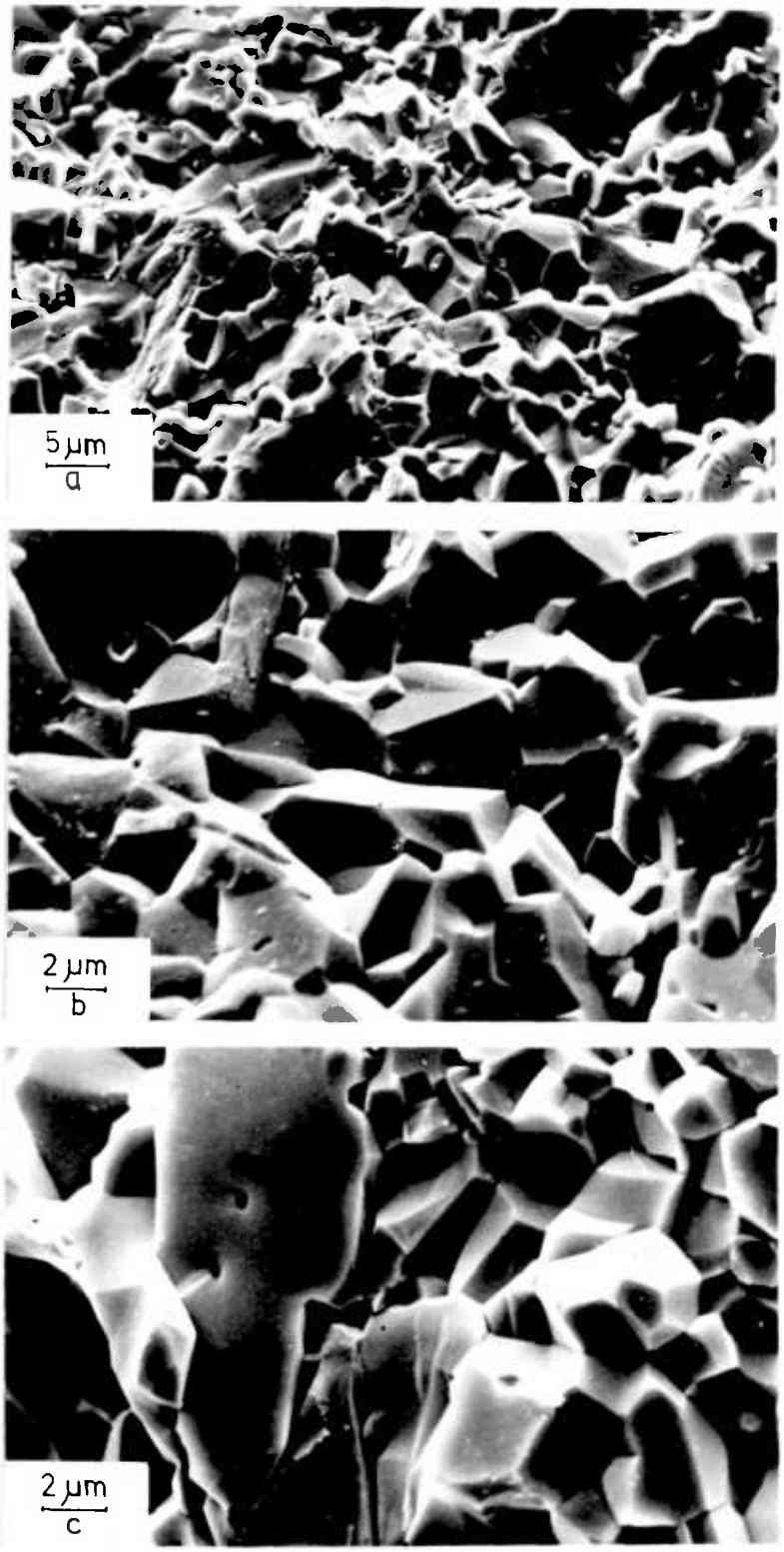


Fig.4.74. Fracture surfaces of alumina D tested at room temperature

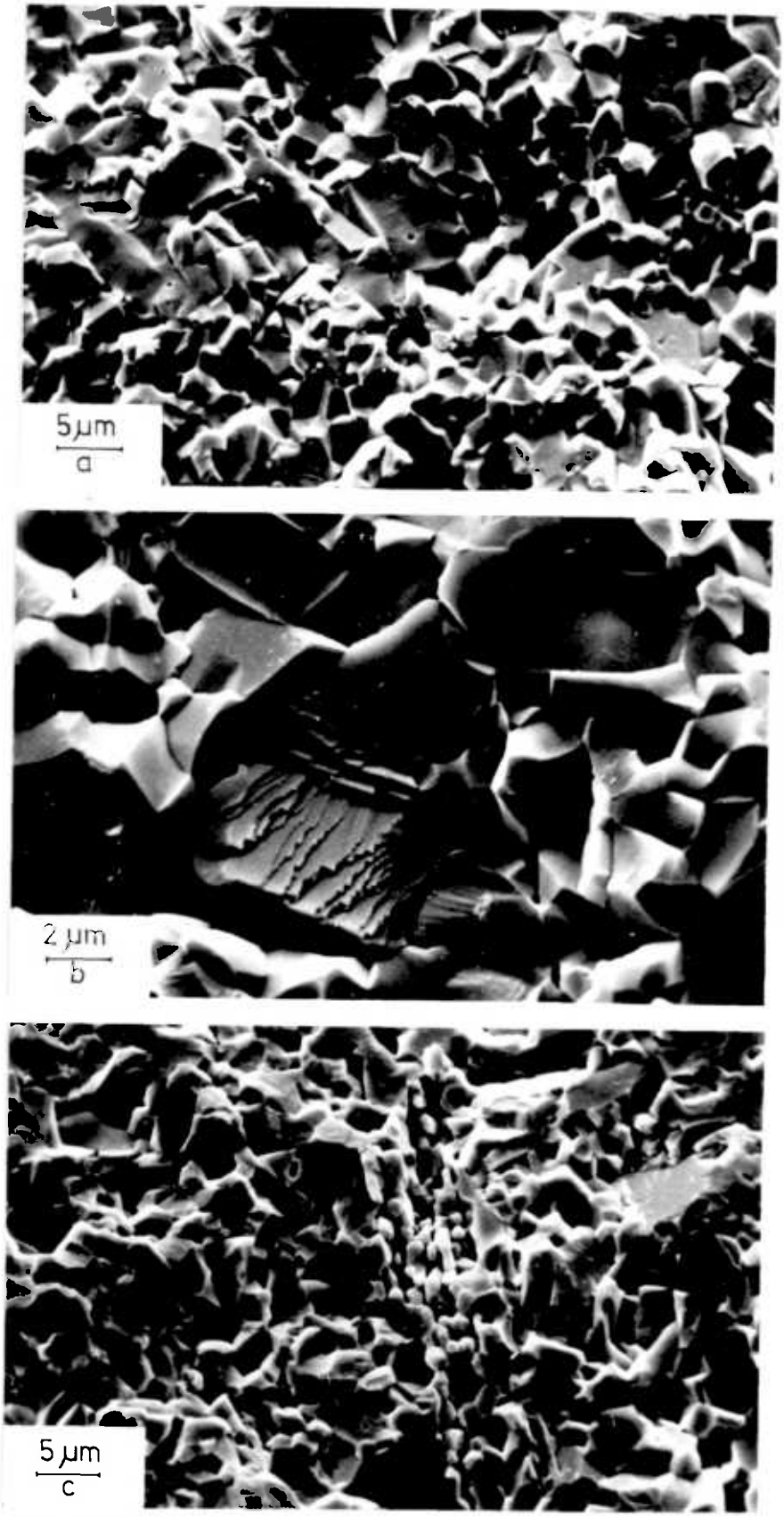


Fig.4.75. Fracture surfaces of alumina D tested at 550°C showing:
a - general micrograph
b - a region of cleavage fracture
c - " " " weakly sintered

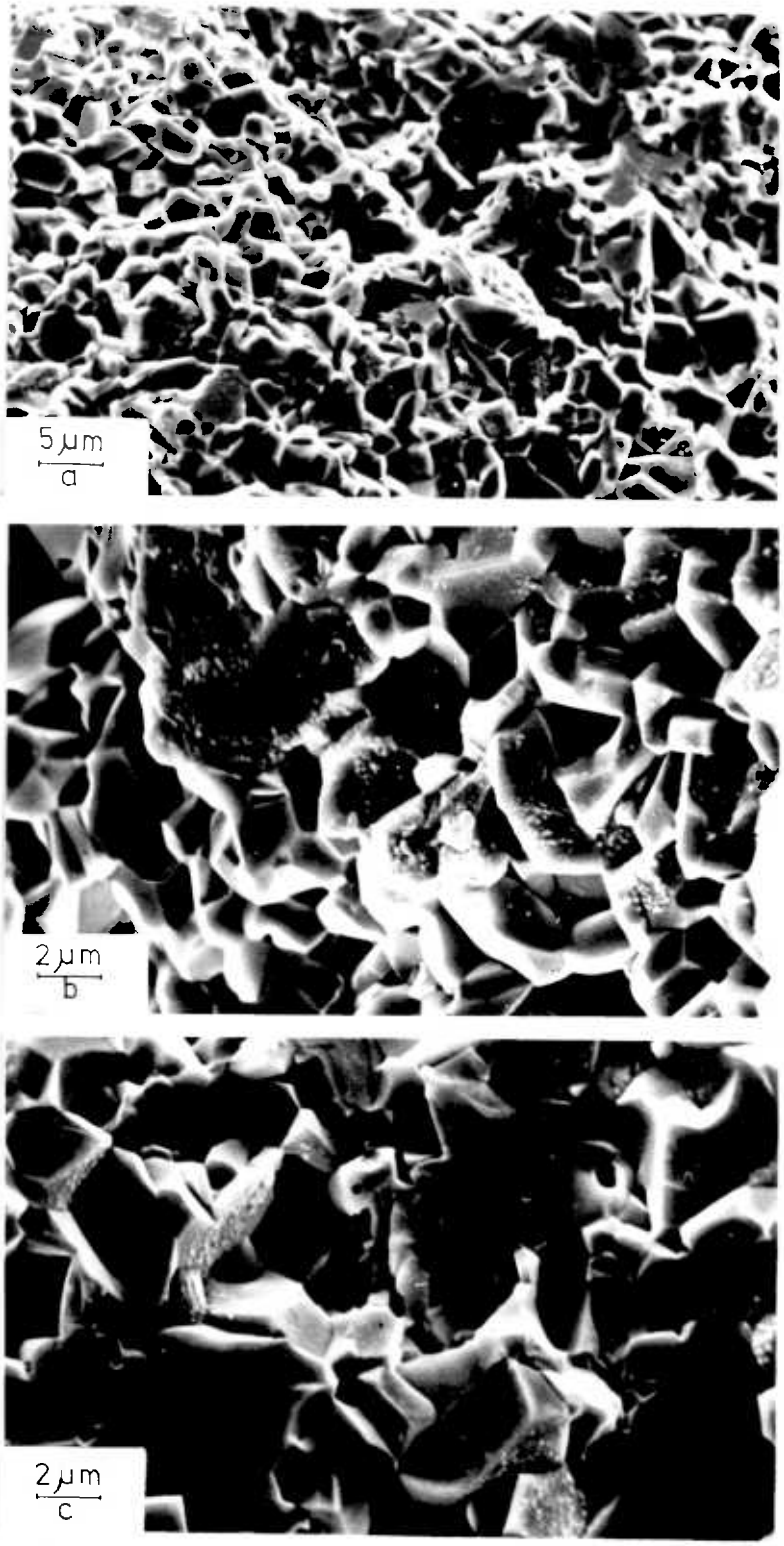


Fig.4.76. Fracture surfaces of aluminas tested at ~1000 °C
a - general view (D)
b,c- voidage at grain boundaries (D)

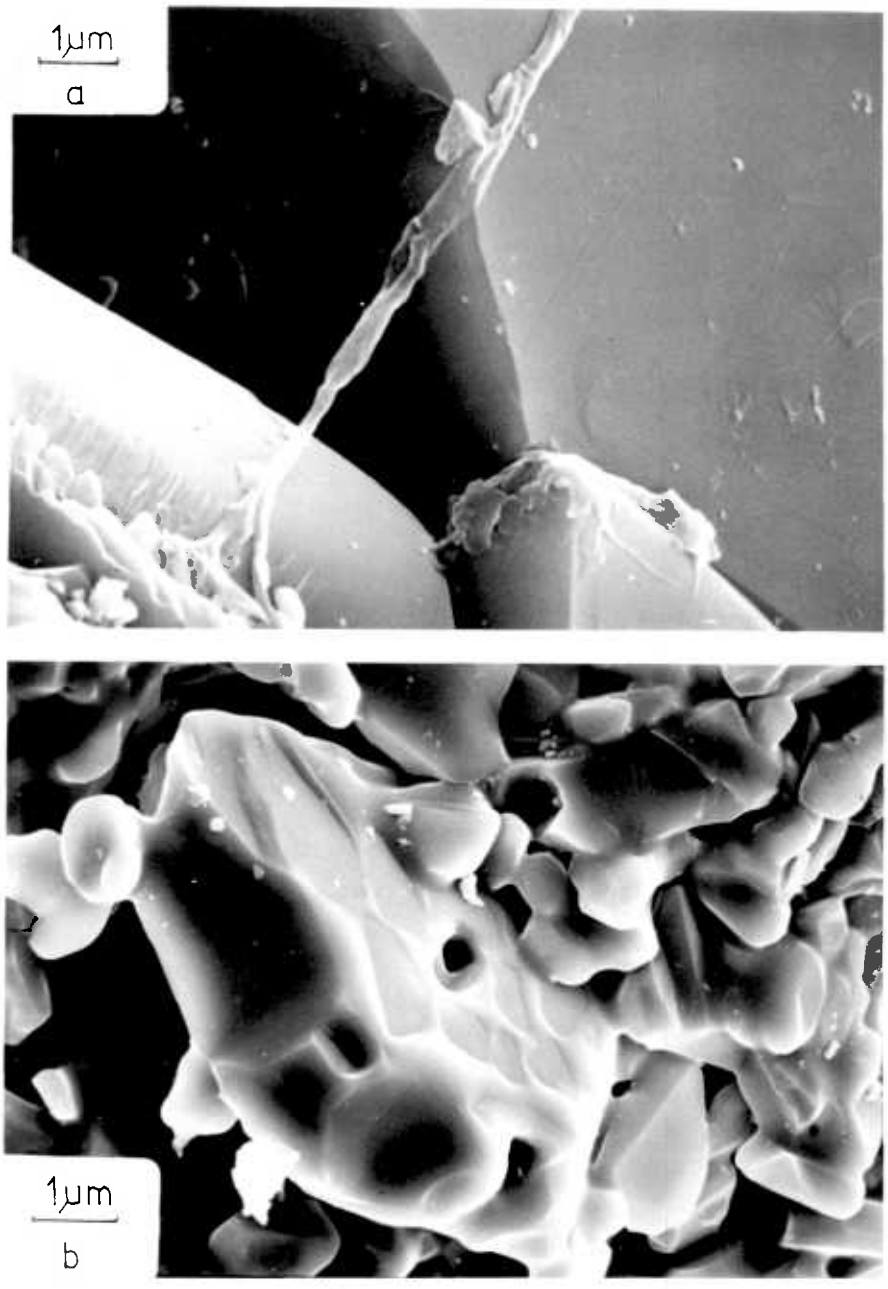


Fig.4.77. Fracture faces of alumina FAO, showing the flow of glassy phase:
a- tested at ~700 °C,
b- " " 900 °C.

CHAPTER 5

CONCLUSIONS AND SUGGESTIONS FOR FURTHER WORK

5.1 CONCLUSION

5.1.1 Effect of Test Geometry, Notching Technique and the Notch Length

Acoustic emissions associated with subcritical crack growth were detected in SENB, DT and DCB specimens of alumina at loads less than the fracture load. These emissions were more marked in the DCB and DT test-pieces than the SENB specimens. Emissions due to subcritical crack growth were mostly low rate, low amplitude and narrow pulse width events, whilst those obtained at the final failure had generally a high rate and more events of high amplitude and wide pulse width.

A linear relationship was obtained between the subcritical crack area and the generated acoustic emission counts for all geometries. For a given geometry the emissions obtained from 1 mm^2 of subcritical crack area were similar for fine and coarse-grained materials, but varied with geometry in the order DCB $<$ DT $<$ SENB. This variation can be attributed in part, to attenuation of emission amplitudes in the order DCB $>$ DT $>$ SENB. The quantitative measurement of the emissions lost due to attenuation was not possible; however, the emissions recorded prior to failure from each test geometry suggested that the acoustic response and so the extent of subcritical crack growth was in the order DCB $>$ DT $>$ SENB. As the result of subcritical crack growth, the true crack length at failure was greater than the initial crack, and correction for subcritical crack growth was found to be necessary for an accurate K_{IC} measurement.

The apparent K_{IC} values varied with geometry in the order SENB $<$ DT $<$ DCB, but after correction for subcritical crack growth the K_{IC} value obtained from SENB tests was in good agreement with

that obtained from DT. The DCB exhibited, even after correction, abnormally high values for K_{IC}. The scanning electron micrographs taken from the fracture surfaces of SENB, DT and DCB specimens showed that fracture was predominantly intercrystalline with some transcrystalline failure in all geometries. Evidence of crack branching was observed on the fracture faces of all geometries, but it occurred more often in DCB specimens. Thus the DCB geometry was found to be the less reliable compared with DT and SENB geometries. The double torsion geometry was the most reliable, as it is a crack length independent test.

Notching technique also influenced the as-measured K_{IC} values. Machine-notched specimens resulted in a reduced fracture toughness compared with that of sharp-cracked specimens. The reason was found to be the damaged notch roots which were observed on the optical and scanning electron micrographs. However, when considering either the damaged zone or the subcritical crack length and adding the larger one to the initial notch length, the results from all different notches were very consistent.

The initial notch length was found to affect the acoustic emission and the apparent fracture toughness. In SENB specimens, as the a/w ratio was increased, the extent of subcritical crack growth increased and thus the acoustic emission. The apparent stress intensity factors calculated from the maximum loads decreased with increasing a/w. However, it was found that if the a/w ratio is kept within the recommended limits, i.e. $0.45 \leqslant a/w \leqslant 0.55$, the variation of the critical stress intensity factor and acoustic responses with a/w is not considerable. In other words, it is within the limits of standard deviation of the results obtained for specimens of $a/w = 0.5$.

5.1.2 Effect of Strain Rate

The mechanical properties and acoustic response of alumina were affected by the strain rate. The modulus of rupture decreased slightly with decreasing strain rate, but the acoustic emission

in the rupture tests occurred only at the failure points, and the number of counts remained unchanged at different strain rates. The apparent fracture toughness values obtained by SENB specimens also decreased with decreasing cross-head speed, but the emissions from these specimens obtained prior to fracture increased with decrease in strain rate. It was found that the acoustic emission count rate dN/dt can be related to the strain rate, $\dot{\varepsilon}$, and the stress intensity factor, K_I, by an equation such as:

$$\frac{dN}{dt} = A(K_I)^n \frac{1}{\dot{\varepsilon}}$$

where A and n are constants depending on the material and test conditions. This equation provided a correlation between the acoustic emission and the fracture toughness of the material.

5.1.3 The Influence of Microstructure

The microstructure had a considerable influence on the mechanical properties and acoustic emission of alumina. There was a decrease in both fracture strength and fracture toughness with increasing porosity which varied with the grain size. When correction was made for porosity using the equation suggested by Knudsen, the strength decreased with increasing grain size. This was also the case for strength and toughness of aluminas with a similar porosity. The inverse grain size dependence of fracture toughness was found to be partly due to the subcritical crack growth and more consistent K_{IC} values obtained for aluminas of different grain sizes when correction for subcritical crack was made to the as-measured K_{IC} values.

The acoustic emission increased with increasing porosity, but there was a tendency toalarger number of emissions, particularly as the number of large isolated pores and grains increased. The results showed that there is no simple correlation between the fracture toughness values and the acoustic emission data. A crude measurement of the acoustic energy from the amplitude

and pulse width distributions showed that although acoustic emission is part of the fracture energy released, it has no direct proportionality to the released energy. In fact, the detected acoustic energy is inversely proportional to the fracture surface energy.

The dispersion of second phase ZrO_2 particles in the alumina matrix influenced the fracture toughness and acoustic response of the composite. Both K_{IC} and the acoustic emission exhibited a maximum before decreasing with increasing volume fraction of ZrO_2. The increased K_{IC} and AE were explained on the basis of energy absorption in the opening of pre-existing microcracks and subcritical crack growth in front of the notch tip.

5.1.4 High Temperature Toughness and AE

Acoustic emission was found to be suitable for monitoring fracture toughness tests at elevated temperatures, and the technique was successfully used up to 1000°C. It was found that there was a change in the mechanism responsible for acoustic emission from test specimens at temperatures above 650°C which resulted in a much larger number of emissions, most of them of low amplitude and pulse width. These were associated with the softening and flow of the grain boundary glassy phase, since aluminas of higher impurity content and finer grain size produced more emissions. The scanning electron micrographs from fracture surfaces tested above 650°C illustrated evidence consistent with grain boundary deformation due to a viscous glassy phase.

The fracture toughness results showed fairly constant values between RT and 650°C, whereas above 650°C the fracture toughness increased with increasing temperature before decreasing rather sharply. The increase was attributed to the dissipation of energy at the crack tip by deformation of the softening glassy phase. Aluminas containing more impurity and finer grain size exhibited more pronounced maxima in K_{IC}. As the temperature increased above the maximum K_{IC}, the viscosity became so low that resistance to fracture was markedly reduced.

5.2 SUGGESTIONS FOR FURTHER WORK

1. The present work has demonstrated the influence of test geometry on fracture toughness and acoustic emission of alumina. It has been shown that both K_{IC} and AE vary with specimen geometry. This was found to be mostly due to the difference in the extent of subcritical crack growth, which varied also with the microstructure of the material and the test environment. The specimen size, surface finish, and condition of side grooves may also have considerable influence on K_{IC} and acoustic response, and should be studied.

2. The measurement of strength of alumina using the modulus of rupture test at room temperature andvarious strain rates showed that in notchless specimens, subcritical crack growth did not occur even at low strain rates. But stress corrosion took place which resulted in the decreased strength at low strain rates, without considerable change in acoustic response. More detailed investigation of stress corrosion of alumina is needed using the AE technique and microscopical examination. Effects of temperature and environment on Al_2O_3 fracture should be investigated.

3. In the comparison of the strength and toughness of alumina FAO with alumina B, both having the same mean grain size but the latter being denser, it has been shown that the strength of alumina B is greater than FAO but the toughness of B is less than FAO. Some reasons for this behaviour have been suggested, but a more detailed study is required to obtain an unambiguous explanation.

4. Fracture toughness testing of different aluminas at elevated temperatures showed a maximum in K_{IC} at around 800°C. This was attributed to the flow of the glassy phase which was accompanied by more acoustic emissions. The AE monitoring of modulus of rupture tests at elevated temperature is required, since subcritical crack growth does not occur in rupture tests and the emissions due to the flow of the glassy phase can be monitored without being accompanied by the emissions from subcritical crack growth. Furthermore, the temperature dependence of the strength of different aluminas is also valuable.

5. The acoustic response of alumina in the present investigation has been obtained during failure of specimens either in bending or tension. The study of the acoustic response of different aluminas in compression would also be interesting.

6. The stress intensity factor has been correlated to the AE count rate by the equation $dN/dt = BK^n$. It has been shown that the values of B and n vary with the material and the specimen geometry. The variation of these constants with test environment and condition is not yet known and is an interesting subject for further work.

APPENDIX

THE FRACTURE TOUGHNESS AND AE OF PORCELAIN

To assess the general applicability of the AE technique for the evaluation of the validity of fracture toughness testing of ceramics, the procedures employed for alumina (Section 4.3) were used for two porcelains with different microstructural characteristics:

(i) The as-received porcelain (P_I) was a commercial material produced by slip-casting and fired at 1140°C for 46 hours.

(ii) Heat-treated porcelain (P_{II}) was produced by subsequently refiring P_I in the laboratory at 1100°C for 24 hours.

The effect of refiring P_I was to increase the grain size and pore size and reduce the total porosity from a value of 6% by volume in the as-received material to about 2% in the heat-treated material. The porosities were measured using a mercury porosimeter[81]. Fig. A.1 shows the microstructure of the two materials. The microstructure of porcelain is very complex, consisting of large grains (mainly quartz) surrounded by very fine multiphase crystals formed from the clay component. A number of intergranular pores, some very large, were present. Shrinkage cracks within the body of as-received blocks were often observed. Microcracks produced during firing were also observed, mainly originating from pores and moving into the large grains. Since on cooling from the refiring temperature the crystalline quartz contracts on average ten to fifteen times more by volume[97] than the other constituent phases of the material, it is not surprising that cracks are seen in the larger quartz grains present in the porcelain. This thermal mismatch, which causes a micro-stress system to be set up in the porcelain, has been considered by some workers[97] to have a

strengthening effect on the porcelain. This effect was confirmed by the modulus of rupture results (see Table A.1), which showed a 27% improvement in strength of the heat-treated porcelain compared with the as-received material.

The fracture toughness of each material was measured using SENB, DT and DCB specimens, and the acoustic emission was monitored. At a cross-head speed of 0.01 cm/min, the load-deflection curves were linear up to a point just prior to failure where a non-linear region was observed, as shown in Fig. A.2. The non-linearity was also observed at the increased cross-head speed of 0.05 cm/min. The stress intensity factors were measured from the maximum load, P_M, and are summarised in column 4 of Table A.2. The as-measured K_{IC} values from all geometries showed an increase of up to 18% for heat-treated porcelain compared with the values for as-received material. The increase in K_{IC} for heat-treated porcelain resulted mainly from the decreased porosity of the material. The microcracks produced due to the thermal mismatch of the phases may also be another reason for the increased K_{IC} in the heat-treated porcelain, as discussed in Section 4.4.3 for $Al_2O_3.ZrO_2$. The K_{IC} data for a given material varied with test geometry in the order DCB $>$ DT $>$ SENB, as observed for alumina.

Acoustic emission started at a load P_s in the linear region of the load-deflection curve, the rate then increasing with load and reaching its maximum at failure (Fig. A.2). The emissions commenced at particularly low loads in DCB and DT tests (column 3 of Table A.2) as in the case of alumina. Microscopical examination demonstrated that subcritical crack growth had occurred prior to failure, producing the emissions detected between P_s and P_M, many of them of low amplitude and narrow pulse width events (see Fig. A.3). The average values for the total number of ring-down counts N_{RT} and events N_{ET} associated with subcritical crack growth are given in columns 5 and 6 of Table A.2. The values varied in the order DCB $>$ DT $>$ SENB, which was again consistent with the results obtained for alumina.

Subsequently some specimens of all geometries were subjected to progressive crack growth at the same cross-head speed

(0.01 cm/min) and the subcritical crack length was measured using a dye penetrant to reveal the crack. The subcritical crack area was then plotted against the corresponding AE data. The results are shown in Figs. A.4 to A.7, and illustrate that the emission counts are a linear function of subcritical crack area. The results were consistent with those obtained for alumina, indicating that the acoustic emission technique can successfully monitor the subcritical crack growth in different ceramics. The curves of Figs. A.4 to A.7 were used to correct the measured K_{IC} values for subcritical crack growth in porcelain.

The subcritical crack lengths obtained during the fracture toughness tests were determined using the AE data given in column 6 of Table A.2 and Figs. A.7 . Adding the subcritical crack length to the initial notch length, enabled corrected K_{IC} values to be determined (column 7 of Table A.2). When the corrected data (see Table A.2) is compared with the as-measured values, it is observed that SENB values have increased to the same level as those for DT specimens which remain unchanged. The DCB values, after correction, become even larger than the SENB and DT values, which is in agreement with the conclusion obtained for alumina ; the DCB geometry appears the least reliable. Unlike alumina which showed little difference between the corrected K_{IC} for fine- and coarse-grained materials of similar porosity, the K_{IC} results of porcelain, both before and after correction, were always larger in the case of the heat-treated material.

Table A.1

Material	Code Number	Density g/cm^3	Porosity %	Maximum Pore Size (μm)	Modulus of rupture MNm^{-2}
As-received	P_I	2.244	6%	110	29.5 ± 0.8
Heat-treated	P_{II}	2.265	2%	150	37.5 ± 0.6

Table A.2

Test Geometry	Material	P_s/P_M	Measured K_{IC} $MN\ m^{-3/2}$	AE due to subcritical crack		Corrected K_{IC} $MNm^{-3/2}$
				$N_{RT} \times 10^3$	N_{ET}	
SENB	P_I	0.87	$0.75 \pm .05$	45.7 ± 21	790 ± 280	0.93
	P_{II}	0.82	$0.79 \pm .02$	139 ± 38	1020 ± 405	0.97
DT	P_I	0.78	$0.91 \pm .04$	67.6 ± 33	3400 ± 1500	0.91
	P_{II}	0.68	$1.05 \pm .08$	162 ± 45	4000 ± 1600	1.05
DCB	P_I	0.77	$0.95 \pm .02$	473 ± 180	4560 ± 1400	1.25
	P_{II}	0.66	1.12 ± 0.2	159 ± 46	2075 ± 950	1.36

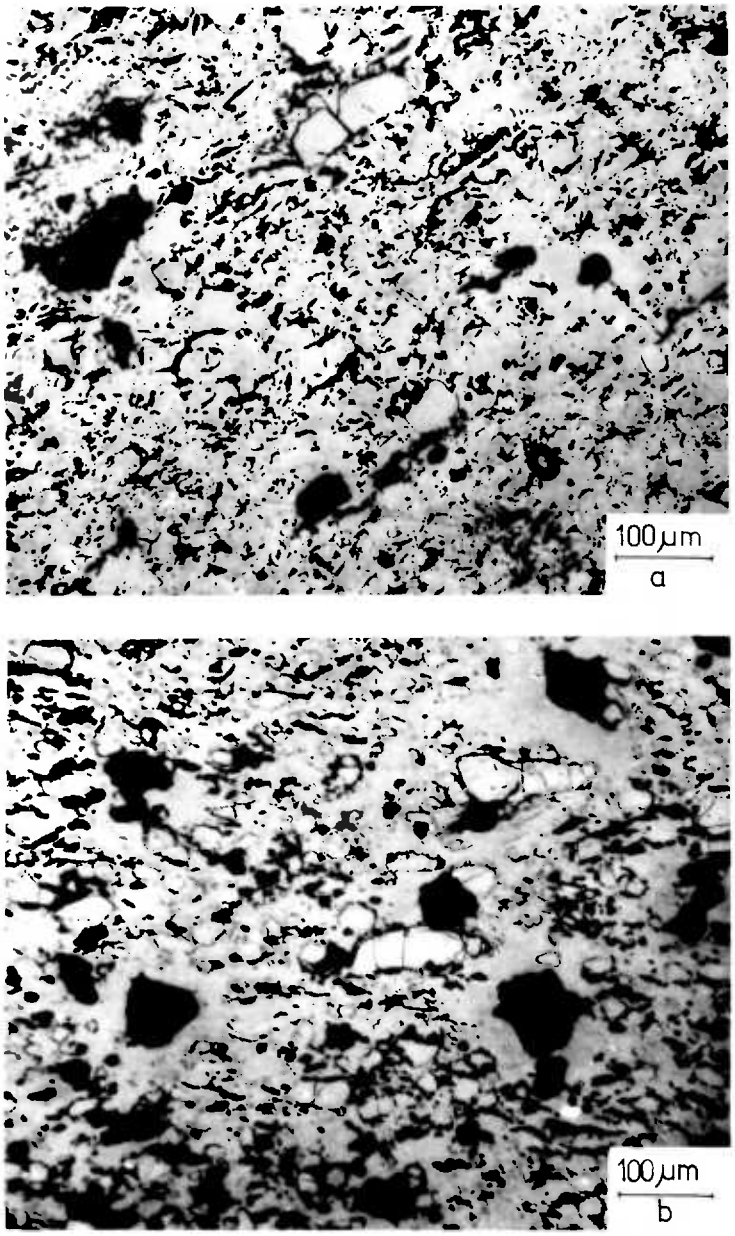


Fig. A.1. Optical micrographs from polished & etched surfaces of porcelain.
a - as-received,
b - heat-treated.

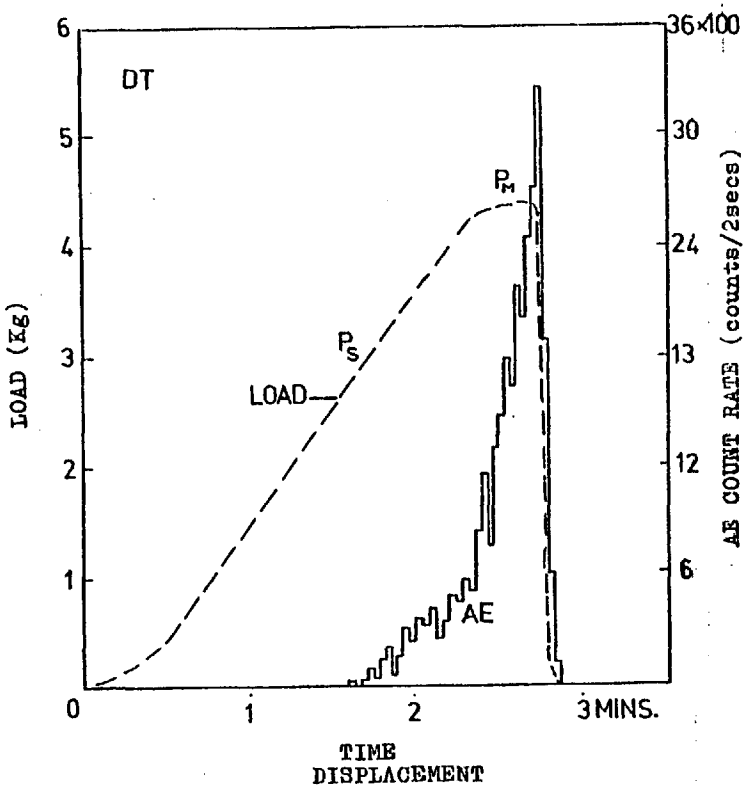


Fig.A.2. Typical load-deflection and AE ring-down count rate-deflection curves for porcelain tested at 0.01 cm/min cross-head speed, using DCB test geometry.

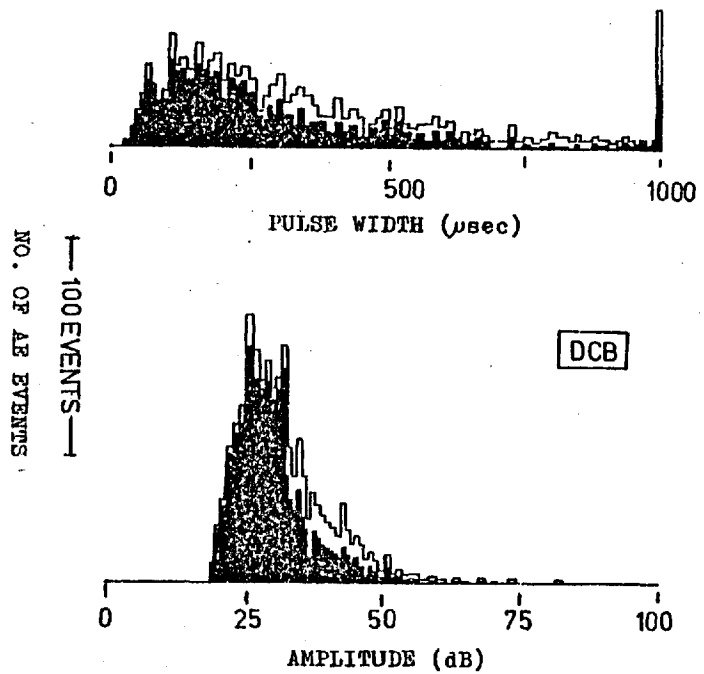


Fig.A.3. The AE amplitude and pulse width distributions obtained for porcelain after subcritical crack growth and final failure.

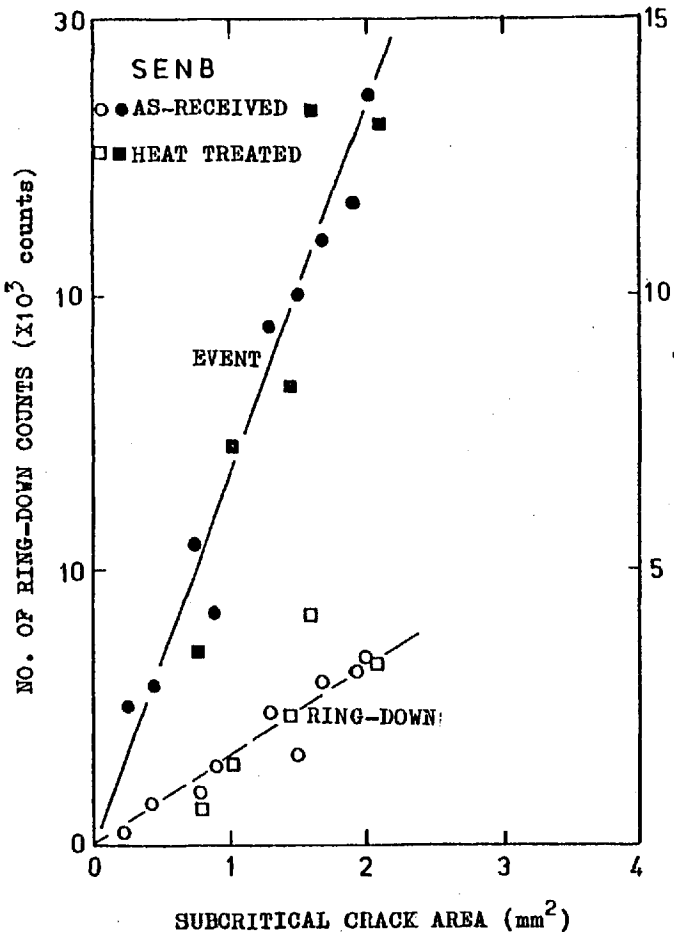


Fig.A.4. The AE as a function of subcritical crack area for porcelain using SENB specimens.

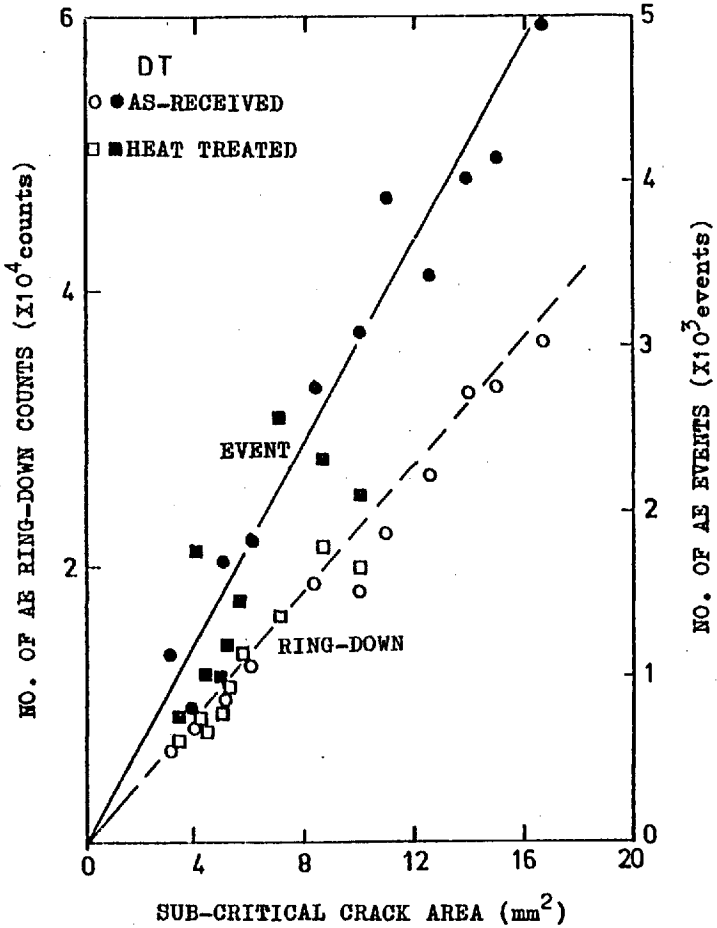


Fig.A.5. The AE as a function of subcritical crack area for porcelain using DT specimens.

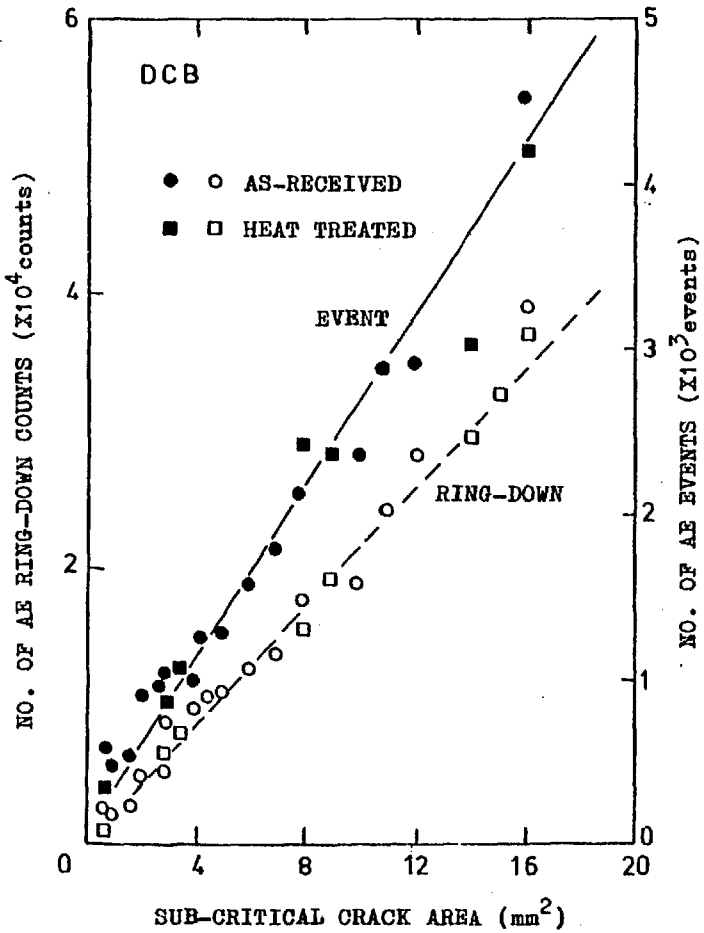


Fig.A.6. The AE as a function of subcritical crack area for porcelain using DCB specimens.

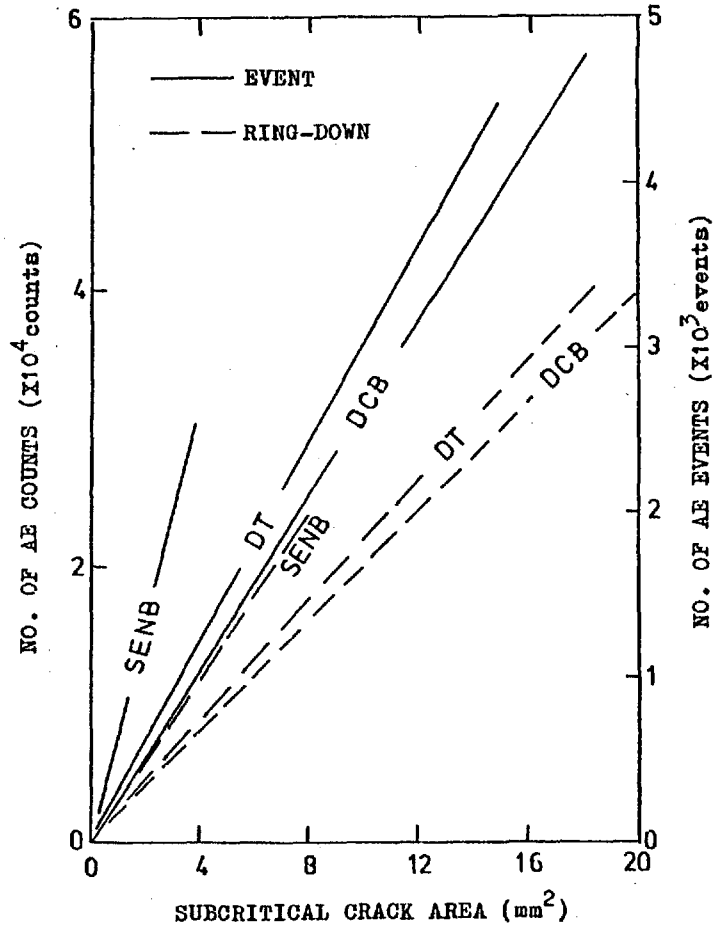


Fig.A.7. The AE as a function of subcritical crack area for porcelain using SENB, DT, and DCB test geometries.

REFERENCES

1. SIMPSON, L.A., J. Amer. Ceram. Soc., 56 (1), (1973), 7-11.
2. MEREDITH, H. and Pratt, P.L.,"Special Ceramics", 6, B.C.R.A., (1975), 107.
3. DALGLEISH, B.J., PRATT, P.L. and SANDFORD, J., Sci. Ceram., 8 (1976).
4. GUTSHALL, P.L. and GROSS, D.E., Eng. Frac. Mech., 1, (1969), 463.
5. SIMPSON, L.A., "Fracture of Ceramics", (Plenum Press, 1970), 567.
6. SIMPSON, L.A., J. Amer. Ceram. Soc., 56 (11), (1973), 610.
7. PRATT, P.L., Frac., 3, I.C.F.A., Waterloo, Canada, 14-24 June (1977).
8. CLAUSSEN, N., PABST, R. and LAHMANN, C.P., Frac. Br. Ceram. Soc., 25, (1975), 139.
9. SIMPSON, L.A., J. Amer. Ceram. Soc., 57 (4), (1974).
10. EVANS, A.G., LINZER, M. and RUSSELL, L.R., Mat. Sci. Eng., 15, (1974).
11. DUNEGAN, H., Met. Eng. Quarterly, 8, (1975).
12. RYSHKEWITCH, E., "Oxide Ceramics", (Academic Press Inc. Ltd., 1960).
13. Data Sheet "Physical Examination of Alumina", BA Chemical Ltd., Norfolk House, St. James's Square, London.
14. HOVE, J.E. and RILEY, W.G., "Modern Ceramics", (John Wiley and Sons, Inc., 1965).
15. BUDWORTH, D.W., "Principles of ceramic density measurement", Dept. Ceramic Refrac. Tech., Univ. Sheffield, U.K.
16. THOMPSON, J.C., "Hot isostatic pressing", Progress Report, Dept. Met. Mat. Sci., Imperial College (1977).
17. CLAUSSEN, N., J. Amer. Ceram. Soc., 59 (12), (1976).
18. GRIFFITH, A.A., Phil. Trans. Roy. Soc. London, 221A, (1920), 163-198.
19. IRWIN, G.R., J. Appl. Mech., 24, (1957), 361.
20. OROWAN, E., Weld. J., 34, (1955), London, 1575-1605.
21. MEREDITH, H., NEWEY, C.W. and PRATT, P.L., Proc. Br. Ceram. Soc., 20, (1972), 229.
22. FELTHAM, P., "Deformation and Strength of Materials", (Butterworths, London, 1966).
23. WIEDERHORN, S.M., Frac. Ceram., NBS Spec. Pub. No. 303 (1969).
24. PARIS, P.C. and SIH, G.C., ASTM Spec. Tech. Pub. No. 381, 30-81.
25. IRWIN, G.R., Frac. Met., Amer. Soc. Met., (1948).
26. WACHTMAN, J.B., TAFFT, W.E., LAM, D.G. and APSLEIN, C.S., Phys. Rev., 122, (1961), 1754.
27. RAWLINGS, R.D., Ph.D. Thesis, Met. Dept., Imperial College (1964).
28. KINGERY, W.D., "Introduction to Ceramics", (John Wiley & Sons, London, 1967), 621.

29. SPRIGGS, R.M., J. Amer. Ceram. Soc., 44, 12 (1961), 628-629.

30. COBLE, R.L. and KINGERY, W.D., J. Amer. Ceram. Soc., 39, (1956), 377-385.

31. BRADT, R.C. and TRESSLER, R.E., 6th Int. Met. Sym., Berkeley, 24-27 Aug. (1976).

32. KNUDSEN, F.P., J. Amer. Ceram. Soc., 42, (1959), 376-387.

33. RICE, R.W., Proc. Br. Ceram. Soc., 20, (1972), 205-257.

34. CARNIGLIA, S.C., Mat. Sci. Res., 3, (1966), 425-271.

35. RICE, R.W., J. Amer. Ceram. Soc., 53 (12), (1970), 698.

36. RICE, R.W., J. Amer. Ceram. Soc., 58 (3-4), (1975).

37. SIMPSON, L.A., RITCHIE, I.G. and LLOYD, D.T., J. Amer. Ceram. Soc., 58, (1975), 537-538.

38. DAVIDGE, R.W., TAPPIN, G.T., Proc. Br. Ceram. Soc., 15 (45), (1970).

39. COPPOLA, J.A. and BRADT, R.C., J. Amer. Ceram. Soc., 55, (1972), 455.

40. DAVIDGE, R.W., Frac. Mech. Ceram. (Plenum Press, 1974).

41. LIPLAI, R.G., HARRIS, D.O., ENGLE, R.B. and TATO, C.A., AE Tech. Met. Res. Lawrance Radlallon Lab., Univ. California, California 94550.

42. KAISER, J.K., Ph.D. Thesis, Technischе Hochschule, Munich (1950).

43. CARLYLE, J.C., M. Tech. Thesis, Brunel Univ. (1974).

44. SCHOFIELD, B.H. et al., ASTM Tech. Rep. (1958), 58-194.

45. TATRO, C.A., Div. Eng. Res., College Eng. Michigan State Univ. (1959).

46. TETELMAN, A.S. and LOW, R., AE Symp., STP 505, ASTM, (1971).

47. GRAHAM, L.J. and ALERS, G.A., North Amer. Rockwell Sci. Center, Calif. 91360 (1972).

48. FAKHR. A., FREYRE, J.E., RAWLINGS, R.D., Proc. Inst. Acoustics, Chelsea College, London (1976).

49. TETELMAN, A.S. and EVANS, A.G., Frac. Mech. Ceram., 2 (1973).

50. WACHTMAN, J.B., J. Amer. Ceram. Soc., 57 (12), (1974), 509-519.

51. EVANS, A.G. and GRAHAM, L.J., Acta Met., 23, (1973), 1303-1313.

52. STEPHENS, R.W.B. and POLLOCK, A.A., J. Acoustical Soc. Amer., 30 (3), (1971).

53. FILIPEZYNSKI, L., PAWLOWSKI, Z. and WEHR, J., "Ultrasonic Methods of Testing Mat.", (Butterworths, London, 1966).

54. POLLOCK, A.A., AE-2, NDT, (1973), 264-269.

55. SWINDLEHURST, W., AE-1, NDT, (1973), 152-156.

56. BRINDLEY, B.J., HOLT, J. and PALMER, I.G., AE-3, NDT, (1973), 299-306.

57. POLLOCK, A.A., "AE", Vol. 1 (Associated Book Pub., Ltd., London, 1973).

58. CURTIS, G., AE-4, NDT, 7 (2), (1974).

59. BETTIE, A.G., Mat. Eva., April (1973), 73-78.

60. POLLOCK, A.A., "AE, Acoustics and Vibration Progress", Ed. R.W.B. Stephens and H.G. Leventhall (Chapman and Hall, London).

61. PARKER, J.A., Proc. Inst. Acous., Chelsea College, London (1976).

62. EVANS, A.G., J. Amer. Ceram. Soc., 58 (5-6), (1975), 240.

63. EVANS, A.G., J. Mat. Sci., 1, (1972), 1137-1146.

64. EVANS, A.G., WIEDERHORN, S.M., J. Mat. Sci., 9, (1974), 270-278.

65. EVANS, A.G. and LINZER, M., J. Amer. Ceram. Soc., 56 (11), (1973), 575.

66. TATTERSALL, H.G. and TAPPIN, G., J. Mat. Sci., 1, (1966), 296.

67. DUNEGAN, H. and TETELMAN, A.S., Eng. Frac. Mech., 2 (38), (1971), 387.

68. GERBERICH, W.W. and HARTBOWER, C.E., Int. J. Frac. Mech., 3, (1967), 185.

69. FENICI, P., KIESEWETTER, N. and SCHILLER, P., Ispra Establishment Biannual Rep. (1974-1975).

70. MORTON, T.M., HARRINGTON, R.M. and BJELETICH, J.G., Eng. Frac. Mech., 5, (1973).

71. WILLIAMS, D.P. and EVANS, A.G., J. Test. Eva., 1 (4), (1973), 264-270.

72. ROMRELL, D.M. and BUNNELLT, L.R., Mat. Eva., (1970).

73. HATMAN, W.F., Mat. Eva., (1974), 204.

74. ENGLE, R.B. and DUNEGAN, H.L., Gordon and Breach Sci. Pub., 2, (1971), 165-181.

75. DUNEGAN, H.L., HARRIS, D.O., TATRO, C.A., Eng. Frac. Mech., 1, (1968), 105-122.

76. WAITE, E.V. and PARRY, D.L., Mat. Eva., (1971).

77. EVANS, A.G. and LINZER, M., Ann. Rev. Mat. Sci., (1977), 179-208.

78. HATANO, H. and MORI, E., J. Acous. Soc. Amer., 59 (2), (1976), 344.

79. CHRISTOFFERSON, B.K., 5th EWGAE Meeting, 15-16 Sept. (1976), Roskilde, Denmark.

80. MURRAY, P. and ALLISON, E.B., Trans. Br. Ceram. Soc., 53, (1959), 335.

81. POROSIMETER, Instructions for Use, Carlo Erba, Divisione Apparecchi Scientifici.

82. SRAWLEY, J.E. and BROWN, W.F., ASTM Spec. Pub. No. 381, 30-81.

83. KEIS, J.A. and CLARK, A.B.J., Proc. 2nd Int. Conf. Frac., Brighton, (1969), Paper 42.

84. Data Sheet, MC500 transducer, AE Tech. Corporation, Sacramento, California 95815, U.S.A.

85. Instructions for 105 System (Tek Totalizer), AE Consultants Ltd., Bar Hill, Cambridge, U.K.

86. Instructions for 921 Amplitude Detector, Dunegan Endevco, Rancho Viejo Rd., San Juan Capistrano, California 92675, U.S.A.

87. Instructions for 920, Dunegan Endevco, California 92675, U.S.A.

88. Instructions for 922, Dunegan Endevco, California 92675, U.S.A.

89. LANKFORD, J., J. Mat. Sci., 13, (1978), 351-357.

90. LANKFORD, J., J. Mat. Sci., 12, (1977), 791-796.

91. DALGLEISH, B.J., FAKHR, A., PRATT, P.L. and RAWLINGS, R.D., Met. Dept. Imperial College, London S.W.7 (to be published).

92. HASSELMAN, D.P.H., KENNEY, G.B. and McKINNEY, K.R., J. Amer. Ceram. Soc., 58 (9-10), (1975), 452.

93. DAVIDGE, R.W., McLAREN, J.R. and TAPPIN, G., J. Mat. Sci., 8, (1973), 1699-1705.

94. DAVIDGE, R.W., Deformation and failure in polycrystalline ceramics, 78, (1970), 1-11.

95. NADEAU, J.S., "Origins of AE in the Fracture of Glass Plates", Univ. British Columbia, Vancouver, B.C., 979-983.

96. VAINBERG, V.E. The Soviet J. NDT, (1977).

97. CREYKE, W.E.C., Joint Meeting Brit. Ceram. Soc. and Soc. Glass Tech., Sheffield, (1968).

98. STATON-BEVAN, A., Met. & Mat. Sci. Dept., Imperial College, London (Private Communication).